Through-Thickness Performance of Adhesive Connections Between FRP Bridge Decks and Steel Main Girders

THÈSE N^{O} 4300 (2009)

PRÉSENTÉE LE 26 FÉVRIER 2009
À LA FACULTE ENVIRONNEMENT NATUREL, ARCHITECTURAL ET CONSTRUIT
LABORATOIRE DE CONSTRUCTION EN COMPOSITES
SECTION D'ARCHITECTURE

ÉCOLE POLYTECHNIQUE FÉDÉRALE DE LAUSANNE

POUR L'OBTENTION DU GRADE DE DOCTEUR ÈS SCIENCES

PAR

Martin Schollmayer

acceptée sur proposition du jury:

Prof. I. Devanthéry-Lamunière, présidente du jury
Prof. T. Keller , directeur de thèse
Prof. J. Knippers, rapporteur
Prof. M. Motavalli, rapporteur
Prof. G. Sedlacek, rapporteur

ÉCOLE POLYTECHNIQUE
FÉDÉRALE DE LAUSANNE

Lausanne, EPFL
2009

Preface

Fiber-reinforced polymer (FRP) bridge deck slabs, offering reduced dead load, shorter construction time and increased durability compared to concrete decks, constitute a promising application for FRP composites. The connecting of FRP decks to steel or concrete main girders remains a challenge however, although mechanical shear stud connections, similar to those used for concrete deck fixation, provide a feasible solution. Nonetheless, the mechanical behavior of this type of connection is complex and difficult to model and reservations exist regarding durability. An alternative, much more material-tailored, technique is adhesive bonding, which reduces construction time and ensures composite action between deck and girders. Adhesive joint behavior in the longitudinal bridge direction was investigated by Herbert Gürtler in his PhD thesis (EPFL Nr. 3135, 2005), while Martin Schollmayer's thesis focuses on the transverse behavior and, combining the results obtained for behaviors in both directions, proposes the basis for a design method for such joints. The complex stress fields in the joints are analytically described and recommendations concerning construction details are given in order to limit stress peaks. Based on a shear-tensile-interaction failure criterion, the structural safety of such joints can be evaluated. I would like to acknowledge the support provided for this research project by Martin Marietta Composites, Raleigh, USA, represented by Grant Godwin.

Prof. Dr. Thomas Keller
CCLab Director/Thesis Director

Abstract

FRP bridge decks offer several advantages compared with conventional concrete bridge decks, particularly their much lower weight, but also their resistance against corrosion as well as easier installation and maintenance. The poorly conceived methods available for connecting FRP bridge decks with their supporting structures – normally steel girders – nonetheless constitute a disadvantage. Connections involving studs or bolts are not appropriate in this case, since FRP is a very brittle material that offers no ductile properties. Bolted connections usually result in much higher stress concentrations, while adhesive bonding is a more material-adapted connection method since larger surfaces can be linked together, thus ensuring reduced stresses.

The bridge system investigated in this thesis consists of a pultruded FRP bridge deck bonded to steel main girders, the bridge's main structural components, which have to transmit the dead and traffic loads to the supports, whereas the bridge deck is spanned in the transverse direction perpendicular to the steel girders. Uplift forces caused by the load-bearing behavior of the bridge deck transverse to the bridge axis lead to through-thickness tensile stresses in the adhesive joint.

The main objective of this thesis is the description of the structural behavior in the transverse direction. This includes analysis of the stresses in the adhesive connection as well as determination of the strength of the joints.

Analytical and experimental investigations were carried out. It was shown, that the tensile stress distribution in the adhesive joint is non-uniform with high stress concentrations below the FRP deck webs of the cellular deck and above the steel girder web. Alternately inclined deck webs thereby induce significantly higher stresses below the vertical webs. A method for the calculation of the stress state in the adhesive layer is proposed which is validated by numerical and experimental results. The material strength of the connection in terms of a combination of tensile through-thickness and shear stresses is established. The total safety factor of the joint was higher than the safety factor of the FRP deck for bending between the main girders. A possible failure process would not start in the adhesive connection between bridge deck and steel girder which eventually could lead to additional failure of other structural members. The system is redundant. Fatigue loading up to 10 million cycles showed no stiffness degradation.

The results of this thesis prove the existence of a good load-bearing behavior under static and fatigue loads of adhesively-bonded joints between pultruded FRP bridge decks and structural steel girders, where the adhesive connection is loaded with uplift forces and moments acting in the bridge deck, in addition to the shear in the connection layer due to composite action. The basis for a design method for adhesively-bonded connections between pultruded FRP bridge decks and steel girders is provided.

Keywords: adhesives, bonding, bridge decks, fiber-reinforced polymers, joints, pultrusion

Zusammenfassung

Im Vergleich zu konventionellen Beton-Brückenfahrbahnplatten, bieten Platten aus GFK einige Vorteile; besonders ihr erheblich geringeres Gewicht, aber auch ihre Korrosionsbeständigkeit sowie die einfachere Montage und Unterhaltung. Ein Nachteil der Verwendung von Verbindungen zwischen GFK-Brückenfahrbahnplatten und ihrer Tragstruktur, in der Regel Stahlträger, ist der Mangel an guten Verbindungsmöglichkeiten. Dübel und Schrauben als Verbindungen sind nicht gut geeignet, da GFK ein sehr sprödes Material ohne duktile Eigenschaften ist. Geschraubte Verbindungen führen in der Regel zu höheren Spannungskonzentrationen, während geklebte Verbindungen geeigneter sind, da größere Flächen miteinander verbunden werden und somit in geringeren Spannungen resultieren.

Das in dieser Arbeit untersuchte Brückensystem besteht aus pultrudierten GFK-Fahrbahnplatten, die auf Stahlträger geklebt werden. Die Stahlträger müssen als Hauptstruktur Eigen- und Verkehrslasten zu den Auflagern leiten, während die Fahrbahnplatte in Querrichtung spannt. Die durch die Tragwirkung in Querrichtung entstehenden abhebenden Kräfte führen zu Zugspannungen in der Klebefuge.

Hauptziel der Arbeit ist die Beschreibung des statischen Verhaltens in Querrichtung. Das beinhaltet die Spannungsanalyse in der Klebschicht, sowie die Ermittlung der maximal aufnehmbaren Last.

Es wurde gezeigt, dass die Verteilung der Zugspannungen in der Klebeverbindung nicht gleichförmig ist und Spannungskonzentrationen unter den Flanschen des Fahrbahnplattenprofils sowie über dem Stahlträgerflansch aufweist. Die schrägstehenden Flansche der Fahrbahnplattenprofils führen zu stark erhöhten Spannungen unter den senkrecht stehenden Flanschen. Es wurde eine Berechnungsmethode für den Spannungszustand in der Klebefuge eingebracht, die mit numerischen und experimentellen Ergebnissen bestätigt wurde. Die maximal aufnehmbare Spannungskombination aus Zug- und Schubspanunngen in der Klebeverbindung wurde ermittelt. Der Sicherheitsfaktor der Verbindung war höher als der der GFK-Platte auf Biegung belastet. Ein eventueller Versagensprozess würde nicht in der Klebeverbindung zwischen Fahrbahnplatte und Stahlträger beginnen, der zu einem Versagen der gesamten Struktur führen würde. Das System ist redundant. Eine Ermüdungsbeanspruchung mit 10 Millionen Lastzyklen führte nicht zu einer Reduzierung der Steifigkeit.

Die Ergebnisse der Arbeit zeigen eine gute Lastabtragung in den geklebten Verbindungen zwischen pultrudierten GFK-Fahrbahnplatten und Stahlträgern unter statischen und dynamischen Lasten, bei denen, neben den Schubkräften aus der

Verbundwirkung, abhebende Kräfte und Momente auf die Klebeverbindung wirken. Grundlagen für eine Bemessungsmethode für geklebte Verbindungen zwischen pultrudierten GFK-Fahrbahnplatten und Stahlträgern wurden in dieser Arbeit erarbeitet.

Stichwörter: Brückenplatte, faserverstärkte Kunststoffe, Pultrusion, geklebte Verbindungen, Klebstoffe

Acknowledgements

During the writing of this thesis, I have received support and encouragement from many people and here I would like to acknowledge those who made a particularly important contribution.

I would like to thank Prof. Dr. Thomas Keller for providing the opportunity to write this thesis and for his guidance and counsel. Special thanks also go to those who agreed to act as jury-members: Prof. Dr.-Ing. J. Knippers, Prof. Dr. M. Motavalli and Prof. Dr.-Ing. G. Sedlacek. In particular many thanks to Prof. Sedlacek for his valuable advices concerning the safety concept.

I would also like to thank the alumni Uwe Klug, Frederik Bode, Philipp Eisenbach and Sebastian Oppel, who wrote their Master theses at the CCLab and helped me directly and indirectly in the accomplishment of this project. I would like to extend my thanks to my former colleagues Till Vallée, Julia de Castro, Herbert Gürtler, Craig Tracy, Sean Dooley, Florian Riebel, Aixi Zhou, Erika Schaumann, Ye Zhang and Yu Bai. In recognition of all her help and support on the administrative side, I would like to express my gratitude to Marlène Sommer.

My special thanks to all the laboratory staff – in particular Sylvain Demierre, Hansjakob Reist and François Perrin – for helping me to set up all the tests. I gratefully acknowledge the support of *Martin Marietta Composites* and especially Grant Godwin.

I appreciated the support and help of Margaret Howett for the English-correction of this document, thanks a lot!

Finally I would like to thank my parents for their support, y sobre todo my grateful thanks to Salomé for her patience while I was working on this thesis.

Contents

Preface i

Abstract iii

Zusammenfassung v

Acknowledgements vii

I Introduction 1

1 Introduction 3
- 1.1 FRP bridge decks with adhesively-bonded connections 3
- 1.2 Objectives 6
- 1.3 Methodology 6
  - 1.3.1 Analytical determination of stress distribution 6
  - 1.3.2 Determination of failure criterion 7
  - 1.3.3 Design method for adhesive connection 7
  - 1.3.4 Experimental validation 8
- 1.4 Thesis organization 8

II State of the art 11

2 The use of FRPs in bridge deck construction to date 13
- 2.1 FRP decks for vehicle bridges 13
  - 2.1.1 Pultruded FRP bridge decks 14
  - 2.1.2 Sandwich bridge decks 17
- 2.2 Connection methods 17
  - 2.2.1 Shear stud connections 17
  - 2.2.2 Bolted connections 18
  - 2.2.3 Clamped connections 19
  - 2.2.4 Bonded connections 20
- 2.3 Conclusions 22

III Experimental investigations and numerical modeling 23

3 Full-scale adhesive connection experiments 25
  3.1 Introduction . . . 25
  3.2 Procedure . . . 25
  3.3 Stresses in adhesive layer of a reference bridge . . . 26
  3.4 Experiment description . . . 28
    3.4.1 Set-up . . . 28
    3.4.2 Numerical modeling of experimental set-up . . . 30
    3.4.3 Materials and specimens . . . 33
    3.4.4 Instrumentation and measurements . . . 37
    3.4.5 Experimental Program . . . 41
  3.5 Experimental results and discussion . . . 42
    3.5.1 Static experiments . . . 42
    3.5.2 Fatigue experiment . . . 55
  3.6 Comparison of experimental results and calculations . . . 55
    3.6.1 Deformation of bridge deck . . . 55
    3.6.2 Differential deformation at adhesive connection . . . 56
  3.7 Conclusions . . . 58

4 Evaluation of combined shear-tensile strength 59
  4.1 Introduction . . . 59
  4.2 Shear-Tensile Interaction Device . . . 59
  4.3 Experimental procedure . . . 61
  4.4 Experimental results . . . 62
    4.4.1 Strength data . . . 62
    4.4.2 Failure mode . . . 63
    4.4.3 Partial safety factor . . . 66
  4.5 Conclusions . . . 67

IV Analytical part 69

5 Influence of the torsional stiffness of steel girders 71
  5.1 Introduction . . . 71
  5.2 Objective . . . 74
  5.3 Procedure . . . 75
  5.4 Determination of the torsional stiffness of steel girders . . . 75
    5.4.1 FE model . . . 76
    5.4.2 FEA Results . . . 79
  5.5 Analytical determination of spring stiffnesses . . . 82

5.6 $\Delta M/F_{\text{up}}$ ratios obtained by a two-dimensional analysis 85
5.7 Conclusions 90

6 Determination of the stress distribution inside the adhesive layer 91
6.1 Introduction 91
6.2 Procedure 91
6.3 Numerical modeling 92
6.3.1 Introduction 92
6.3.2 Beam model 93
6.3.3 Modular deck unit (MDU) model 97
6.3.4 Conclusions from numerical modeling 103
6.4 Analytical determination of σ_z stresses 104
6.4.1 Stress distribution in x-direction 104
6.4.2 Stress distribution in y-direction 109
6.4.3 Determination of $\sigma^+_{z,\max}$ 111
6.5 Influence of bending moments on through-thickness stresses 114
6.6 Comparison with experimental results 117
6.7 Conclusions 120

7 Concept for a design method 121
7.1 Introduction 121
7.2 Determination of shear stresses in adhesive connection 122
7.2.1 Assumptions 122
7.2.2 Calculation of shear stresses 123
7.3 Design example 124
7.3.1 Through-thickness tensile stresses 125
7.3.2 Shear stresses 126
7.4 Material resistance of adhesive connection and comparison 127
7.5 Conclusions 128

V Conclusions 129

8 Conclusions 131
8.1 Structural behavior in transverse direction 131
8.2 Stress state in adhesive connection 132
8.3 Design method 132
8.4 Contribution to state of the art 133
8.5 Future research 134
8.5.1 Material 134
8.5.2 Structural system and details 134

8.5.3 Long-term and fatigue behaviors 135

VI Appendix 137

A Diagrams and photos from full-scale adhesive connection experiments 139
A.1 Diagrams of exp. *C1-1* 142
A.2 Diagrams of exp. *C1-2* 143
A.3 Diagrams and photos of exp. *C2-1* 145
A.4 Diagrams and photos of exp. *C2-2* 148
A.5 Diagrams and photos of exp. *C3-1* 151
A.6 Diagrams and photos of exp. *C3-2* 154
A.7 Comparison of experimental results and calculations 157

B Steel girder geometries with respective torsional stiffnesses k_ϑ 161

C Stress analysis parameter study diagrams 163
C.1 Dependence of factor n_x on ratio $\frac{t_{sw}}{t_p}$ 163
C.2 Comparison of analytical and numerical results 164
C.3 Superposed stress distributions 175

Bibliography 181

List of Figures 189

List of Tables 195

Nomenclatures 197

Index 201

Curriculum vitæ 203

Part I

Introduction

1 Introduction

1.1 FRP bridge decks with adhesively-bonded connections

Fiber-reinforced polymers (FRPs) offer a lightweight and innovative alternative to traditional materials such as steel and concrete in structural engineering. In bridge engineering especially, pultruded FRP bridge decks present several advantages compared to conventional concrete decks:

- Light weight (approximately one fifth of that of a concrete deck with similar geometry) combined with the high strength of the material;
- Faster installation on the construction site;
- Chemical resistance (e.g. against de-icing salts) of the material, and therefore reduced maintenance costs.

However, many technical problems related to the structural design of bridges with pultruded FRP decks have still not been solved, or at least only partially. These include the connection between the main girders and the bridge deck: *Bonding* and *Bolting* are the two main – but contrasting – connection methods used for FRP structural components. *Bonding* is the connection of structural parts using adhesives. *Bolting* is the connection of members using mechanical junctions.

As FRP materials are brittle and anisotropic, care must be taken wherever stress concentrations occur, and this particularly applies to bolted connections since the latter usually result in much higher stress concentrations than bonded ones. Therefore, adhesive bonding is a more material-adapted connection method than bolted connections, since larger surfaces can be linked together, thus ensuring reduced stresses.

The bridge system investigated in this thesis consists of a pultruded FRP bridge deck bonded to steel main girders. A simple sketch explaining the system is shown in Figure 1.1 on the following page. The steel girders are the bridge's main structural components, which have to transmit the dead and traffic loads to the supports, whereas the bridge deck is spanned in the transverse direction perpendicular to the steel girders. The two structural components are bonded together by an adhesive layer with a thickness of approximately 6–20 mm. This relatively thick adhesive layer is necessary to compensate tolerances, i.e. to adjust differences in the level of the supporting steel girders.

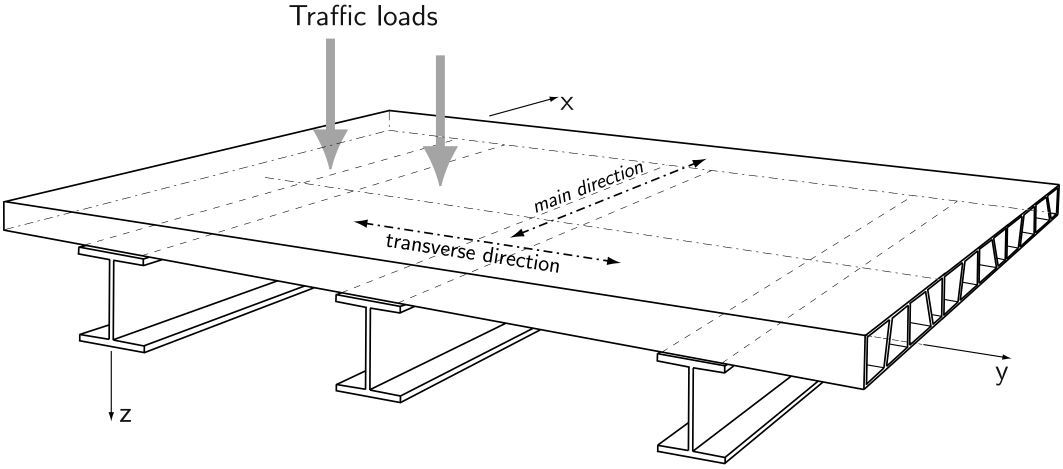

Figure 1.1: Basic diagram of a pultruded FRP bridge deck adhesively bonded to steel girders

In bridges with FRP decks built to date, almost all connection methods involved mechanical fastening, such as bolts or clamps. The main advantages of adhesively-bonded connections compared to existing ones are:

- Reduced labor costs. Mechanical connections with shear studs, bolts and clamps require a great deal of work on the construction site, such as drilling holes in the bridge deck and welding mechanical fasteners to steel girders (see Section 2.2, page 17 ff.).
- Prevention of high stress concentrations, due to the larger areas which are linked to each other.
- Composite action resulting from the bonded connection between the bridge deck and steel girder that increases the stiffness and strength of the whole structure, therefore allowing a reduction in the amount of material used for the steel girders.

Different stress conditions in the adhesive layer may be caused by the following phenomena:

1. Shear stresses in the longitudinal direction due to composite action between the pultruded FRP bridge deck and the steel girders (τ_{xz} in Figure 1.2).*

---

*Shear stresses τ_{yz} that might occur due to horizontal loadings are assumed to be negligibly small.

2. Normal through-thickness stresses (σ_z): compression stresses in the adhesive layer occur due to loading of the bridge deck, but tensile stresses also occur due to uplift force and bending moment. The distribution and amount of the uplift force and bending moment mainly depend on the rotational stiffness of the supporting steel girders, see Figures 1.2 and 1.3.

All stress conditions must be taken into account simultaneously.

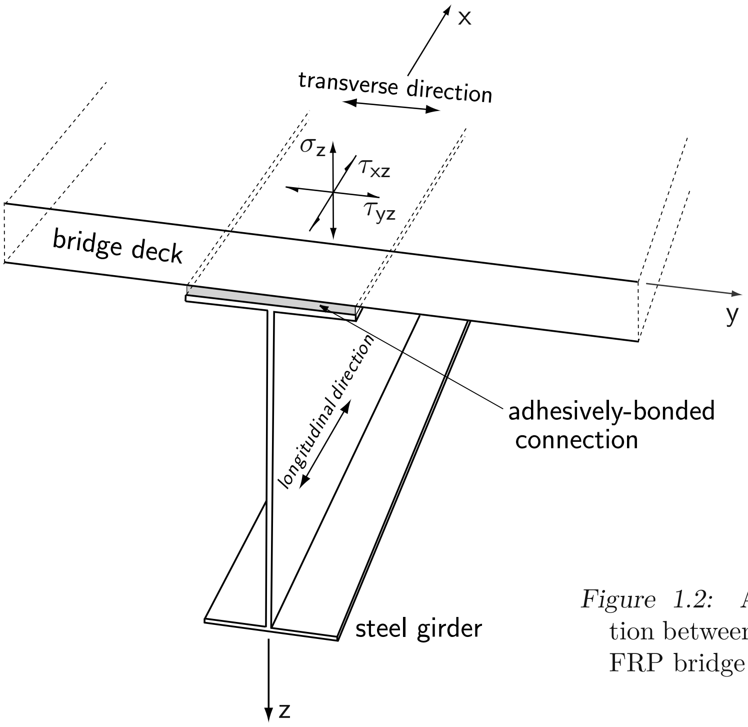
x
transverse direction
σ_z
τ_{xz}
τ_{yz}
bridge deck
y
longitudinal direction
adhesively-bonded connection
steel girder
z

Figure 1.2: Adhesively-bonded connection between steel girder and pultruded FRP bridge deck

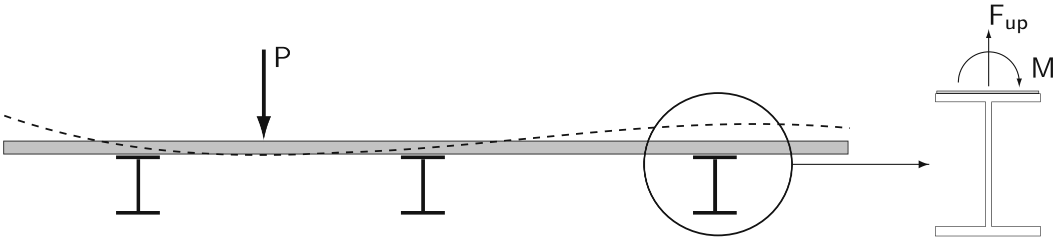

Figure 1.3: Uplift force and bending moment in adhesive layer caused by load on bridge deck

1.2 Objectives

The increased use of FRP bridge decks over recent years calls for the development of connection methods for this kind of structural member. The longitudinal behavior of FRP bridge decks adhesively bonded to steel girders has recently been investigated in [Gür04, KG05a, KG05b]. Composite action between the bridge deck and the steel girders leads to shear stresses in the adhesive connections.

Uniformly distributed and single loads on the bridge deck can result in uplift forces that lead to through-thickness tensile stresses inside the adhesive layer. Both stress conditions – shear due to composite action in the longitudinal direction as well as through-thickness tension due to uplift forces and bending in the transverse direction – have to be analyzed and the determined stresses compared to the material resistance.

The main objective of this thesis is the description of the structural behavior in the transverse direction. This includes analysis of the stresses in the adhesive connection as well as determination of the strength of the connections. Existing knowledge regarding the behavior in the longitudinal direction will be integrated into the investigations carried out in this thesis, resulting in a method allowing the structural design of adhesively-bonded connections between pultruded FRP bridge decks and steel main girders.

The achievement of this objective involved the following steps:

1. Experimental investigations concerning the through-thickness strength of an adhesive connection between FRP deck and steel girder.
2. Investigation of the influence of the steel girder geometry (i.e. its torsional stiffness) on the distribution of through-thickness stresses in the adhesive connection.
3. Numerical modeling and analytical description of the through-thickness stress distribution resulting from inner reaction forces.
4. Determination of a combined through-thickness tensile-shear failure criterion as basis for the design of the connection.

1.3 Methodology

1.3.1 Analytical determination of stress distribution

Based on an analytical determination of the through-thickness stresses σ_z, it will be possible to calculate the maximum tensile stresses inside the adhesive layer and the surface mats of the FRP bridge deck caused by uplift forces and bending moments inside the bridge deck, taking into account the torsional stiffness of the steel girders.

1.3.2 Determination of failure criterion

According to previous research, the strength of bonded connections using pultruded FRP materials depends mainly on the shear-tensile stress combination inside the surface layer of the FRP. As investigated in [Val04], a characteristic failure mode, a fiber-tear failure (according to [ast00]), occurs in the surface mat layers of the pultruded material (see Figure 1.4).

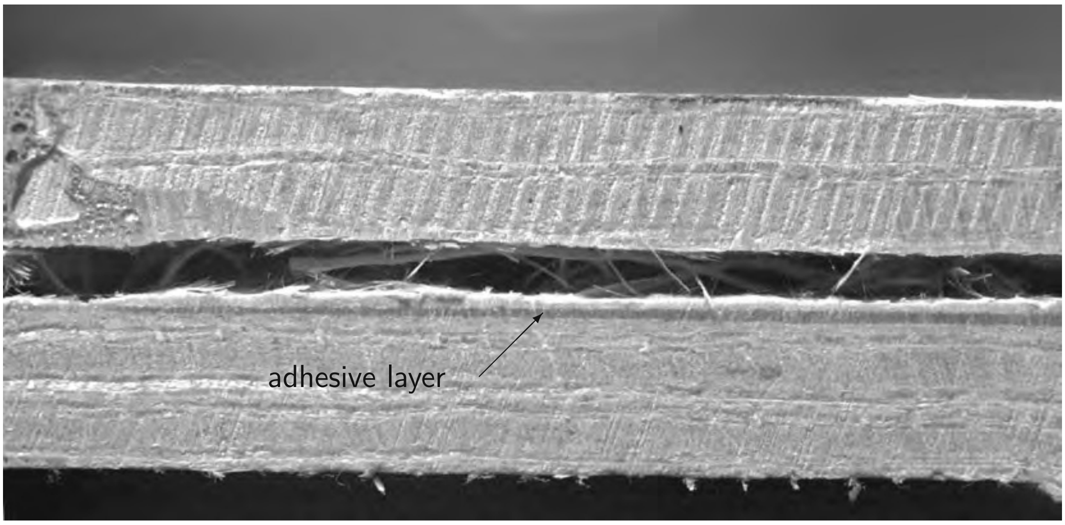

Figure 1.4: Failure in surface mat layers of pultruded FRP material [KS04]

The through-thickness tensile and shear strengths will be investigated in small-scale experiments using the Shear-Tensile Interaction Device developed in the *CCLab* (see Figure 4.1 on page 60). This allows the simultaneous loading of bonded coupons with a through-thickness tensile force and a shear force. The stress interaction behavior of tension and shear stresses will be especially examined and a combined failure criterion will be developed based on these experiments.

1.3.3 Design method for adhesive connection

For the designing of the adhesive layer between the steel girder and the FRP bridge deck, the determined stresses in the surface mat layers of the bridge deck are compared with the corresponding material resistance.

Basically, stresses due to design loads S_d are compared with the design value of material strength R_d of the adhesively-bonded connections ($R_d \overset{!}{\geq} S_d$) ; safety factors are also provided.

1.3.4 Experimental validation

The design method will be validated by large-scale experiments on six full-scale adhesive connections between pultruded FRP bridge decks and steel girders. As a result, a method for designing adhesively-bonded connections in a bridge consisting of an FRP bridge deck adhesively bonded to steel main girders will be proposed.

1.4 Thesis organization

The organization of the thesis is shown in Figure 1.5 on page 10. The thesis is divided into five parts:

Part I introduces the key issues involved in the subject.

Part II, the *State of the art*, describes the use of pultruded FRP bridge decks and the methods used to connect them to steel girders in the past, demonstrating the need for adhesively-bonded connections between bridge decks and steel girders.

Part III, the experimental part, comprises two chapters:

The behavior of a full-scale adhesive connection is investigated in Chapter 3 *(Full-scale adhesive connection experiments)*. The adhesively-bonded connections are tested in a cantilever beam set-up. The connections are loaded with pure uplift forces.

In Chapter 4, *Evaluation of the combined shear-tensile strength*, the material strength of the adhesive connections is investigated. The maximum stress combinations leading to a failure in the surface mat layers of the FRP material are described, which is essential for prediction of failure in the adhesive connection.

Part IV is the analytical part of the thesis.

In Chapter 5 the influence of the torsional stiffness of the steel girders on inner forces acting in the adhesive connection is investigated. The structure of the bridge is analyzed and a simplification of the structure is developed in order to obtain a method allowing analytical calculations on 2D systems.

Chapter 6 *(Determination of the stress distribution inside the adhesive layer)* provides an analytical method to approximate the stress distribution inside the adhesive layer and makes comparisons with FEM calculations.

Chapter 7 introduces a *Concept for a design method* for adhesively-bonded connections between FRP bridge decks and steel girders, using the results elaborated in this thesis.

Part V presents the conclusions drawn in this thesis.

Part VI is the Appendix, containing additional figures and tables.

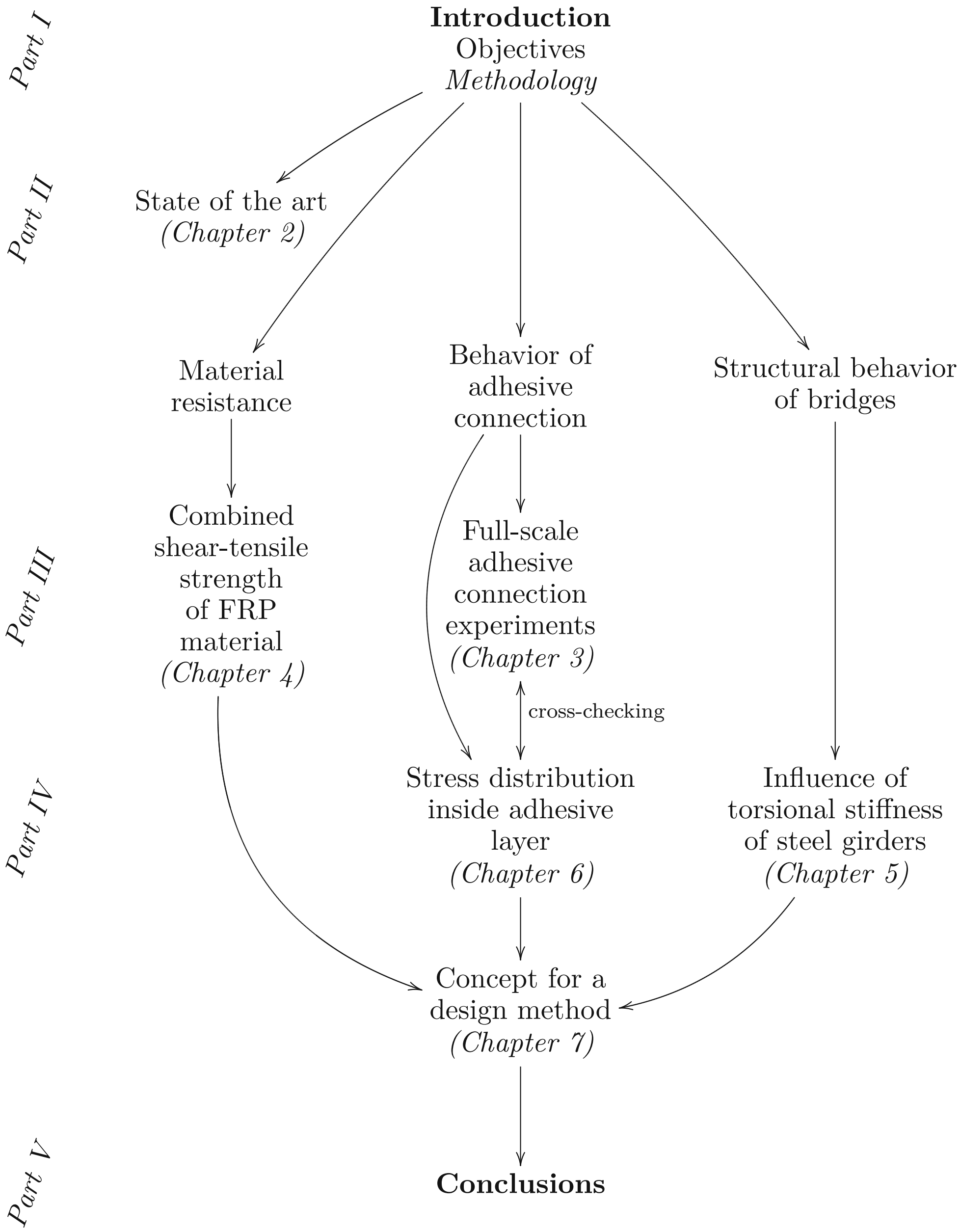
Part I
Introduction
Objectives
Methodology
Part II
State of the art
(Chapter 2)
Material resistance
Behavior of adhesive connection
Structural behavior of bridges
Part III
Combined shear-tensile strength of FRP material
(Chapter 4)
Full-scale adhesive connection experiments
(Chapter 3)
cross-checking
Part IV
Stress distribution inside adhesive layer
(Chapter 6)
Influence of torsional stiffness of steel girders
(Chapter 5)
Concept for a design method
(Chapter 7)
Part V
Conclusions

Figure 1.5: Methodology and organization

Part II

State of the art

2 The use of FRPs in bridge deck construction to date

The first use of FRPs in civil engineering structures dates back to the 1950s, for one-story single-family houses for instance. Over the last two decades the importance and use of composite materials have expanded from intermediate technology systems, employing the labor-intensive hand lay-up fabrication process, to high-tech automated production methods such as pultrusion, filament winding and hot press techniques [Hol94]. The use of FRP structural components such as pultruded fiber-reinforced polymers in civil engineering is somewhat limited however compared to the use of steel and concrete, and is mostly confined to specialty applications where resistance to highly corrosive environments, electromagnetic transparency, or a low weight-to-strength ratio is required [BW94].

Compared to other materials used in the field of civil engineering, there is still a great deal of demand for research to develop a wide range of different applications concerning the utilization of FRPs by civil engineers. The use of adhesive bonding for load-bearing elements is rare in civil engineering structures and there is therefore no standard code concerning this kind of engineering application.

2.1 FRP decks for vehicle bridges

FRP bridge decks offer several advantages over reinforced concrete bridge decks:

- → Exhibiting a very high material strength-weight ratio and extreme resistance against frost and de-icing salts, these materials are suitable for bridge deck applications, thus providing a more durable and lightweight alternative to concrete bridge decks.
- → The simple, modular nature of FRP bridge deck construction is an additional benefit. Installation is relatively rapid, reducing inconvenience to the traveling public [AK02].
- → Furthermore, they can advantageously replace concrete decks: due to the very low dead loads (approximately 20 % of those of concrete bridge decks), live loads can be increased, for example by adding lanes without any increase in girder loading [LCC$^+$02].

Several FRP bridge deck concepts have been developed, some of which are shown in Figure 2.1 on the facing page. The following fabrication techniques are used for FRP bridge decks: pultrusion, filament winding, vacuum-assisted resin transfer molding (VARTM), resin infusion and hand lay-up. The FRP bridge decks available on the market can be divided into two major groups: those consisting of pultruded profiles (see Figure 2.1(a), 2.1(b) and 2.1(d)) and those consisting of sandwich panels (Figure 2.1(c) and 2.1(e)).

2.1.1 Pultruded FRP bridge decks

Pultrusion* is probably the best method for producing composite bridge decks since it involves low processing costs and ensures a high performance level due to repeatability [Kar96].

The first pultruded bridge deck system was developed in the early 1990s in England. In 1994 the Bonds Mill bridge was built using *ACCS*† elements, developed and manufactured by *Maunsell Structural Plastics* [LHTH95]. The Bonds Mill bridge, with a span of 8.5 m, was the first all-composite bridge.

Pultruded bridge decks usually comprise a *slot and key* system, i.e. parts with a width of approximately 30 to 50 cm are pultruded and bonded together, see Figure 2.1(a) on the next page. Apart from certain short span bridge deck systems, pultruded bridge decks always have main girders as support, usually made of steel.

The most common bridge deck in the U. S. is the *DuraSpan*™ system produced by *Martin Marietta Composites*. Its fabrication began in 1992, and today more than 25 bridges incorporating this deck are already in use [Ame, mmc05]. Some of these bridges were originally built with concrete bridge decks and then upgraded by replacing these with pultruded versions [SG02].

A very special project, which was also extensively reported in literature, is the *Kings Stormwater* bridge [BZL$^+$00, KSB$^+$00, BKSK01, SKZH01]. This uses prefabricated thin carbon shells as girders, which are produced by filament winding and then filled with lightweight concrete on site. A pultruded bridge deck is connected to the tube structure using a rather complicated and labor-intensive method. A cross section of the bridge is shown in Figure 2.2, and a connection detail in Figure 2.5 on page 18.

The *Virginia Tech Deck* consists of quadratic pultruded profiles with a width of 152 mm and two 10-mm additional face panels which are bonded to the top and bottom using an epoxy adhesive [TL00]. The system is shown in Figures 2.6 and 2.7 on page 19.

---

* The term *pultrusion* is a combination of *pull+extrude*. A very detailed description of the pultrusion process can be found in the *ASM Handbook, Vol. 21* [Hen01].

† *ACCS* – Advanced Composite Construction System

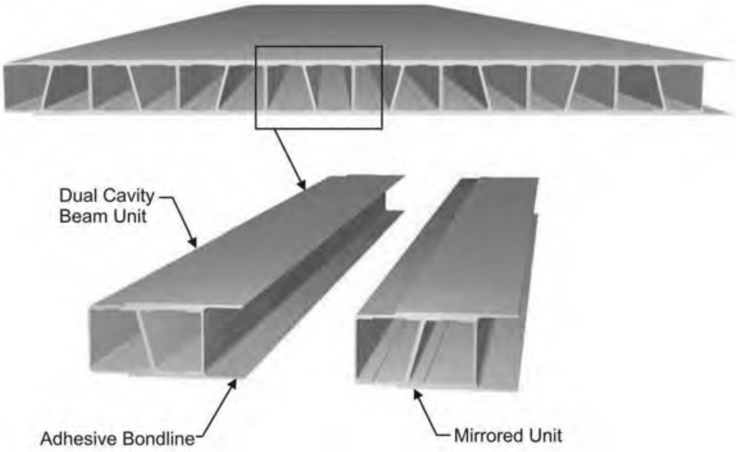
Dual Cavity Beam Unit
Adhesive Bondline
Mirrored Unit

(a) The *DuraSpan* bridge deck system (pultruded)

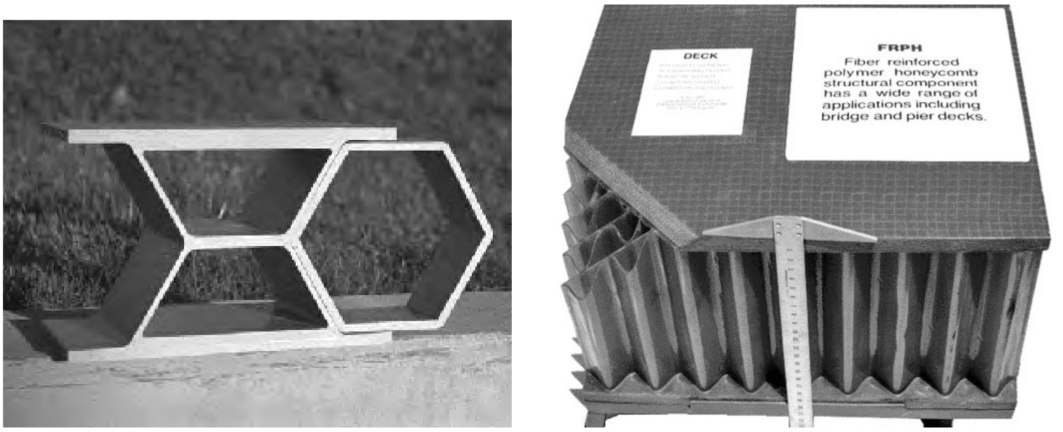
DECK
FRPH
Fiber reinforced polymer honeycomb structural component has a wide range of applications including bridge and pier decks.

(b) Superdeck (pultruded) (c) Kansas (sandwich, hand lay-up)

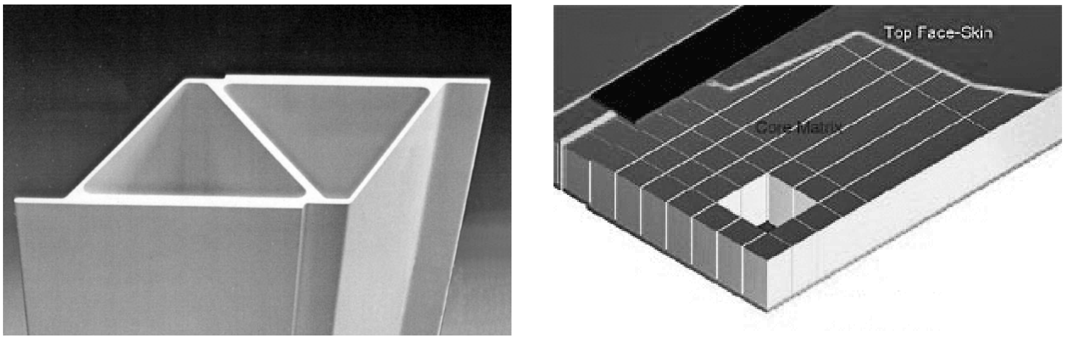
Top Face-Skin
Core Matrix

(d) Asset (pultruded) (e) Hardcore (VARTM)

Figure 2.1: Different FRP bridge deck systems [KCDD01]

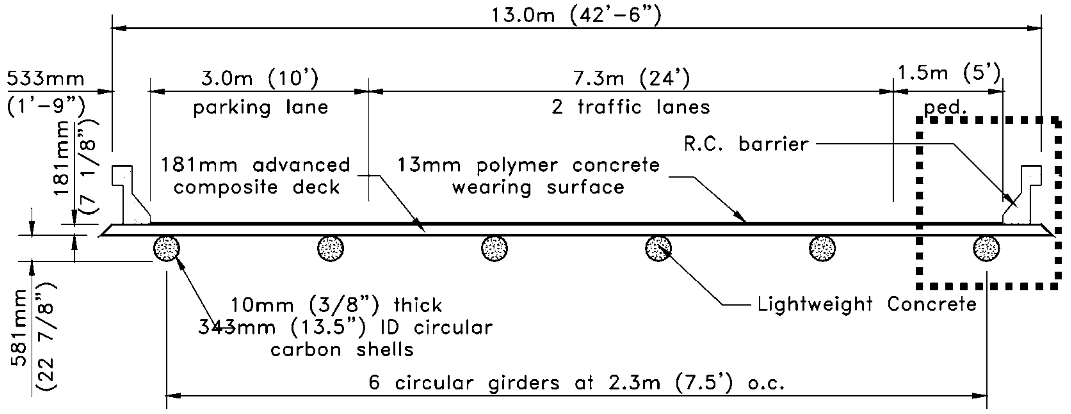
13.0m (42'-6")
533mm
(1'-9")
3.0m (10')
parking lane
7.3m (24')
2 traffic lanes
1.5m (5')
ped.
181mm
(7 1/8")
R.C. barrier
181mm advanced
composite deck
13mm polymer concrete
wearing surface
581mm
(22 7/8")
10mm (3/8") thick
343mm (13.5") ID circular
carbon shells
Lightweight Concrete
6 circular girders at 2.3m (7.5') o.c.

Figure 2.2: Cross section of *Kings Stormwater* bridge [ZKHS04]

In 2002 the West Mill public highway bridge was opened in the county of Oxfordshire, U. K. In addition to the pultruded bridge deck of the 10-m-span bridge, built using the ASSET ‡ system from the Danish company Fiberline, the structural girders are also composed of pultruded profiles. A cross section is shown in Figure 2.3. All connections between the stringer and the bridge were adhesively bonded using an epoxy adhesive [LCC$^+$02].

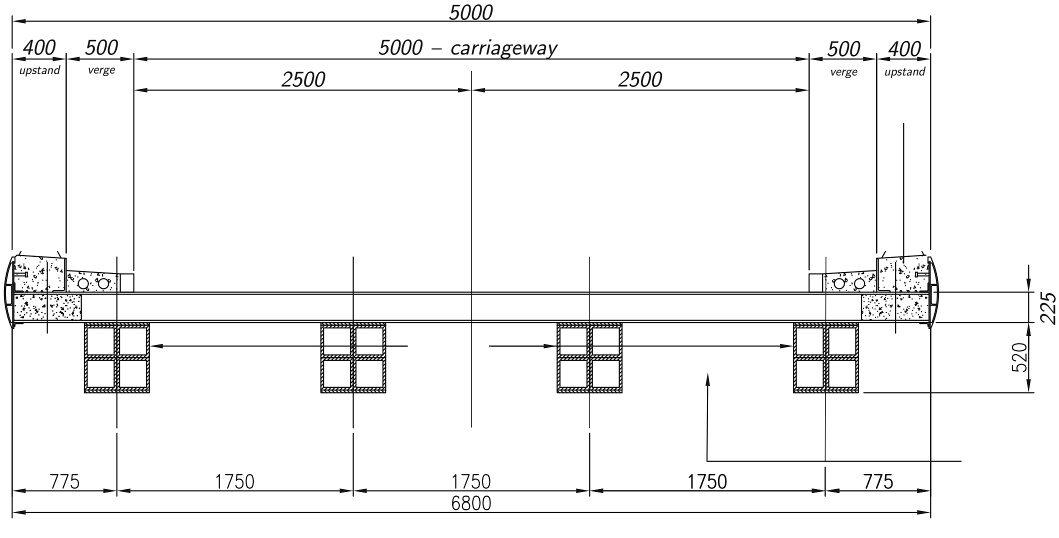
5000
400
upstand
500
verge
5000 – carriageway
500
verge
400
upstand
2500
2500
225
520
775
1750
1750
1750
775
6800

Figure 2.3: Cross section of *West Mill* bridge

---

‡adv*A*nced *S*tructural *S*yst*E*ms for *T*omorrow's infrastructure

2.1.2 Sandwich bridge decks

Sandwich decks are composed of very stiff, strong face sheet panels which bear flexural loads, bonded to a lightweight core material [HA03]. The best known and most used sandwich panel systems in bridge construction are the *Kansas* and *Hardcore* decks [BBB$^+$02], see Figure 2.1(c) and 2.1(e).

Kansas Structural Composites, Inc. manufactures an FRP deck composed of top and bottom face sheets with a sinusoidal honeycomb FRP core. The first all-composite bridge in the U. S. was built over No-Name Creek near Russel/Kansas in 1996 using the *Kansas* deck [DQX$^+$01, KSC]. The 7.6-m-span two-lane bridge was installed without any supporting steel girders or concrete stringers with a 19-mm-thick polymer concrete surface; even the guard rails are made of pultruded profiles.

The *Hardcore* deck system is fabricated using a mainly automated technology known as *VARTM*[§]. The first bridge using the *Hardcore* bridge deck was built in 1997 in Delaware, U. S., has a total span of 23 m and is supported by concrete girders. In some cases this deck was also used to replace old concrete bridge decks in renovations and to improve the load rate of bridges [AK02].

2.2 Connection methods

Possible ways of connecting FRP bridge decks and structural girders are mechanical fastening, adhesive bonding or a combination of both [ZÅBB01, ZK04]. Whichever connection is chosen, resistance to loading according to design codes and environmental effects and ease of construction must be taken into account. Connection methods can be divided into concepts with and without composite action: most systems using mechanical fastening do not transfer in-plane shear, i.e. they work without composite action. Adhesively-bonded connections are able to guarantee composite action between the steel girder and FRP bridge deck (see [Gür04]).

In the following, existing deck-to-girder connections are discussed. All connections have to transfer horizontal in-plane and vertical (uplift) forces between deck and girders.

2.2.1 Shear stud connections

The use of shear stud connections in combination with pultruded FRP bridge decks requires accurate and complex work to be carried out on the construction site: holes have to be drilled into the bridge deck at the locations of the shear studs and the shear studs are then welded to the girder. According to [RBD04] field welding is recommended in order to avoid any potential misalignment between the holes and the studs. The internal space must be blocked off, e.g. with cardboard, foam inserts or composite sleeves, and is filled with non-shrink grout. The hole on the surface is covered with a flat sheet. A typical example of a bridge with shear stud connections is shown in Figure 2.4. This type of installation is fairly labor-intensive and thus expensive. The manufacturing of the grout pockets, which have to be closed to prevent the non-shrink grout from spilling out, is a particularly complicated step in the installation process. Furthermore, little is known concerning the durability of this connection type.

[§] *V*acuum-*A*ssisted *R*esin *T*ransfer *M*olding

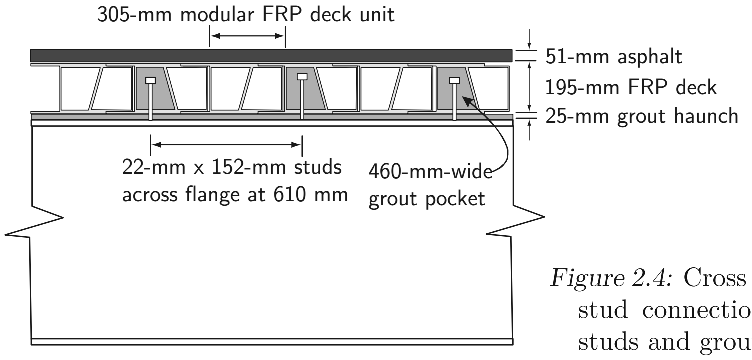
305-mm modular FRP deck unit
51-mm asphalt
195-mm FRP deck
25-mm grout haunch
22-mm x 152-mm studs across flange at 610 mm
460-mm-wide grout pocket

Figure 2.4: Cross section of girder with shear stud connections showing haunch, shear studs and grout pocket [THPR04]

A similar connection method involves the use of dowels in the case of concrete girders as shown in Figure 2.5, which requires a considerable amount of complicated, accurate and time-consuming work.

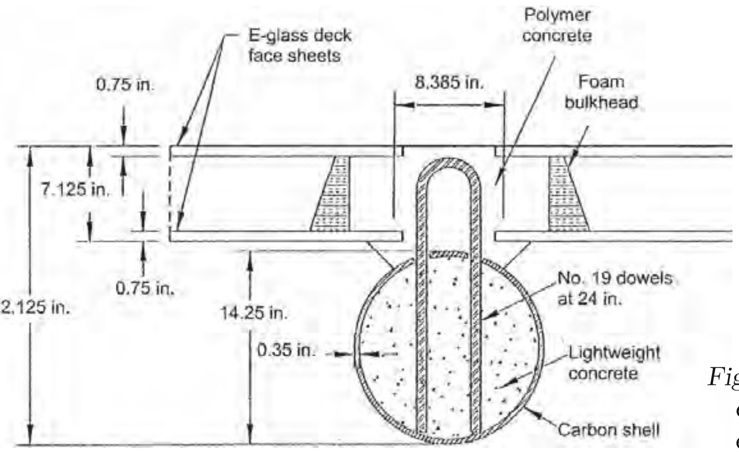
E-glass deck face sheets
Polymer concrete
0.75 in.
8.385 in.
Foam bulkhead
7.125 in.
0.75 in.
22.125 in.
14.25 in.
No. 19 dowels at 24 in.
0.35 in.
Lightweight concrete
Carbon shell

Figure 2.5: Deck-to-girder connection using dowels [Sei01]

2.2.2 Bolted connections

Two kinds of bolted connections are shown in Figures 2.6 and 2.7, both used with the *Virginia Tech Deck*, which is comprised of standard pultruded square profiles and face panels on the top and bottom. The profiles are bonded together using steel rods to apply a clamping force and also as an anchorage for the hook bolts, see Figure 2.6. Figure 2.7 shows two examples of the same bridge deck system using simple bolts, with a steel sleeve enclosing the top face panel and with only a bolt fixing the lower face panel.

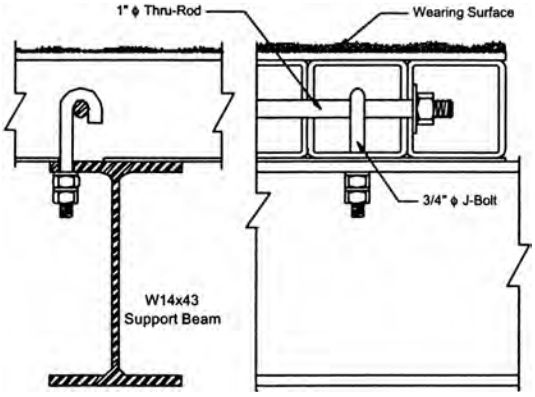
1" ϕ Thru-Rod
Wearing Surface
3/4" ϕ J-Bolt
W14x43
Support Beam

Figure 2.6: Hook bolt connection between deck and support member [ZCLC01]

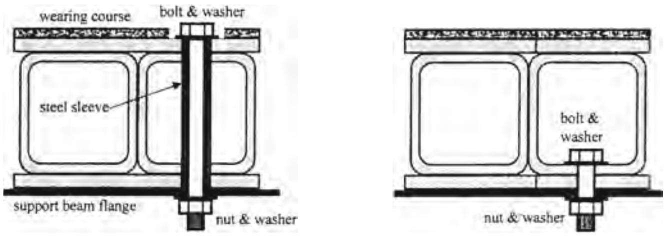
wearing course
bolt & washer
steel sleeve
support beam flange
nut & washer
bolt &
washer
nut & washer

(a) Bolt with steel sleeve enclosing top face panel

(b) Bolt fixing lower panel

Figure 2.7: Bolted connection used with *Virginia Tech Deck* [TL00]

2.2.3 Clamped connections

Clamped connections are often used with sandwich decks. Due to the varying section height, which is often more than 50 cm, connection is not as simple as with pultruded decks. Furthermore, sandwich decks do not provide the hollow space between the face panels which could be used for installing the connections and these connections therefore have to be placed outside the bridge deck, as is the case with clamped connections.

Figure 2.8 shows a connection used with the *Kansas* deck. The clamp-type connections are placed as panel-to-panel joints, with each joint comprising an FRP tube containing the connection. Holes are drilled through the tube and steel bolts are used to secure a clamping device installed underneath the top flange of the girder [RBD04]. All the previously described connection types do not guarantee any – or only partial – composite action between the main girder and the bridge deck.

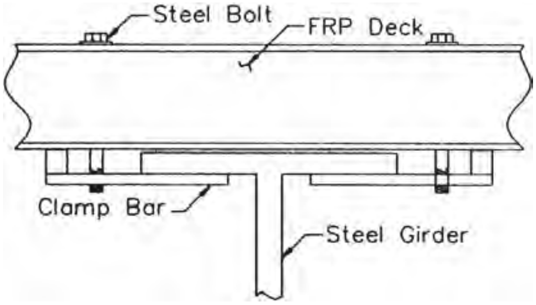

Figure 2.8: Cross section of girder and clamped connection [RBD04]

2.2.4 Bonded connections

The main advantage of adhesively-bonded connections over mechanical fastening is the avoidance of stress concentrations, which is important mainly when brittle materials, such as FRPs, are used. Furthermore, full composite action between the deck and the girder is guaranteed [Gür04].

Although adhesive bonding is successfully applied in many branches of industry (e.g. the automotive industry), it is rarely used in civil engineering. Typical applications are the strengthening of concrete columns and beams with carbon fiber-reinforced polymer strips, the bonding of facade elements to steel structures and adhesive fillings for sealing up fugues [Kla02]. Bonding as a method of connecting load-bearing members is still not widely used in civil engineering however.

The use of bonding in bridge engineering dates back to 1955: in Marl (Germany) a 56-m-span steel bridge with bonded connections was built, with the polyester resin *Vestopal LZ*® used as adhesive. The structural parts were joined using hybrid connections (bonded and bolted), thereby improving joint stiffness thanks to the adhesive [TD64].

Adhesively-bonded connections between a prefabricated concrete bridge deck and steel girders were used in the late 1960s in bridges built in Germany [HK68, Krä69, Hän76]. This was the first time that adhesive bonding was used for connections of this type, which were designed without the need for any supplementary bolts. A two-component epoxy adhesive was used for adhesive layers with a thickness of between 5 mm and 15 mm. One reason for using adhesive connections was the time-saving achieved, while another was to profit from the high shear capacity of the adhesive connection to ensure composite action between bridge deck and steel girder. Between 1968 and 1992 seven bridges with spans ranging from 15 m to 32 m were built in the former German Democratic Republic [Fie01].

In a pedestrian bridge built in 1997 in Pontresina, Switzerland consisting of two simple beams each with a 12.5-m span, fully load-bearing bonded connection members were used. One girder comprised mechanical fasteners only, while the connections of the other girder were also adhesively bonded. Experiments showed that the girder with bonded connections was stiffer, even after removal of the bolts [SK99].

Adhesively-bonded connections with pultruded FRP bridge decks have only been used recently in road bridges. An example of a bridge built exclusively with pultruded FRP elements which were adhesively connected is the previously mentioned *West Mill bridge* [LCC$^+$02], shown in Figure 2.3.

A hybrid bridge girder concept with adhesively-bonded and compositely acting FRP deck was developed and described in [Gür04]. The girder concept was investigated both experimentally and analytically: in a first step, the in-plane load-bearing performance of FRP decks acting compositely as part of the top chords of steel girders was investigated. In a second step, the static and fatigue behaviors of four full-scale girders were examined by means of four-point bending tests, see Figure 2.9. Finally, a design method for hybrid FRP-steel girders with flexible shear connections was established.

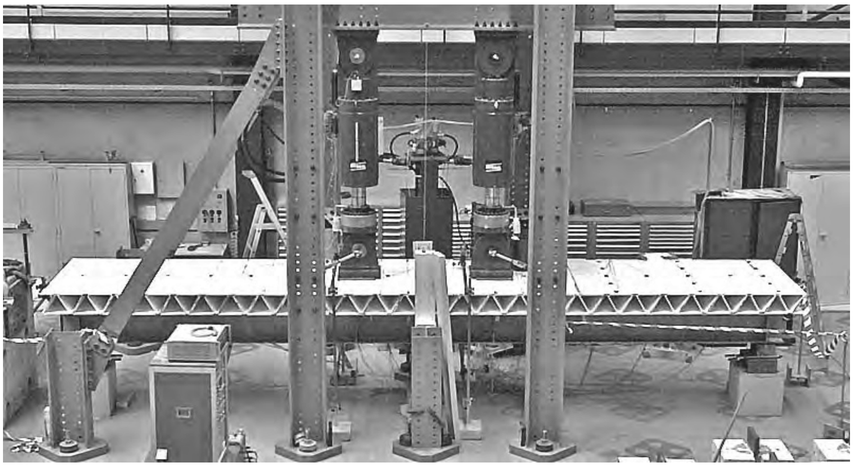

Figure 2.9: Hybrid bridge girder in four-point bending test [Gür04]

The project showed that the composite action between FRP bridge deck and steel girder increases stiffness and resistance and considerably reduces the deflections of the composite girders, while the manufacturing method is reliable and effective and the connection provides full composite action. Thus the assumption of full composite action is justifiable even for high adhesive thicknesses and soft adhesives. The developed design method allows determination of cross-sectional stress/strain distribution and deflections of FRP-steel composite girders in the elastic region. The method provides results similar to the values measured in the experiments and is therefore also well suited for determining the load-bearing behavior of FRP-steel composite girders. It was shown that adhesive bonding is a feasible and reliable connection technique for FRP-steel composite girders.

2.3 Conclusions

The methods used to connect pultruded FRP bridge decks to steel girders to date all involve mechanical fastening using bolts or studs as connection elements. These methods are generally very time-consuming in the construction process and therefore expensive. Furthermore, they are not adapted to the very brittle properties of FRP materials, since high stress concentrations occur at connection points in the bridge decks. Bonding is therefore a connection method that can allow several of the disadvantages related to existing and still applied connection methods to be avoided.

While in [Gür04] the composite action between the bridge deck and structural steel girders was investigated and described, i.e. the behavior in the longitudinal direction, this thesis will investigate and present the hitherto lacking description of the transverse behavior of adhesively-bonded connections acting in a system with FRP bridge decks spanned over several steel girders.

Part III

Experimental investigations and numerical modeling

3 Full-scale adhesive connection experiments

3.1 Introduction

The experiments described in this chapter were carried out in order to examine the static and fatigue behaviors and failure mode of adhesively-bonded connections between pultruded FRP bridge deck elements and steel girders subjected to uplift forces due to traffic loads. The main objective of these full-scale adhesive connection experiments was the validation of the developed calculation method (see Chapters 6 and 7).

3.2 Procedure

Calculations were performed prior to the experiments to determine the stress situation in the adhesive layer under unfavorable loadings on a reference bridge. The intention was to define the loading for the experimental series, to ensure a similar stress condition in the adhesive layer of the connection to that in the reference bridge. These theoretical investigations and the experimental program comprised the following steps:

1. FE modeling and analysis of a reference bridge section with adhesively-bonded connection between structural steel girders and FRP bridge deck to determine the maximum tensile through-thickness stresses that could occur in the bridge's connection layer.

2. Establishment of a test set-up for the experiments based on the results obtained for the reference bridge. The set-up is a cantilever system loaded in such a way that a similar stress situation occurs in the adhesive layer to that determined from calculations on the reference bridge.

3. Modeling of the geometry of the test set-up in an FEA program to analyze and validate the stress situation occurring in the adhesive layer.

4. Performance of six quasi-static experiments and one fatigue experiment. It was assumed that six experiments would provide an adequate set of test data. A fatigue experiment was performed over a period of three months in order to prove the resistance of the adhesively-bonded connection to traffic loads.

5. Evaluation, analysis and interpretation of the experimental results and comparison to the previously performed numerical calculations.

3.3 Stresses in adhesive layer of a reference bridge

Since the objective of the experimental series was to perform tests with a similar through-thickness stress condition in the adhesive layer as would occur in a bridge, a part of a reference bridge was modeled for numerical calculations. As the through-thickness tensile stresses in the adhesive layer are influenced by the transversal load-bearing behavior, the bridge span plays only a secondary role. Therefore, a section was modeled and subjected to traffic loads according to the European code EC 1. The total width of the reference bridge was 10.8 m with a girder distance in the transverse direction of 2.7 m, see Figure 3.1 on the next page. Due to symmetry boundary conditions the calculation was made on a 3.6-m-long bridge section, while a 1.8-m-long section of a bridge was modeled. An important deciding factor for this section length was the stress distribution inside the bridge deck, as shown in [KS04], for a bridge deck system with a transverse span of 2.7 m : 90 % of the load is borne by four pultruded profiles (loaded on a 0.4 m × 0.4 -m load pad). It was therefore assumed that the loads are transmitted to the girders by no more than 8 bridge deck profiles. The model consisted of twelve (two times six) bridge deck profiles, with four extra profiles being modeled to prevent any potential influence from the free edges. The upper flange of the steel girder was 400 mm wide with an adhesive thickness of 8 mm.

The bridge section was modeled using the FE program *Ansys*. For all members the volume element *SOLID 185* was used. For the bridge deck, orthotropic material properties as indicated in Table 3.3, page 35, were chosen. The steel girders consisted of isotropic elements with an elastic modulus of $E_s = 210\,\text{kN/mm}^2$. The adhesive layer was modeled as an isotropic material with an elastic modulus of $E_\text{adh} = 4.5\,\text{kN/mm}^2$, which corresponds to the tensile modulus of the *SikaDur 330* epoxy resin. The single loads, 150 kN each, were placed 0.6 m inside the symmetry axis. This resulted in the four-wheel load model as defined in the EC 1. In addition, uniformly distributed loads were placed on the bridge deck: $9\,\text{kN/m}^2$ on the lane where the single loads were placed, and $2.5\,\text{kN/m}^2$ on the remainder of the bridge deck.

The average through-thickness tensile stress in the adhesive layer was $0.15\,\text{N/mm}^2$, the maximum tensile stresses occurring over steel girder ③, at a distance of 60 cm from the symmetry axis (B in Figure 3.1) with a tensile stress $\sigma^+_{z,\text{max}} = 0.54\,\text{N/mm}^2$ (in the serviceability limit state). The peak occurred under the same bridge deck web on which the loads were placed, the vertical web next to it exhibiting much lower stress values. Another stress peak occurred right at the edge of the model (A).

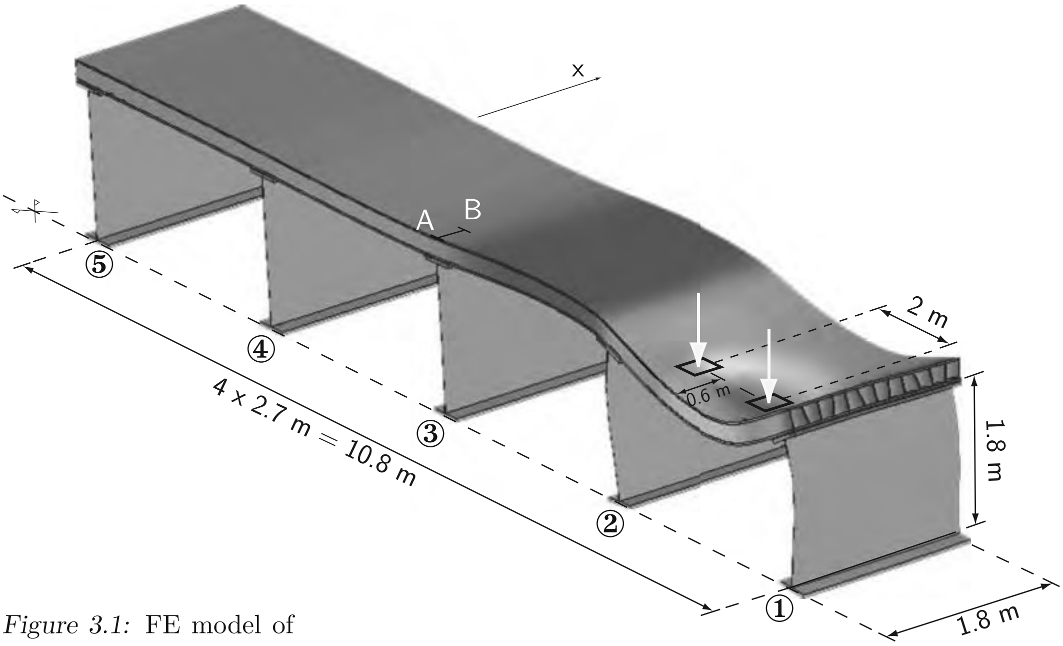

Figure 3.1: FE model of reference bridge

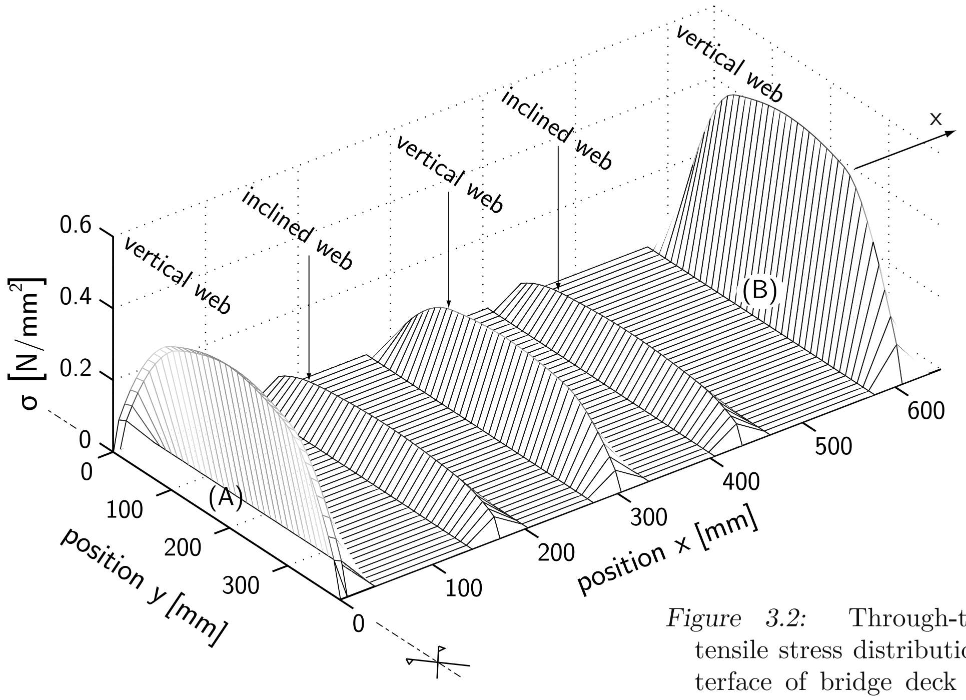

Figure 3.2: Through-thickness tensile stress distribution in interface of bridge deck and adhesive layer of girder ③ between points A and B (locations shown in Figure 3.1)

The stress distribution in the adhesive layer is shown in Figure 3.2, where x indicates the longitudinal direction of the steel girders. The curve shows that the maximum through-thickness stresses occurred beneath the vertical webs. The stresses beneath the inclined webs were approximately half as great, and no through-thickness stresses were transmitted between the webs. The distribution of tensile stresses σ_z^+ in y-direction is symmetric, indicating that no moments were transferred through the connection layer.

A relatively coarse mesh was chosen for this FE model, since the objective of the calculations on the reference bridge model was not the investigation of stress concentrations. Therefore, an exact determination of the stress peak value $\sigma_{z,\max}^+$ was not possible, while the average through-thickness tensile stress in the adhesive layer could be determined with sufficient accuracy.

3.4 Experiment description

3.4.1 Set-up

The experiments were carried out on two set-ups for logistical reasons, although both set-ups had an identical geometry. The structure acted like a cantilever beam: one end of the 3.5-m-long and 1.25-m-wide bridge deck was bonded to an HEM 200* profile with a length of 1.3 m, which was fixed to a steel frame as shown in Figures 3.3 to 3.5 and A.1 on page 139. The center part of the slab was supported in the vertical direction only. The structure was loaded on the end opposite to the end with the adhesive connection, the load being introduced through a steel profile over the whole width.

The structural system is shown in Figure 3.3: the intention was to install an experimental set-up acting like a beam with two simple supports, as illustrated in the lower sketch of Figure 3.3. This set-up was considered the most suitable for simulating the stress situation that would also occur in the adhesive connection of an actual bridge. The assumption of an end-support acting as a simple support was made and validated with an FEA of the test set-up described in Section 3.4.2. Since the steel girder and adhesive joint were sufficiently flexible, no moments were transmitted through the adhesive connection. The diagram in Figure 3.10 on page 32

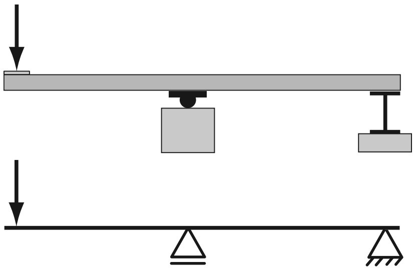

Figure 3.3: Structural system of test set-up

---

[*] A cross section of the profile is shown in Figure 3.6. Table 3.1 gives the dimensions.

shows that there is a very small bending moment influence, which shifts the center of the stress distribution curve to the right. However, this effect was negligibly small and it could be concluded that the support condition was indeed that of a simple support.

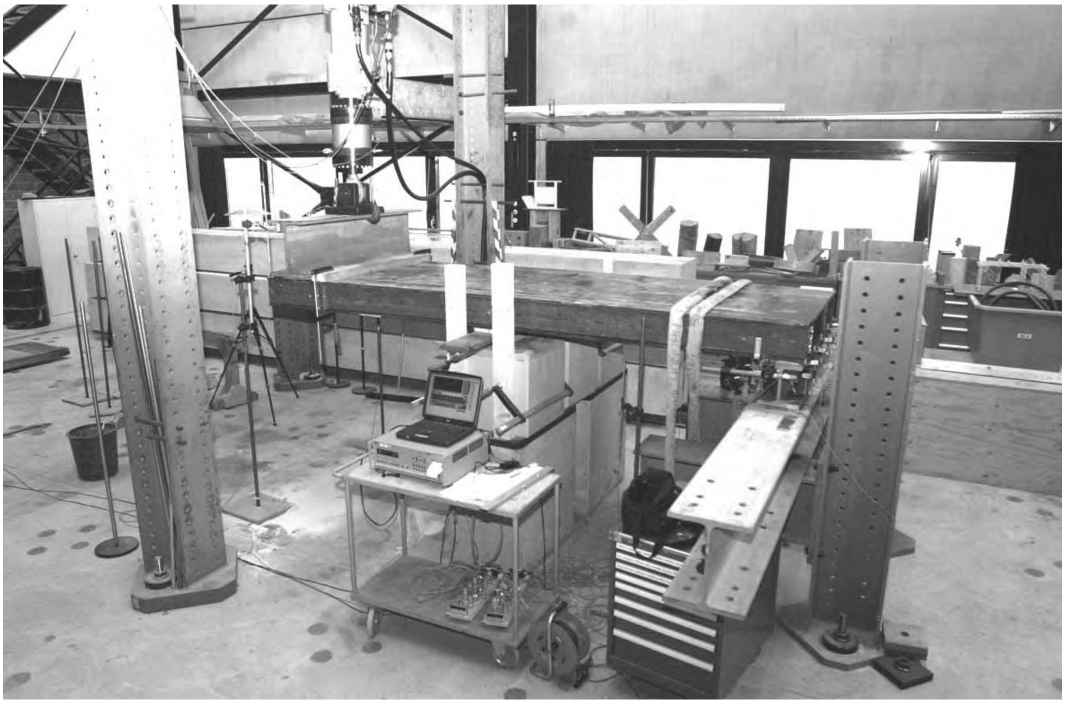

Figure 3.4: Set-up for *C2fat*, *C2-1* and *C3-1*

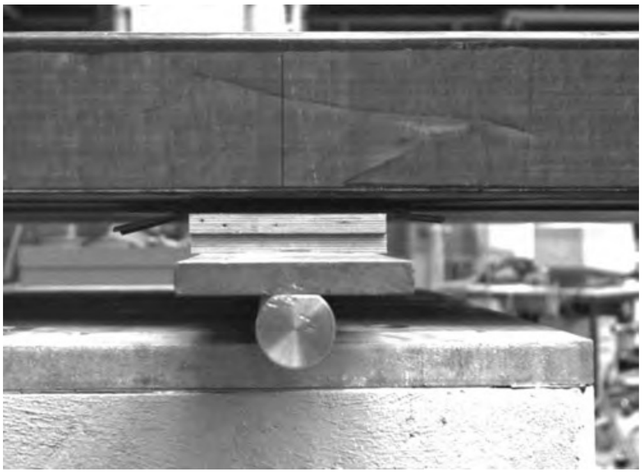

Figure 3.5: Roller support at $\ell/2$

Table 3.1: HEM 200 steel girder geometry

HEM 200 steel girder		
height	h	220 mm
flange width	b_f	206 mm
web thickness	t_w	15 mm
flange thickness	t_f	25 mm
curvature	r	18 mm

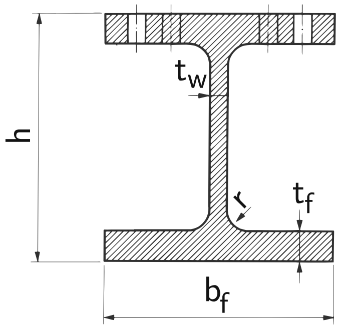

Figure 3.6: HEM geometry [Sta05]

3.4.2 Numerical modeling of experimental set-up

The aim of modeling the experimental set-up was, on the one hand, to assure that the stress condition in the experimental adhesive connection was similar to that in the modeled reference bridge and, on the other hand, the model was to be used for comparison and validation of the experimental results.

The test set-up used in the experiments was modeled using the Finite Element program *Ansys*. All materials – the steel girder, adhesive and FRP bridge deck – were modeled with 20-knot volume elements (*Ansys* element *SOLID 185*). For the FRP material, orthotropic properties were taken into account, which are shown in Table 3.3 on page 35. The adhesive was modeled as an isotropic material with an elastic modulus $E_{\mathrm{adh}} = 4500\,\mathrm{N/mm}^2$. One half of the specimen, consisting of four cells, was modeled taking advantage of symmetry boundary conditions, which meant that the complete model consisted of eight cells. The model was loaded on the area shown in Figure 3.7(a) with a uniformly distributed unit load per load area. The geometry with the corresponding materials and a part of the meshed model are shown in Figure 3.7 on the facing page. The mesh was densified over the support, and four layers were used to model the 8-mm-thick adhesive layer.

Two paths along which the stress distributions were determined had been defined in the model: one in the longitudinal direction of the steel girder and adhesive connection (x-direction), the other in the transverse direction (y-direction), as shown in Figure 3.8. The paths were located on the lower surface of the bridge deck above the adhesive layer, i.e. in the bridge deck/adhesive interface.

The resulting stress distribution along the path in x-direction is shown in Figure 3.9. The value of the ordinate $\sigma/\bar{\sigma}$ is the stress value σ related to the mean stress value $\bar{\sigma} = \frac{F_{\mathrm{up}}}{A_{\mathrm{adh}}}$. The investigated path with the highest stress concentration

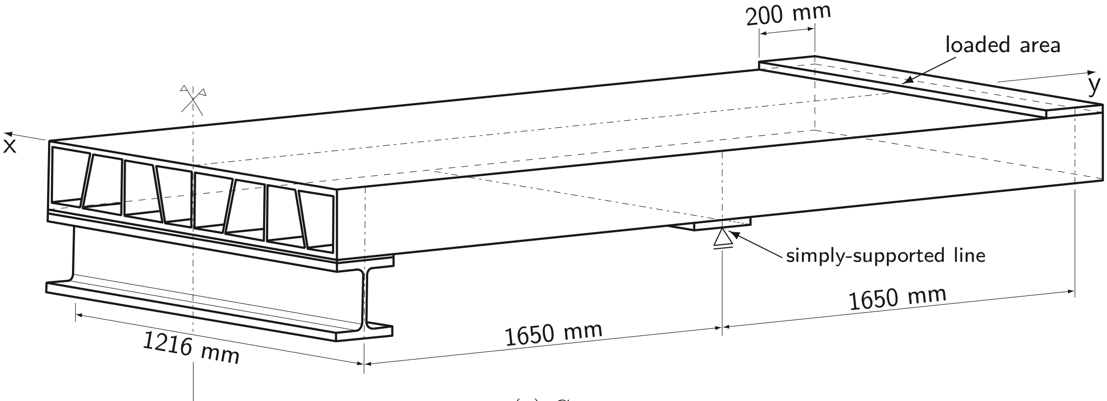
200 mm
loaded area
y
x
simply-supported line
1650 mm
1650 mm
1216 mm
z

(a) Geometry

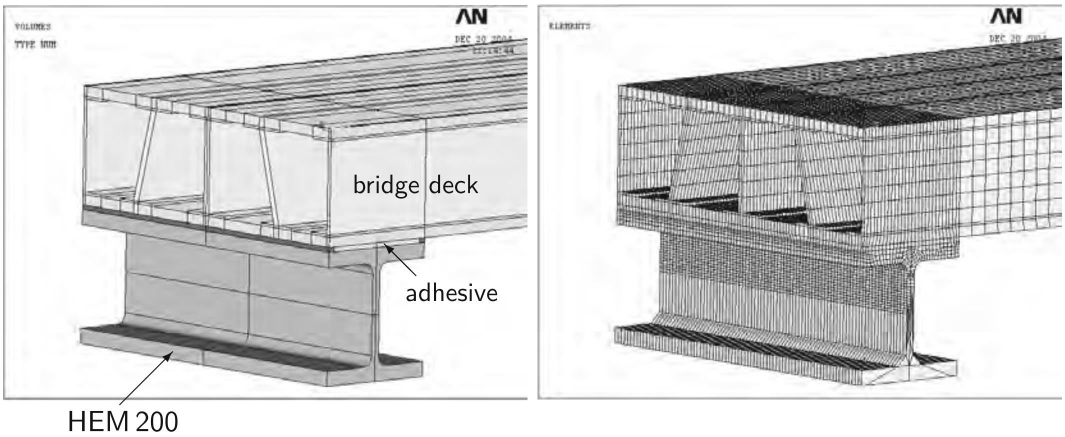
bridge deck
adhesive
HEM 200

(b) Materials (c) Meshed model

Figure 3.7: FE model of test set-up

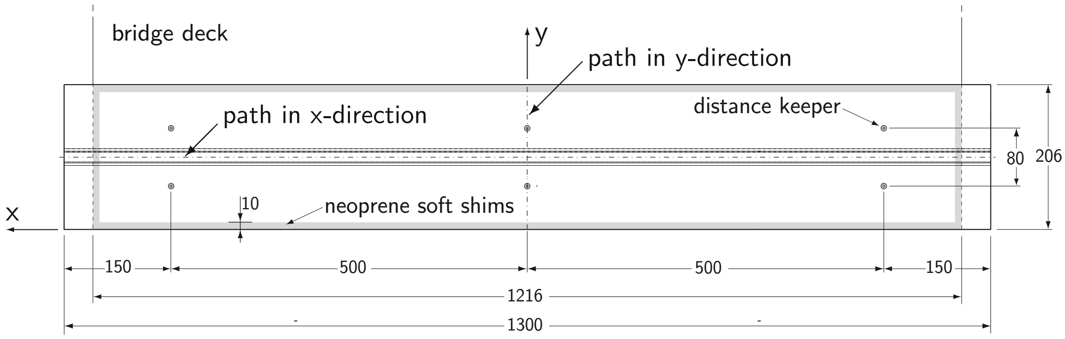
bridge deck
y
path in y-direction
path in x-direction
distance keeper
80
206
x
10
neoprene soft shims
150
500
500
150
1216
1300

Figure 3.8: Top view of steel girder surface — all values in [mm]

was located under every second vertical web, for example at $x = 0$ and $x = 608$ mm. This is due to the different influence areas of the vertical webs, which result from the inclined webs.

The distribution along the path in y-direction is shown in Figure 3.10. This shows an almost symmetric stress distribution, confirming that only an uplift force existed at the support, the accompanying moment remaining negligibly small, i.e. the support condition was not a clamped one, but a simple support. The highest stress peak was in the middle of the adhesive connection immediately above the web of the steel girder. Its value was more than twelve times higher than that of the average through-thickness stress in the adhesive layer.

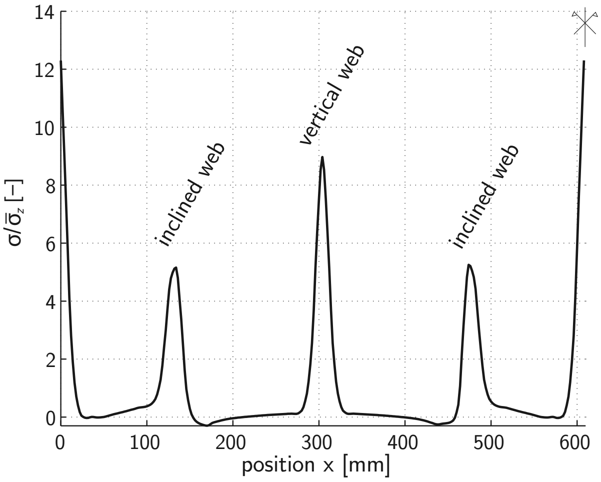

Figure 3.9: Normalized through-thickness tensile stress distribution in adhesive layer/bridge deck interface (x-direction) over center of steel girder, based on FEA

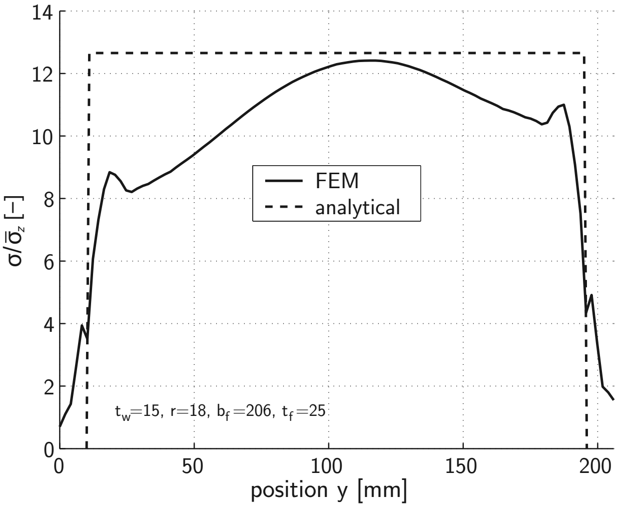

Figure 3.10: Normalized through-thickness tensile stress distribution in adhesive layer/bridge deck interface (y-direction) below vertical web at $x = 608$ mm, based on FEA

The results of the stress analysis showed that the stress distribution in the adhesive connection was very similar to that in the modeled reference bridge, described in Section 3.3. *SLS*- and *ULS*-loads for the experiments were determined from these results in order to have a similar stress condition in the adhesive layer for the experiments as would occur in the adhesive connection layer of a bridge.

3.4.3 Materials and specimens

The pultruded bridge deck elements used for the experimental series were composed of four *DuraSpan 766* profiles. The trapezoidal dual-cell profiles were formed by a pultrusion process and assembled by bonding with a structural polyurethane adhesive (see Figure 2.1(a) on page 15).

The DuraSpan 766 bridge deck

The cross section of a single profile is shown in Figure 3.11. The GFRP material consisted of E-glass fiber rovings embedded in an isophthalic polyester resin. The rovings were stitched into multi-ply structural fabrics with different orientations. The fabrics were combined with additional rovings and mats. Two primary lay-up schemes were used. The laminate around the cells was biased with 66% ±45° and 34% 0° plies to increase the web shear stiffness; the face sheet laminate, top and bottom, was biased with 60% 0° and 20% 90° and ±45° to increase the overall stiffness of the deck. Burn-off tests and microscopical cuts were made to examine the fiber architecture of the material. The total fiber content by weight was 60%. Figure 3.12 shows a sample after a burn-off test, and Figure 3.13, page 35, a microscopical cut through the material of the upper 6 mm of a top (or bottom) panel.

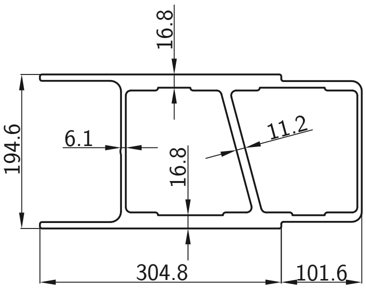

Figure 3.11: Cross section of a *DuraSpan*$^{\mathrm{TM}}$ *766* element — all values in [mm]

Table 3.2 on the following page shows the material properties of the fibers and resin used for the production of the *DuraSpan* deck. The material properties of the deck itself, given by the manufacturer, are shown in Table 3.3. These were determined from coupons of the corresponding parts of the bridge deck.

The deck exhibited a strongly orthotropic load-bearing behavior due to the different fiber architectures and different structural behaviors (system orthotropy) in the longitudinal and transverse directions. From the structural point of view, the webs and face sheets formed relatively strong I-beams in the longitudinal direction, strengthened by the face sheet reinforcements in the web areas. In the transverse

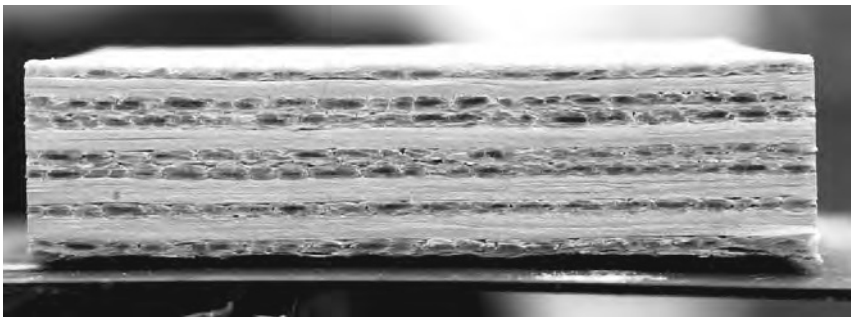

Figure 3.12: Sample after pyrolysis

direction, however, the deck exhibited a relatively weak *Vierendeel*[†] behavior due to the cellular structure. This behavior is described in detail in [Gür04]. The loads were borne primarily by transverse bending in the webs and face sheets. The low stiffness of the bonded joints further weakened the transverse behavior.

Table 3.2: Material properties [KS04]

(a) Fiber properties

Fibers	
Type:	E-glass fibers
Manufacturer:	*Johnston Industries*
Young's modulus (longitudinal)	$E_L = 72\,000$ N/mm^2
Ultimate tensile strength	$\sigma^+_{\text{max}} = 3\,448$ N/mm^2
Coefficient of thermal expansion	$\alpha = 1.6$ K^{-1}

(b) Resin properties

Resin	
Type:	Isophthalic Polyester *(Aropol 7334Z-15)*
Manufacturer:	*Ashland Chemicals*
Young's modulus	$E = 3\,380$ N/mm^2
Ultimate tensile strength	$\sigma^+_{\text{max}} = 75.8$ N/mm^2
Ultimate compression strength	$\sigma^-_{\text{max}} = 117.2$ N/mm^2
Coefficient of thermal expansion	$\alpha = 5.8$ K^{-1}

[†] Vierendeel [Meunier], (Jules-)Arthur, (1852–1940), Belgian engineer and writer

Table 3.3: Mechanical properties of *DuraSpan 766* deck (according to manufacturer) [KS04]; stiffness moduli and Poisson's ratios

	top and bottom sheets	web walls
E_y	21 240 N/mm^2	17 380 N/mm^2
E_x	11 790 N/mm^2	9 650 N/mm^2
E_z	4 140 N/mm^2	4 140 N/mm^2
G_{xy}	5 580 N/mm^2	7 170 N/mm^2
G_{yz}	600 N/mm^2	600 N/mm^2
G_{xz}	600 N/mm^2	600 N/mm^2
ν_{xy}	0.32 [-]	0.3 [-]
ν_{yz}	0.3 [-]	0.3 [-]
ν_{xt}	0.3 [-]	0.3 [-]

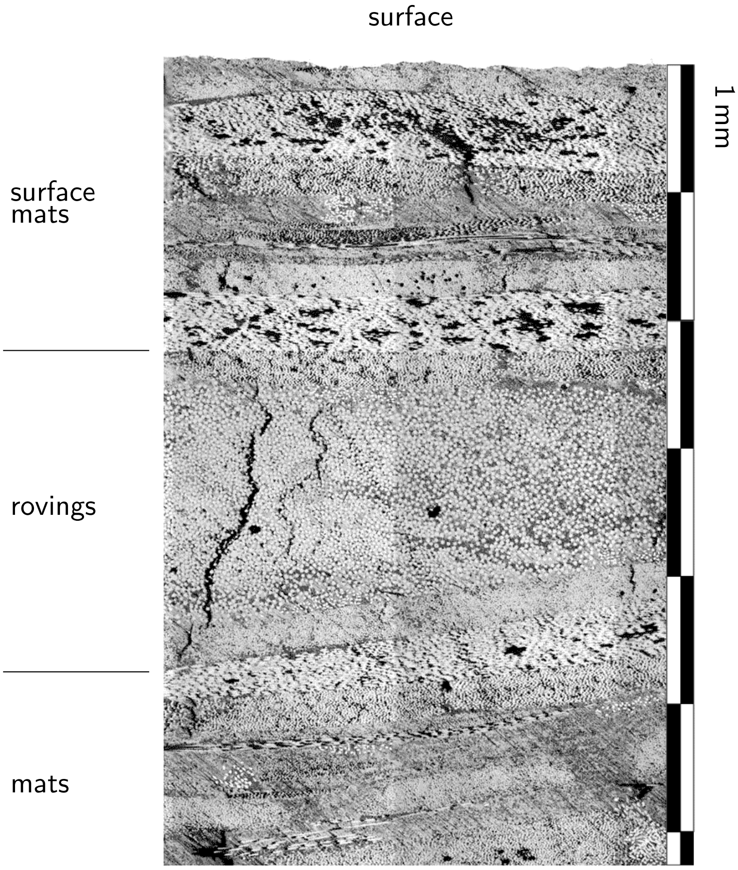

Figure 3.13: Microscopical cut through upper 6 mm of material of a *DuraSpan 766* top panel

Specimens

Each deck specimen was composed of four 3.5-m-long *DuraSpan 766* bridge deck elements. The specimens, designated *C1* to *C3*, are listed in Table 3.4. Each specimen was used for at least two experiments as, since the deck was not damaged in the tests (except the surface in the region of the adhesive connection), the specimens were turned over after the first test and their opposite sides used for a further experiment. Therefore the designations *C1-1* and *C1-2* refer to the same specimen *(C1)*, but to two different experiments. Specimen *C2* was used for three experiments: before the two static experiments *C2-1* and *C2-2* were performed, a fatigue experiment *(C2-fat)* was carried out using the same specimen and adhesive connection as that used in experiment *C2-1*.

Table 3.4: Specimens and test dates

Deck specimen	Experiment	Type	Set-up[a]	Test date
C1	*C1-1*	static	1	25 Nov. 2003
	C1-2	static	1	28 Nov. 2003
C2	*C2-fat*	fatigue	2	19 Dec. 2003 – 2 March 2004
	C2-1	static	2	2 March 2004
	C2-2	static	1	9 Aug. 2004
C3	*C3-1*	static	2	4 March 2004
	C3-2	static	1	13 July 2004

---

[a] set-up 1 is shown in Figure A.1 on page 139, set-up 2 in Figure 3.4 on page 29

Deck-girder connection

The adhesive used for the connection between the bridge deck and the steel girder was *SikaDur 330*, a thixotropic two-component resin on an epoxy resin base, whose mechanical properties are shown in Table 3.5 on the facing page. In order to assure a constant adhesive thickness, distance keepers (of 8-mm height) were welded onto the surface of the steel girder at the locations indicated in Figure 3.8 on page 31. Neoprene shims with a thickness and width of 10 mm were glued near to all edges of the steel girder, as shown in the horizontal projection in Figure 3.8 on page 31. This resulted in an adhesive surface of $1196 \times 186\,\mathrm{mm}^2$ and an adhesive thickness in the specimens of 8–10 mm. This thickness was also assumed to be a reasonable value in a bridge, since it allows the compensation of any inaccuracies that might occur on the construction site.

Table 3.5: Material properties of *Sikadur 330* adhesive

Sikadur 330		
Density ρ	1.31	kg/l
E-modulus (flexural, ISO 178)	3 800	N/mm^2
E-modulus (tensile, ISO 53 455)	4 500	N/mm^2
Tensile strength $\sigma^+_{\max}$	30	N/mm^2
Elongation at rupture $\varepsilon^+_{\max}$	0.9	%

To guarantee good adhesion conditions, the steel surface was sanded. The surface of the bridge deck, bonded to the steel girders, was machine-sanded with *100-grid* sand paper before bonding. After grinding, the surfaces were cleaned with acetone in order to obtain a fat- and dust-free surface.

Specimen *C1* was prepared in a slightly different way to specimens *C2* and *C3*, its surfaces being machine-sanded twice until they were no longer shiny. However, in the first two experiments (*C1-1* and *C1-2*), adhesion problems that occurred on the bridge deck surface were investigated, as described in Section 3.5.1. Subsequent specimens were therefore prepared differently, the surface being ground until the glass fibers of the surface mats were visible, as shown in Figure A.2 on page 140 in the Appendix. The different surface preparation had a significant effect on the adhesion between the adhesive layer and the bridge deck surface, as shown in the following.

3.4.4 Instrumentation and measurements

Displacement transducers

For displacement measurements, 14 displacement transducers were used: two at the loading point (# 1 and # 2), two between the middle support and the steel girder (# 3 and # 4, see Figure 3.14 on the following page), five at the bonded connection on the inner side (# 5 to # 9, see Figures 3.15–3.17) and five at the bonded connection on the outer side (# 10 to # 14, see Figures 3.15 and 3.18–3.19). While transducers # 1 to # 4 measured absolute values in the vertical direction, # 5 to # 14 measured the differential distances between the FRP deck and the steel flange. Further specifications of the transducers are listed in the calibration protocol in Tables A.1 to A.3, page 140 ff. The accuracy of the transducers was ±0.01 mm.

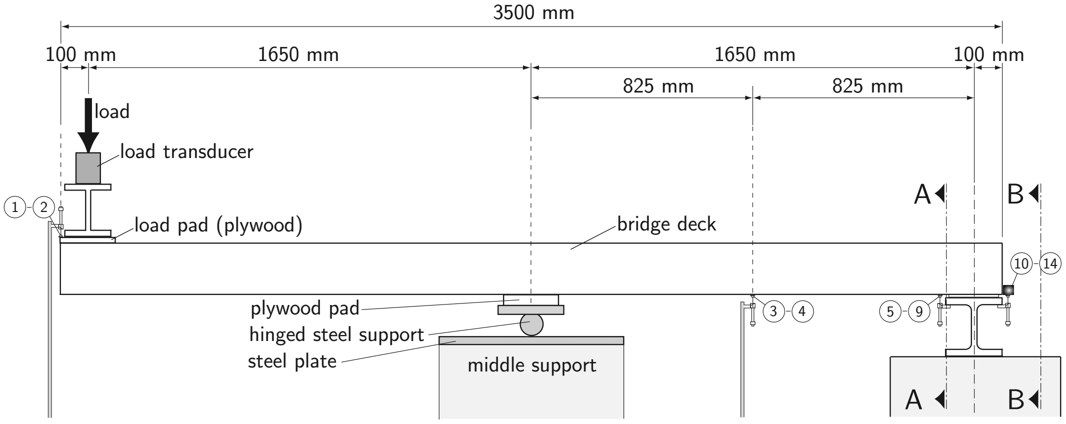
3500 mm
100 mm
1650 mm
1650 mm
100 mm
825 mm
825 mm
load
load transducer
①-②
load pad (plywood)
bridge deck
A
B
⑩-⑭
plywood pad
hinged steel support
steel plate
middle support
③-④
⑤-⑨
A
B

Figure 3.14: Elevation of specimen in set-up. The circled numbers show measurement equipment used in experiments: displacement transducers # 1 to # 14; Sections A-A and B-B are shown in Figures 3.16 and 3.18; a detailed view of the adhesive connection is shown in Figure 3.15

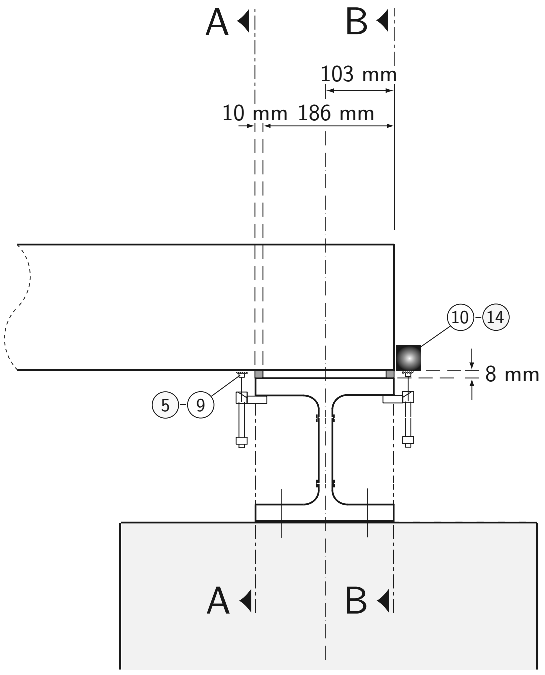
A
B
103 mm
10 mm
186 mm
⑩-⑭
8 mm
⑤-⑨
A
B

Figure 3.15: Detail of Figure 3.14. Displacement transducers # 5 to # 14

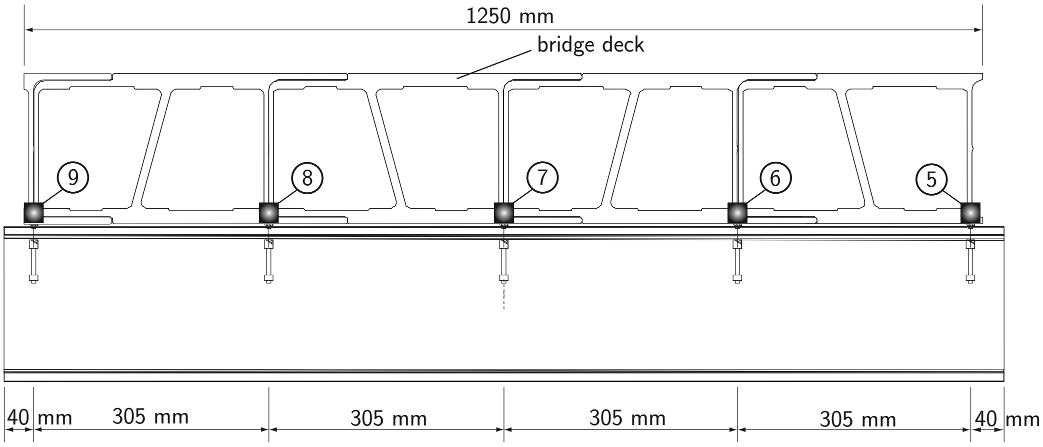
1250 mm
bridge deck
9
8
7
6
5
40 mm
305 mm
305 mm
305 mm
305 mm
40 mm

Figure 3.16: Section A-A: displacement transducers # 5 to # 9 on inner side

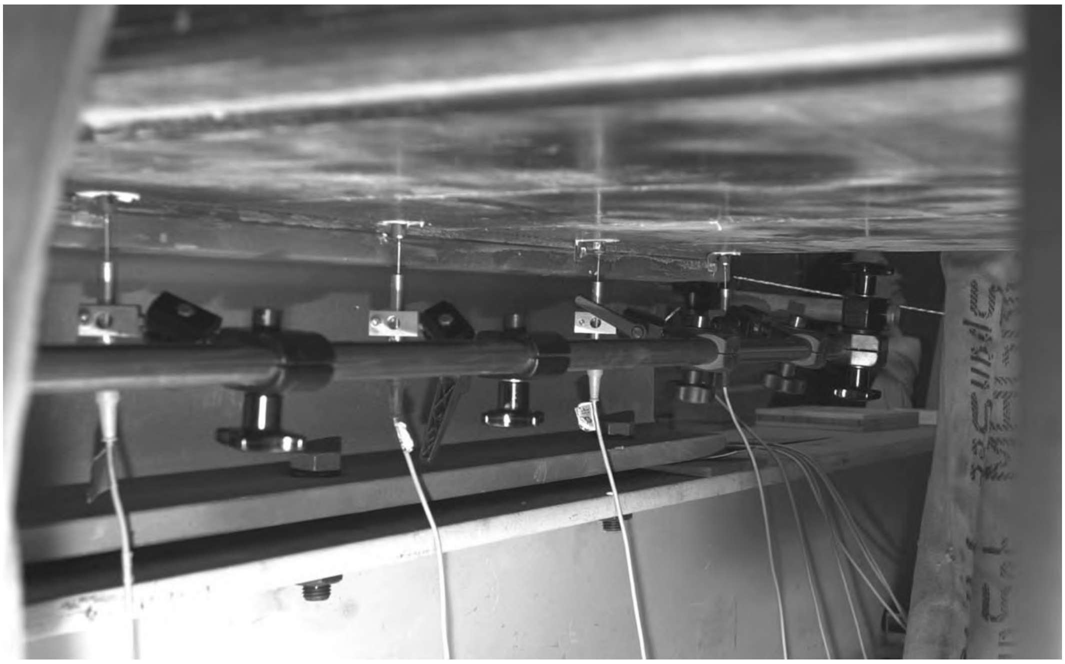

Figure 3.17: Displacement transducers measuring deformations at adhesive bond between edge of bridge deck and steel girder on inner side

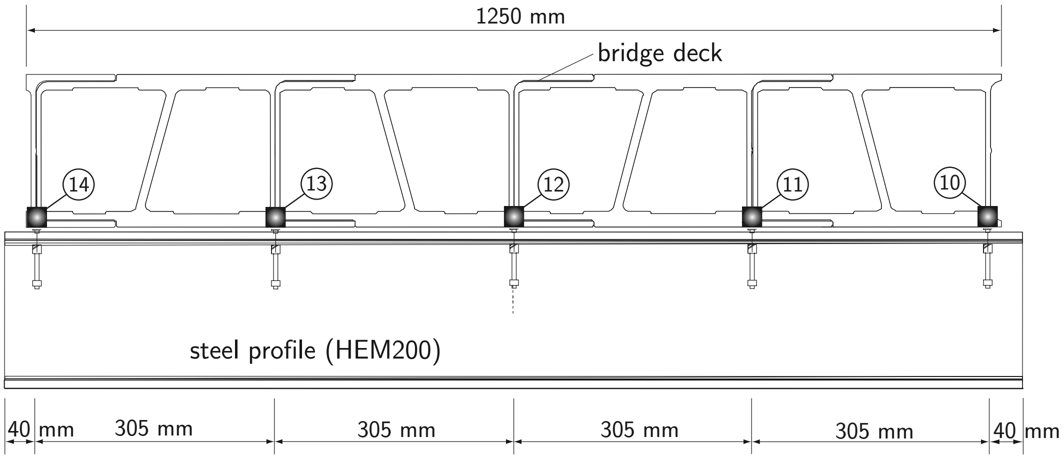
1250 mm
bridge deck
14
13
12
11
10
steel profile (HEM200)
40 mm
305 mm
305 mm
305 mm
305 mm
40 mm

Figure 3.18: Section B-B: displacement transducers # 10 to # 14 on outer side

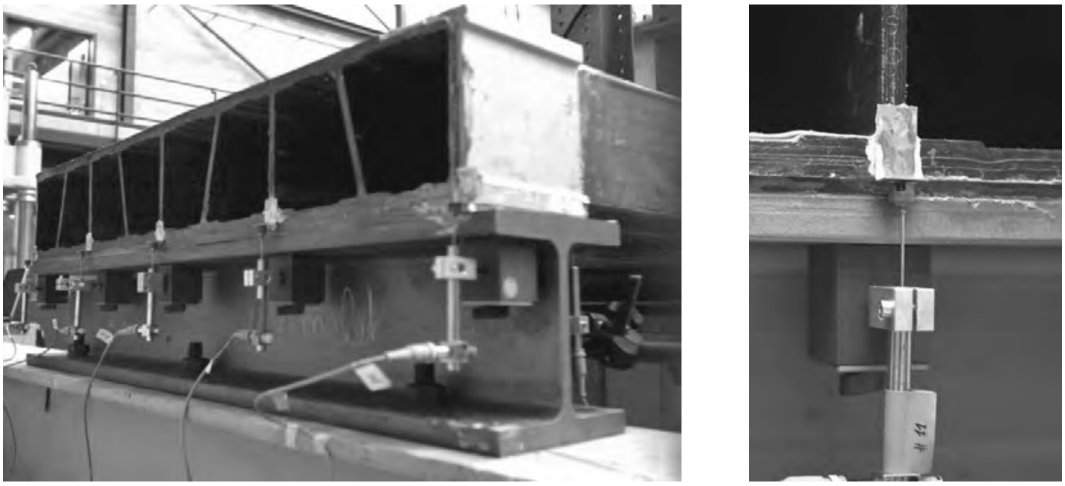

(a) Disposition of transducers

(b) Single displacement transducer

Figure 3.19: Displacement transducers measuring deformations at adhesive bond between edge of bridge deck and steel girder on outer side

3.4.5 Experimental Program

Six static tests and one fatigue experiment were performed. The complete program with the corresponding set-ups is shown in Table 3.4.

Static experiments

Each static experiment was performed in three steps:

1. loading up to the *SLS*[‡]-load (34 kN) and unloading;
2. loading up to the *ULS*[§]-load (51 kN) and unloading;
3. loading until failure.

The *SLS*- and *ULS*-loads for the full-scale adhesive experiments were determined using the FE models of the reference bridge, i.e. the corresponding load in the experiments caused a similar stress situation in the adhesive layer as traffic loads according to the design code (EC 1) would effect in the connection layer of a bridge. Calculations using the FE model of the reference bridge resulted in a maximum average through-thickness tensile stress of $0.15\,\mathrm{N/mm^2}$ inside the connection area of eight bridge deck profiles. In the experiments, this stress value multiplied by the connection area resulted in an uplift force of 34 kN. Since the loading force equals the uplift force, the *SLS*-load was determined as 34 kN. In the *ULS*, traffic loads are increased by factor $\gamma_F = 1.5$. For the experiments, this resulted in a *ULS*-load of 51 kN. All experiments were driven displacement-controlled at a rate of $2\,\frac{\mathrm{mm}}{\mathrm{min}}$.

Fatigue experiment

The fatigue experiment *(C2-1)* was performed over a period of 70 days with 10^7 load cycles. The fatigue load range $\Delta F_{\mathrm{fat}} = 12\,\mathrm{kN}$ was determined using the fatigue load model taken from the EC 1 on the FE model described in Section 3.3. An average through-thickness tensile stress of $0.055\,\mathrm{N/mm^2}$ was determined. This resulted in the uplift force of 12 kN in the experimental set-up.

The structure was loaded (force-controlled) with a frequency of 1.7 Hz between $F_{\mathrm{fat,min}} = 4\,\mathrm{kN}$ and $F_{\mathrm{fat,max}} = 16\,\mathrm{kN}$. At each 1 million cycles a static experiment was carried out; the specimen was loaded with the SLS-load and the displacement at the loading point measured.

[‡] To satisfy the *Serviceability Limit State* criteria, a structure must remain functional for its intended use subject to routine loading, and as such the structure must not cause occupant discomfort under routine conditions.

[§] To satisfy the *Ultimate Limit State*, the structure must not collapse when subjected to the peak design load for which it was designed. Thus the structural element being analyzed is shown to be safe when the factored loads are less than their factored resistance. The ultimate limit state is defined as the most unfavorable loading according to the design code, i.e. it is not necessarily the structure's failure state.

3.5 Experimental results and discussion

3.5.1 Static experiments

The specimens in all experiments exhibited an almost linear-elastic behavior until a brittle failure. The load-displacement response of the cantilever structure in all experiments, measured at the loading point, is shown in Figure 3.20 on the next page. In all experiments failure occurred mainly in the surface layer mats of the pultruded material, i.e. a fiber-tear failure. The rest of the bridge deck structure remained undamaged in each test. Table 3.6 shows the ultimate loads F_u of each test with their corresponding mean stress $\bar{\sigma}_z = \frac{F_u}{A_{\text{adh}}}$.

Table 3.6: Experimental results

Test	F_u[kN]	$\bar{\sigma}_z$ @ failure $\left[\frac{\text{N}}{\text{mm}^2}\right]$
C1-1	120.3	0.54
C1-2	96.3	0.43
C2-1 [a]	139.4	0.63
C2-2	191.6	0.86
C3-1	186.0	0.84
C3-2	188.0	0.85
average[b]	176.3	0.79
st. dev.[c] s	±24.7	0.11

[a] after fatigue experiment
[b] specimens *C2* and *C3* only
[c] standard deviation

Due to the different surface preparation for the first specimen (as described in the following), only the results of specimens *C2* and *C3* were used to calculate the average values and standard deviations. The average ultimate load for these experiments was $\bar{F}_u$ =176.3 kN with a standard deviation of $s = 24.7$ kN. This led to a maximum average tensile through-thickness stress of $\bar{\sigma}_z = \frac{\bar{F}_u}{A_{\text{adh}}} = \frac{176.3\,\text{kN}}{186\,\text{mm} \cdot 1196\,\text{mm}} = 0.79\,\frac{\text{N}}{\text{mm}^2}$ with a standard deviation of $s = 0.11\,\frac{\text{N}}{\text{mm}^2}$.

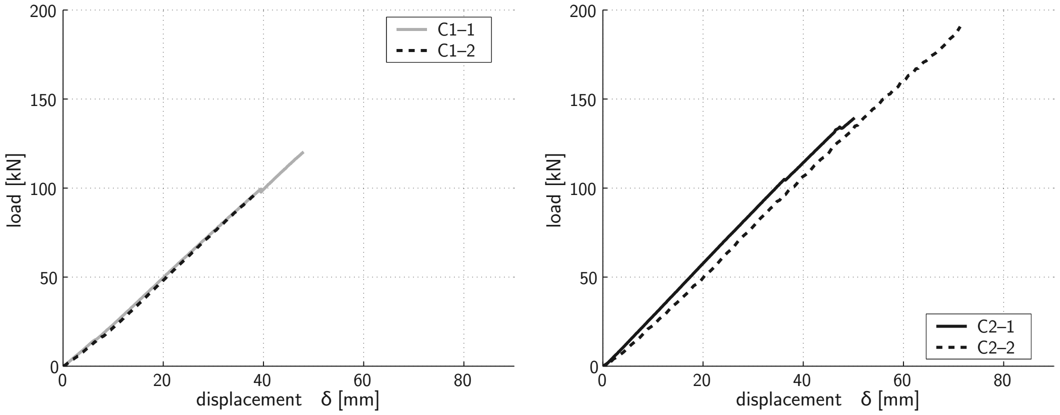

(a) Specimen *C1*

(b) Specimen *C2*

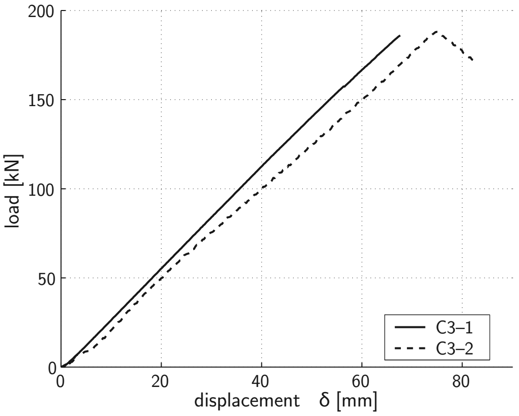

(c) Specimen *C3*

Figure 3.20: Average deflection of transducers # 1 and # 2 at loading points of all experiments

Experiment C1-1

No audible cracks occurred until a load of 99 kN. In the graph in Figure 3.20(a), an offset appears at this load. The load could then be increased until the ultimate load of 120 kN. Diagrams of the displacement at the adhesive connection recorded by transducers # 11 to # 14 are shown in Figure A.3 on page 142. The measured results differ within the range of the transducers' accuracy (±0.01 mm), causing a lot of scatter. The maximum value, 0.1 mm, was measured by transducer # 13. Transducers # 5 to # 10 did not provide usable results due to technical problems.

Regarding the surfaces of the failed adhesive connections and the ultimate loads, notable differences between the first two experiments *(C1-1* and *C1-2)* and the following experiments could be observed. This was partly due to the different surface preparation, described in Section 3.4.3, and partly because the adhesive was not optimally prepared at some locations. Figure 3.21 shows the surface of the failed adhesive layer on the steel girder in experiment *C1-1*. It has some areas of good adhesion, where fibers were pulled out from the surface layer mats of the bridge deck, but also areas without adequate adhesion, caused by the imperfect curing of the adhesive at some locations and air bubbles, which weakened the adhesive connection at other locations. This resulted in the relatively low ultimate load of 120 kN, which was far below the average value of the test series.

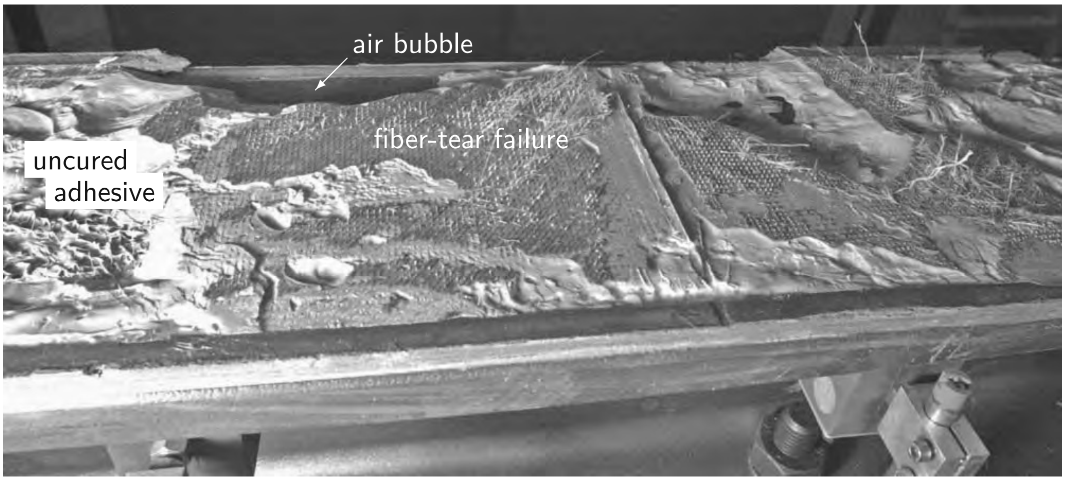

Figure 3.21: Surface of failed adhesive connection on steel girder *(C1-1)*

Experiment C1-2

As shown in Figure 3.20(a) by the load-deflection curve, the ultimate load was reached at 96 kN. The displacements measured on the outer side of the adhesive connection were much smaller, within the range of the transducers' accuracy, see

Figures A.4 and A.5, pages 143–144, which show the diagrams obtained from each displacement transducer. Figure 3.22 shows the distribution of the measured differential displacements at the adhesive connection on the inner side. The maximum displacement was measured in the center of the adhesive connection (at transducer # 7). This peak was reached because the connection at this location exhibited a non-linear behavior (see Figure 3.23) which probably occurred due to delamination of the surface layer mats.

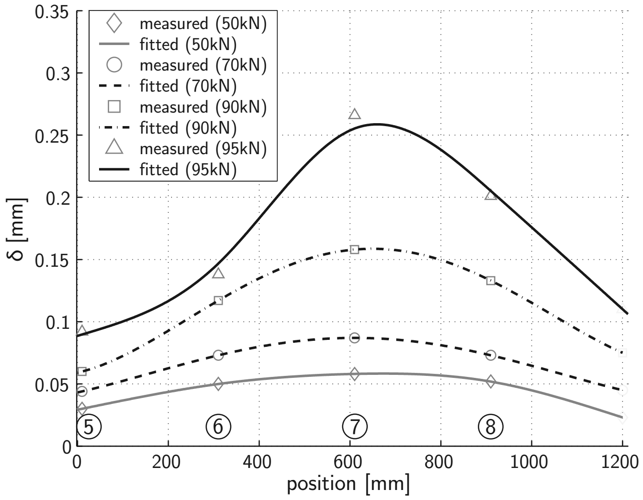

Figure 3.22: Specimen *C1-2*: distribution of differential displacements in bonded connection (inner side, transducers # 5 to # 8)

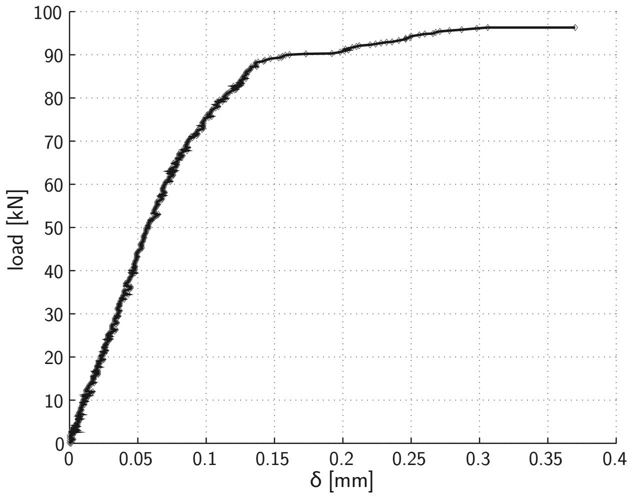

Figure 3.23: Load-displacement curves of transducer # 7 on inner side of adhesive connection *(C1-2)*

As a consequence of experiment *C1-1*, more care was taken concerning the preparation of the adhesive while manufacturing the adhesive connection for *C1-2*. This meant that the two adhesive components were mixed more slowly and carefully in order to prevent the introduction of air bubbles. After failure (at 96 kN), the adhesive was observed to be in perfect condition, i.e. without any air bubbles and perfectly cured. However, only a light fiber-tear failure occurred, as shown in Figure 3.24, with only parts of fibers being torn out of the FRP's surface material. Based on this, the surface preparation was improved as previously described.

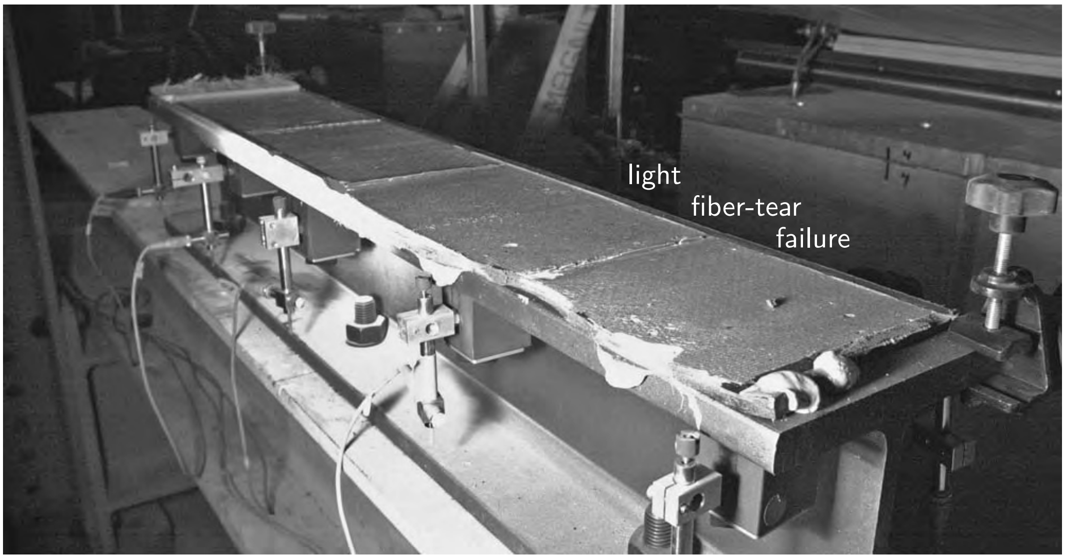

Figure 3.24: Surface of failed adhesive connection on steel girder (*C1-2*)

Experiment C2-1

The failure in experiment *C2-1* occurred in two stages: a first crack with a significant displacement occurred at 105 kN and a second one at 135 kN. Two offsets at these loads are visible in the diagram showing the measurements of the deflections at the loading point (see Figure 3.20(b) on page 43). The failure then occurred at 139 kN, initiating in the center of the adhesive connection, in the region of tranducers # 7 and # 12. This can be seen in the graphs obtained from the displacement transducers located at the adhesive connection with the two measured kinks at 105 kN and 135 kN (see Figure 3.25). The distribution of the displacements on the inner side of the connection also showed high displacements in the center of the connections, see Figure 3.26.

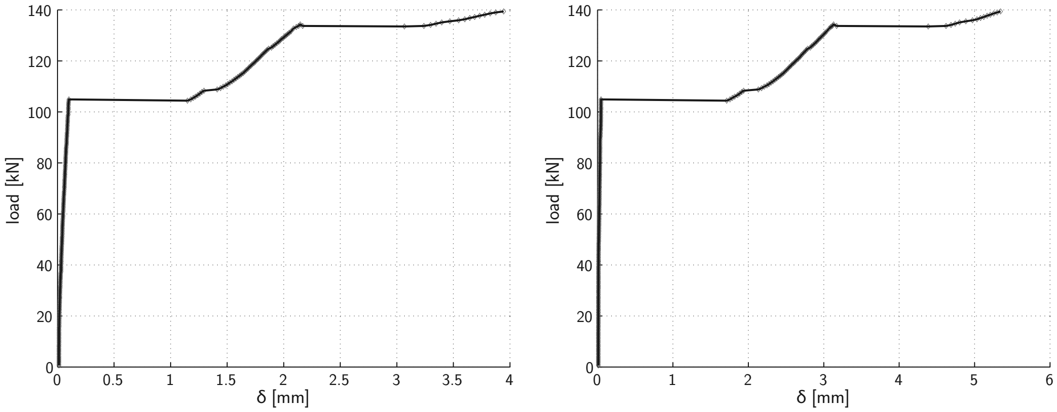

(a) Transducer # 7 (b) Transducer # 12

Figure 3.25: Load-displacement curves of two transducers on inner and outer sides of adhesive connection *(C2-1)*

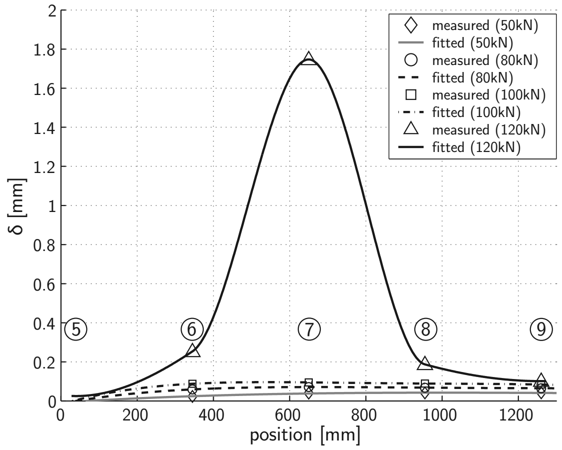

Figure 3.26: Specimen *C2-1*: distribution of differential displacements in bonded connection (inner side); transducers # 5–9

The failure in the center of the connection occurred in the steel/adhesive interface, with a fiber-tear failure predominating in the rest of the connection (compare the failed surfaces of the bonded connection between the steel girder and the bridge deck in Figure 3.27). Figures A.7 and A.8 on pages 146–147 show the diagrams obtained from each displacement transducer at the adhesive connection on the inner and outer sides. Since the measured results on the outer side were within the range of the transducers' accuracy, satisfactory diagrams could only be obtained from the inner side.

The specimen had been used for the fatigue test before the static test was performed, which could explain the relatively low failure load, see Table 3.6 on page 42.

A further reason could be the steel/adhesive interface failure over approximately one third of the connection area.

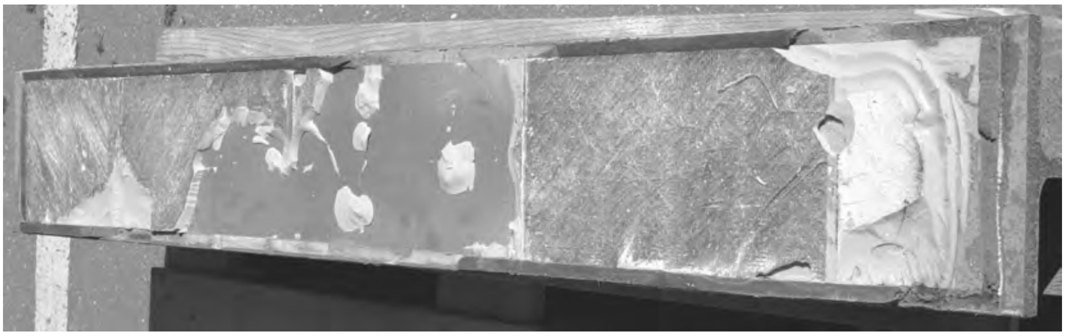

(a) view of girder

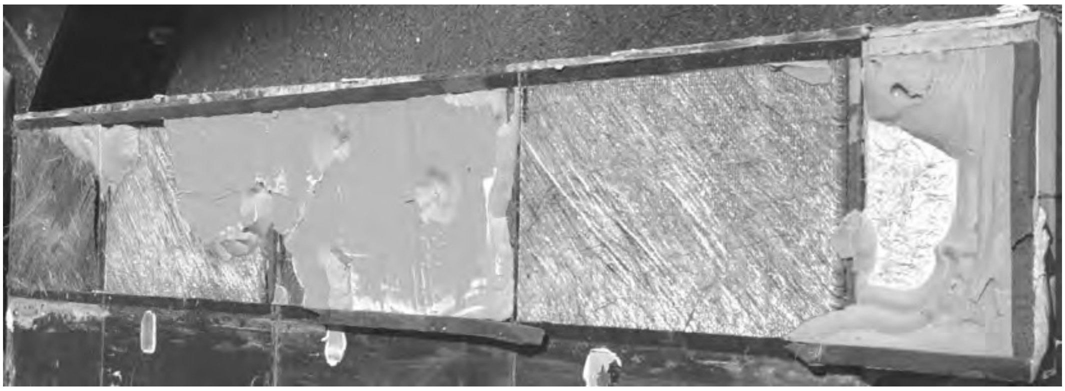

(b) view of deck

Figure 3.27: Surface of failed connection, specimen *C2-1*

Experiment C2-2

The ultimate load occurred at 192 kN, and no offsets could be observed in the load-deformation curve as shown in Figure 3.20(b) on page 43. In terms of connection quality this experiment was obviously the best, which was also demonstrated by the behavior during the test: only a small non-linear deformation could be seen at 120 kN as shown in the diagram in Figure 3.28 and the first audible crack occurred shortly before the connection failed. The fact that all parts of the connection failed almost simultaneously and in the same manner is apparent in Figure 3.29, since all transducers measured similar displacements.

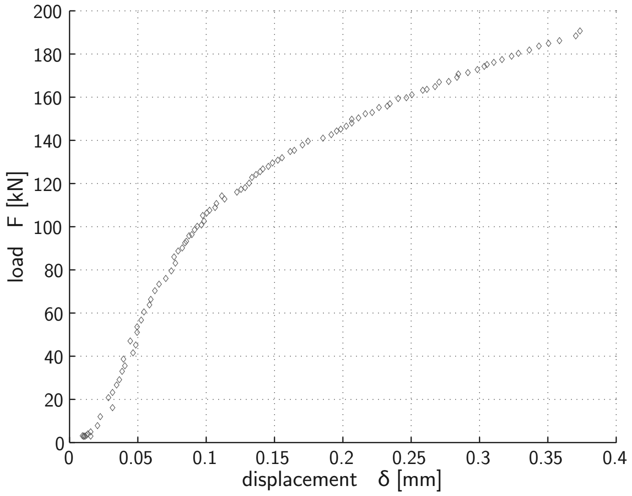

Figure 3.28: Specimen *C2-2*: transducer # 5

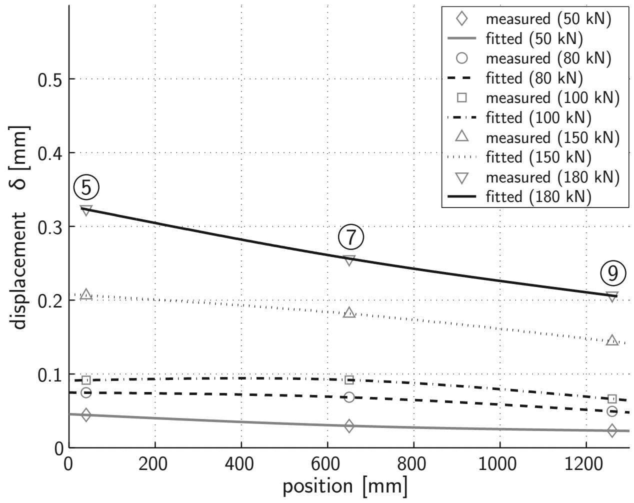

Figure 3.29: Specimen *C2-2*: distribution of differential displacements in bonded connection (inner side, transducers # 5 to # 9)

In contrast to the failure in the previously described test, which comprised different modes in various areas, the failure in experiment *C2-2* was the same throughout the whole area of the adhesive connection. It was characterized by a fiber-tear failure, where large parts of mats were torn out of the bridge deck's surface material, see Figures 3.30 on the following page and A.9, page 148 in the Appendix.

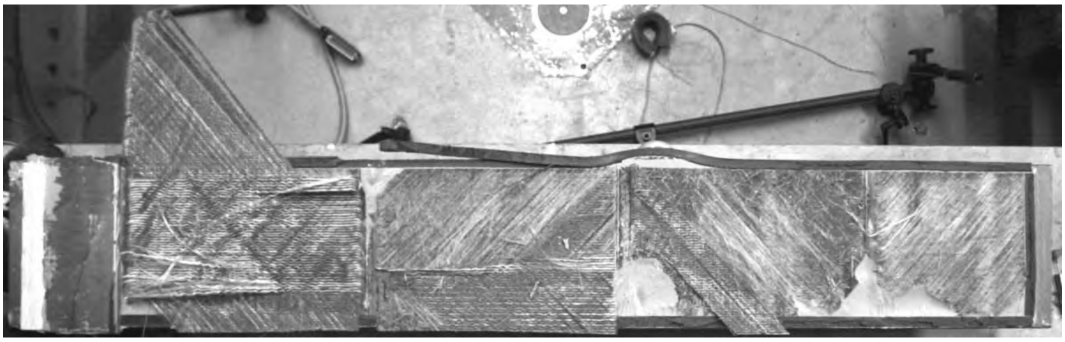

(a) view of girder

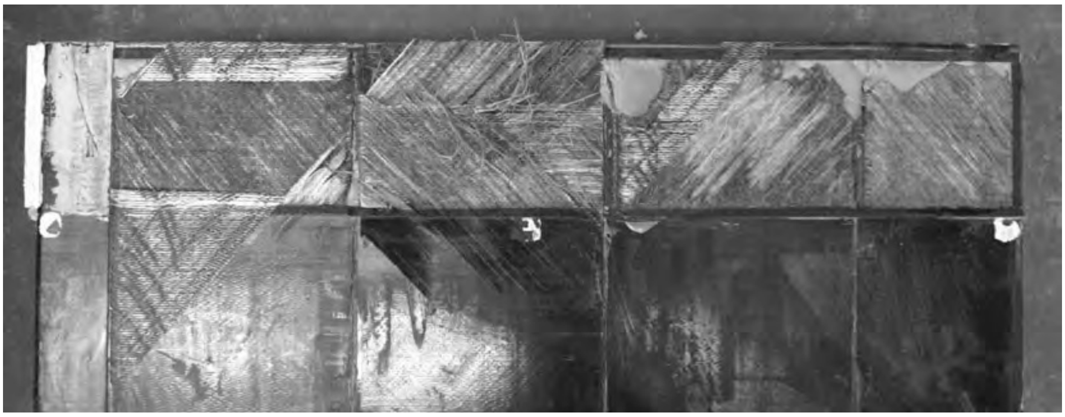

(b) view of deck

Figure 3.30: Failed adhesively-bonded connection (*C2-2*)

Experiment C3-1

The failure load was measured at 186 kN, and an offset in the load-deflection curve can be seen at 155 kN, see Figure 3.20(c). The behavior in experiment *C3-1* was similar to that in *C2-1*: a significant crack at a load of 90 kN was audible, which can also be observed in the graphs in Figure 3.31. This failure was initiated in the region of transducers # 5 and # 10, as also shown in the distributions of the differential displacements of the transducers on the inner side, see Figure 3.32.

The failure in this experiment was a fiber-tear failure, but in some areas failure also occurred in the adhesive and the interface between the steel and the adhesive. Figure 3.33 on page 52 shows the failed surface, and Figures A.12 and A.13, pages 151–152, show the single diagrams obtained from the displacement transducers at the bonded connection on the inner and outer sides.

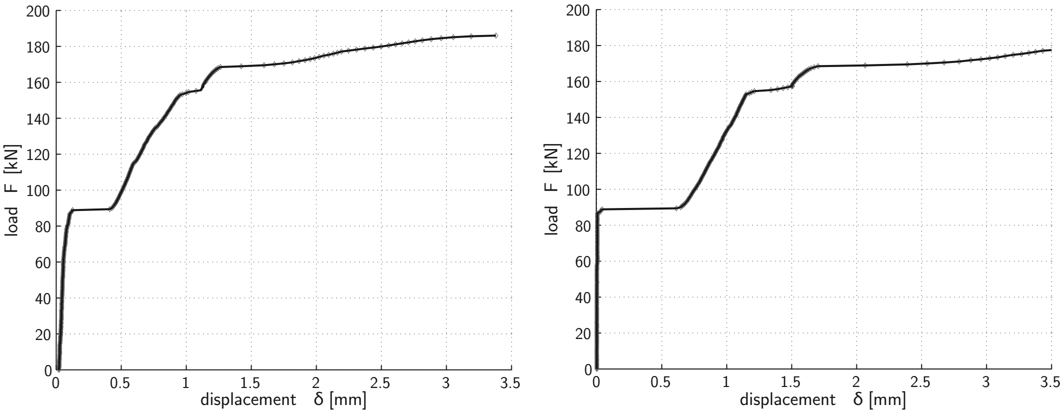

(a) Transducer # 5

(b) Transducer # 10

Figure 3.31: Load-displacement curves of two transducers on inner and outer sides of adhesive connection *(C3-1)*

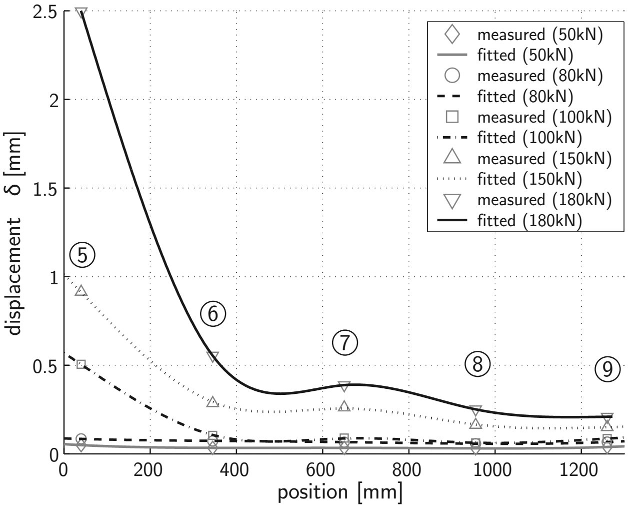

Figure 3.32: Specimen *DS C3-1*: distribution of differential displacements in bonded connection (inner side); transducers # 5–9

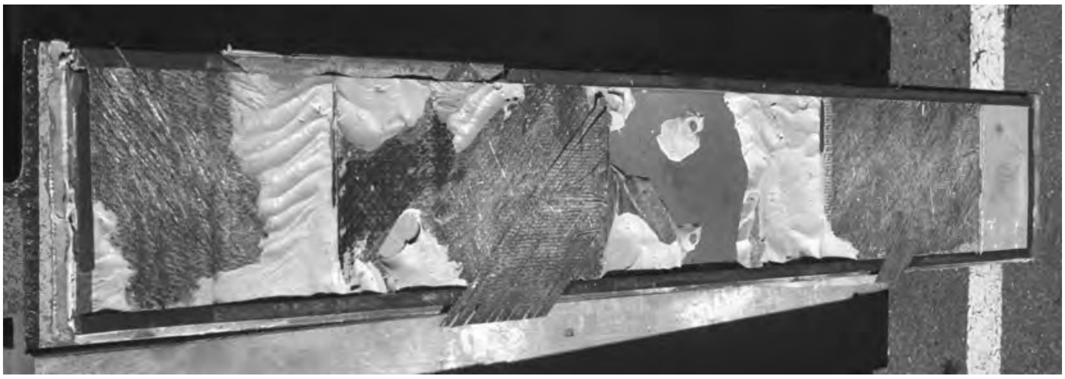

(a) view of girder

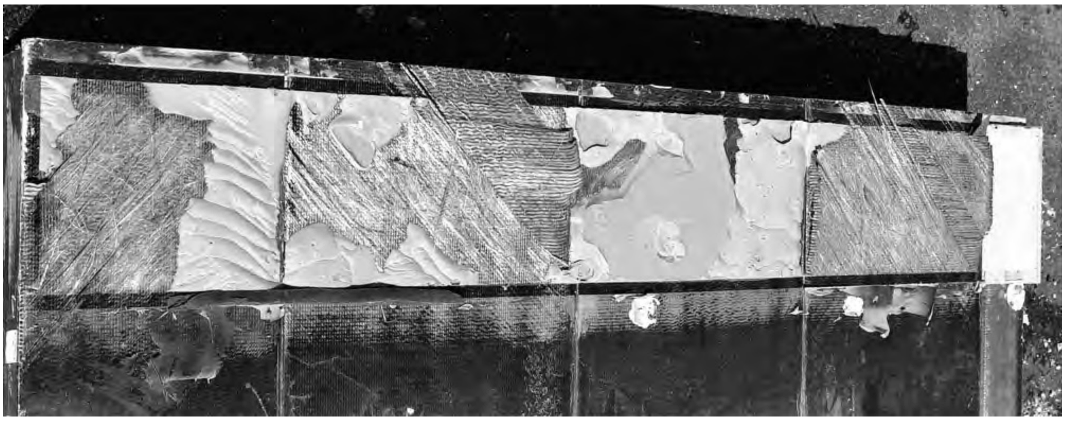

(b) view of deck

Figure 3.33: Failed bonded connection (*C3-1*)

Experiment C3-2

Up until a load of approximately 160 kN, no acoustical cracks occurred. Then, the failure was indicated by a number of audible cracks until a bigger crack occurred at the ultimate load of 188 kN. The connection did not fail completely after the ultimate load was reached however. The deflection increased as the load decreased to almost 20 kN (see the corresponding graph in Figure 3.20(c)).

Figure 3.34 shows the graphs obtained from transducers # 5 and # 10, the region where the highest displacements at the connection were measured. The distribution of the differential displacements at the adhesive connection, shown in Figure 3.35, also indicates that failure initiated on the side near to transducer # 5; the transducers measured very similar displacements up until a load of approximately 160 kN.

Figures A.17 and A.18, pages 155 and 156, show the displacements of each transducer at the adhesive connection.

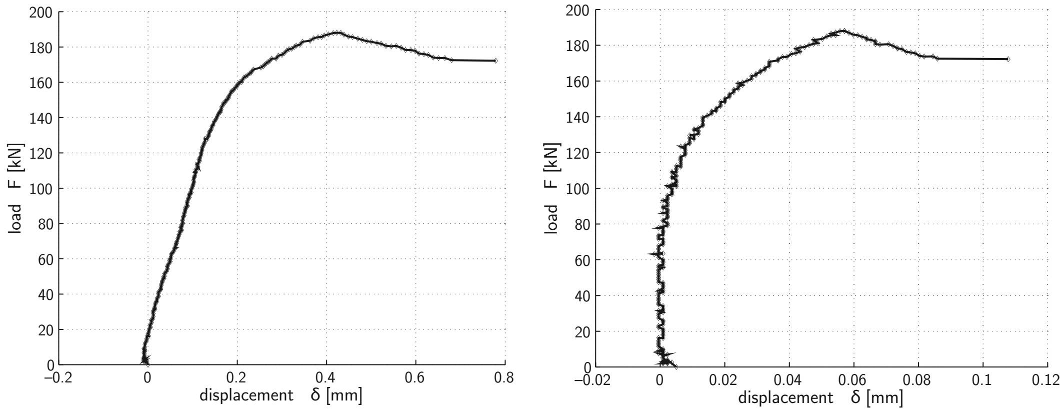

(a) Transducer # 5

(b) Transducer # 10

Figure 3.34: Load-displacement curves of two transducers on inner and outer sides of adhesive connection *(C3-2)*

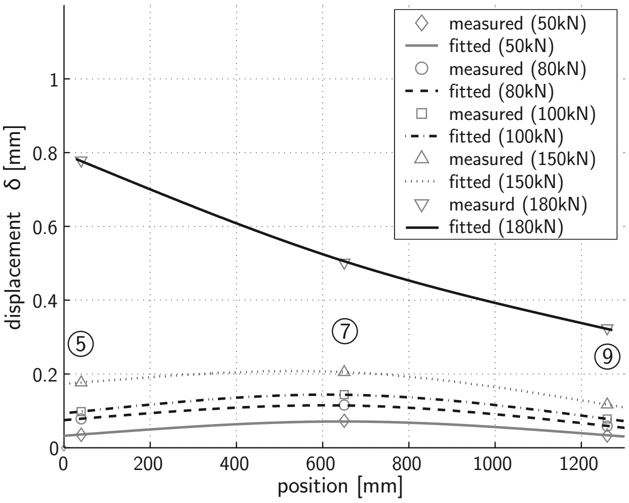

Figure 3.35: Specimen *DS C3-2*: distribution of differential displacements in bonded connection (inner side)

Fiber-tear failure was again the dominant failure mode in this experiment, see Figure 3.36. Most fibers were torn out of the FRP material, with some remaining on the surface of the adhesive layer.

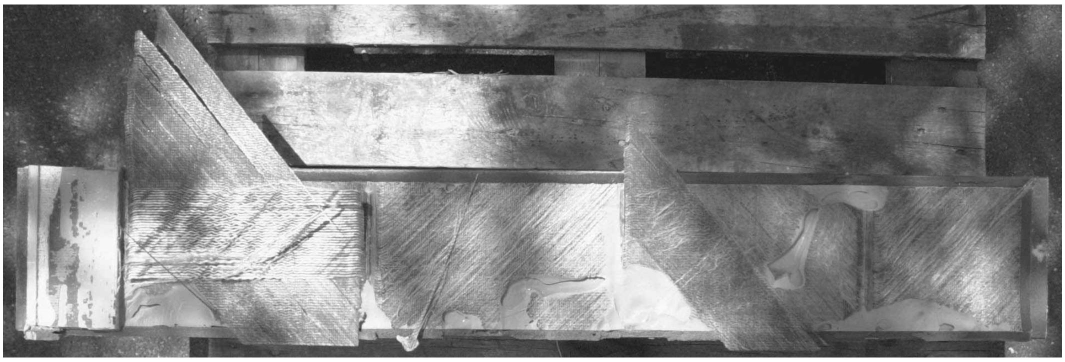

(a) view of girder

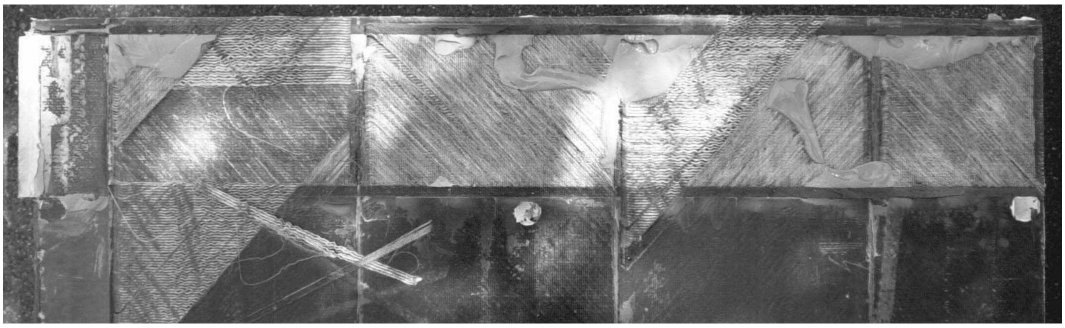

(b) view of deck

Figure 3.36: Failed bonded connection (*C3-2*)

3.5.2 Fatigue experiment

The structure was loaded before the fatigue experiment and after every one million cycles during the experiment with the SLS-load. The displacements of these loadings are shown in Figure 3.37. The stiffness before the first million fatigue cycles was lower than in subsequent measurements. This was due to the slackness in the whole structure (including the columns and steel girders with all bolted connections), which was obviously lower after the one million cycles. No perceptible loss of stiffness occurred during the fatigue experiment, and no damage was visually detected.

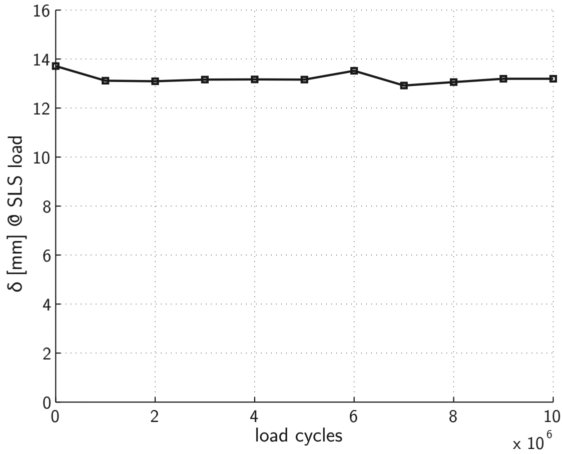

Figure 3.37: Fatigue test *C2-fat*; displacement is measured at loading point

3.6 Comparison of experimental results and calculations

The results obtained using the FE model described in Section 3.4.2, page 30 ff., were compared to the values measured in the experiments. Since the FE calculations were made linearly, only deformations in the linear-elastic range were compared. An uplift force of 80 kN in the adhesive connection was chosen as a reference value for comparisons, since all specimens exhibited a linear-elastic behavior at least up to this value.

3.6.1 Deformation of bridge deck

Displacement transducers # 1 and # 2

The bridge deck deflection at the loading point was measured by displacement transducers # 1 and # 2 and the average of these value was used for the diagrams in Figure 3.20. These values were compared to the deflection calculated by FEA using the model described in Section 3.4.2. The average displacement measured at 80 kN was 30.3 mm ± a standard deviation of 1.86 mm. The displacement obtained using the FE model was 32.3 mm. The maximum displacement was overestimated by only 7 % by the FE calculation. The detailed results are shown in Table A.4 on page 157.

Displacement transducers # 3 and # 4

The measured data and FE results are shown in Table A.5 on page 157. Measurement problems occurred in experiment *C2-2*. The average measured displacement was −1.86 mm ±0.4 mm, while the calculated displacement was −2.02 mm, corresponding to an overestimation of 9 %.

3.6.2 Differential deformation at adhesive connection

Deformation on inner side (# 5 to # 9)

The distribution of the average differential displacements is shown in Figure 3.38, and the numerical results of the experiments are given in Table A.6 on page 158. Figure 3.38 shows the data for all specimens, including *C1*, since the deformations were measured in the linear-elastic range, without any damage occurring in any of the experiments. Since the structure is symmetric, the distribution of the displacements computed by the FE analysis also has a symmetric shape. In the real structure the measurements obtained from these transducers showed little difference.

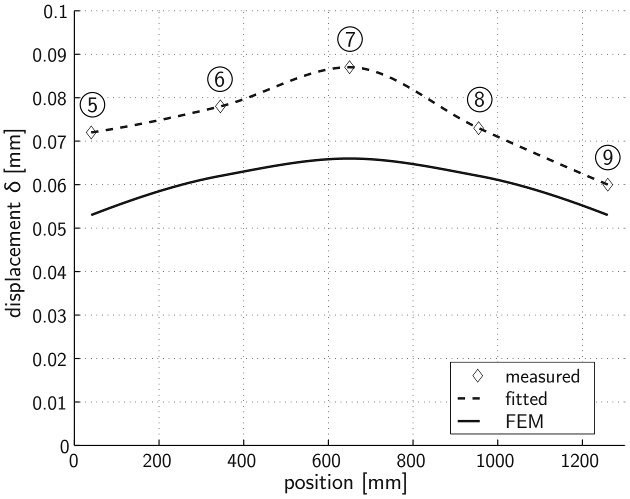

Figure 3.38: Comparison of calculated and measured average displacements at bonded connection on inner side at a load of 80 kN

As shown in Figure 3.38, the difference between the experimental results and the calculated values reaches 36 % at transducer # 5. This was probably because the FE model was too stiff, i.e. the elastic moduli of the FRP and the adhesive, determined in coupon tests, were too stiff when used for a structure of the size used in the experiments. Irregularities in the material do not occur in a perfectly shaped small coupon, but have a significant influence in bigger structures. Since the global behavior was in fairly good agreement with the calculation, it was probably the adhesive that was modeled with an E-modulus which was too stiff.

Deformation on outer side (# 10 to # 14)

Figure 3.39 shows the average distribution measured by the transducers in all experiments. The numerical data is given in Table A.7, page 159. Since transducer # 10 did not provide any results in some experiments, the average value shown in the diagram is not representative, see Table A.7. Again, as in the previous diagram, in Figure 3.38 the measurements show values up to 35 % higher than the FE results (at transducer # 11).

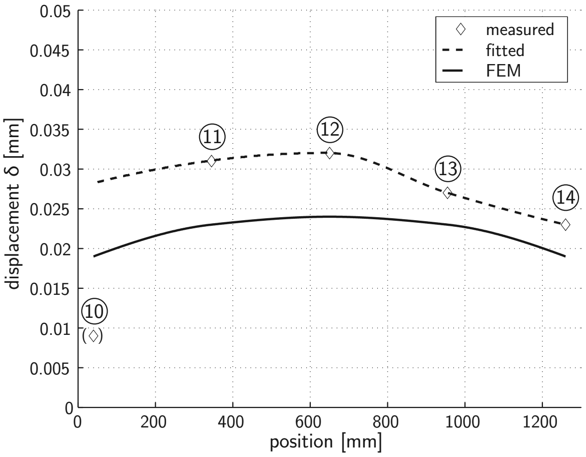

Figure 3.39: Comparison of calculated and measured average displacements at bonded connection on outer side at a load of 80 kN

Degree of support-fixation

The measured average deformations on the inner and outer sides at a loading of 80 kN were $\delta_i = 0.074\,\text{mm}$ and $\delta_o = 0.028\,\text{mm}$. Therefore, the average deformation in the center of the connection was $\bar{\delta} = 0.051\,\text{mm}$ with an average strain of $\bar{\varepsilon} = \frac{0.051\,\text{mm}}{D}$, where D is the measured distance in z-direction between the two points δ_i and δ_o. $EA_{\text{adh}} \cdot \bar{\varepsilon}$ must equal the uplift force $F_{\text{up}} = 80\,\text{kN}$. In addition to the deformation due to the uplift force, an extra $\pm 0.023\,\text{mm}$ at the edges result from the bending moment, which is related to a strain of $\varepsilon_M = \frac{0.023\,\text{mm}}{D} = 0.45\,\bar{\varepsilon}$. The corresponding bending moment is :

$$\begin{aligned} M &= \frac{2}{3} \cdot 186\,\text{mm} \cdot \frac{2}{3} \cdot \varepsilon_M \cdot \frac{1}{2} EA = \frac{2}{3} \cdot 186\,\text{mm} \cdot \frac{2}{3} \cdot 0.45\,\bar{\varepsilon} \cdot \frac{1}{2} EA \\ &= 0.0186\,\text{m} \cdot \bar{\varepsilon} \cdot EA \end{aligned}$$

The bending moment in a clamped support would be :

$$M_{\text{full}} = \frac{1}{2} \cdot 1.65\,\text{m} \cdot 80\,\text{kN} = 66\,\text{kNm} = 0.825\,\text{m} \cdot \bar{\varepsilon} \cdot EA$$

The relationship between the support-fixation of the two systems is $\frac{0.0186}{0.825} = 0.025454$, which means that the degree of the support-fixation in the experiment was only approximately 2.5 % of the moment in the case of a clamped connection.

3.7 Conclusions

The experimental series showed that, as previously assumed, failure almost always occurs inside the FRP material in the surface layer mats in a brittle way, if the surface preparation was adequate. The dominant failure mode was a fiber-tear failure.

An average tensile through-thickness stress in the adhesive layer of $\bar{\sigma}_z = 0.79\,\mathrm{N/mm^2}$ at failure was determined in the experimental series.[¶] The ratio of the average failure load to the load in the serviceability limit state was $\frac{F_u}{F_{SLS}} = 5.2$, and that of the failure load to the ultimate limit state load was $\frac{F_u}{F_{ULS}} = 3.5$, i.e. the total safety factor was 3.5, which is higher than the safety factor of the FRP deck for bending between main girders.

The FE analysis and the measurements showed that the adhesive connection on the steel girder acted as a simple support. The rotation mainly resulted from the rotational flexibility of the adhesive joint. As shown in the previously performed calculations, the bending moment in the adhesive connection was negligibly small. The comparison to the FE model described in Section 3.4.2 showed good agreement between measurements and numerical model, especially for the global behavior of the structure: the displacements at the loading point and their calculations differed only by approximately 7 %. The agreement between measurements and calculations at the adhesive connection was not as good as that between the rest of the data, since very small displacements within the range of the transducers' accuracy were measured. The maximum difference between measured and calculated values was 36 %, probably due to an E-modulus in the FEA which is stiffer than it would be in reality.

Further comparisons of calculated and measured stress conditions are made in Section 6.6, page 117 ff.

[¶] As mentioned, specimen *C1* was not included for the determination of the average stresses.

4 Evaluation of combined shear-tensile strength

4.1 Introduction

Through-thickness normal stresses due to moments and uplift forces caused by traffic loads transmitted by the bridge deck in the transverse bridge direction are predominately tensile stresses. This stress situation also occurred in the full-scale adhesive connection experiments, described in Chapter 3. In the longitudinal direction, shear stresses are caused due to the composite action between bridge deck and steel girders. This behavior is described in detail in [Gür04].

In order to determine a failure criterion, both stress components have to be taken into account: the through-thickness tensile stresses σ_z^+ resulting from forces acting in the transverse direction as well as the shear stresses τ_{xz} resulting from the composite action in the longitudinal direction.

Existing failure criteria for FRP composite materials developed by HART-SMITH [HS98a, HS98b, HS02], TSAI-HILL [TW71] or PUCK [Puc96], for example, could be used chiefly for predicting joint strength. However, the fiber architecture of pultruded sections is not layered in a comparable way to traditional laid-up composites. The determination of reliable through-thickness material properties is particularly difficult. To determine the ultimate strength of the FRP material in relation to the two stress components, the through-thickness tensile stresses σ_z^+ and shear stresses τ_{xz}, a device was developed at the *CCLab* that is able to load coupons incorporating the two stress components simultaneously. A failure criterion based on experimental investigation was developed [Val04], which considers the interaction of through-thickness tensile and shear stresses at the failure location, i.e. in the fiber-mat layers. This criterion is applied in the following.

4.2 Shear-Tensile Interaction Device (STI-Device)

The STI-Device was designed to measure the material strength of the bonded connections used with pultruded FRP material, see Figure 4.1 on the following page. The device is fully described in [Val04], and only a basic description follows at this point.

Two main loading mechanisms coexist, as shown in the diagram in Figure 4.2 on the next page:

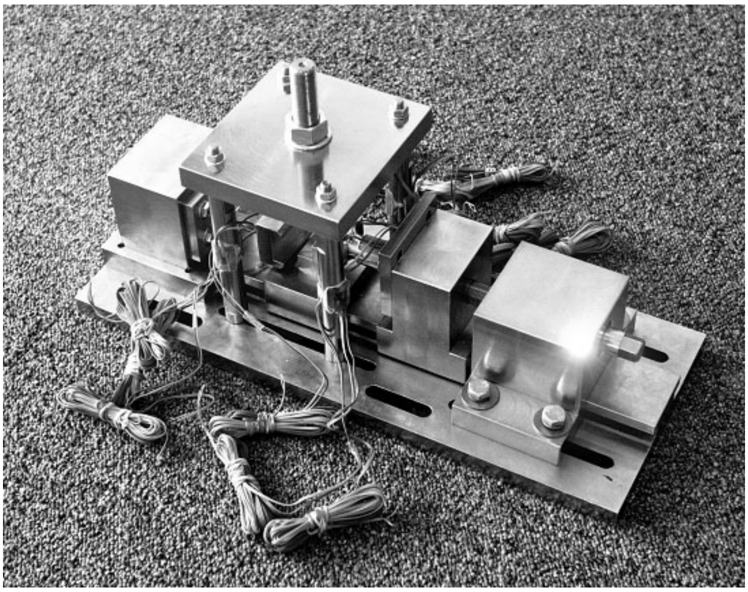

Figure 4.1: Shear-Tensile Interaction Device

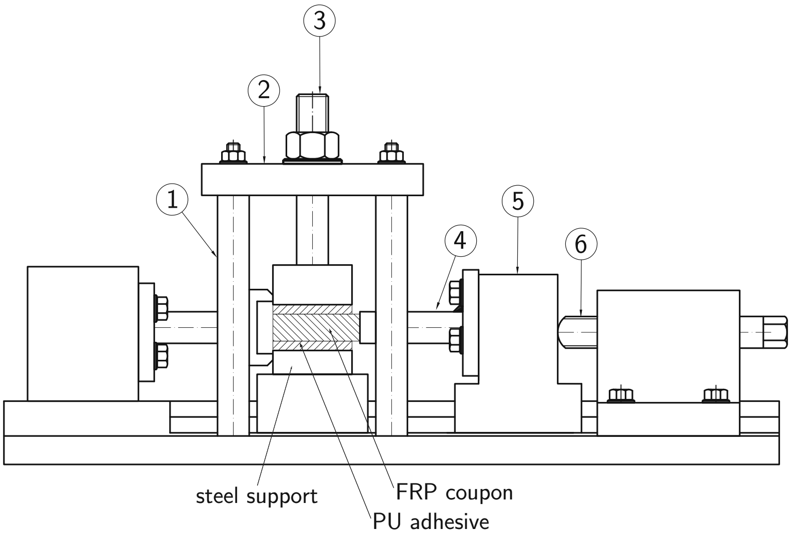
3
2
1
5
4
6
steel support
FRP coupon
PU adhesive

Figure 4.2: Diagram of Shear-Tensile Interaction Device

1. The tensile loading mechanism consists of 4 columns ①[*] supporting a steel plate ②. The load is introduced through a bolt ③ with a pitch of 1.5 mm, see Figure 4.1.

2. The shear loading mechanism consists of a horizontal bolt through which the load is applied, that exerts pressure on the FRP (elements ④ to ⑥) to induce shear.

Both forces can be applied simultaneously.

4.3 Experimental procedure

The experimental investigations were carried out on 50×50-mm FRP coupons cut from the top or bottom panels of the *DuraSpan 766* material, where the steel girders are connected to the bridge deck.

The FRP samples were bonded to the steel supports using polyurethane, see Figure 4.2, in which the unidirectional fibers were oriented perpendicularly to the axis of the shear mechanism. This was done to reflect the conditions inside the adhesively-bonded joints. Previous investigations have shown that the relatively soft polyurethane adhesive results in homogeneous and constant stress fields in the steel/FRP interface.

Before bonding, the steel surface was sanded, cleaned and degreased using acetone, and the FRP surface veil was mechanically abraded down to the first visible fibers of the mat then also cleaned and degreased using acetone.

To produce the material strength σ-τ-interaction diagram, experimental investigations involving both tensile and shear loading had to be carried out. While the pure[†] tensile loading and the pure shear loading mechanisms are obvious, the loading mechanism for a given combination of shear force $S = S_0$ and tensile force $H = H_u$ consists of the following procedure:

1. Imposing the shear force S_0 by acting on the shear loading mechanism (elements ④ to ⑥);

2. Acting on the tensile mechanism (element ③) by increasing the corresponding force H while verifying that the previously imposed shear load S_0 has not changed. If the shear force increases or decreases outside a range of $\pm 3\,\mathrm{N/mm^2}$, it should be readjusted;

3. The tensile force H has to be increased to the failure value H_u.

---

[*] The numeration relates to the diagram shown in Figure 4.2.

[†] The terms pure tensile and pure shear loading are used in the sense of *only* $\tau_{xz,u}$ and *only* $\sigma_{z,u}$ respectively, and **not** a combination of both.

The formulas used to calculate the stresses from the forces are the following:

$$\begin{aligned}\sigma_{z,u} &= \frac{H_u}{A} \\ \tau_{xz,u} &= \frac{S_u}{2A}\end{aligned} \tag{4.1}$$

with $A = a^2$ and a being the dimension of the specimens.

Each time this procedure was carried out successfully, one point of the σ-τ-interaction diagram was drawn.

4.4 Experimental results

4.4.1 Strength data

In order to be able to draw an interaction diagram, a total of 30 individual samples were tested according to the procedure described above.

The 30 samples were divided into six *groups* of five: the first one was used to determine the *pure* tensile strength $\sigma^+_{z,u}$, the last one to determine the *pure* shear strength $\tau_{z,u}$, and the four others to determine the strength under different combinations of through-thickness and shear stresses. The resulting experimental values are listed in Table 4.1.

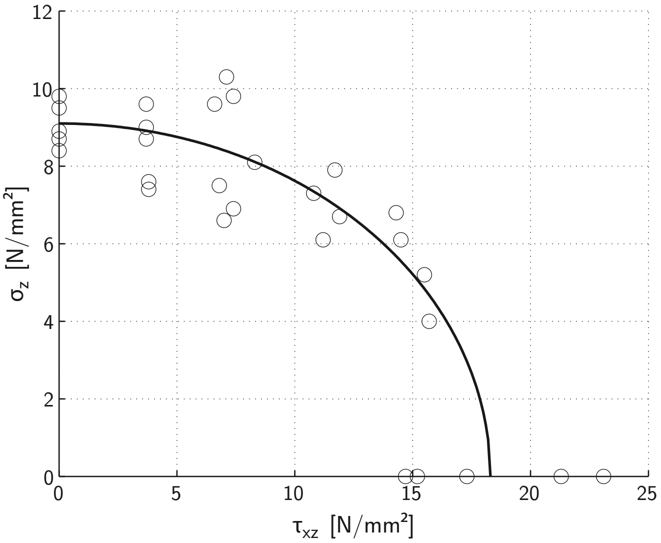

Figure 4.3: Material strength diagram based on experimentally obtained values

# 1		# 2		# 3		# 4		# 5		# 6	
τ	σ	τ	σ	τ	σ	τ	σ	τ	σ	τ	σ
0	8.4	3.7	8.7	6.6	9.6	11.9	6.7	11.7	7.9	23.1	0
0	9.8	3.8	7.4	7.0	6.6	6.8	7.5	15.5	5.2	15.2	0
0	8.9	3.7	9.0	7.4	6.9	10.8	7.3	14.5	6.1	21.3	0
0	9.5	3.7	9.6	8.3	8.1	7.1	10.3	15.7	4.0	14.7	0
0	8.7	3.8	7.6	7.4	9.8	11.2	6.1	14.3	6.8	17.3	0

Table 4.1: Experimental values $\left(\text{in } \left[\frac{\text{N}}{\text{mm}^2}\right]\right)$

As shown in [Val04], the best fitting curve for the gathered data displayed in Table 4.1 is Equation 4.2:

$$\mathfrak{F}(\sigma_z, \tau_{xz}) = \left(\frac{\sigma_z}{\kappa_\sigma \cdot \sigma_{z,u}}\right)^2 + \left(\frac{\tau_{xz}}{\kappa_\tau \cdot \tau_{xz,u}}\right)^2 = 1 \tag{4.2}$$

where $\sigma_{z,u}$ $(= 9.1\,\text{N/mm}^2)$ and $\tau_{xz,u}$ $(= 18.3\,\text{N/mm}^2)$ are the averaged values of the *pure* tensile and shear strengths of the investigated FRP material. The stresses in the coupons were uniformly distributed, as shown in [Val04], and therefore no correction factors were needed.

The correction factors κ_σ and κ_τ, as defined in [Val04], are used to take stress concentrations in joints into account. For the application of this failure criterion to the adhesive connections of the investigated bridge decks, the correction factors have values of between one and four. Due to the extent of the stressed surface, no size effect was assumed and therefore factor $\kappa_\sigma = \kappa_\tau = 1$.

Figure 4.3 on the facing page shows the gathered data: on the x-axis the shear strength values $\tau_{xz,u}$, on the y-axis the through-thickness strengths $\sigma_{z,u}$. The best fitting curve, according to Equation 4.2, is overlaid.

4.4.2 Failure mode

The failure mode observed after testing the individual samples was a *fiber-tear failure*, since neither the adhesive layer nor the adhesive-steel connection failed prematurely. The observed failure mode was the same as that which occurred in the experiments described in Chapter 3. In most cases, the fiber-tear failure affected the surface layer mat (down to 3 mm) of the tested FRP sample (see Figures 4.4 (shear-dominated) and 4.5 (tensile-dominated)).

In some cases failure did not occur in the first layer, but deeper inside the FRP sample, as can be seen in Figure 4.4(c) to (e). The failure in the tensile-dominated experiments clearly occurred slightly deeper (down to 3 mm) inside the material than

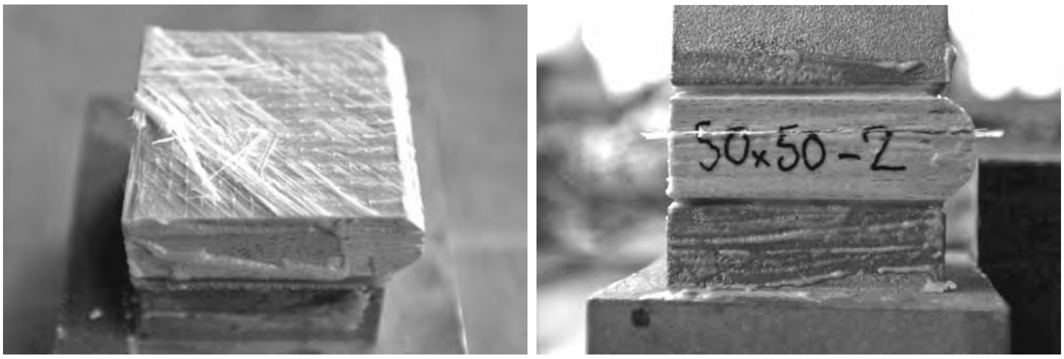

(a) # 1-1 (b) # 1-2

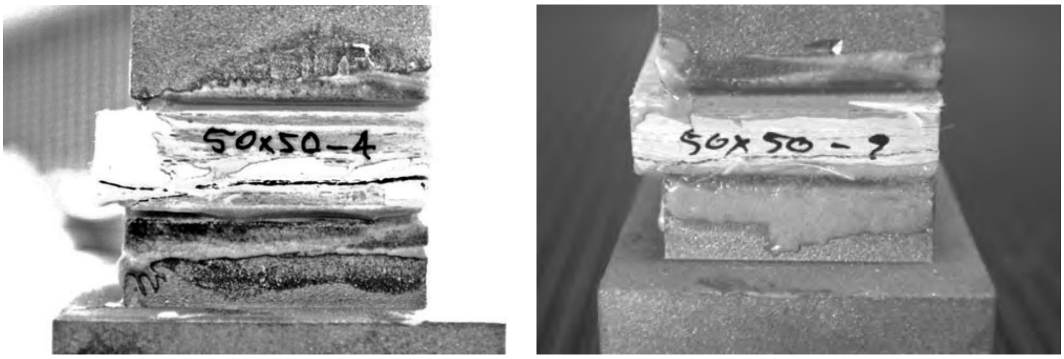
50x50-4
50x50 - 9

(c) # 1-4 (d) # 2-4

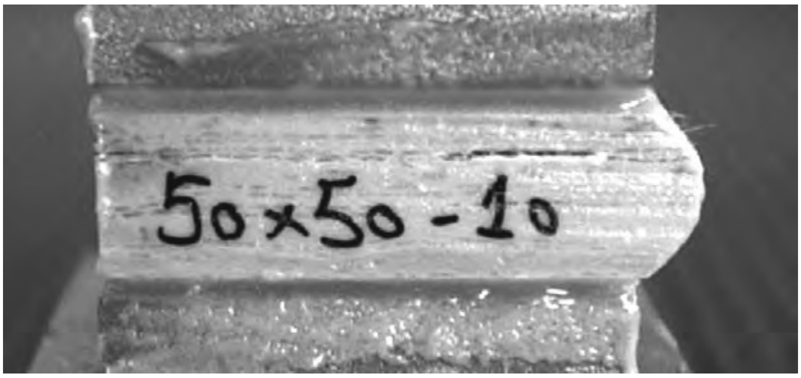

(e) # 2-5

Figure 4.4: Failure modes of STI coupons (tensile-dominated)

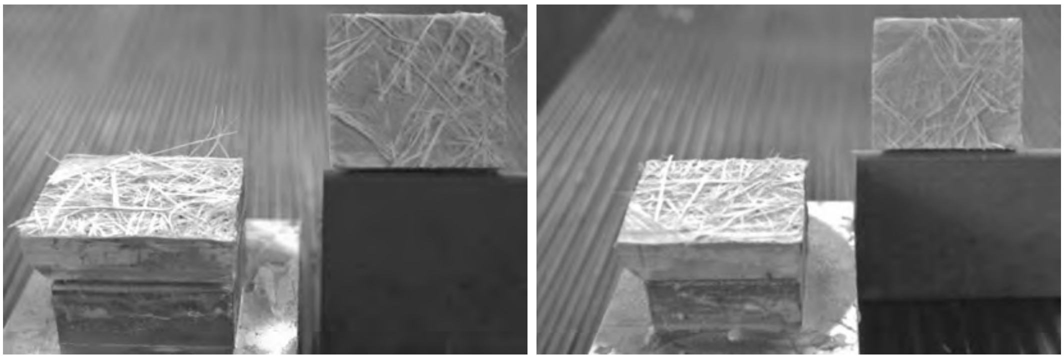

(a) # 3-4

(b) # 5-1

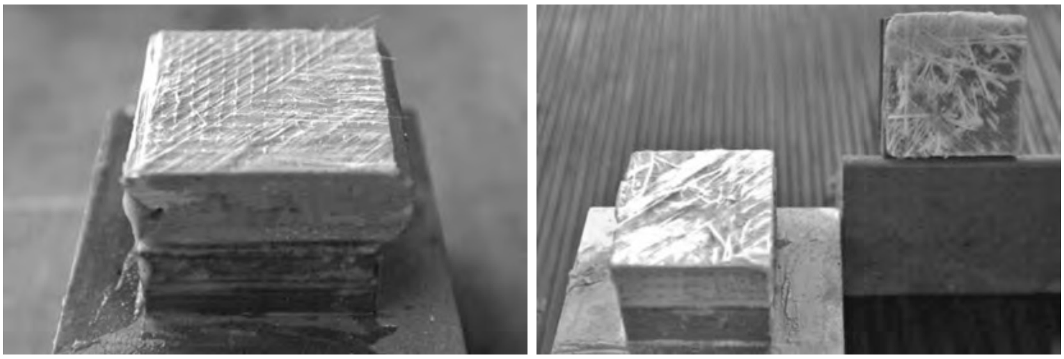

(c) # 5-4

(d) # 6-3

Figure 4.5: Failure modes of STI coupons (shear-dominated)

in the shear-dominated experiments, in which it almost always occurred at a depth of approximately 0.5 mm from the surface. This was probably only characteristic of the coupon tests however, since such a deep failure was not observed in the full-scale experiments in which a pure tensile stress condition existed.

4.4.3 Partial safety factor

In the design concept according to current codes, the characteristic loadings are increased by load factors, while the material resistance is reduced by material safety factors.

$$\gamma_F \cdot S_k \overset{!}{\leq} \frac{R_k}{\gamma_M} \qquad \leadsto \qquad S_d \overset{!}{\leq} R_d \tag{4.3}$$

γ_F – load factor
γ_M – partial safety factor
S_d – loading in the ultimate limit state *(ULS)*
R_d – material strength reduced by the partial material safety factor γ_M

According to EN 1990 [Eur02], Annex D, the characteristic value may be determined from tests using

$$R_k = R_m\,(1 - k_{kn} \cdot \nu_R) \tag{4.4}$$

where

k_{kn} is the fractile coefficient for determining 5 % fractile of the frequency distribution of R, see [Eur02] – Annex D.

Since 30 samples were tested, k_{kn} may taken as $k_{kn} = 1.645$. Hence the characteristc value is

$$\begin{aligned} R_k &= R_m\,(1 - 1.645 \cdot 0.117) \\ &= R_m \cdot 0.808 \end{aligned} \tag{4.5}$$

The partial safety factor γ_M results from

$$\gamma_M = \frac{R_k}{\gamma_M} = \frac{1 - k_{kn} \cdot \nu_R}{1 - k_{dn} \cdot \nu_R} \tag{4.6}$$

where k_{dn} is derived in [Eur02] for a reliability index $\beta = 3.80$:

$$k_{dn} = 3.13. \tag{4.7}$$

Therefore the γ_M-factor reads

$$\gamma_M = \frac{1 - 1.645 \cdot 0.117}{1 - 3.13 \cdot 0.117} = 1.28 \tag{4.8}$$

In general the reliability index $\beta = 3.80$ applies to structures with ductile behavior and mean consequences of failure. As the failuree behavior of the adhesive connections for combined shear and tension may be classified as brittle (due to lack of pre-warning by large deformations), the use of $\beta = 3.80$ can only be justified by failure path consideration of the complete FRP-deck-system including the adhesive joint.

In fact the weakest link in th full FRP-deck system is the plate-structure, in particular at the adhesively-bonded connections between the pultruded profiles, the failure of which would not be catastrophic but only affect the serviceability. Hence the adhesive joint of the deck to the main girders takes profit from the 'pre-warning' from serviceability failure of the deck structure and only needs to be designed for 'overstrength' by ordinary ultimate limit state design.

The partial safety factor of a similar material tested in [Val04] is $\gamma_M = 1.32$. A material safety factor of $\gamma_M = 1.28$ seems reasonable when compared to safety factors of similar materials in [Cla96].

4.5 Conclusions

The experimental investigations described in this chapter have shown that:

- → The FRP material's resistance to a combined loading of through-thickness tensile stresses σ_z and shear stresses τ_{xz} can be described by a quadratic interaction function.
- → The observed failure mode was the same as that which occurred in the experiments carried out in Chapter 3.
- → A partial material safety factor for the tested material was determined as being $\gamma_M = 1.28$.
- → The failure mode in both types of experiments in Chapters 3 and 4 was the same. It can therefore be concluded that the failure criterion can also be applied for the full-scale adhesive connections.

The comparison between the results of the full-scale adhesive connection experiments and the coupon tests is made in Section 6.6.

Part IV

Analytical part

5 Influence of the torsional stiffness of steel girders

5.1 Introduction

Traffic loads on the bridge lead to moments and shear in the bridge deck. Looking at a cross section through the bridge along the transverse direction, three different structural behaviors are possible, depending on the deck's support conditions. These are shown in Figure 5.1, page 72, with their static systems and qualitative distributions of bending moments in the deck:

(a) The torsional stiffness of the steel girder is very low and therefore the steel girders act as simple supports, see Figure 5.1(a).

(b) The torsional stiffness of the steel girder has a significant value. The steel girder does not act as a simple support; a part of the bending moment of the bridge deck is transmitted into the steel girder as a torsional moment. In the structural system this torsional stiffness is delineated by a spring stiffness. The torsional moment has the value of the difference ΔM between the bending moments in the deck over the steel girder, see Figure 5.1(b).

(c) The steel girder is very stiff in terms of torsion, e.g. a box girder. As a result, the entire bending moment in the bridge deck is transmitted into the steel girder as a torsional moment, see Figure 5.1(c).

Steel bridges usually incorporate stiffeners, at least at the supports or locations where single loads are applied, which transmit the forces into the girder section and prevent the buckling of the web. They can also have the function of connecting the steel girders in the transverse direction using additional profiles or connecting other structural elements to the girder however.

Furthermore, stiffeners (as shown in Figure 5.3 on page 76), which are usually added to the steel girder over the support, have a certain influence on the torsional flexibility of the girder by reducing warping[*] of the section. One way of reducing

---

[*] *Warping* is the cross-sectional deformation in the axis (x-)direction of the girder, resulting from the warping torsion. (German: *Wölbkrafttorsion*) Picture taken from[Pet98].

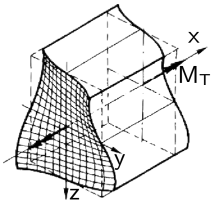

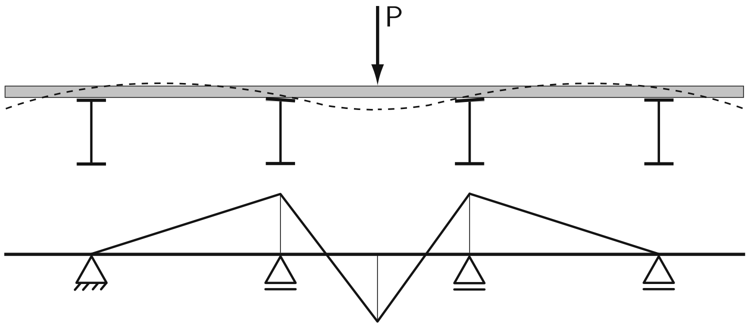

(a) Torsional flexible steel girders, acting without any restraint, with qualitative bending moment distribution

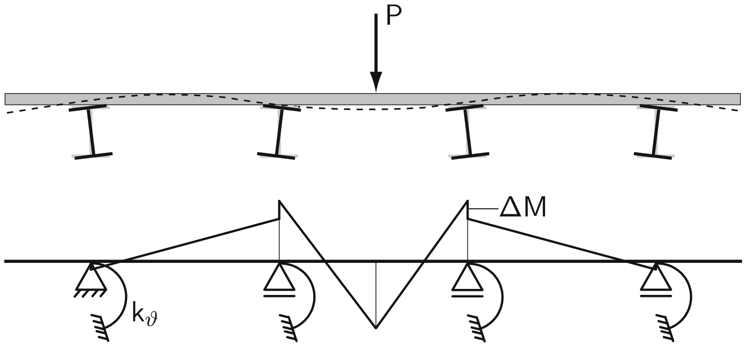

(b) Steel girders with partial torsional stiffness and the qualitative bending moment distribution

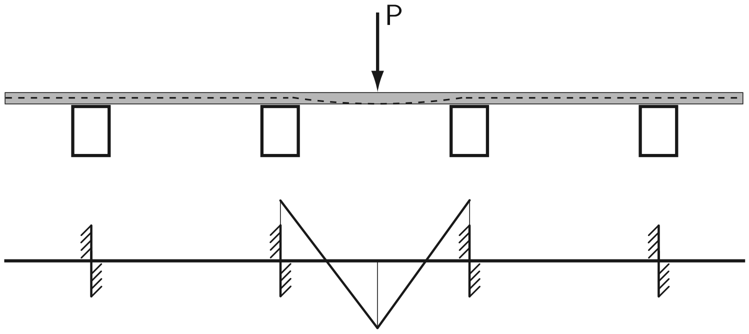

(c) Steel girders with high torsional stiffness acting as a full restraint

Figure 5.1: Influence of steel girder's torsional stiffness on bending moment in bridge deck

warping stiffness are stiffeners that do not fill the whole section. Such a stiffener must still of course be able to transmit the point loads (at the supports for example) into the section.

The different structural behaviors have the following influence on the stress distribution inside the adhesive connection between the bridge deck and the steel girders:

1. In the system shown in Figure 5.1(a), a pure vertical force without eccentricities is acting over the support, i.e. in the connection between girder and deck. When uplift forces are present, the through-thickness tensile distribution is uniform.
2. In the system in Figure 5.1(b), bending moments are transmitted from the bridge deck through the adhesive connection to the upper steel flange, in addition to the vertical force. These bending moments lead to a linear stress distribution transverse to the flange. The tensile stresses due to bending increase the uniformly distributed tensile stresses resulting from uplift forces in the adhesive connections.
3. Since the whole bending moment acting in the bridge deck has to be transferred by the adhesive connection to the steel girder, very high through-thickness stresses occur at the edge of the adhesive layer of this system, as shown in Figure 5.1(c).

Generally, an adhesive thickness of 8 mm sufficiently reduces stress concentrations, as has been shown in Section 3.6. Therefore, a moment distribution as shown in Figure 5.1(a) would be the normal case. However, a thickness of almost 0 mm might occur locally due to inadequate tolerances on the construction site. Therefore, this unfavorable case, as shown in Figure 5.1(b), is investigated and the adhesive layer is disregarded in the following (while a distribution as shown in Figure 5.1(c) is hypothetical).

Due to the fixed adhesive connection between the FRP deck and the steel girder, the FRP deck, when loaded, imposes a rotation φ on the upper flanges of the steel girders. The dimension of this rotation depends on the torsional stiffness of the steel girder. The rotation φ of the flange is a combination of the section's rotation *and* the section's deformation, see Figure 5.2.

Because of the relatively low torsional stiffness of I-steel profiles, the restraint imposed by the girders cannot be considered as being a full restraint, but may be represented by a torsional spring with the corresponding spring stiffness k_ϑ, as shown in Figure 5.1. Theoretically, the spring stiffness k_ϑ is not a property of the steel profile, but of the whole static system consisting of the steel profile and restraints such as stiffeners filling the cross section and preventing warping. Moreover, the relationship between a torsional moment M_T imposed on the steel profile and the corresponding rotation φ of the flange, the spring stiffness k_ϑ, as shown in Equation 5.1, depends on the position x along the steel girder.

$$k_\vartheta = \frac{M_T}{\varphi} \tag{5.1}$$

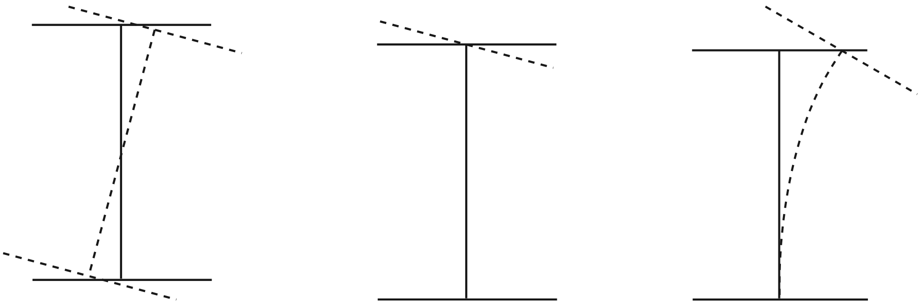

(a) Rotation of whole cross section

(b) Deformation of web-to-flange junction, rotation of upper flange

(c) Deformation of web

Figure 5.2: Components of φ

5.2 Objective

The main aim of this chapter is the investigation of the influence of the torsional stiffness of the steel girder on the distribution of through-thickness stresses in the adhesive connection. Since the experimental investigations documented in Chapter 4 showed that the FRP failure is triggered by a combination of tensile through-thickness stresses σ_z^+, and shear stresses τ_{xz}, it is important to describe the additional tensile stresses resulting from the (partial) restraint of the FRP deck due to the torsional stiffness of the steel girders.

The objective of the numerical and analytical investigations developed in this chapter is the determination of the influence of the (partial) restraint of the bridge deck due to the torsional stiffness of the steel girders on the stress distribution at the failure location (the outer mat layer of the FRP deck). As mentioned above, the possible rotation in the adhesive joint is disregarded.

5.3 Procedure

Two different approaches can be adopted to determine the torsional stiffness of the steel main girders:

- → Analytical solutions, based on different levels of modeling:
  - – The simplest approach, based on the St. Venant[†] formulation for torsion, which does not take into account the warping of the section (see [Fri83]);
  - – Warping torsion, obtained from a quadratic differential equation, which takes into account the warping of the section, but still respects the Bernoulli hypothesis, which does not take into account local deformations of the section or
  - – the General Beam Theory (GBT) [Sch89], which allows local deformations of the section to be analytically taken into account.
- → Numerical solution, based on the Finite Element Method.

Owing to the relatively complex structural configuration to be investigated (steel girders with stiffeners, bonded FRP deck on top etc.), it was considered that the St. Venant approach would be too basic to provide accurate results and that both the Warping Torsion Theory and the General Beam Theory would be too complex to use owing to the need to incorporate the stiffeners. Thus the necessary calculations were made using FEA, especially because it also enables local deformations to be determined.

The plausibility of the FEA was checked analytically in Section 5.5 with formulas describing the Warping Torsion [Fri83, OH96] on a simplified girder with a symmetric cross section (to the two main axes) and without any stiffening members.

5.4 Determination of the torsional stiffness k_ϑ of steel girders

The objective of this section is to investigate the influence of the geometry of the steel girders and disposition of the stiffeners on the magnitude and distribution of the torsional stiffness along the span of the bridge. The procedure chosen to approximate the steel girders' torsional stiffness by rotational springs was as follows:

- → Modeling of one steel girder (including the stiffeners);
- → loading the modeled girder with a torsion moment M_T and
- → calculating the corresponding spring stiffness using Equation 5.1.

[†] Adhémar Jean Claude Barré de Saint Venant, 1797–1886.

5.4.1 FE model

A parameter study was done on a steel girder using the FEA program *Ansys*. The geometry of the modeled girder is shown in Figure 5.3. The geometry of the steel girder consisted of an assembly of areas which were spanned between six (or nine with stiffeners) key points. The key point model of the cross section is shown in Figure 5.4 on the facing page, and the meshed girder in Figure 5.5.

The girder is supported at six points of the lower flange, as the supporting steel girder of a bridge would be supported. In order to obtain one fixed support and one roller support, at $x = 0$ the displacements in x-, y- and z-directions are constrained, and at $x = \ell$ only the displacement in y- and z-directions is constrained. The top flange was fixed in the horizontal direction perpendicular to the girder's direction.

The following parameters can be changed in the model: the width of the top flange $b_{f,t}$, width of the bottom flange $b_{f,b}$, height of the section h, stiffener height h_s, thickness of the top flange $t_{f,t}$, thickness of the bottom flange $t_{f,b}$, thickness of the web t_w and girder span ℓ.

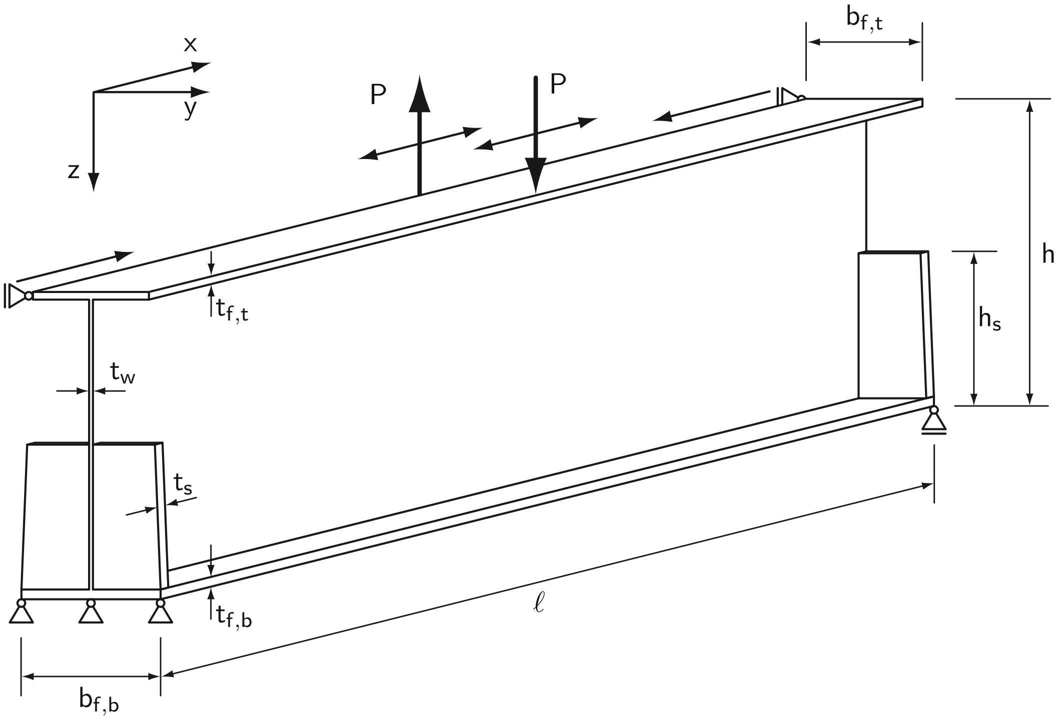

Figure 5.3: Steel girder loaded with a pair of forces

The calculations are made under the assumption that all materials remain within the linear elastic range, assuming that the final bridge design will limit the level of the stresses to that below the yield stresses. The steel was modeled as an isotropic

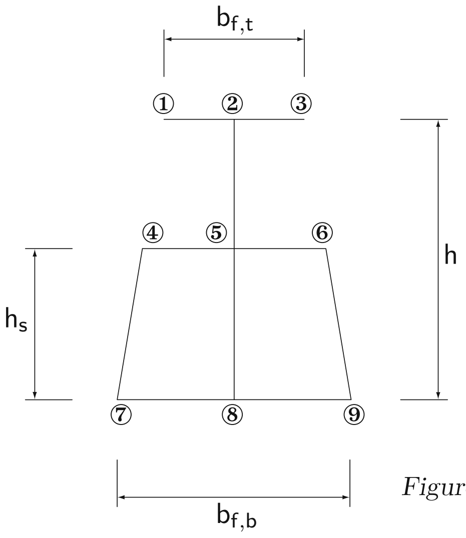

Figure 5.4: Key points of cross section in FE model

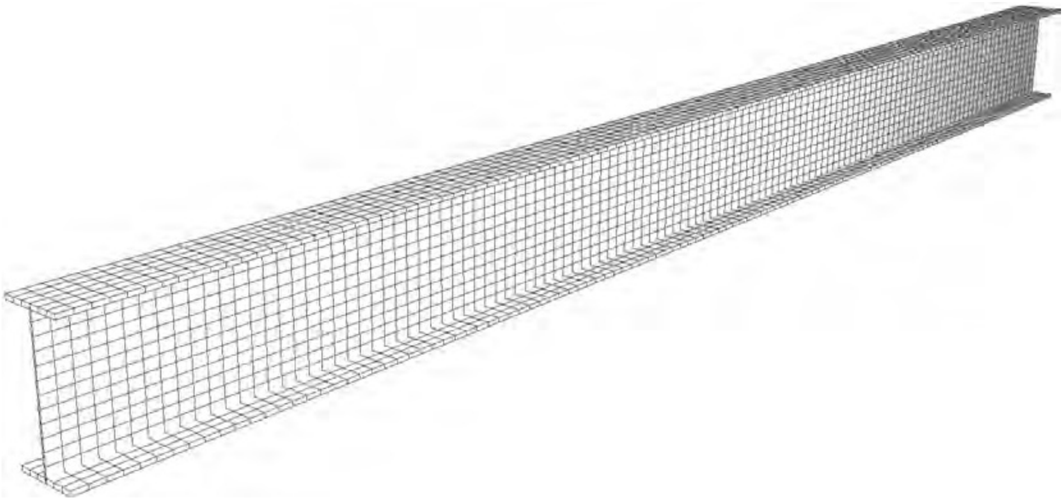

Figure 5.5: Meshed girder

material with a Young's modulus of $E_s = 210\,\mathrm{kN/mm^2}$ [OH96]. Shell elements were used for the model which were sufficiently accurate to investigate the global bearing behavior. The element type chosen was *SHELL 93*.

The applied moment M_T is simplified as two loads of $P = 1\,\mathrm{N}$ pointing in opposite directions. These loads are located at the edge of the upper flange at various locations along the girder. In the real system, the torsional moment would be transmitted linearly. The chosen loading case therefore slightly overestimates the local deformations of the upper flanges.

The rotation φ of the upper flange will be expressed by the vertical displacements u_z of the key points ① and ③ where the loads are applied. The spring stiffness k_ϑ in Equation 5.1 on page 74 can be calculated as follows:

$$M = P \cdot b_{f,t} = 1\,\mathrm{N} \cdot b_{f,t} \tag{5.2}$$

$$\Delta u_z = u_z^{①} - u_z^{③} \tag{5.3}$$

$$\varphi = \frac{\Delta u_z}{b_{f,t}} \tag{5.4}$$

$$k_\vartheta = \frac{M}{\varphi} = \frac{1\,\mathrm{N} \cdot b_{f,t}^2}{\Delta u_z} \quad [\mathrm{Nmm}] \tag{5.5}$$

The values shown in Table 5.1 were fixed and did not change in the parameter study. Subsequent to the parameter study, a set of different geometries for various spans was analyzed. The results are shown in Tables B.1 to B.5 on pages 161 ff.

Table 5.1: Fixed dimensions of modeled girder

span length	ℓ	$= 10\,\mathrm{m}$
section height	h	$= 750\,\mathrm{mm}$
top flange width	$b_{f,t}$	$= 300\,\mathrm{mm}$
bottom flange width	$b_{f,b}$	$= 360\,\mathrm{mm}$
bottom flange thickness	$t_{f,b}$	$= 25\,\mathrm{mm}$
web thickness	t_w	$= 10\,\mathrm{mm}$
stiffener height	h_s	$= 375\,\mathrm{mm}$
stiffener thickness	t_s	$= 30\,\mathrm{mm}$

The influence of

- → the top flange thickness,
- → the web thickness,
- → the stiffeners,
- → the number of stiffeners and
- → the span

on the deformation of the girder's cross section was investigated using the FE model as follows:

Influence of top flange thickness $t_{f,t}$

It was of interest, for further calculations, to determine at which locations the rotation, as expressed by Equation 5.1, resulted from the global St. Venant rotation of the profile and from local bending of the flanges or the web. This was investigated on the girder shown in Figure 5.3, featuring a stiffener at each end ($h_s = h/2$). The top flange thickness varied between 4 mm and 16 mm.

Influence of web thickness t_w

The web thickness plays an important role with regard to the torsional stiffness of a girder. Again a girder with the basic dimensions given in Table 5.1 is examined. The different web thicknesses t_w varied between 4 mm and 16 mm, while the top flange thickness remained constant ($t_{f,t} = 20\,\mathrm{mm}$). Stiffeners were included at each end ($h_s = h/2$).

Influence of stiffener height h_s

The influence of stiffener height was investigated: for the girder in Figure 5.3 the initial values given in Table 5.1 were used. The height of the stiffeners varied between $h_s = 0.5\,h$ and a full stiffener ($h_s = 1.0\,h$) connected with the flange.

Variation in number of stiffeners

The stiffeners shown in Figure 5.3 on page 76 are located at the supports. More stiffeners could be used, for example to connect cross-beams to the girder. The flexibility of a section due to different numbers of stiffeners, with 2, 3, 4 and 12 stiffeners equally distributed over the girder, was compared. The stiffeners had the height of $h_s = 0.5\,h$, the girder's dimensions as listed in Table 5.1 on the preceding page were used.

5.4.2 FEA Results

Influence of top flange thickness

Figure 5.6 on the following page shows the curvature of the upper flange between the two loading points in the center of the girder, causing the torsional moment M_T. The deformations u_z provide information concerning:

- → The straightness of the top flange.

→ The rotation of the top of the web, expressed by the inclination of the curves in the middle of the flange.

With regard to the former, it could be clearly recognized that with increasing flange thicknesses $t_{f,t}$, the deformations tended to be more and more linear; from thicknesses $t_{f,t}$ of 10 mm onwards, they could be considered as being almost linear. This means that from $t_{f,t} = 10$ mm onwards, the rotation φ results mainly from the flexibility of the web. In bridges, flange thicknesses of less than 10 mm are not generally used.

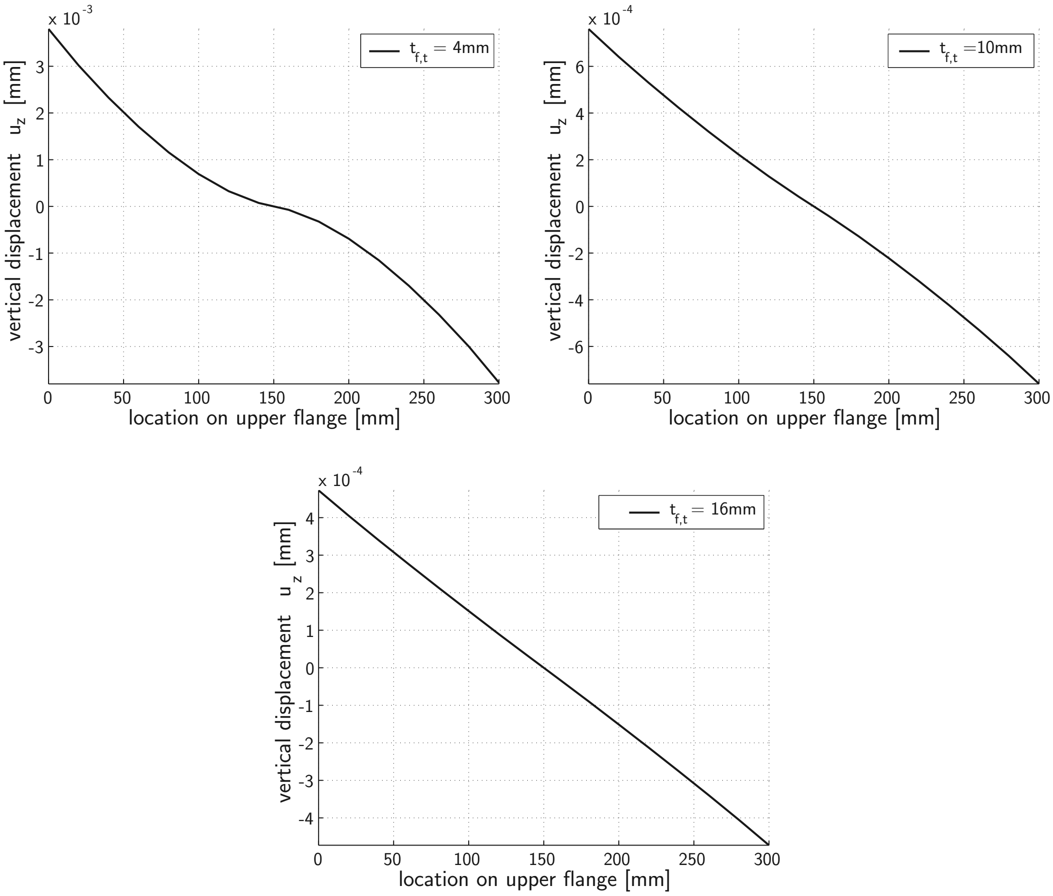

Figure 5.6: Deflections of upper flange for different flange thicknesses $t_{f,t}$

Influence of web thickness

The diagram in Figure 5.7 shows that the smaller the web thickness, the more equally distributed is the spring stiffness of the section. With a web thickness of 4 mm the spring stiffness at the supports is almost the same as the spring stiffness at mid-span, whereas for the web thickness of 16 mm the spring stiffness varies more throughout the girder. The zone influenced by the stiffener is larger when thicker webs are used, but negligible in the case of webs thinner than 12 mm. This leads to a peak at about a quarter (and three-quarters) of the girder's length for girders with web thicknesses of between 12 and 16 mm. For girders with thinner webs, the zone influenced by the stiffeners is much smaller and does not have a stiffening effect that is measurable at the top flange. Therefore a stiffener that fills half of the profile's height has a greater influence on rotational stiffness in the case of thicker webs. Over the supports, stiffness noticeably decreases owing to the free ends.

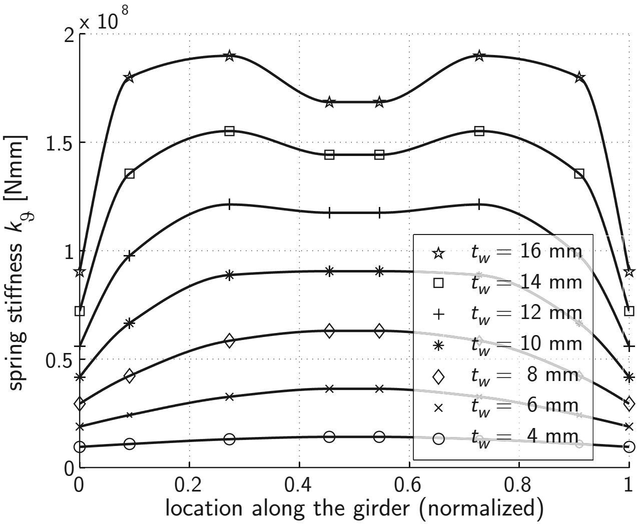

Figure 5.7: Influence of variation of web thicknesses on torsional stiffness of girder

Influence of stiffener height

The spring stiffness, measured over a large area in mid-span, is not markedly influenced by the height of the stiffeners at the ends of the span, see Figure 5.8. This is valid for a stiffener height of up to $h_s = 0.98\,h$. As long as the stiffener does not fill the whole section, it can be considered as being approximately constant over 80 % of the span. The reason for this is that there is still a considerable amount of flexibility resulting from the top of the web. For stiffeners filling the whole cross section, the spring stiffness increases asymptotically, due to the fact that lateral bending of the web is prevented. Even then however, the torsional stiffness k_ϑ increases only over the last 15–20 % of the span towards the ends, not affecting the mid-span where this influence remains minor. The torsional flexibility of the considered girder hardly depends on the stiffener height, as long as it is not connected to the top flange.

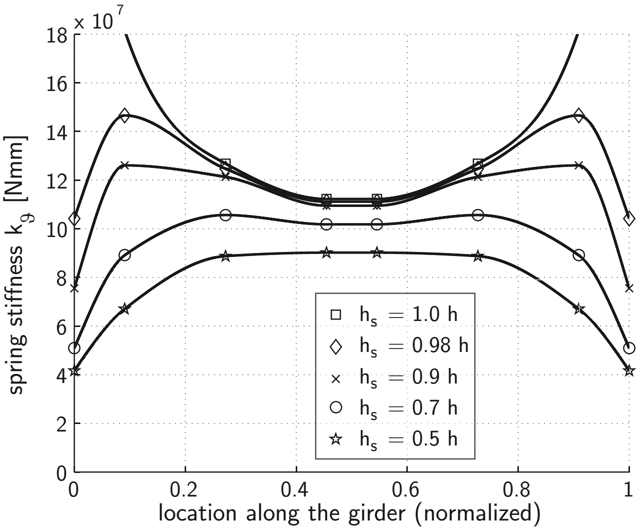

Figure 5.8: Influence of stiffener height at supports

Influence of number of stiffeners

The plot showing the influence of the number of stiffeners on the spring stiffness is shown in Figure 5.9 on the next page. It can be seen that with an increasing number of stiffeners, spring stiffness does not noticeably increase. Even if twelve stiffeners are used, resulting in an unrealistic stiffener-to-stiffener distance of less than one meter, the flexibility of the steel girder remains approximately the same as the torsional flexibility of the girder if only two support stiffeners are used. This again shows that the flexibility of the steel girders originates from the top of the web.

5.5 Analytical determination of spring stiffnesses

An analytical calculation was carried out by using formulas describing the warping torsion as a plausibility check for the FEA. The stiffnesses are calculated and plotted over the length of the beam. For both methods, analytical and numerical, a girder of the same geometry, as shown in Figure 5.10, is used. The analytical model does not respect local deformations, i.e. the Bernoulli hypothesis is included. Therefore *fork bearings*[‡] were also applied at the supports in the FE model.

[‡] Bearing at the end of a girder that prevents deformations in orthogonal directions to the beam's (x-)axis as well as rotations around the x-axis; the warping of the cross section is not constrained. In German *Gabellager*.

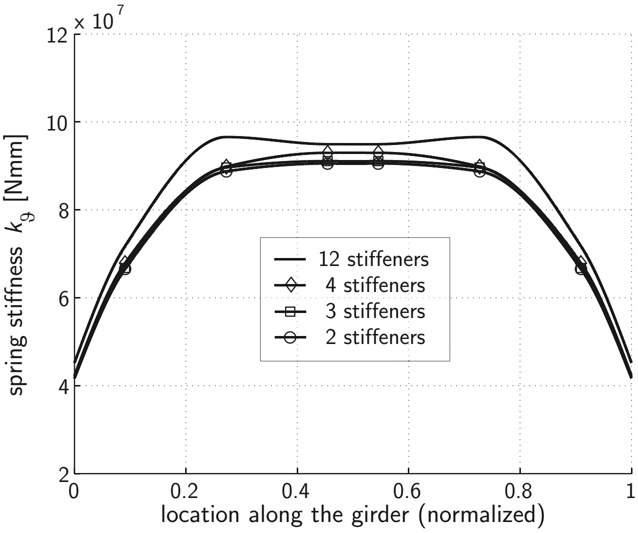

Figure 5.9: Influence of number of stiffeners on k_ϑ

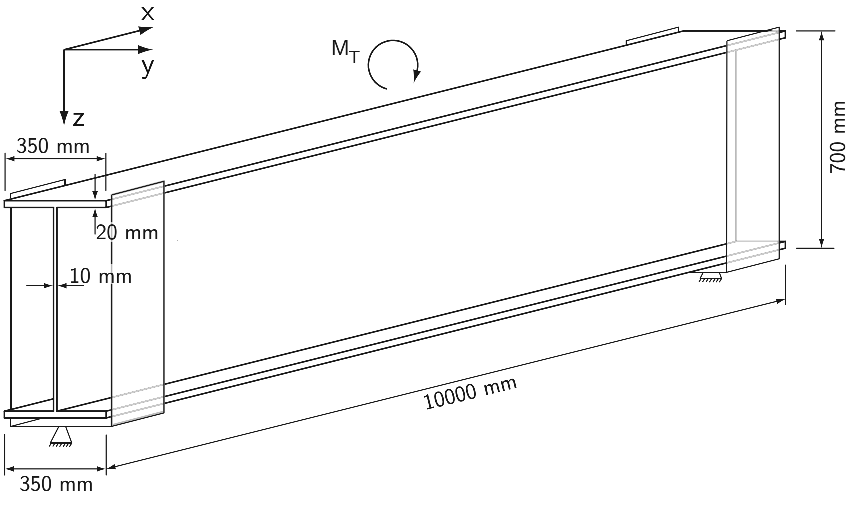
x
y
z
M_T
350 mm
20 mm
10 mm
700 mm
10000 mm
350 mm

Figure 5.10: Model used for analytical and FE calculations

For sections where warping plays an important role[§], the relationship between applied torsion moment M_T and rotation φ can be determined by solving the differential equation describing the mechanics of the problem. For simply-supported beams with symmetric cross sections and fork bearings, the solution can be found in [OH96, Fri83, RCL72]:

$$
\begin{aligned}
\vartheta(x) &= \frac{M_T}{EI_\omega \cdot \lambda^3}\left[\frac{\lambda \cdot x}{2} - \frac{\sinh\left(\lambda \cdot \frac{\ell}{2}\right)}{\sinh(\lambda \cdot \ell)} \cdot \sinh(\lambda \cdot x)\right] \\
&\text{where} \\
\lambda &= \sqrt{\frac{GI_T}{EI_\omega}} = 6.625\,\mathrm{m}^{-1} \\
I_T &= \frac{2}{3}\, t_f^3\, (b_f - 0.63\, t_f) + \frac{t_w^3}{3}\, (h - 2\, t_f) \\
&\quad + \left[\frac{(r + \frac{t_w}{2})^2 + (r + t_f)^2 - r^2}{2 \cdot r + t_f}\right]^4 \cdot 2\, \frac{t_w}{t_f}\left(0.145 + 0.1\, \frac{r}{t_f}\right) \\
&= 1.880 \cdot 10^{-3}\,\mathrm{m}^4 \\
&\text{— } 2^{\text{nd}} \text{ degree torsion moment of inertia} \\
t_f &= t_{f,b} = t_{f,t} \\
I_\omega &= \frac{t_f \cdot b_f^3 (h - t_f)^2}{24} = 1.652 \cdot 10^{-5}\,\mathrm{m}^6 \\
&\text{— } 2^{\text{nd}} \text{ degree warping torsion moment of inertia}
\end{aligned}
\tag{5.6}
$$

The initial parameters given in Table 5.2 were used.

Table 5.2: Dimensions of modeled girder

Young's modulus	E_s	$= 210\,000\,\mathrm{N/mm^2}$
shear modulus	G_s	$= 81\,000\,\mathrm{N/mm^2}$
flange width	b_f	$= 350\,\mathrm{mm}$
flange thickness	t_f	$= 20\,\mathrm{mm}$
web thickness	t_w	$= 10\,\mathrm{mm}$
section height	h	$= 700\,\mathrm{mm}$
radius[a]	r	$= 0\,\mathrm{mm}$

[a] radius of web-to-flange junction of an I-cross section

The torsional stiffness is determined from Equation 5.1, page 74.

[§] As for the open I-profiles used in the current bridge model.

Comparison of analytic and FEA results

The spring stiffness for the girder shown in Figure 5.10 can be plotted over the span of the girder, and the result is displayed in Figure 5.11 versus the torsional stiffnesses obtained analytically and by FEA.

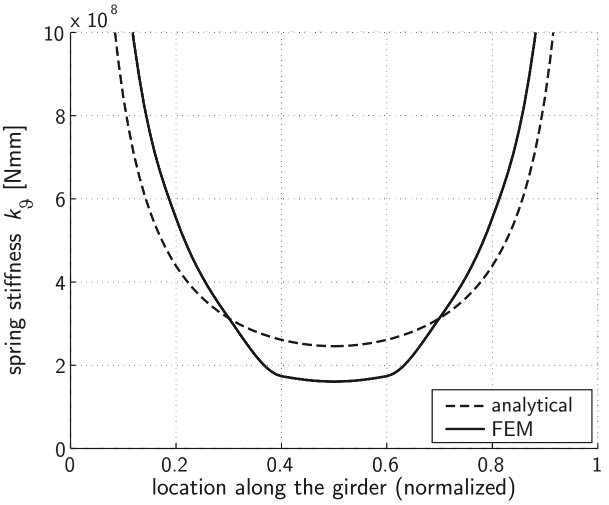

Figure 5.11: Analytic and FE results for torsional stiffnesses

Since cross-sectional deformations are not respected in this model, deformations over the supports are not considered, which leads to a spring stiffness at the girder's ends of $k_\vartheta = \infty$.

As the two graphs show good congruence, it can be concluded that the FE calculations are validated by the analytical results. For the purpose of the FRP bridge, the FEA results are more reliable than the analytical ones because local deformations are considered.

5.6 $\Delta M/F_{\mathrm{up}}$ ratios obtained by a two-dimensional analysis

A typical cross section of a bridge with steel main girders and an FRP bridge deck with bonded connections is considered, see Figure 5.12(a) [KS04]. The cross section is reduced to a two-dimensional static system, shown in Figure 5.12(b): each steel girder has been replaced by a vertical support and a spring with the torsional stiffness k_ϑ of the corresponding steel girder. Various torsional stiffnesses k_ϑ, relating to different steel girders for bridges with spans of between $\ell = 10\,\mathrm{m}$ and $30\,\mathrm{m}$, are assumed and taken from Tables B.1 to B.5, page 161 ff., which cover realistic dimensions of steel main girders used in bridges with lengths of between 10 m and 30 m. The steel girders have stiffeners at each support with the height $h_s = 0.5\,h$.

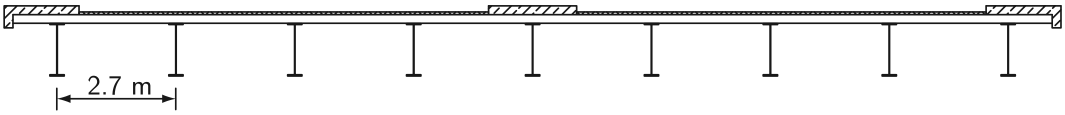

(a) Basic cross section of a bridge

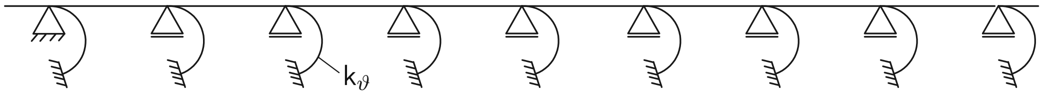

(b) Structural system with torsion springs

Figure 5.12: Cross section of a bridge system with bonded connections

The aim of this section is the determination of the reaction forces ΔM and F_{up} in the bridge deck over the steel girders (see Figure 5.1 on page 72) resulting from the most unfavorable load combinations. The obtained $\Delta M/F_{\mathrm{up}}$ ratios will then be used for the determination of the maximum through-thickness stresses σ_z in the adhesive layer.

The objective is to find the following:

1. The load combination resulting in the maximum $\Delta M/F_{\mathrm{up}}$ ratio over a steel girder.

2. The load combination resulting in the maximum reaction force F_{up}.

With these load combinations, the most unfavorable stress situation in the adhesive layer can be determined.

Maximum $\Delta M/F_{\mathrm{up}}$ ratio

The purpose is to achieve a high bending moment in one of the supports and to have tensile stress from an uplift force in the adhesive layer simultaneously. The load disposition, shown in Figure 5.13 on page 88, was found by determining the maximum values of all possible load combinations. A second axle load could be disregarded, since it would act advantageously. The maximum $\Delta M/F_{\mathrm{up}}$ ratio occurs over the third steel girder (from the right). The obtained reaction forces ΔM and F_{up} for different steel girders with their corresponding torsional stiffnesses are shown in Table 5.3. The reaction forces in the table are characteristic values, without safety factors. The torsional stiffnesses were determined from FEA calculations as described in Section 5.4. The reaction forces were calculated on a two-dimensional static system, shown in Figure 5.12(b).

Table 5.3: Maximum $\Delta M/F_{\mathrm{up}}$-ratio with tension in the adhesive

k_ϑ [kNm]	ΔM[kNm]	F_{up} [kN]	$e = \Delta M/F_{\mathrm{up}}$ [mm]
400	0.065	2.333	27.9
380	0.062	2.339	26.5
360	0.059	2.344	25.2
340	0.056	2.350	23.8
320	0.053	2.356	22.5
300	0.050	2.361	21.2
280	0.046	2.367	19.4
260	0.043	2.373	18.1
240	0.040	2.379	16.8
220	0.037	2.384	15.5
200	0.034	2.390	14.2
180	0.030	2.396	12.5
160	0.027	2.402	11.2
140	0.024	2.408	10.0
120	0.021	2.414	8.7
100	0.017	2.420	7.0
80	0.014	2.426	5.8
70	0.012	2.429	4.9
60	0.010	2.432	4.1
50	0.009	2.435	3.7
40	0.007	2.438	2.9
30	0.005	2.441	2.0
20	0.003	2.444	1.3
10	0.002	2.448	0.8
5	0.001	2.449	0.4
3	0.001	2.450	0.3
1	0	2.450	0
0	0	2.450	0

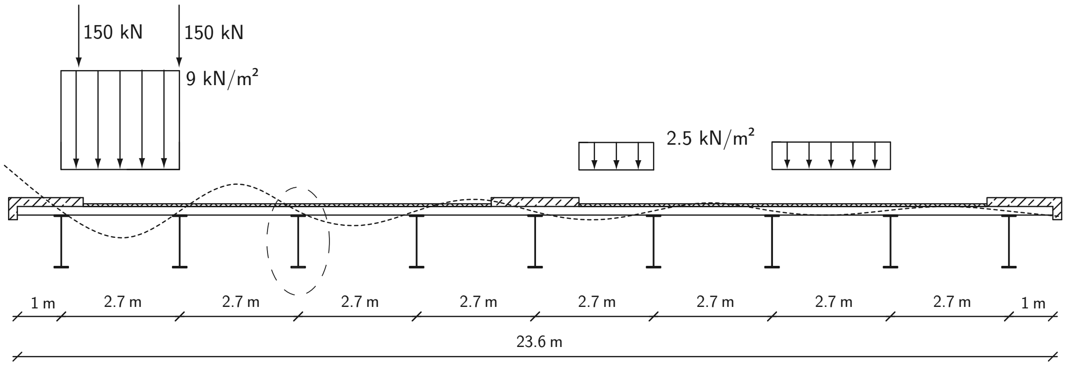
150 kN
150 kN
9 kN/m²
2.5 kN/m²
1 m
2.7 m
2.7 m
2.7 m
2.7 m
2.7 m
2.7 m
2.7 m
2.7 m
1 m
23.6 m

Figure 5.13: Load setting for maximum $\Delta M/F_{\text{up}}$ ratio with tensile stress in adhesive with corresponding (qualitative) deformation of bridge deck

Maximum uplift force F_{up}

To obtain the maximum possible tensile stress that might occur in the adhesive layer, the load is disposed on the model bridge as shown in Figure 5.14. The maximum uplift force occurs over the third steel girder (from the right). The parameter study results for this load case are shown in Table 5.4.

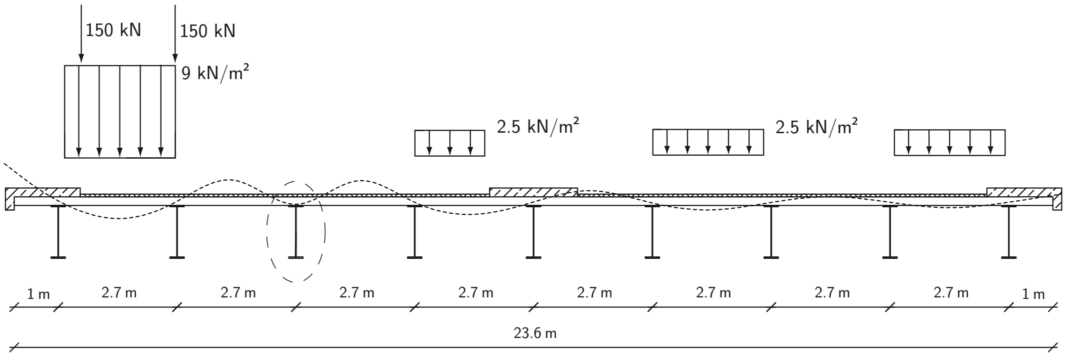
150 kN
150 kN
9 kN/m²
2.5 kN/m²
2.5 kN/m²
1 m
2.7 m
2.7 m
2.7 m
2.7 m
2.7 m
2.7 m
2.7 m
2.7 m
1 m
23.6 m

Figure 5.14: Load disposition for maximum tensile stress in adhesive layer with corresponding (qualitative) deformation of bridge deck

The results given in Tables 5.3 and 5.4 will be used for the determination of the stress situation in the adhesive layer in Section 6.5.

Table 5.4: Maximum tension in adhesive layer

k_ϑ [kNm]	ΔM[kNm]	F_{up} [kN]	$e = \Delta M/F_{\mathrm{up}}$ [mm]
400	0.046	3.081	14.9
380	0.044	3.088	14.2
360	0.042	3.096	13.6
340	0.040	3.103	12.9
320	0.038	3.110	12.2
300	0.035	3.117	11.2
280	0.033	3.125	10.6
260	0.031	3.132	9.9
240	0.029	3.139	9.2
220	0.026	3.147	8.3
200	0.024	3.154	7.6
180	0.022	3.162	7.0
160	0.019	3.169	6.0
140	0.017	3.177	5.4
120	0.015	3.185	4.7
100	0.012	3.192	3.8
80	0.010	3.200	3.1
70	0.009	3.204	2.8
60	0.007	3.208	2.2
50	0.006	3.212	1.9
40	0.005	3.216	1.6
30	0.004	3.220	1.2
20	0.003	3.224	0.9
10	0.002	3.228	0.6
5	0.001	3.230	0.3
3	0	3.230	0
1	0	3.230	0
0	0	3.230	0

5.7 Conclusions

The torsional stiffness of the steel main girders in a bridge system with bonded FRP bridge deck may have considerable influence on the stress distribution in the adhesive layer, if a minimal adhesive layer thickness (8–10 mm) is not respected. Steel girders with various geometries and their influence on torsional stiffness were analyzed using finite element calculations and analytically validated. It was established that determination of torsional stiffnesses using FEA provides more applicable results because local deformations are considered.

Furthermore, the influence of the web thickness and the stiffeners on the torsional stiffness k_ϑ was determined: for girders with thin webs, stiffness is equally distributed over the girder's length, with decreasing stiffness over the supports. Stiffeners at the girder's ends have a greater influence on torsional stiffness for web thicknesses > 12 mm. However, it was also noticed that stiffeners have a relatively small influence on torsional stiffness if they are not connected to the top flange.

The influence of the adhesive layer on rotational stiffness was disregarded in the calculations, which is the most disadvantageous case. As shown in the experiments described in Chapter 3, an adhesive thickness of 8–10 mm can be sufficient to provide a flexible connection that prevents stress concentrations, even in combination with a stiff steel girder. The adhesive layer thickness is also a design parameter, which can be defined by the engineer, in order to prevent stress concentrations in certain locations, as for example above a stiffening element in the steel girder.

The results elaborated in this chapter supply the basic data for the determination of tensile stresses in the adhesive layer. This is carried out in Section 6.5 by superposing stress distributions resulting from pure uplift forces and moment loadings on the adhesive layer between bridge deck and steel girder.

6 Determination of the stress distribution inside the adhesive layer

6.1 Introduction

The aim in this chapter is to determine the locations and values of stress concentrations in the adhesive layer resulting from vertical tensile forces and moments. A method that allows the stress distribution to be calculated using analytical formulas will be proposed.

A stress concentration factor μ will be determined, which indicates the magnitude of the stress concentrations related to the average tensile stress $\bar{\sigma}_z^+$ in the adhesive connection. The distribution of the tensile through-thickness stresses σ_z^+ is dependent on several parameters, such as the steel girder geometry, type of adhesive and adhesive layer thickness as well as on the geometry and material properties of the bridge deck.

6.2 Procedure

The maximum vertical through-thickness tensile stresses $\sigma_{z,\max}^+$ are evaluated via the followings steps:

1. Calculation of the uplift forces and bending moments transmitted by the bridge deck to the steel girder.
2. Determination of the corresponding adhesive connection area which has to transmit the forces.
3. Calculation of the average through-thickness stress $\bar{\sigma}_z^+$ inside the adhesive connection.
4. Determination of the stress concentration factors and their application to calculate the maximum stresses $\sigma_{z,\max}^+$ inside the adhesive layer, or more precisely in the surface mat layers of the FRP material where the failure occurs.

The determination of the stress concentration factors is accomplished in several stages:

1. An FE parameter study is carried out on several geometries of FRP bridge decks in Section 6.3. The distribution of the through-thickness stresses and the location of stress concentrations are determined. The study investigates the influence of the web thickness of the deck and the web's inclination on the stress distribution.
2. An analytical determination of the through-thickness stresses is carried out in Section 6.4. This is divided into the stress distribution in the steel girder's (x-) direction (Section 6.4.1) and the distribution in the bridge deck's pultrusion (y-) direction (Section 6.4.2). Combining these distributions gives the maximum through-thickness stresses $\sigma^{+}_{z,\max}$ (Section 6.4.3).
3. Analytical and numerical results are compared and discussed and stress concentration factors are determined.

All calculations are performed under the following assumptions:

1. The material behavior in all stress states is linear-elastic.
2. The material properties of the bridge deck elements and the adhesive are shown in Table 3.3 on page 35 and Table 3.5 on page 37.
3. Only uplift forces are considered initially; the influence of bending moments in the bridge deck above the adhesive layer is investigated in Section 6.5.

6.3 Numerical modeling

6.3.1 Introduction

Two models with different geometries were generated for FE calculations:

1. A beam model, described in Section 6.3.2 on the facing page.
2. A modular deck unit (MDU) model, described in Section 6.3.3 on page 97.

Two different models were created for the following reasons: the beam model was used to simulate the structure's global behavior. This includes, for instance, the behavior of the adhesive connection resulting from the inner forces in the bridge deck, such as shear, which is mainly transmitted via the bridge deck webs and could not be simulated in the modular deck unit (MDU) model.

The MDU model was made especially for local stress analysis. Due to the reduced geometry, an improved mesh compared to the relatively coarse mesh used in the beam model was possible. The coordinate directions are as follows:

- x is the bridge's longitudinal direction (see Figure 1.1, page 4, and Figure 6.2),
- y-direction is the bridge's transverse and the bridge deck's pultrusion direction,
- z-direction is the vertical (through-thickness) direction.

6.3.2 Beam model

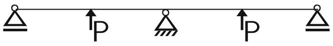

Figure 6.1: Static system

The model was used to determine the influence of the web's angle α_{sw} on the maximum value of the σ_z^+ stress. As already mentioned, only pure uplift forces were considered in this first step. This was done by using the static system shown in the adjacent Figure 6.1. Due to symmetry boundary conditions (see below), the structure can be described by a continuous girder. The deck is loaded on the lower side. A load pad (200 mm × 608 mm) was modeled for the FE calculations in order to guarantee a realistic load introduction. This geometric set-up was chosen in order to obtain a pure uplift force over the middle adhesive connection, with a symmetric bending moment distribution above the adhesive layer; the loaded profile is not inclined over the middle support. Furthermore, the load is not introduced on the top panel (as in the MDU model in Section 6.3.3), but through the webs of the profile, i.e. the uplift force results from the shear in the bridge deck. The load was set to $p = 1\,\mathrm{N/mm^2}$ on the load pad, which was of the same size as the adhesive connection layer.

The calculations were made using *Ansys* with the *SOLID 185* element type. The model's geometry is shown in Figure 6.2 on the next page. It has two planes with symmetric boundary conditions: the front plane (in the x-z-direction) and one side (y-z-direction), which results in an effective width of four instead of two two-cell bridge deck profiles. The steel girder under the investigated adhesive connection is also in a symmetry plane, and therefore only a quarter of it was modeled. The lower part of the steel girder was not modeled because it has no influence on the stress distribution in the adhesive layer, in this case, of a pure uplift force. The support at the end of the structure is located on the upper side of the bridge deck, and thus will only work under pressure. A span of 2.7 m was chosen, which is a reasonable span for common bridge decks, see [KS04].

Several types of deck geometries with different web inclinations α_{sw} in the range of 55° to 90° were investigated. A geometry with a web inclination smaller than 55° was not investigated as it was not considered structurally reasonable, since it would act disadvantageously with regard to the bending stiffness of the bridge deck. Every second web of these bridge decks is inclined, the webs in between being vertical, see Figure 6.3(a) to 6.3(d) on page 95. All FE calculations were performed in the linear-elastic range with the same bridge deck geometry concerning the thicknesses

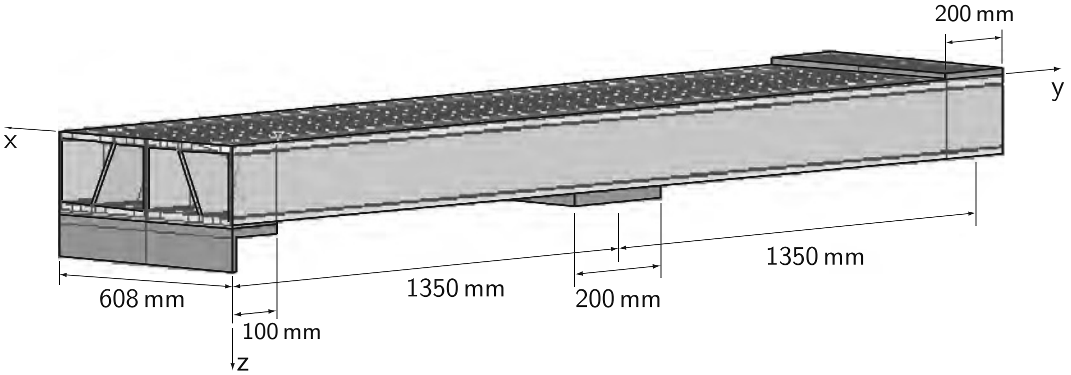

Figure 6.2: Symmetric 3D-model

of the webs and face sheets (see Table 6.1), but different web inclinations, as shown in Figure 6.3.

Influence of web inclination on stress distribution

The computed stress distributions in x-direction at $y=0$ are shown in Figure 6.4. The σ_z stresses are taken from the adhesive-FRP interface, $\bar{\sigma}_z$ being the average stress in the adhesive layer of the middle support. An inclined web transfers smaller stresses in z-direction than does a less inclined web. This means that the vertical web next to the inclined web transfers the highest stresses. Factor κ_{σ_z}, in Figure 6.5, describes the increase in the maximum stress due to a web inclination α_{sw} in relation to the stress distribution under a bridge deck with only vertical webs ($\alpha_{sw}=90°$).

$$\kappa_{\sigma_z}(\alpha_{sw}) = \frac{\sigma^+_{z,\max}(\alpha_{sw})}{\sigma^+_{z,\max}(\alpha_{sw} = 90°)} \tag{6.1}$$

With increasing web inclination, maximum stresses attain a value which can be twice as high for a web inclination of 55° as that occurring in the case of a geometry with only vertical webs.

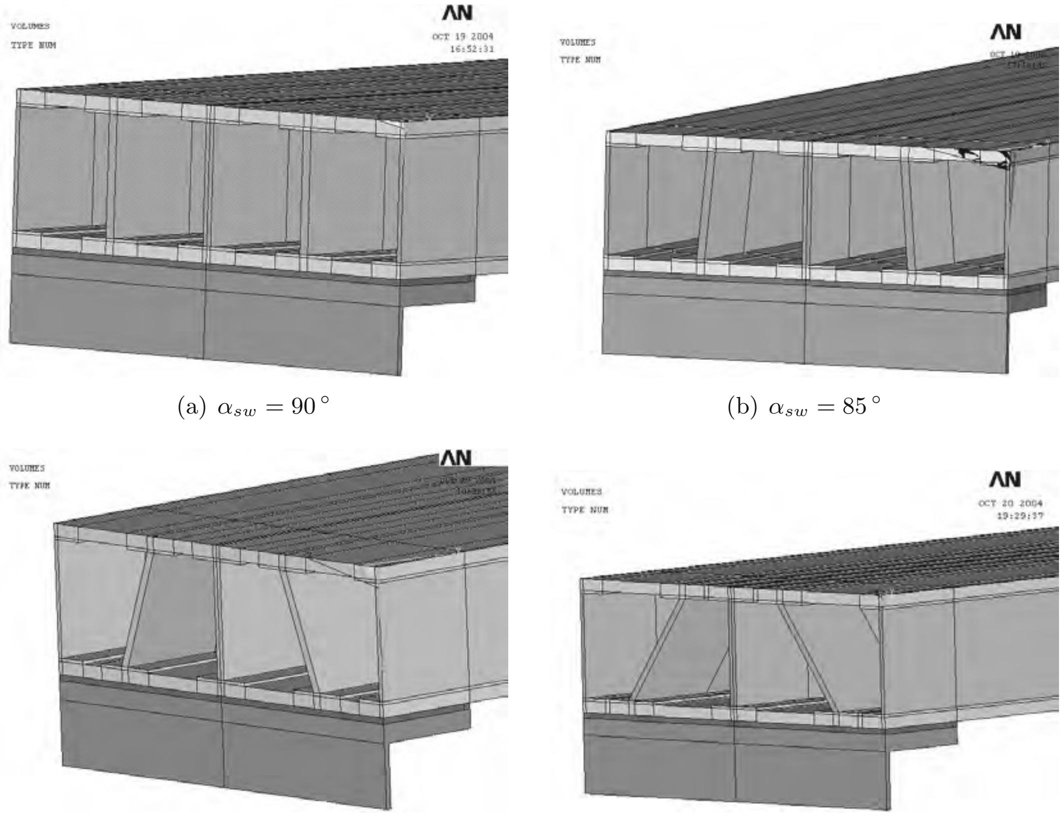
VOLUMES
TYPE NUM
OCT 19 2004
16:52:31
VOLUMES
TYPE NUM
VOLUMES
TYPE NUM
VOLUMES
TYPE NUM
OCT 20 2004
19:29:37

(a) $\alpha_{sw} = 90\,^\circ$ (b) $\alpha_{sw} = 85\,^\circ$

(c) $\alpha_{sw} = 70\,^\circ$ (d) $\alpha_{sw} = 55\,^\circ$

Figure 6.3: FE models with different web inclinations

Table 6.1: Bridge deck geometry of beam model

component	dimensions		
deck height	H_{ds}	=	195 mm
web thickness	t_{sw}	=	12 mm
face sheet thickness	t_p	=	21 mm
adhesive thickness	t_{adh}	=	8 mm

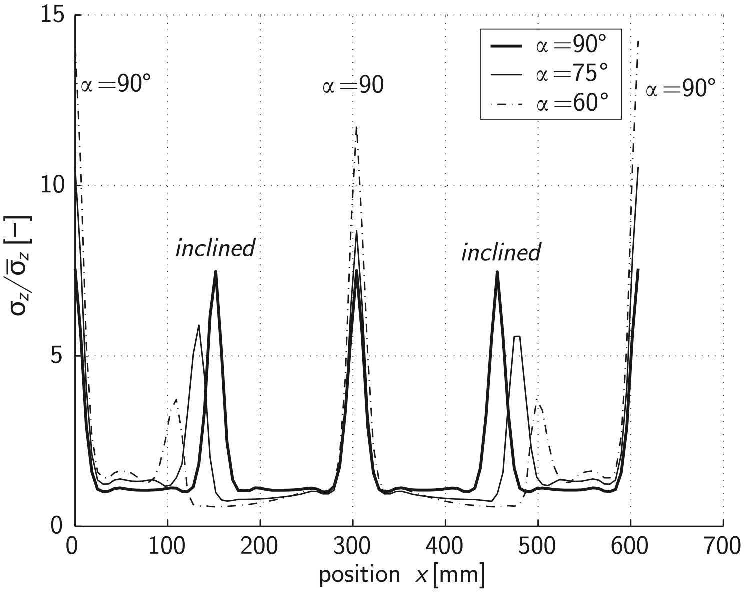

Figure 6.4: Distribution of σ_z stresses in x-direction over center of steel girder (at $y = \frac{b_f}{2}$) in adhesive-FRP interface

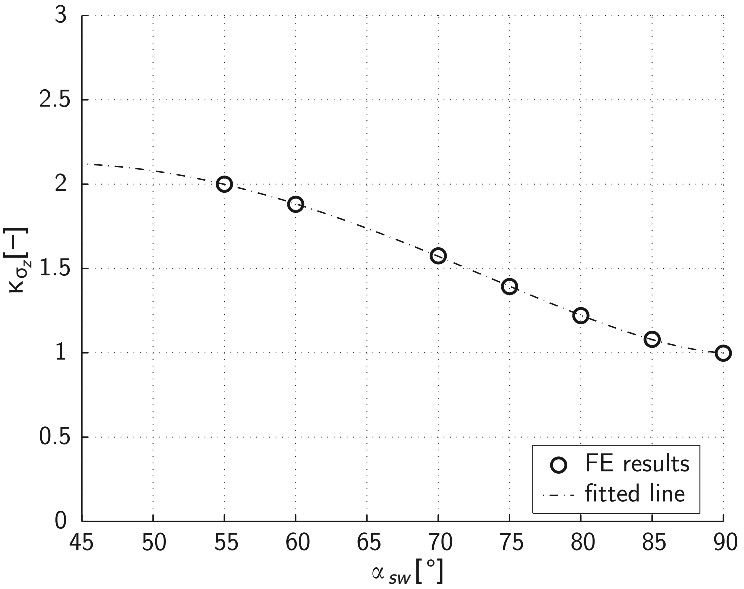

Figure 6.5: κ_{σ_z} depending on different web inclinations

6.3.3 Modular deck unit (MDU) model

The MDU model is reduced to one section, which includes only a part of the bridge deck, adhesive layer and steel girder. Symmetry boundary conditions were considered, allowing a further reduction of the modeled section. Figure 6.6 shows the modeled unit in its position inside the bridge and the different materials of which it is composed.

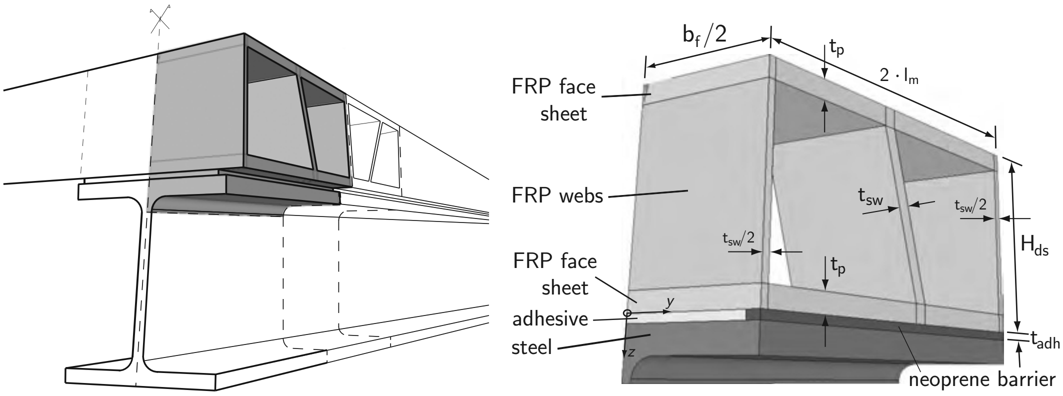

(a) The darkened part was modeled with finite elements for numerical calculations

(b) Materials used in model

Figure 6.6: Modeled section

Different geometries were modeled:

1. A model with only vertical webs, the *VS*-geometry, shown in Figure 6.7, was basically used for cross-checking the analytical results referred to in Section 6.4 on page 104, but also to investigate the influence of the web thickness.

2. A model with inclined webs, the *IS*-geometry (see Figure 6.8 on the following page).

3. A derivative of the *IS*-model, the *DS*-geometry, which corresponds to the *DuraSpan 766* geometry. The *IS*- and *DS*-geometries were mainly used to investigate the influence of a changing panel thickness. The *DS* model is shown in Figure 6.9[*], page 99.

The geometric values of the three models are given in Table 6.2.

---

[*] The neoprene barrier was also modeled, but is not distinguishable from the other material in Figure 6.9(b).

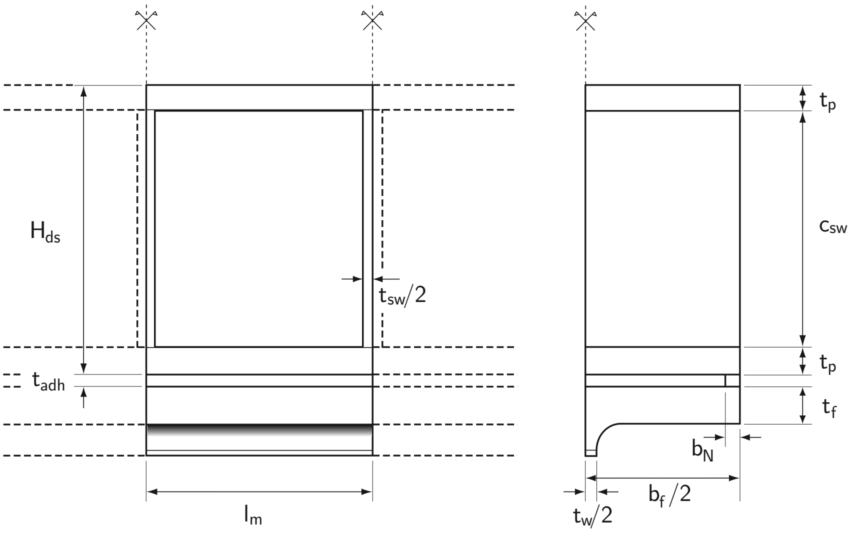
H_{ds}
$t_{sw}/2$
t_{adh}
l_m
t_p
c_{sw}
t_p
t_f
b_N
$b_f/2$
$t_w/2$

Figure 6.7: Model with vertical webs: *VS*-geometry

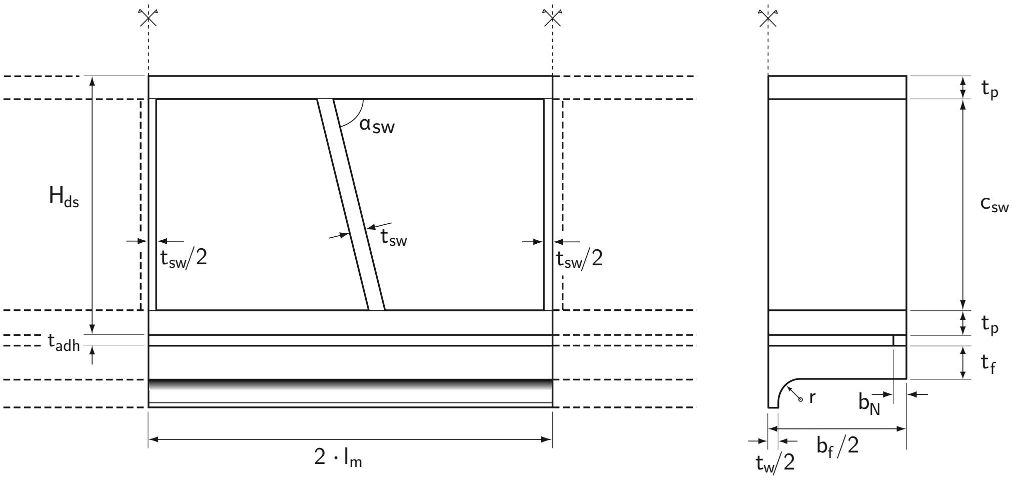
α_{sw}
H_{ds}
t_{sw}
$t_{sw}/2$
$t_{sw}/2$
t_{adh}
$2 \cdot l_m$
t_p
c_{sw}
t_p
t_f
r
b_N
$b_f/2$
$t_w/2$

Figure 6.8: Model with inclined webs: *IS*-geometry

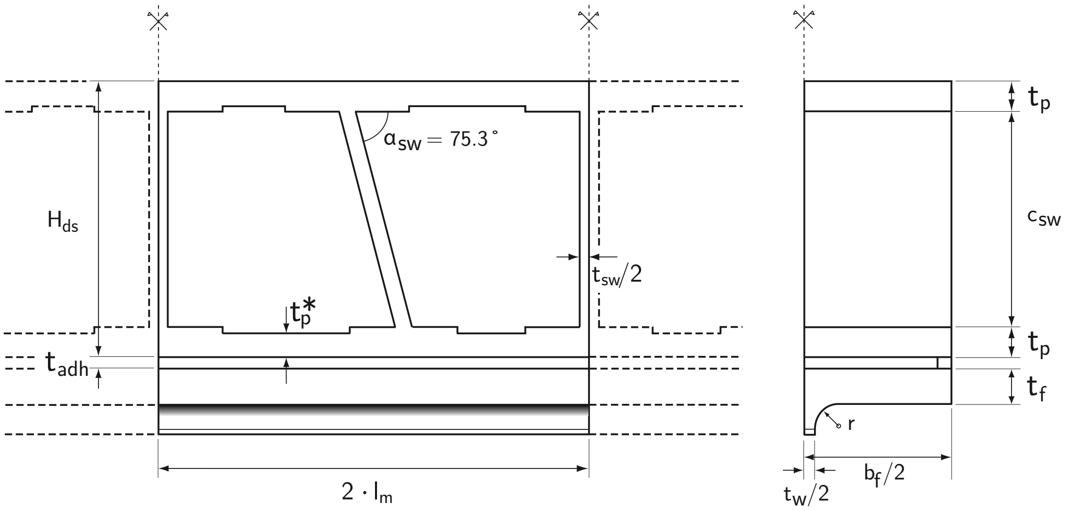
αsw = 75.3°
Hds
tsw/2
tp*
tadh
2 · lm
tp
csw
tp
tf
r
bf/2
tw/2

(a) geometry

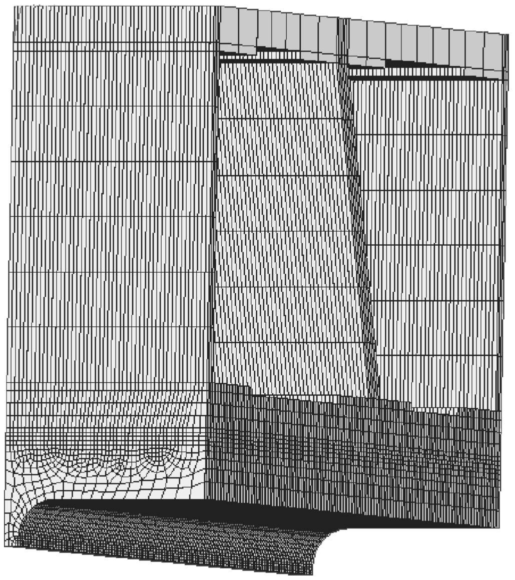

(b) meshed model

Figure 6.9: Model with inclined webs: *DS*-geometry

Table 6.2: Specific values used for calculation of *VS*-, *IS*- and *DS*-geometries (see Figures 6.7 to 6.9)

deck height	H_{ds}	$= 195$	mm
module length	l_m	$= 152$	mm
basic web thickness[a]	t_{sw}	$= 12$	mm
face sheet thickness	t_p	$= 21$	mm
face sheet thickness	t_p^*	$= 18$	mm
web inclination[b]	α_{sw}	$= 75.3$	°
adhesive thickness	t_{adh}	$= 8$	mm

---

[a] Average values from the specimens described in Section 3.4.3 were taken. Therefore values differ slightly from the geometry shown in Figure 3.11. In the case of the *VS*-geometry variations with greater web thicknesses were also analyzed.

[b] For *IS*- and *DS*-geometries only.

Only the upper part of the steel girder was modeled as shown in Figures 6.6 to 6.9. The model was fixed in all directions on the cut area of the flange. Each model was loaded with uniformly distributed line loads on the model's top face over the three webs. The resulting uplift force leads to an average through-thickness tensile stress $\bar{\sigma}_z = 1\,\frac{\mathrm{N}}{\mathrm{mm}^2}$.

Results for VS-geometry

The bridge deck's web thickness has a considerable influence on the shape of the stress distribution and therefore on the stress concentration and its magnitude. This also concerns the transverse (y-)direction, and particularly the longitudinal (x-)direction.

FE analyses of vertical through-thickness stresses σ_z^+ showed that these stresses are concentrated beneath the webs, while the areas between the webs were not loaded at all, see Figure 6.10. Furthermore, the stress distributions in y-direction exhibit stress concentrations near to the edges, which are smaller than in the center however.

The thinner the web, the more significant the stress peaks near to the edges. Under a very thick web, the stress peaks disappear, see Figure 6.11(a), and the stresses are generally smaller. In the longitudinal direction, vertical through-thickness stresses are only transmitted under the webs. σ_z stresses do not occur within a distance of approximately 15 mm of the edge of the web, see Figure 6.11(b). $\bar{\sigma}_z$ is defined by the average stress in the adhesive layer between two bridge deck webs, which is $1\,\mathrm{N/mm^2}$ in this case, as previously stated.

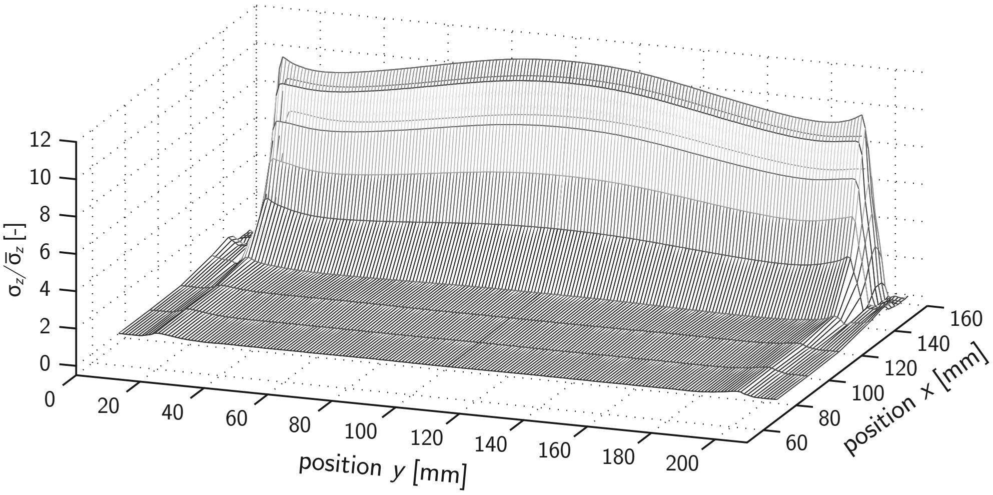

Figure 6.10: Normalized stress distribution $\sigma_z/\bar{\sigma}_z$ in FRP-adhesive interface (*VS*-geometry); the vertical webs are placed at $x=0$ mm and $x=152$ mm

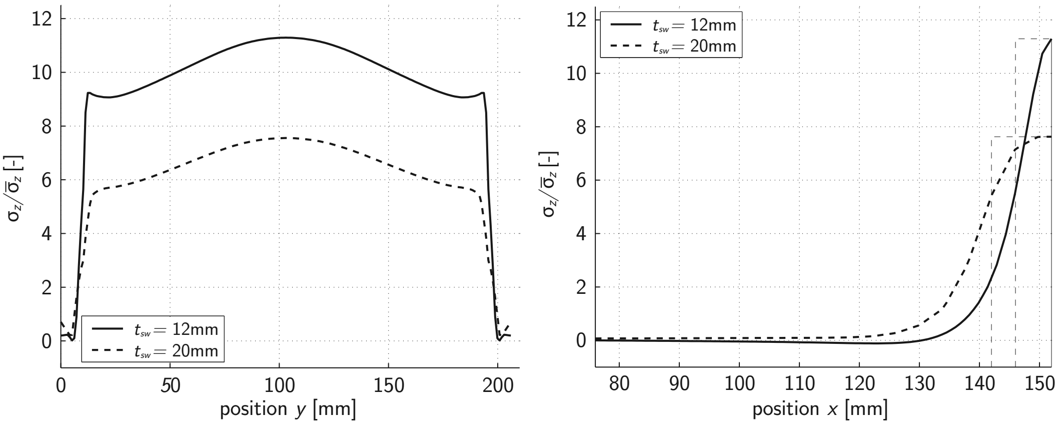

(a) Stress distribution in transverse direction

(b) Stress distribution in longitudinal direction

Figure 6.11: Stress distribution of vertical through-thickness (σ_z) stresses in FRP-adhesive interface (determined by *VS*-geometry); the center of the vertical web is placed at $x=152$ mm

Results for IS- and DS-geometries

Comparisons of the two models (see Figures 6.8 and 6.9) showed that the section with the thinner lower bridge deck face sheet ($t_p \leftrightarrow t_p^*$, see Figure 6.9(a)) had no influence on the shape of the stress distribution in the adhesive layer. A stress distribution in the adhesive layer calculated with the *DS* model is shown in Figure 6.12. Comparisons with the *IS* model showed the same results.

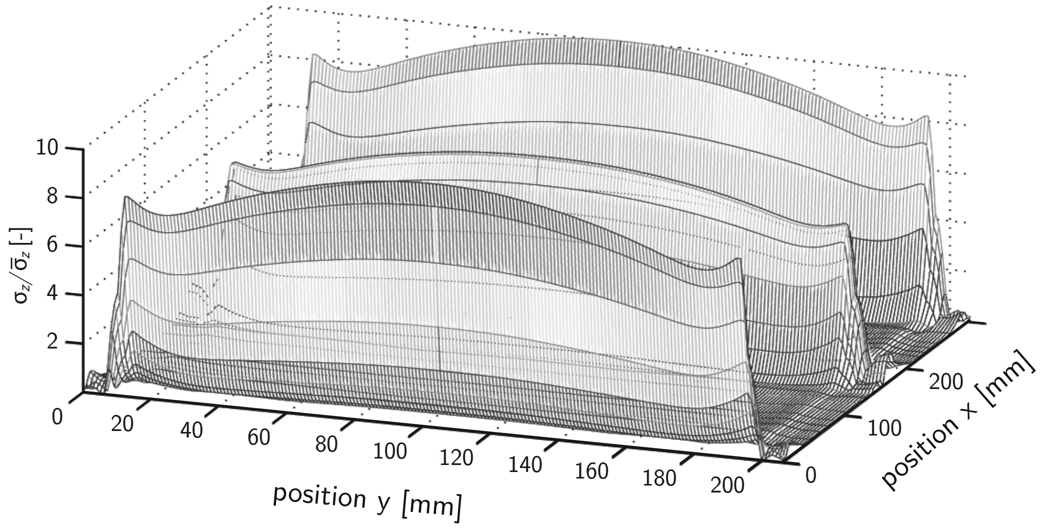

Figure 6.12: Normalized stress distribution $\sigma_z/\bar{\sigma}_z$ in FRP-adhesive interface (*DS*-geometry)

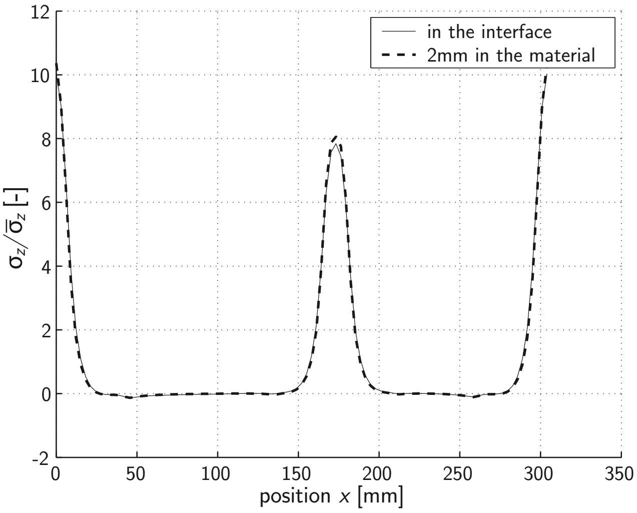

Figure 6.13: Stress distribution in longitudinal direction on surface and inside FRP material (*IS*-geometry)

The calculations also showed that the stress states on the FRP-adhesive interface and inside the FRP material (down to a depth of $\sim 2\,\mathrm{mm}$) are almost the same (see Figure 6.13 on the preceding page). As shown in Chapters 3 and 4, the failure usually occurs in the surface layer mats. Therefore, it is important to know that no distinction between the stress states in the FRP-adhesive interface and the FRP surface layer mats needs to be made.

6.3.4 Conclusions from numerical modeling

With the beam model, the effect of the webs and their inclinations on the stress distribution in the adhesive layer was shown. To describe this effect, the factor κ_{σ_z} was defined and determined, which describes the increase of the stress concentration beneath the bridge deck webs, depending on their inclination. It was shown that inclined webs increase the normal through-thickness stress in the adjacent vertical webs by up to a factor of 2.

The MDU models were used for more precise investigations of the stress distributions. They showed that the normal through-thickness stresses are mainly distributed beneath the bridge deck webs. Between the webs, they almost disappear. In the y-direction, the maximum stress distribution occurs in the center over the steel girder's web with stress concentrations near to the edges. Investigations involving different steel girder geometries showed that the stress concentration near to the edges always has a smaller value than the maximum in the center. The stress distribution on the surface and 2 mm inside the FRP material is the same.

6.4 Analytical determination of σ_z stresses

The method used to determine the analytical stress distribution will enable the shape of the σ_z stress distribution to be described using analytical formulas. When the average stresses $\bar{\sigma}_z^+ \left(= \frac{F_{\mathrm{up}}}{A_{\mathrm{adh}}}\right)$ in the adhesive layer are known, the maximum value $\sigma_{z,\max}^+$ can be calculated by comparing the volume under the analytical stress distribution described by a function f with the volume being determined by the mean stresses and the area of the bonded connection, see Equation 6.2. In this section, the calculations are made under the assumption that there are no bending moments acting in the adhesive layer. The influence of bending moments in the bridge deck over the steel girder is investigated in Section 6.5.

$$\begin{aligned} \bar{\sigma}_z^+ \cdot A_{\mathrm{adh}} = F_{\mathrm{up}} &= \sigma_{z,\max}^+ \cdot \int\int_{A_{\mathrm{adh}}} f(x,y)\,\mathrm{d}x\,\mathrm{d}y \\ \text{with} \quad f(x,y) &= \text{stress distribution} \end{aligned} \tag{6.2}$$

With the FE analysis carried out in Section 6.3 it was shown that the stress distribution in x-direction depends mainly on the bridge deck geometry. Section 6.4.1 describes the distribution by these geometric values. The distribution in y-direction (Section 6.4.2), on the other hand, is mainly related to the geometry of the steel girder.

6.4.1 Stress distribution in x-direction

In the following section the stress distribution for FRP bridge decks with vertical webs is investigated and is subsequently adapted to bridge deck geometries which also include inclined webs.

It is assumed that the σ_z stresses are only concentrated beneath the webs, as shown by the FE stress analysis in Section 6.3. Therefore, a limited area beneath the webs wherein stresses are transmitted from the bridge deck to the connective adhesive can be determined. Vertical through-thickness stresses outside this area are negligibly small; an example is shown in Figure 6.12 on page 102. As shown in Figure 6.14 on the next page, the area beneath the stress distribution can be calculated from the geometry of the bridge deck[†], which gives the base width b_{bs} under the bridge deck webs in the deck-adhesive interface. The influence angle for the spreading of the stresses in the lower face sheet was assumed to be 45 %.

Based on the width b_{bs}, the stress distribution in x-direction is approximated by Equation 6.3 on the facing page, which describes a function of cosine to the power of

---

[†] The web thickness t_{sw} and the panel thickness t_p.

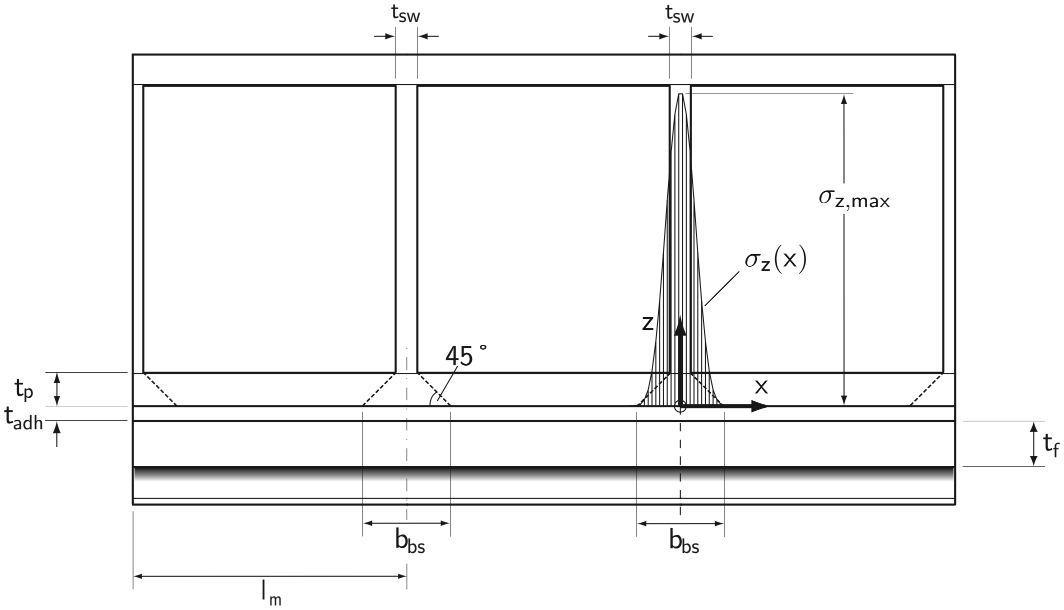

Figure 6.14: Effective width b_{bs}; a σ_z distribution is drawn under the third web

a factor n_x, depending on the ratio $\frac{t_{sw}}{t_p}$. Equation 6.3 describes the stress distribution in the interface between the adhesive layer and steel girder under each web.

$$\sigma_z(x) = \sigma_{z,\max} \cdot \cos^{n_x}\left(\frac{\pi}{b_{bs}}\,x\right) \tag{6.3}$$

$$\begin{aligned} &\text{for} \quad -\frac{b_{bs}}{2} \leq x \leq \frac{b_{bs}}{2} \\ &\text{with} \quad b_{bs} = t_{sw} + 2\,t_p \end{aligned}$$

By varying the bridge deck's web thickness t_{sw} and the panel thickness t_p, the influence of the ratio $\frac{t_{sw}}{t_p}$ on the stress distribution in the FRP-adhesive interface was examined (see the curves in Figures 6.15 to 6.18). Further diagrams are shown in Appendix C.1, page 163. The factor n_x influences the shape of the cosine curve approximating the stress distribution. Integer values of between 2 and 8 showed good agreement with the shapes of the distributions obtained by the numerical calculations, especially for values ± 20 mm around the maximum stress value. For the *VS*-geometry with a web thickness $t_{sw} = 12$ mm and a panel thickness $t_p = 21$ mm, the optimal factor n_x would be five, see Figure 6.17.

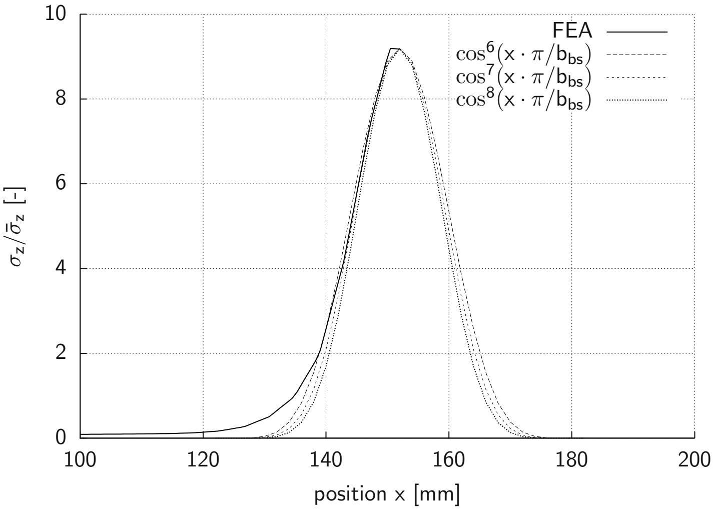

Figure 6.15: Comparison of FE results (*VS*-geometry) and analytical stress distribution in FRP-adhesive interface $\frac{t_{sw}}{t_p} = \frac{8\,\text{mm}}{26\,\text{mm}} \approx 0.31$; $n_x = 6 \cdots 8$

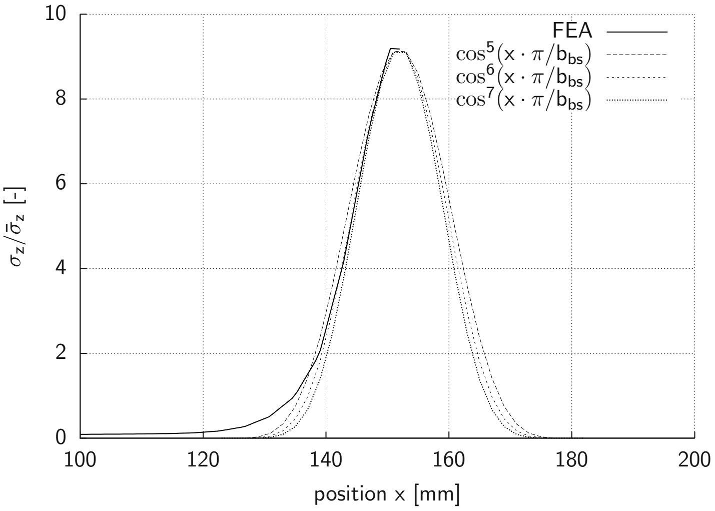

Figure 6.16: Comparison of FE results (*VS*-geometry) and analytical stress distribution in FRP-adhesive interface $\frac{t_{sw}}{t_p} = \frac{10\,\text{mm}}{24\,\text{mm}} \approx 0.42$; $n_x = 5 \cdots 7$

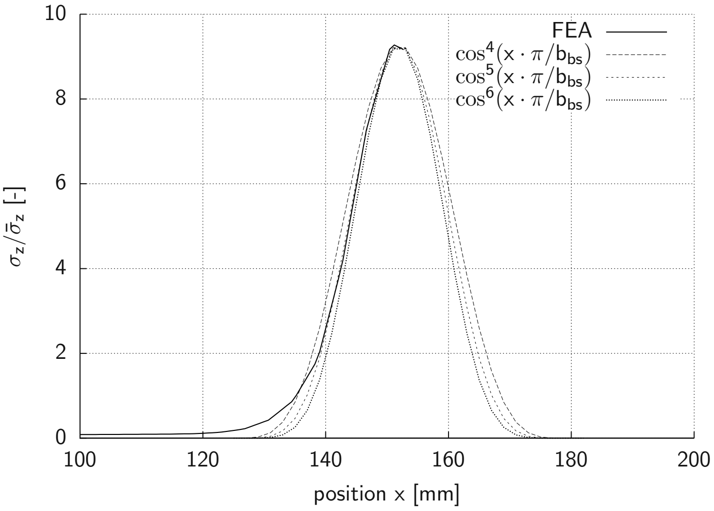

Figure 6.17: Comparison of FE results (*VS*-geometry) and analytical stress distribution in FRP-adhesive interface
$\frac{t_{sw}}{t_p} = \frac{12\,\text{mm}}{21\,\text{mm}} \approx 0.57$;
$n_x = 4 \cdots 6$

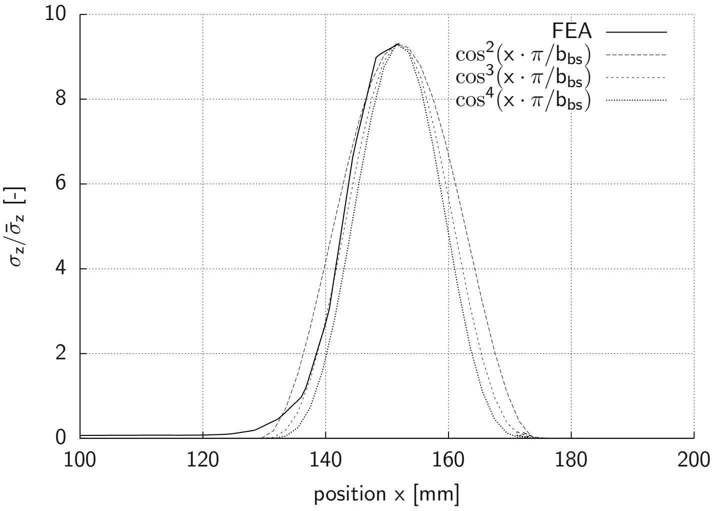

Figure 6.18: Comparison of FE results (*VS*-geometry) and analytical stress distribution in FRP-adhesive interface
$\frac{t_{sw}}{t_p} = \frac{15\,\text{mm}}{15\,\text{mm}} \approx 1$;
$n_x = 2 \cdots 4$

The results of the numerical calculations are included in Figure 6.19 on the next page, which shows the resulting factors n_x for several web thickness to panel thickness ratios $\frac{t_{sw}}{t_p}$ ranging between 0.3 and 2. The factors determined with FEA could be approximated by the function shown in Equation 6.4:

$$n_x = \frac{3}{\frac{t_{sw}}{t_p} + 0.05} \tag{6.4}$$

As defined in Equation 6.2, the stress distribution in the adhesive connection is described by a function $f(x, y)$. The determination was carried out in two steps:

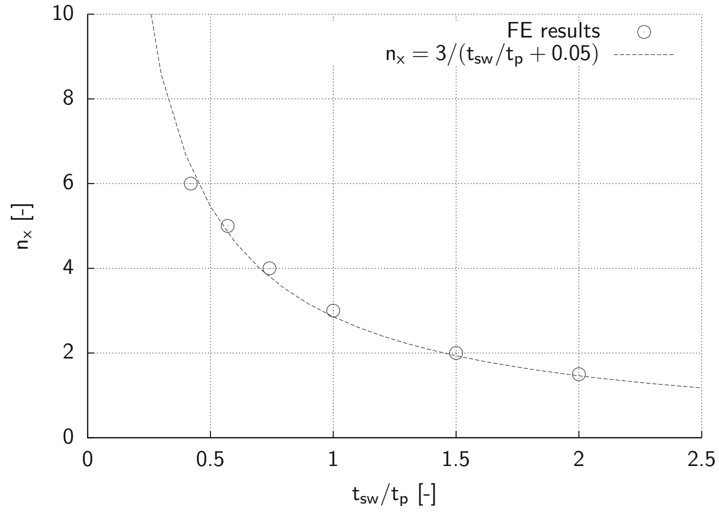

Figure 6.19: Factor n_x as a function of the ratio of web thickness to panel thickness

firstly by describing the distribution in x-direction (in this section) and secondly in y-direction (Section 6.4.2).

The value of the definite integral (B_x) of the stress distribution in x-direction (Equations 6.5 to 6.7) is required for the determination of $\sigma_{z,\max}$ and has been calculated for different values of n_x.[‡] The value determined in Equations 6.5 to 6.7 is the area B_x under the stress distribution in x-direction and therefore the inner integral in Equation 6.2.

For $n_x = 5$

$$B_x = \sigma_{z,\max} \int_{-\frac{b_{bs}}{2}}^{\frac{b_{bs}}{2}} \cos^5\left(\frac{\pi}{b_{bs}}\,x\right)\,\mathrm{d}x = \sigma_{z,\max}\cdot\frac{16\,b_{bs}}{15\,\pi} = 0.340\cdot b_{bs}\cdot\sigma_{z,\max} \tag{6.5}$$

For $n_x = 6$

$$B_x = \sigma_{z,\max} \int_{-\frac{b_{bs}}{2}}^{\frac{b_{bs}}{2}} \cos^6\left(\frac{\pi}{b_{bs}}\,x\right)\,\mathrm{d}x = \sigma_{z,\max}\cdot\frac{5\,b_{bs}}{16} = 0.313\cdot b_{bs}\cdot\sigma_{z,\max} \tag{6.6}$$

[‡] For the analytical solution of the definite integrals, the *Mathematica* program was used.

For $n_x = 7$

$$B_x = \sigma_{z,\max} \int\limits_{-\frac{b_{bs}}{2}}^{\frac{b_{bs}}{2}} \cos^7\left(\frac{\pi}{b_{bs}}\, x\right) \mathrm{d}x = \sigma_{z,\max} \cdot \frac{32\, b_{bs}}{35\, \pi} = 0.291 \cdot b_{bs} \cdot \sigma_{z,\max} \tag{6.7}$$

6.4.2 Stress distribution in y-direction

The numerical calculations on the geometries in Section 6.3 showed that the stress distribution in y-direction is approximately constantly distributed over its length, see Figure 6.12 on page 102. Most configurations have their maximum value $\sigma_{z,\max}$ in the middle of the length b_f and further (smaller) peaks near to the steel girder's edge, as shown in various diagrams calculated on different geometries (see Appendix C.2, page 164 ff.). The investigated steel girders had the following parameters: web thickness t_w between 6 and 22 mm, flange width b_f between 220 and 450 mm and flange thickness t_f between 23 and 50 mm. All reasonable geometries were covered by these values.

It is not possible to describe the stress distributions in y-direction by a close-form equation, apart from using equations comprising too many factors. Therefore, a stress distribution composed of linear and constant functions is used. To approximate the stress distribution in the direction from one edge of the steel flange to the other, an effective inner width b_i is defined by Equation 6.8, taken from [OH96, DIN90] and extended by a term designating the adhesive thickness, see Figure 6.20. In this equation a spread of the stresses inside the steel with an influence angle of 1 : 2.5 is assumed. It is supposed that the stresses over this inner width attain their maximum value $\sigma_{z,\max}$. From this maximum value, the stress distribution decreases towards the edges of the effective width b_{eff}, which is the steel flange's width b_f, minus the width of the neoprene barrier b_N, see Equation 6.9.

$$b_i = t_w + 1.61\, r + 5\, t_f + 2\, t_{\mathrm{adh}} \tag{6.8}$$

$$b_{\mathit{eff}} = b_f - 2\, b_N \tag{6.9}$$

where t_w is the steel girder web thickness, r the radius of the steel girder's web-to-flange junction, t_f the steel flange thickness, t_{adh} the adhesive thickness, b_f the steel flange width and b_N the width of the neoprene barrier.

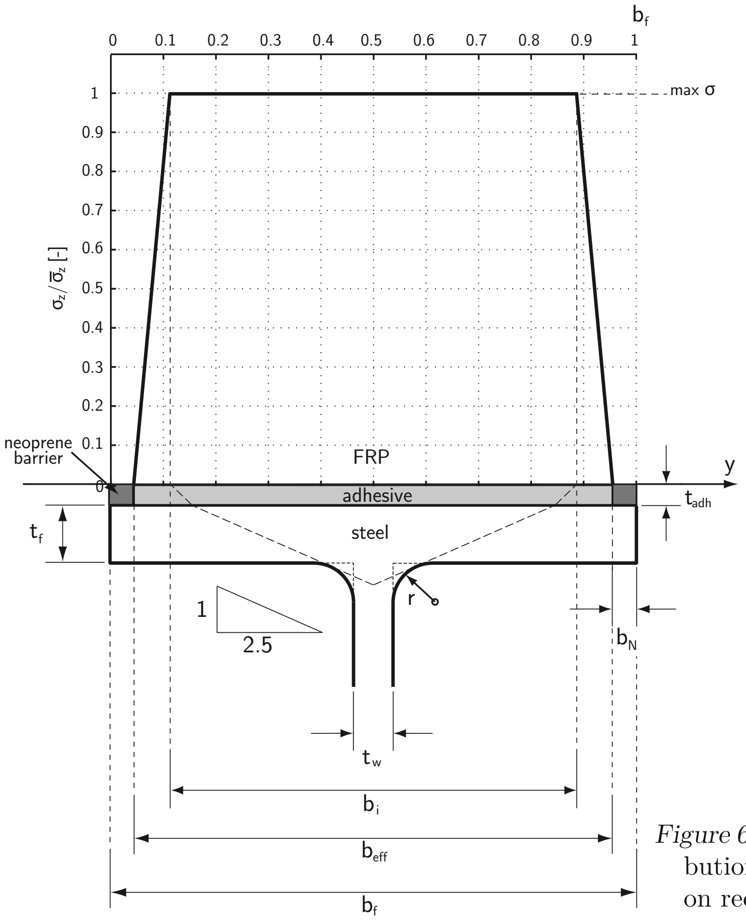

Figure 6.20: Simplified stress distribution in y-direction depending on reduced widths b_{eff} and b_i

The distribution of the through-thickness stresses σ_z along a path in y-direction is shown in Equation 6.10. It is a symmetric function composed of three segments: a linear function with the slope χ starting at the edge ($y = b_N$), a constant part with the width b_i, and another linear function up to the other edge, see Figure 6.20. $\bar{\sigma}_z$ is determined by the whole area beneath the function, including the side caps.

$$\frac{\sigma_z}{\bar{\sigma}_z}(y) = \begin{cases} \chi\, y + \psi & \text{for} \quad b_N \leq y \leq \frac{b_f - b_i}{2} \\ 1 & \text{for} \quad \frac{b_f - b_i}{2} < y < \frac{b_f + b_i}{2} \\ -\chi\, y + \omega & \text{for} \quad \frac{b_f + b_i}{2} \leq y \leq \frac{b_f + b_{eff}}{2} \end{cases} \tag{6.10}$$

with

$$\chi = \frac{2}{b_f - b_i - 2\,b_N}; \quad \psi = -\frac{2\,b_N}{b_f - b_i - 2\,b_N}; \quad \omega = \frac{2\,(b_f - b_N)}{b_f - b_i - 2\,b_N}$$

6.4.3 Determination of $\sigma^{+}_{z,\max}$

In order to calculate $\sigma^{+}_{z,\max}$, the stress distribution in the interface of the lower bridge deck panel is obtained by combining the distributions in x- and y-directions (Equations 6.3 and 6.10) and Equation 6.11. The graph for a typical geometry with vertical webs is shown in Figure 6.21.

$$\sigma_z(x,y) = \sigma_{z,\max} \cdot \cos^{n_x}\left(\frac{\pi}{b_{bs}}\,x\right) \cdot \begin{cases} (\chi\,y+\psi) & \text{for} \quad b_N \leq y < \frac{b_f-b_i}{2} \\ 1 & \text{for} \quad \frac{b_f-b_i}{2} \leq y \leq \frac{b_f+b_i}{2} \\ (-\chi\,y+\omega) & \text{for} \quad \frac{b_f+b_i}{2} < y \leq \frac{b_f+b_{\mathit{eff}}}{2} \end{cases} \tag{6.11}$$

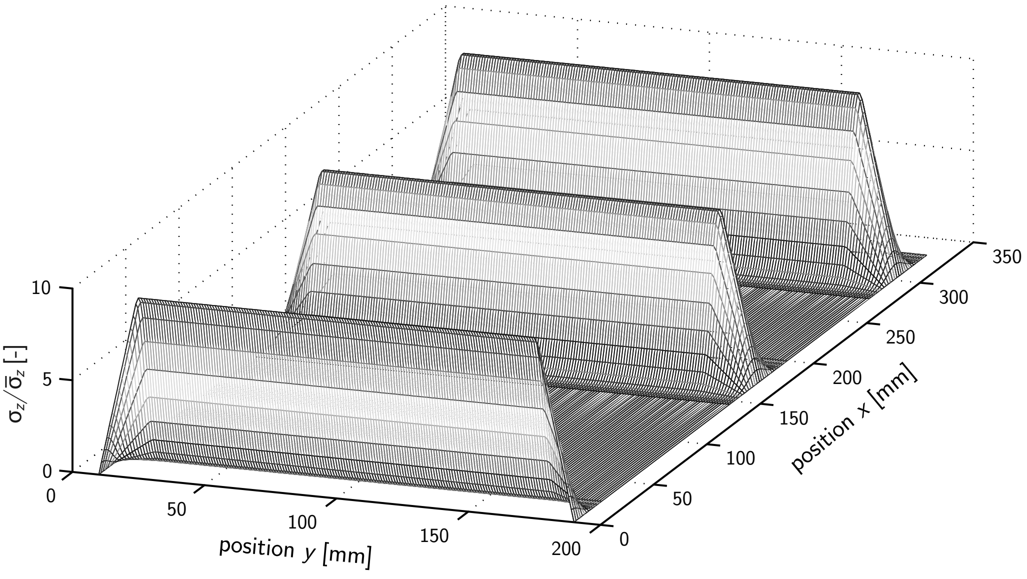

Figure 6.21: Analytically determined stress distribution in interface of adhesive and lower bridge deck panel for $t_{sw} = 12\,\text{mm}$, $t_p = 21\,\text{mm}$, $t_w = 10\,\text{mm}$, $r = 0$, $b_f = 200\,\text{mm}$, $t_f = 25\,\text{mm}$, $\alpha_{sw} = 90°$

The volume under this graph equals the vertical force F_{up} which is transmitted from the bridge deck to the steel girder. Equation 6.12 is the sum of the distributions under all bridge deck webs of the corresponding adhesive layer.

$$
\begin{aligned}
F_{\mathrm{up}} &= \sum_{j=1}^{n} \int_{x_j-\frac{b_{bs}}{2}}^{x_j+\frac{b_{bs}}{2}} \int_{b_N}^{b_f-b_N} \sigma_z(x,y)\,\mathrm{d}x\,\mathrm{d}y \\
&= \sum_{j=1}^{n} \left[\int_{x_j-\frac{b_{bs}}{2}}^{x_j+\frac{b_{bs}}{2}} \int_{b_N}^{b_i} \underbrace{2\cdot\sigma_{z,\max}\cdot\cos^{n_x}\left(\frac{\pi}{b_{bs}}\,x\right)\frac{2\,(y+b_N)}{b_f-b_i-2\,b_N}}_{\text{stress distribution of \textit{side caps}}} \mathrm{d}x\,\mathrm{d}y \right. \\
&\qquad \left. + \int_{x_j-\frac{b_{bs}}{2}}^{x_j+\frac{b_{bs}}{2}} \int_{\frac{b_f-b_i}{2}}^{\frac{b_f+b_i}{2}} \underbrace{\sigma_{z,\max}\cdot\cos^{n_x}\left(\frac{\pi}{b_{bs}}\,x\right)\cdot b_{\mathit{eff}}}_{\text{stress distribution of \textit{middle part}}} \mathrm{d}x\,\mathrm{d}y \right]
\end{aligned}
\tag{6.12}
$$

Equation 6.13 solves the definite integral of the stress distribution under one vertical web for $n_x = 5$, which is the appropriate factor for a bridge deck with a ratio $t_{sw}/t_p = 12/21$, see Figure 6.19 on page 108.

$$
\begin{aligned}
F_{\mathrm{up},j} &= 2\cdot\sigma_{z,\max}\cdot \int_{-\frac{b_{bs}}{2}}^{\frac{b_{bs}}{2}} \int_{b_N}^{\frac{b_f-b_i}{2}} \cos^5\left(\frac{\pi}{b_{bs}}\,x\right) \frac{2\,(y+b_N)}{b_f-b_i-2\,b_N}\,\mathrm{d}x\,\mathrm{d}y \\
&\qquad + \sigma_{z,\max}\cdot \int_{-\frac{b_{bs}}{2}}^{\frac{b_{bs}}{2}} \int_{\frac{b_f-b_i}{2}}^{\frac{b_f+b_i}{2}} \cos^5\left(\frac{\pi}{b_{bs}}\,x\right)\cdot b_{\mathit{eff}}\,\mathrm{d}x\,\mathrm{d}y \\
&= \sigma_{z,\max}\left(2\cdot\frac{4\,b_{bs}\,(b_f-b_i-2\,b_N)}{15\,\pi} + \frac{16\,b_{bs}\,b_i}{15\,\pi}\right)
\end{aligned}
\tag{6.13}
$$

By incorporating Equations 6.14 and 6.15, the stress concentration factor μ_{σ_z} results in Equation 6.16, which describes the ratio of the maximum to the average value of the σ_z stress distribution.

$$
\bar{\sigma}_z = \frac{F_{\mathrm{up},j}}{A_{\mathrm{adh}}} = \frac{F_{\mathrm{up},j}}{b_{\mathit{eff}}\cdot l_m}
\tag{6.14}
$$

$$
\mu_{\sigma_z} = \frac{\sigma_{z,\max}}{\bar{\sigma}_z}
\tag{6.15}
$$

$$
\mu_{\sigma_z}(n_x = 5) = b_{\mathit{eff}}\cdot l_m \left(\frac{8\,b_{bs}\,(b_f-b_i-2\,b_N)}{15\,\pi} + \frac{16\,b_{bs}\,b_i}{15\,\pi}\right)^{-1}
\tag{6.16}
$$

Equation 6.16 determines the stress concentration factor μ_{σ_z} for vertical webs with a ratio $t_{sw}/t_p = 12/21$. Comparisons between analytically and numerically determined stress distributions for several steel girder geometries are shown in Figure 6.22 and Appendix C.2, page 164 ff. The stress distributions on steel girders with thin webs and wide flanges exhibit remarkable stress concentrations in the center of the connection layer over the web, see Figure 6.22(a) and 6.22(b). On geometric sets with a higher $\frac{t_w}{b_f}$-ratio, the difference between the stress concentration in the center and at the edges is not as great, see Figure 6.22(c) and 6.22(d). The analytically determined maximum stress is generally slightly lower than that determined by FEA, with values differing by up to 20 %. Steel girders with thick webs and narrow flanges showed better agreement than geometries with slender webs and thin, wide flanges.

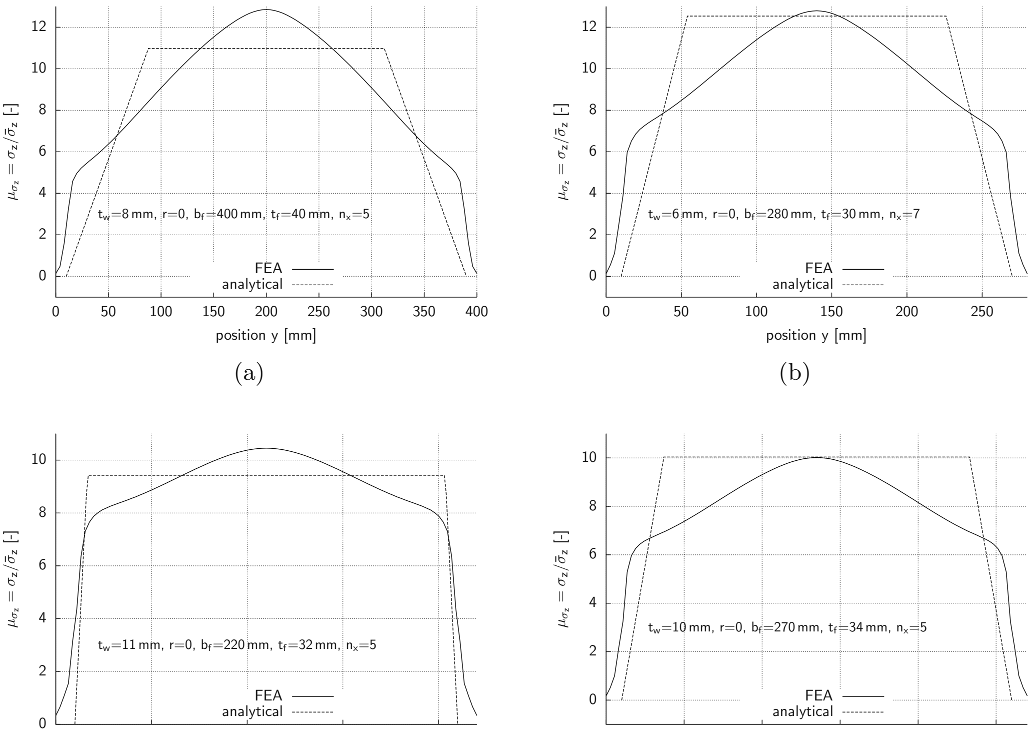

(a) (b)

(c) (d)

Figure 6.22: Stress distribution shapes

The influence of inclined webs is taken into account by using additional factor

κ_{σ_z}, which was determined in Section 6.3.2. The maximum tensile through-thickness stress is therefore determined by

$$\sigma_{z,\max} = \bar{\sigma}_z \cdot \mu_{\sigma_z} \cdot \kappa_{\sigma_z} \tag{6.17}$$

6.5 Influence of bending moments on through-thickness stresses

Although the bending moments in the bridge deck can generally be disregarded (as shown in Section 3.4.2), the calculation of the stress distribution due to an uplift force in combination with a bending moment is shown in the following. The stress situation inside the adhesive connection of a bridge resulting from the uplift forces and the moments acting on the adhesive connection is determined as described in Chapter 5.

Determination of stress distribution due to a bending moment

The calculations to determine the distribution of through-thickness stresses σ_z due to a moment loading are made on the *VS*-geometry described in Section 6.3.3. The loading of the model is shown in Figure 6.23. Instead of a linear distribution of the stresses introduced to the model, it was loaded with two uniformly distributed loads p_{z,M_0} for technical reasons relating to the FE program. The moment M_0 resulting from the stresses is shown in Equation 6.18.

$$\begin{aligned} M_0 &= p_{z,M_0} \cdot \frac{1}{2} b_f \cdot l_m \cdot \frac{1}{2} b_f \\ &= \frac{1}{4} \cdot p_{z,M_0} \cdot l_m \cdot b_f^2 \end{aligned} \tag{6.18}$$

where b_f is the steel girder's flange width (disregarding b_N) and l_m is the distance between the webs in the bridge deck.

As described in Section 6.3.3, page 97 ff., each model was loaded with uniformly distributed line loads on its upper face over the webs, resulting in an uplift force

$$F_{\mathrm{up},0} = p_z \cdot b_f \cdot l_m \tag{6.19}$$

with $p_z = 1\,\mathrm{N/mm^2}$.

The ratio $e = \frac{\Delta M}{F_{\mathrm{up}}}$ (see Chapter 5, with ΔM and F_{up} as forces acting inside the bridge deck), defines the linear combination for the superposition of both distribu-

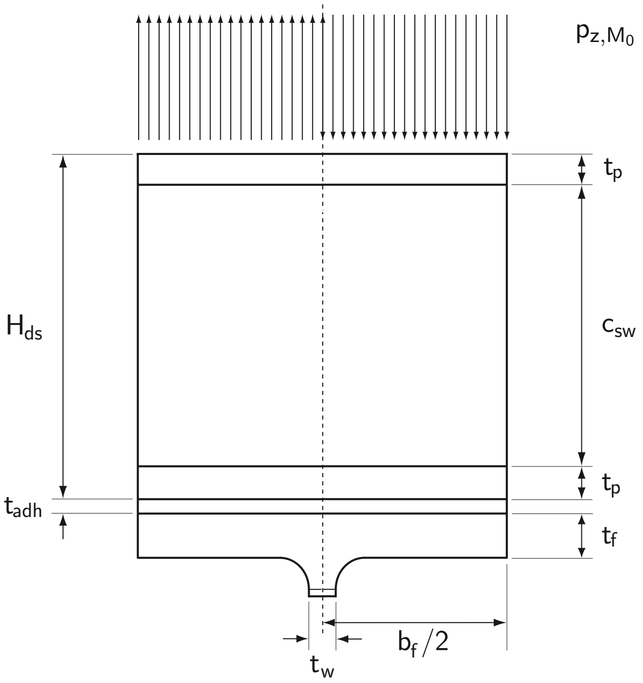

Figure 6.23: Loading of FE model with *VS*-geometry

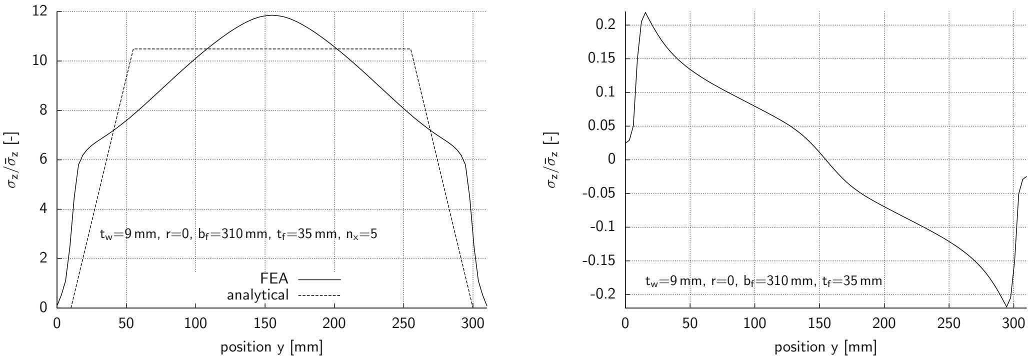

(a) Stress distribution due to centrical loading (uplift force in adhesive layer)

(b) Stress distribution due to asymmetric loading (see Figure 6.23)

Figure 6.24: Stress distribution shapes in adhesive layer

tions, see Equation 6.20.[§]

$$e = \frac{\Delta M}{F_{\text{up}}} = \frac{M_0}{F_{\text{up},0}} = \frac{\frac{b_f^2}{4} \cdot l_m \cdot p_{z,M_0}}{b_f \cdot l_m \cdot p_z} = \frac{b_f}{4} \cdot \frac{p_{z,M_0}}{1 \left[\frac{\text{N}}{\text{mm}^2}\right]} \tag{6.20}$$

$$\rightsquigarrow \quad p_{z,M_0} = e \cdot \frac{4}{b_f} \quad \left[\frac{\text{N}}{\text{mm}^2}\right] \tag{6.21}$$

The stress distributions were determined by applying $p_{z,M_0} = \frac{4}{b_f}$, as shown in Figure 6.24(b) on the preceding page and further diagrams in Appendix C.2 for example. These values must therefore be multiplied by eccentricity e to obtain the moment distribution for each steel girder and this moment distribution is added to the distribution resulting from the pure uplift force.

The steel girder geometry of the example shown in Figure 6.24 is described in Table B.2 on page 161 and has a torsional stiffness on the upper flange of $k_\vartheta = 85.56\,\text{kNm}$. In Table 5.3 on page 87, eccentricity e can be obtained from k_ϑ. An interpolation leads to $e = 6.2$. The superposed graph $(F_{\text{up}} + \Delta M)$ is displayed in Figure 6.25 on the next page, showing that the stresses due to the bending moment have a small effect on the stress distribution. They result in an increase of stresses near to one edge of the interface, but not the maximum stress value $\sigma_{z,\max}$, which was calculated from the pure uplift loading. Therefore, the analytically determined value also represents a very good approximation of the maximum stress value of the superposed loading.

The graphs show that the width of the FE distribution is slightly greater than the distribution obtained using the analytical solution. This is because the neoprene barrier was also modeled in the FE model and transmits a small amount of stresses. This has no influence on the results concerning the maximum stresses however.

This procedure was applied to all investigated steel girder geometries (see Tables B.1 to B.5, pages 161–162), with the result the stress distributions fitted well for each investigated case, i.e. for all steel girders the stress increase was not higher than the maximum stress due to the pure uplift force and the analytically determined maximum stress could approximate the maximum value obtained by numerical calculations. The diagrams concerning this investigation are shown in Appendix C.3, page 175 ff. It can be concluded that it is not necessary to take the bending moment effect into account for calculation of the maximum tensile stresses.

[§] F_{up} is the uplift force acting in the bridge deck, while $F_{\text{up},0}$ is the uplift force acting on the FE model.

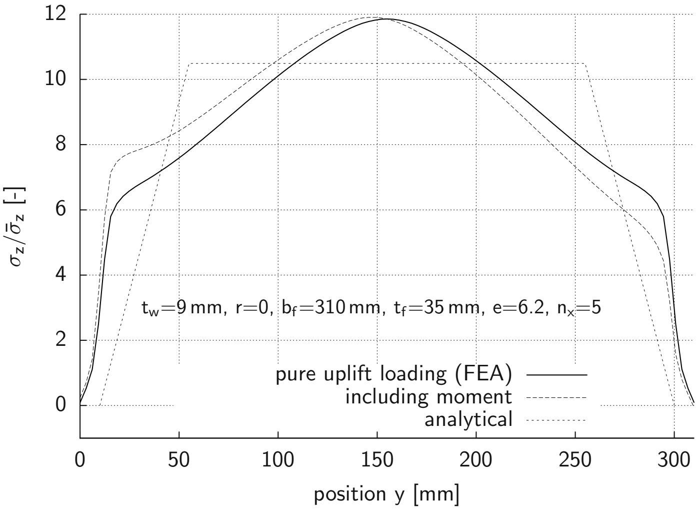

Figure 6.25: Superposition of distributions due to F_{up} (see Figure 6.24(a)) and moment ΔM (see Figure 6.24(b))

6.6 Comparison with experimental results

The investigations carried out in this chapter allow the stress concentration values of the experiments described in Chapter 3 to be calculated. The stress concentration in the adhesive connection is defined by the ratio of the maximum stress to the average stress $\left(\frac{\sigma_{z,\max}}{\bar{\sigma}_z} = \mu_{\sigma_z} \cdot \kappa_{\sigma_z}\right)$, see Section 6.4.3. When the average tensile stress $\bar{\sigma}_z^+$ in the adhesive connection is known, the maximum stress is obtained by multiplying it by the factors $\mu_{\sigma_z} \cdot \kappa_{\sigma_z}$.

Determination of μ_{σ_z} and κ_{σ_z} for geometry used in full-scale experiments

Factor μ_{σ_z} is calculated using Equation 6.16, page 112. The geometric values for the *HEM 200* steel girder and the *DuraSpan 766* bridge deck are shown in Table 6.3.

Table 6.3: Geometric values of *HEM 200* steel girder and *DuraSpan 766* bridge deck for determination of μ_{σ_z}

steel girder flange width	b_f	=	206 mm
steel girder flange thickness	t_f	=	25 mm
steel girder web thickness	t_w	=	15 mm
steel girder curvature	r	=	18 mm
adhesive thickness	t_{adh}	=	8 mm
neoprene barrier thickness	b_N	=	10 mm
module length	l_m	=	152 mm
bridge deck web thickness	t_{sw}	=	12 mm
bridge deck panel thickness	t_p	=	21 mm
web inclination (bridge deck web)	α_{sw}	=	75.3°

With Equation 6.22 (compare Eq. 6.8 on page 109), b_i is calculated:

$$\begin{aligned} b_i &= t_w + 1.61\,r + 5\,t_f + 2\,t_{\text{adh}} \\ &= 15\,\text{mm} + 1.61 \cdot 18\,\text{mm} + 5 \cdot 25\,\text{mm} + 2 \cdot 8\,\text{mm} \\ &= 185\,\text{mm} \end{aligned} \tag{6.22}$$

b_{bs} is defined in Equation 6.3 (see Figure 6.14):

$$b_{bs} = t_{sw} + 2\,t_p = 12\,\text{mm} + 2 \cdot 21\,\text{mm} = 54\,\text{mm} \tag{6.23}$$

With the ratio $t_{sw}/t_p = 12/21$, factor n_x is determined, according to Figure 6.19 on page 108, as being 5. With these values, factor μ_{σ_z} can be calculated (Equation 6.24), as described in Section 6.4.3 (Equation 6.16).

$$\begin{aligned} \mu_{\sigma_z} &= b_{eff} \cdot l_m \left(\frac{8\,b_{bs}\,(b_f - b_i - 2\,b_N)}{15\,\pi} + \frac{16\,b_{bs}\,b_i}{15\,\pi} \right)^{-1} \\ &= \frac{186\,\text{mm} \cdot 152\,\text{mm}}{\frac{8 \cdot 54\,\text{mm}\,(206\,\text{mm} - 185\,\text{mm} - 2 \cdot 10\,\text{mm})}{15\,\pi} + \frac{16 \cdot 54\,\text{mm} \cdot 185\,\text{mm}}{15\,\pi}} \\ &= 8.31 \end{aligned} \tag{6.24}$$

Finally the web inclination ($\alpha_{sw} = 75.3°$) has to be considered by incorporating κ_{σ_z} (see Figure 6.5 on page 96):

$$\kappa_{\sigma_z} = 1.425$$

leading to

$$\kappa_{\sigma_z} \cdot \mu_{\sigma_z} = 1.425 \cdot 8.31 = 11.84 \tag{6.25}$$

The value of factors $\kappa_{\sigma_z} \cdot \mu_{\sigma_z}$ determined by FEA, given in Figure 3.10 on page 32, is 12.41, which is approximately 6 % lower than the analytically determined value.

Determination of tensile through-thickness stresses

In order to obtain the maximum through-thickness tensile stress, $\kappa_{\sigma_z} \cdot \mu_{\sigma_z}$ have to be multiplied by the average through-thickness stress $\bar{\sigma}_z$ acting in the adhesive connection at the average ultimate load.

In the full-scale adhesive connection experiments described in Chapter 3, an average ultimate load $\bar{F}_u = 176.3\,\text{kN}$ (see Table 6.5) was determined, which corresponds to a maximum average tensile through-thickness stress of $\max \bar{\sigma}_z = \frac{\bar{F}_u}{A_{\text{adh}}} = 0.79\,\frac{\text{N}}{\text{mm}^2}$. This leads to an analytically determined maximum stress at failure of $\sigma_{z,\text{max}} = \max \bar{\sigma}_z \cdot \mu_{\sigma_z} \cdot \kappa_{\sigma_z} = 0.79\,\frac{\text{N}}{\text{mm}^2} \cdot 11.84 = 9.35\,\frac{\text{N}}{\text{mm}^2}$. The maximum stress value determined by FEA is $\sigma_{z,\max} = 9.8\,\frac{\mathrm{N}}{\mathrm{mm}^2}$. The ultimate through-thickness tensile stress $\sigma_{z,u}$ determined from the coupon tests in Chapter 4, is $9.1\,\mathrm{N/mm}^2$, i.e. the results of the full-scale and the coupon experiments differ by approximately +8 % and +14 % respectively. All values are given in Table 6.4.

Table 6.4: Comparison of experimental and computed results for $\sigma_{z,u}$ (ultimate through-thickness tensile strength)

Determination/calc. method	$\bar{\sigma}_z\left[\frac{\mathrm{N}}{\mathrm{mm}^2}\right]$	$\mu_{\sigma_z}\cdot\kappa_{\sigma_z}[-]$	$\sigma_{z,u}\left[\frac{\mathrm{N}}{\mathrm{mm}^2}\right]$	$\sigma_{z,\max}\left[\frac{\mathrm{N}}{\mathrm{mm}^2}\right]$
coupon test		–	**9.1**	
full-scale adhesive connection	0.79			
FEA		12.41		**9.80**
analytical		11.84		**9.35**

Table 6.5 shows the results of the full-scale adhesive connection experiments (described in Chapter 3) with their maximum stress values.

Table 6.5: Experimental results

Experiment	ultimate load [kN]	$\bar{\sigma}_z\left[\frac{\mathrm{N}}{\mathrm{mm}^2}\right]^a$	$\sigma_{z,\max}\left[\frac{\mathrm{N}}{\mathrm{mm}^2}\right]^b$
C2-1	139.4	0.63	7.45
C2-2	191.6	0.86	10.18
C3-1	186.0	0.84	9.95
C3-2	188.0	0.85	10.06
average	176.3	0.79	9.35
stand. dev.[c] s	±24.7	0.11	1.31

---

[a] at failure

[b] assuming a stress concentration factor of $\mu_{\sigma_z}\cdot\kappa_{\sigma_z}$=13.12

[c] standard deviation

No comparison with the reference bridge described in Section 3.3 was made since the stress concentrations determined in these FE calculations were not very accurate due do the relatively coarse mesh.

6.7 Conclusions

An analytical method to calculate the maximum stress concentration in the adhesive layer is determined and numerically validated in this chapter. The analytical description offers the possibility of approximating the maximum stresses in the adhesive connection by a formula without the need to perform complicated FE modeling. It was observed that the stresses are concentrated under the bridge deck webs, with a maximum value over the center of the steel girder and stress concentrations near to the steel girder's edge, which are in any case smaller than the maximum value occurring over the center however.

Furthermore, the superposition of standardized stress distributions due to uplift forces F_{up} and bending moments ΔM in the bridge deck was effected. It was observed that for all investigated steel girder geometries, the bending moment in the bridge deck has a relatively small influence on the stress distribution in the adhesive layer. The stress distribution diagrams in Appendix C.3, page 175 ff. show the negligible effect of the bending moment. Therefore, the analytical method described in Section 6.4 is applicable for any steel girder geometry.

The FE models constituted a key element for the development of the analytical method since they were used for cross-checking, see figures in Appendix C.3, page 175. Several typical steel girder geometries were calculated using FEA and the analytical method. The comparison of the results obtained using these methods shows a good correlation with the graphs.

The experimental validation was provided with the experiments described in Chapter 3, and the comparison of the stresses was made in Section 6.6, with experimentally and analytically determined stresses showing good congruence.

7 Concept for a design method

7.1 Introduction

The objective in this chapter is to formulate the strength of the adhesive connection and compare it to the stresses occurring in the adhesive connection. These include the through-thickness stresses σ_z resulting from the inner forces acting in the transverse direction and the shear stresses τ_{xz} resulting from the composite action between the bridge deck and the steel girders in the longitudinal direction. To comply with current civil engineering codes, the calculations should be made at the design value level, usually denoted by subscript *d*. This verification is formulated by Equation 7.1:

$$S_d \overset{!}{\leq} R_d \tag{7.1}$$

where S_d denotes the design value of the stresses and R_d the design value of the material resistance.

The design values of the resistance result from the experimental investigations carried out in this thesis reduced by a material safety factor determined by statistical calculations using the experimental results obtained for the FRP material, as shown in Chapter 4. The material strength in the failure layer depends on the combination of normal through-thickness tensile stresses σ_z and shear stresses τ_{xz}.

The through-thickness tensile stresses σ_z were investigated in Chapter 6. This included a description of the determination of the maximum tensile stress based on specific geometric values according to the type of bridge deck and steel main girder. It is also necessary to determine the magnitude of the shear stresses τ_{xz} acting in the failure layer of the FRP material. While the through-thickness stresses σ_z do not depend on the degree of composite action between the bridge deck and the steel girders, the shear stresses τ_{xz} do.

Having determined both stress components, σ_z and τ_{xz}, the material resistance interaction diagram plotted in Figure 4.3 on page 62 can be used to compare the structure's resistance to the stresses on the design level, determined by a load combination.

7.2 Determination of shear stresses in adhesive connection

Due to the composite action between the FRP bridge deck and the steel girder, shear stresses τ_{xz} act in the adhesive bond.

7.2.1 Assumptions

Two general assumptions can be made [Gür04]:

1. A linear strain distribution over the height of the steel girder and the bridge deck. This assumption takes into account full composite action between the bridge deck and the steel girder as well as a linear stress distribution inside the bridge deck, which presupposes that the bridge deck webs transfer the full in-plane shear from the lower to the upper face sheet. This assumption is the more conservative one concerning the stresses.

2. A non-linear strain distribution with decreasing strains over the height of the bridge deck, which means that the upper face sheet is less loaded, in terms of axial stresses σ_x, than the lower one. As experimental investigations in [Gür04] showed, the strain distribution is not linear over the height for certain bridge deck types due to shear-lag effects.

Linearly distributed axial strains

Figure 7.1 shows an elevation of a bridge girder with an FRP bridge deck with full composite action: the axial strains ε_x are linearly distributed over the height. Since the materials used do not have the same stiffnesses, as expressed by their Young's moduli, the corresponding stress profiles decrease abruptly at the interfaces of the materials.

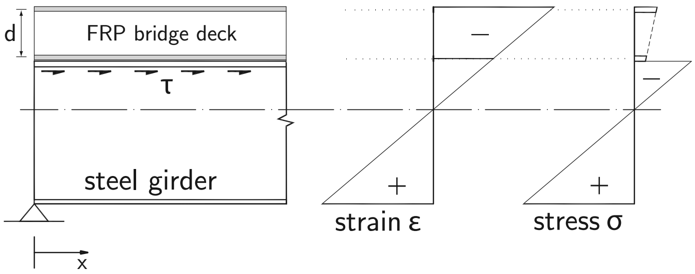

Figure 7.1: Strain and stress distribution in steel girder and FRP bridge deck

The determination of shear stresses in sections subjected to bending (and the resulting shear forces) are described in [Fri83]. The shear stresses τ_{xz} are calculated using Equation 7.2:

$$\tau_{xz} = \frac{V \cdot S_z}{I_y \cdot t} \tag{7.2}$$

where V is the shear force, S_z the first moment of area, I_y the moment of inertia and t the width of the material over which the shear stress is calculated. The relationship expressed above is only valid for homogeneous materials; if materials with different elastic moduli are used, the most common way of determining the shear stresses τ_{xz} is to geometrically adapt the section by modifying the cross section of the corresponding face sheet to an equivalent cross section by applying factor n_0, defined in Equation 7.3:

$$n_0 = \frac{E_s}{E_{x,FRP}} \tag{7.3}$$

where E_s is the E-modulus of steel and $E_{x,FRP}$ that of the FRP material, as given in Table 3.3, page 35.

Non-linearly distributed axial strains

Experimental investigations described in [Gür04] showed that, at least for the investigated *DuraSpan* deck, the strain distribution across the webs of the two face sheets was not linear up to failure, see Figure 7.2. The investigated *ASSET* deck, on the other hand, exhibited an almost linear strain distribution. The non-linear strain distribution implies that the stress profile over the height cannot be directly derived using Bernoulli's law.

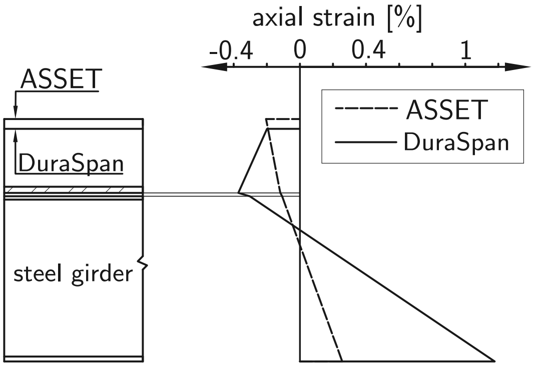

Figure 7.2: Strain distribution in steel girder and *ASSET* and *DuraSpan* bridge decks [Gür04]

7.2.2 Calculation of shear stresses

In the following the assumption regarding the linearly distributed stresses is applied, since it is the more conservative one concerning the stress state in the adhesive connection.

The effective width of the two face sheets of the FRP deck is a significant value for the calculations. According to experimental investigations documented in [Gür04] the effective width of the face sheets changes with the load level: the axial strain profiles across the width of the face sheets were described as being almost constant for loads within the elastic range, while they narrowed noticeably towards the steel girders for loads close to the failure loads, leading to a non-linear behavior of the investigated girder.

An effective width b_{eff} of 1.5 m was assumed for the *DuraSpan* deck, based on experimental results. For the calculations, b_{eff} is scaled down to an equivalent width $b_{eq} = b_{eff}/n_0$. When all the geometric parameters and material properties have been established, the shear stresses can be calculated using Equation 7.2 for different configurations.

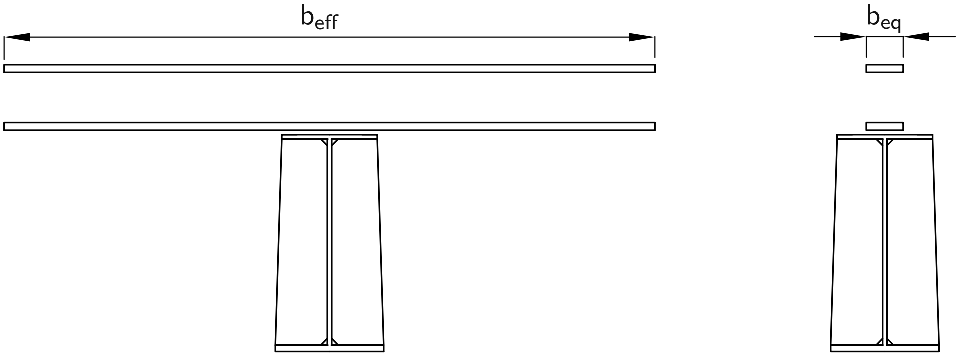

Figure 7.3: Original and adapted cross sections

7.3 Design example

In the following, the determination of the stress state in the adhesive connection is shown by way of an example: a bridge with a 30-m span has nine steel girders of 2.2-m height with a girder distance of 2.7 m. The data required for the calculation is given in the adjacent Table 7.1. A *DuraSpan 766* bridge deck is used. The geometric data is given in Table 6.2 on page 100. The thickness of the adhesive connection between the steel girders and the FRP bridge deck is assumed to be $t_{\text{adh}} = 8$ mm; the neoprene barrier width b_N is 10 mm.

Table 7.1: Geometric data concerning steel girder

		[mm]
web thickness	$t_w =$	20
flange width	$b_f =$	270
flange thickness	$t_f =$	30
radius	$r =$	0

7.3.1 Through-thickness tensile stresses

The through-thickness tensile stresses in the adhesive connection are determined using the method described in Chapter 6. The input data required consists of the uplift force acting on the adhesive connection, plus certain specific geometric values concerning the bridge deck and the steel girder. With these values, b_i can be determined according to Equation 6.8 on page 109:

$$\begin{aligned} b_i &= t_w + 5\,t_f + 2\,t_{\mathrm{adh}} \\ &= 20\,\mathrm{mm} + 5 \cdot 30\,\mathrm{mm} + 2 \cdot 8\,\mathrm{mm} \\ &= 186\,\mathrm{mm} \end{aligned} \tag{7.4}$$

b_{bs} is defined in Equation 6.3 (cp. Figure 6.14):

$$b_{bs} = t_{sw} + 2\,t_p = 12\,\mathrm{mm} + 2 \cdot 21\,\mathrm{mm} = 54\,\mathrm{mm} \tag{7.5}$$

As the ratio t_{sw}/t_p of the *DuraSpan 766* bridge deck is 12/21, factor n_x is 5, cp. Figure 6.19 on page 108. Factor μ_{σ_z} is calculated using Equation 7.6 (cp. Equation 6.16).

$$\begin{aligned} \mu_{\sigma_z} &= b_{eff} \cdot l_m \left(\frac{8\,b_{bs}\,(b_f - b_i - 2\,b_N)}{15\,\pi} + \frac{16\,b_{bs}\,b_i}{15\,\pi} \right)^{-1} \\ &= \frac{(270\,\mathrm{mm} - 2 \cdot 10\,\mathrm{mm}) \cdot 152\,\mathrm{mm}}{\frac{8 \cdot 60\,\mathrm{mm}\,(270\,\mathrm{mm} - 186\,\mathrm{mm} - 2 \cdot 10\,\mathrm{mm})}{15\,\pi} + \frac{16 \cdot 60\,\mathrm{mm} \cdot 186\,\mathrm{mm}}{15\,\pi}} \\ &= 10.3 \end{aligned} \tag{7.6}$$

This means that, for a bridge deck geometry with vertical webs, the maximum through-thickness tensile stress would be approximately ten times the average stress. Factor μ_{σ_z} is the maximum of the analytically determined normalized stress distribution, cp. Figure 7.4.

The web inclination ($\alpha_{sw} = 75.3°$) has to be considered by incorporating κ_{σ_z} (see Figure 6.5 on page 96):

$$\kappa_{\sigma_z} = 1.425$$

leading to

$$\kappa_{\sigma_z} \cdot \mu_{\sigma_z} = 1.425 \cdot 10.3 = 14.7 \tag{7.7}$$

The maximum stress value is roughly 15 times higher than the average through-thickness stress in the adhesive connection, which can easily be determined by dividing the uplift force by the connected area. The uplift force can be calculated in

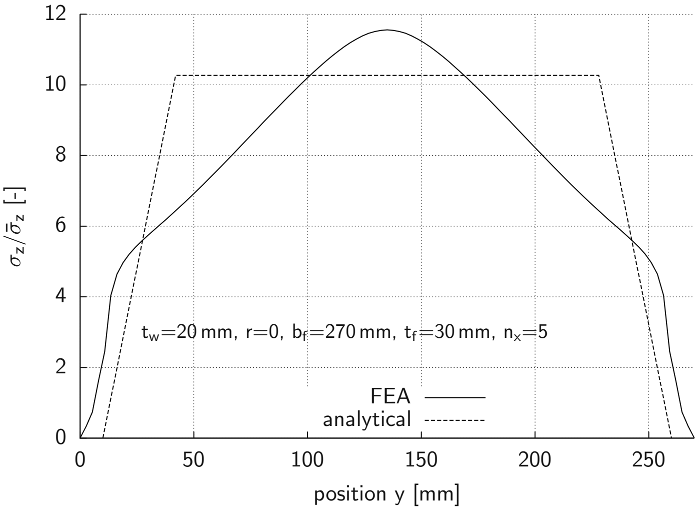

Figure 7.4: Normalized through-thickness tensile stresses

different ways, for example by a simple two-dimensional system, as used in Chapter 5: Table B.5 on page 162 shows that the chosen girder has a torsional stiffness $k_\vartheta = 144.64\,\text{kNm}$, resulting in an uplift force of $F_{\text{up}d} = 1.5 \cdot 3.17\,\text{kN} = 4.76\,\text{kN}$, as shown in Table 5.4. It is assumed that this uplift force acts in the adhesive connection over an area of one bridge deck element, as investigated in Section 3.3. Investigations in Section 6.5 showed that the influence of the maximum through-thickness tensile stress due to bending moments in the bridge deck can be disregarded. Since the adhesive layer on the steel girder has a width of only 250 mm ($= 270\,\text{mm} - 2\,b_N$), this area is $A = 0.3\,\text{m} \times 0.25\,\text{m} = 0.075\,\text{m}^2$. The width of the influenced area was assumed to be 0.3 m as the calculations on the reference bridge in Section 3.3 showed that the load is mainly transferred by one bridge deck web. This results in an average through-thickness stress $\bar{\sigma}_z^+ = 4.76\,\text{kN}/0.075\,\text{m}^2 = 0.063\,\text{N/mm}^2$, which leads to a maximum tensile stress of

$$\sigma^+_{zd,\max} = 0.063\,\text{N/mm}^2 \cdot 14.7 = 0.92\,\text{N/mm}^2. \tag{7.8}$$

7.3.2 Shear stresses

For the specific cross sectional values S_z and I_y, the size of the cross section of the FRP material has to be adapted for the calculations. This adaptation depends on the ratio n_0 of the material's stiffnesses:

$$n_0 = \frac{E_s}{E_{FRP}} = \frac{210\,000}{11\,790} = 17.8 \tag{7.9}$$

The equivalent width of the FRP material in the calulations is defined in Equation 7.10, as determined in [Gür04]:

$$b_{equ} = \frac{b_{eff}}{n_0} = \frac{1500\,\mathrm{mm}}{17.8} = 84\,\mathrm{mm} \tag{7.10}$$

For the girder examined in Section 7.3.1, the shear stresses are calculated by applying Equation 7.2. A linear strain distribution is assumed.

$$\tau_{xzd} = \frac{V_d \cdot S_z}{I_y \cdot (b_f - 2\,b_N)} = 0.76\,\frac{\mathrm{N}}{\mathrm{mm}^2} \tag{7.11}$$

where V_d results from the uniformly distributed traffic load of $9\,\mathrm{kN/m^2}$ × the girder distance of 2.7 m and an axle load of 150 kN. The loads are increased by the factor $\gamma_F = 1.5$, cp. Equation 7.12:

$$V_d = 1.5\left(9\,\frac{\mathrm{kN}}{\mathrm{m}^2} \cdot 2.7\,\mathrm{m} \cdot \frac{30\,\mathrm{m}}{2} + 150\,\mathrm{kN}\right) = 772\,\mathrm{kN} \tag{7.12}$$

The geometric values of the cross section used in Equation 7.11 are the following:

$$\begin{aligned} I_y &= 3.611 \cdot 10^{10}\,\mathrm{mm}^4 \\ S_z &= 8.932 \cdot 10^{6}\,\mathrm{mm}^3 \end{aligned} \tag{7.13}$$

7.4 Material resistance of adhesive connection and comparison

The maximum stress combinations of tensile strength $\sigma_{z,u}$ and shear strength $\tau_{xz,u}$ in the adhesive connection were determined in Chapter 4. The experimentally determined material strength values are shown in Figure 4.3 on page 62 approached by a fitting curve described by Equation 4.2 for $\kappa_\sigma = \kappa_\tau = 1$. The combined shear-tensile strength determined in Chapter 4, reduced by the material safety factor, is shown in Figure 7.5, representing the material resistance on the design level. This material safety factor was determined in Section 4.4.3 as being $\gamma_M = 1.28$. The quadratic function, the material resistance on the design level, is the curve shown in Figure 7.5, with a maximum tensile strength $\sigma^+_{z,d} = \frac{9.1\,\mathrm{N/mm^2}}{1.28} = 7.1\,\mathrm{N/mm^2}$ (in the case of no simultaneous shear stress), and a maximum shear strength $\tau_{xz,d} = \frac{18.3\,\mathrm{N/mm^2}}{1.28} = 14.3\,\mathrm{N/mm^2}$.

The result for the example calculated in Section 7.3 is represented by a circle in Figure 7.5. This procedure was applied for the steel girder geometries shown in Tables B.1 to B.5 in combination with a bridge deck (of the *DS*-geometry). Each tensile-shear combination value is represented by a + in Figure 7.5. The maximum tensile through-thickness stress and shear stress on the design level are approximately 7 times higher than the material resistance, which is the combined shear-tensile strength reduced by the material safety factor γ_M, determined in Chapter 4.

Every experimental result determined using the full-scale connection (Table 6.5 on page 119), divided by the material safety factor, is indicated by an ×. The results show good agreement with the results obtained from the coupon experiments, which formed the basis for the determination of the material resistance. The average value obtained from the full-scale experiments (as shown in Table 6.5) is 14 % higher than the average value obtained from the coupon experiments.

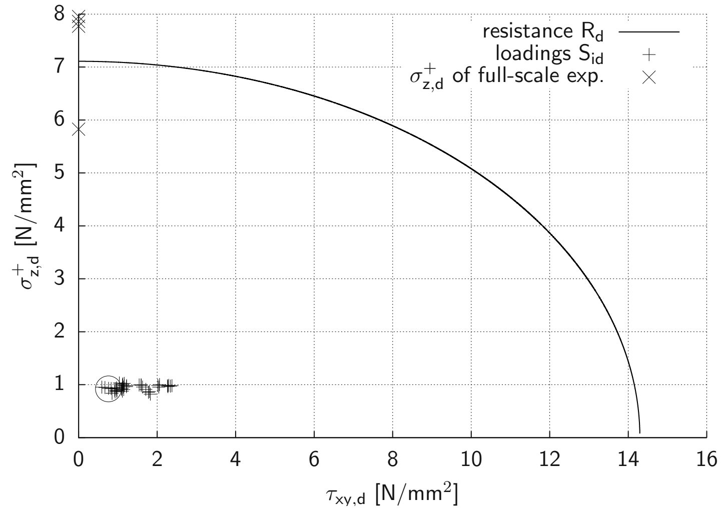

Figure 7.5: Material resistance and shear-tensile stress combinations of various girders due to design loads

7.5 Conclusions

All the information required to calculate the stresses in the adhesive layer due to traffic loading and the resistance of the adhesively-bonded connection between the bridge deck and the structural steel girders has been provided in the previous chapters, forming the basis for a design method.

The calculation of a tensile-shear combination for one specific set of geometries was made in the example proposed in Section 7.3. Furthermore, the steel girder geometries used in Section 5.6 were analyzed concerning the shear-tensile combination acting in the adhesive layer.

The comparison of the stresses obtained from the loading with the resistant stresses was made on the design level and it was proved that for all considered cases, $S_d \leq R_d$ is achieved with a large safety margin. The calculations clearly demonstrate that the static loading of the FRP deck/steel girder joint is uncritical, even if the combined through-thickness shear and tensile stresses are taken into account.

Part V

Conclusions

8 Conclusions

Most of the methods used for connecting FRP bridge decks to steel girders until now are not material adapted. Since FRP is a brittle material, load-introduction points – like mechanically fastened joints – are problematic locations: bolts or studs used as connection elements, which introduce the loads locally, lead to high stress concentrations. With adhesively-bonded joints however, larger areas can be linked together, thus preventing stress concentrations. A further important structural aspect is the composite action resulting from the bonded connection between the bridge deck and the steel girder, which increases the stiffness and strength of the whole structure and therefore allows a reduction in the amount of material used for the steel girders.

While several aspects of the performance of this type of adhesively-bonded connection have already been investigated, little was known concerning the through-thickness performance of such connections. The aim of this thesis was to provide this knowledge and the results showed that adhesively-bonded connections can be used for most bridge deck and steel girder geometries.

8.1 Structural behavior in transverse direction

Loads are transmitted by the bridge deck to the steel girder, causing uplift forces and moments in the connections between bridge deck and steel girders. As far as the global behavior is concerned, it was concluded that these connections usually act as simple supports, the required rotation mainly resulting from the flexibility of the adhesive connection.

The torsional stiffness of the steel main girders in a bridge system with bonded FRP bridge decks may have a significant influence on the stress distribution in the adhesive layer if a minimum adhesive layer thickness is not respected. An adhesive thickness of 8–10 mm would be sufficient to provide a flexible connection that prevents stress concentrations, even in combination with a stiff steel girder. The adhesive layer thickness is also a design parameter which can be defined by the engineer in order to prevent stress concentrations in certain locations, as for example above a stiffening element in the steel girder. Furthermore, the stiffeners of the steel girders should not be connected to the upper flanges.

8.2 Stress state in adhesive connection

The maximum through-thickness tensile stresses due to uplift forces occur at locations where a vertical web of the FRP bridge deck crosses a steel girder. Under this vertical web, the maximum stress level is reached over the center of the steel girder, with stress peaks occurring near to the edges of the flange. It was concluded that the influence of a bending moment in the bridge deck over the steel girder can be disregarded, providing that the adhesive thickness is sufficient or that the steel girder has sufficient flexibility. Therefore, the through-thickness stresses can be determined (as described in Section 6.4) on the assumption that a loading on the adhesive connection acts as a pure uplift force without eccentricities, i.e. no moment.

Full-scale adhesive experiments were performed in order to validate the results of the numerical and analytical modeling. The experimental investigations showed that failure almost always occurred in the surface layer mats of the FRP material with a brittle behavior. A maximum average tensile stress of $0.79\,\mathrm{N/mm^2}$ at failure was derived from the experiments, which corresponds to a maximum tensile through-thickness stress of $\sigma_z^+ = 9.8\,\mathrm{N/mm^2}$. A good agreement between experimental results and numerical calculations was shown.

8.3 Design method

The basis for a design method that verifies the structural safety in the ultimate limit state due to traffic loads on the bridge is proposed. This comprises the determination, on the one hand, of the maximum stresses inside the adhesive layer and, on the other, of the material strength of the adhesive connection. A method for the calculation of the tensile through-thickness stresses is provided; the maximum shear stresses in the adhesive layer were calculated on the basis of [Gür04].

The material resistance of the adhesive connection is characterized by a combination of tensile through-thickness and shear strengths. This combined shear-tensile strength could be described by a quadratic equation with a tensile strength $\sigma_{z,u} = 9.1\,\mathrm{N/mm^2}$ and shear strength $\tau_{xz,u} = 18.3\,\mathrm{N/mm^2}$ determined with coupon experiments. As also shown in the full-scale adhesive connection experiments, the predominant failure mode in the coupon experiments was a fiber-tear failure, signifying that the material strength determined with these coupons is also applicable to full-scale adhesive connections in an actual bridge. The determined tensile through-thickness strength differed from the strength determined in the full-scale experiments by only 8 %. The material safety factor for the adhesively-bonded connection was determined as being $\gamma_M = 1.28$. An important task in the design process is to ensure that failure does not start in the adhesive connection which eventually could lead to additional failure of other structural members. A redundant system must be guaranteed.

Design examples of various geometries proved a good load-bearing behavior of adhesively-bonded joints between FRP bridge decks and structural steel girders. It was shown that the stress state due to traffic loads is sufficiently below the material resistance.

The fatigue behavior was investigated with a full-scale adhesive experiment; after 10^7 load cycles, no visible damage or changes in structure stiffness could be observed.

8.4 Contribution to state of the art

→ The results of this thesis prove the existence of a good load-bearing behavior under static and fatigue loads of adhesively-bonded joints between pultruded FRP bridge decks and structural steel girders, where the adhesive connection is loaded with uplift forces and moments acting in the bridge deck, in addition to the shear in the connection layer due to composite action. Therefore, a more material-adapted method to connect FRP bridge decks with structural steel girders is proposed, compared to the commonly used mechanically fastened connections involving bolts or studs, since high stress concentrations are prevented.

→ The connection acts as a simple support for the FRP bridge deck, if a certain adhesive thickness is provided, since the rotation mainly results from the adhesive layer. Therefore, the adhesive thickness also constitutes a design parameter because it influences the rotational stiffness of the connection. The bending moment acting in the bridge deck can thus be disregarded for the determination of the through-thickness tensile stresses in the adhesive connection.

→ The through-thickness tensile stress distribution curve in the adhesive connection layer between an FRP bridge deck and a steel girder reaches a peak over the center of the steel girder with stress concentrations near the edges, where a vertical web of the FRP bridge deck crosses a steel girder. The maximum level is approximately twelve times the average stress in the adhesive layer.

→ The developed analytical model is a method for estimating the tensile through-thickness stress in the adhesive layer between an FRP bridge deck and steel girders without the use of FEA. This can be done for different geometries of bridge decks and steel girders.

→ The thesis provides the basis for a design method for adhesively-bonded connections between pultruded FRP bridge decks and steel girders.

8.5 Future research

8.5.1 Material

The shear-tensile material resistance of the connection was determined on the *DuraSpan 766* bridge deck; other materials with a different fiber architecture may have a different resistance. Depending on the project and type of bridge deck, experimental investigations must be carried out to determine the resistance of the adhesive connection.

The calculations and full-scale connection experiments were made using a relatively stiff and brittle epoxy adhesive. Further investigations should be carried out with different adhesives in order to examine their influence on structural behavior; adhesives exhibiting a ductile behavior could further reduce stress concentrations for example.

8.5.2 Structural system and details

The full-scale adhesive experiments were carried out using one specific bridge deck and steel girder geometry. Further experiments with other geometries would provide additional confirmation regarding the validation of the design method.

This thesis, in combination with [Gür04], offers the possibility of designing adhesively-bonded connections between structural steel girders and an FRP bridge deck, acting together as a composite unit. These methods were developed and validated on simple girders, with positive bending moments. In a continuous girder, however, negative bending moments will also act in the regions over the supports, where the bridge deck will not act as a compression member, but will be loaded by tension. This behavior was basically investigated and described in [KS06]. The tensile stength and behavior of the *DuraSpan 766* bridge deck were described, but not the behavior of a whole composite girder with negative bending moments.

In the case of girders with very high torsional stiffness, e.g. box girders or sections with stiffeners combined with a thin adhesive thickness, additional investigations regarding the stress distribution should be carried out. Further studies regarding structural details – for example above supports, where the rotational stiffness is limited – should be made.

The bonding technique used on the construction site is important for economic reasons. Adhesive thicknesses of approximately 8 mm may require a special bonding procedure for example and although this is probably not an academic task, it remains a sensitive consideration requiring special attention at the planning level.

8.5.3 Long-term and fatigue behaviors

The experimental investigations in this thesis were mainly carried out for quasi-static and short-term conditions and the long-term behavior of adhesively-bonded connections was not considered and still has to be investigated. This concerns the durability as well as the creep behavior of the joint. Furthermore, since the investigations were performed in laboratory conditions, the effects of environmental conditions such as temperature and humidity on adhesively-bonded connections between FRP bridge decks and steel girders must also be analyzed. One fatigue experiment was carried out, but for a better understanding of the fatigue behavior, further investigations are necessary.

Part VI

Appendix

A Diagrams and photos from full-scale adhesive connection experiments

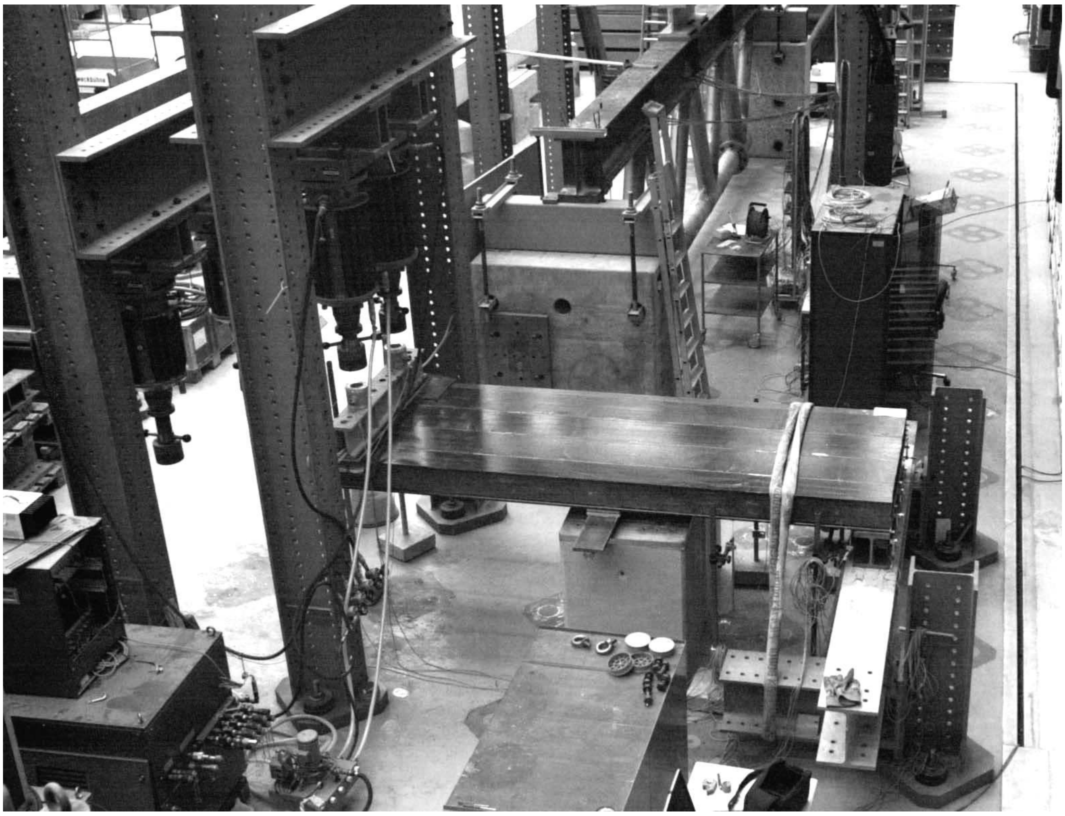

Figure A.1: Set-up for *C1-1*, *C1-2*, *C2-2* and *C3-2*

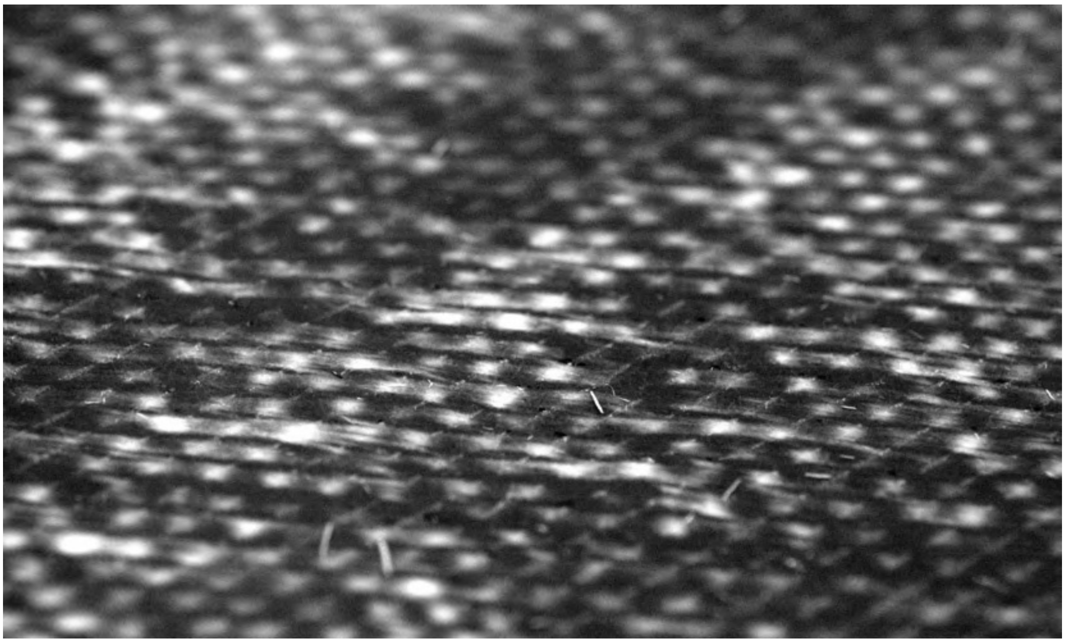

Figure A.2: Roughened surface before bonding (specimen *C2*)

Table A.1: Calibration list of experiments *C1-1* and *C1-2*

channel no.	id.	serial no.	type	capacity	k-factor	date
1	# 1	8 541	W 100	±100 mm	117.7	30 10 2003
2	# 2	1 484	W 100 K	±100 mm	99.88	30 10 2003
3	# 3	62 775	W 100 K	±100 mm	102.0	30 10 2003
4	# 4	1 486	W 100 K	±100 mm	100.3	30 10 2003
5	# 5	8 961	W 10 K	±10 mm	10.24	19 11 2003
6	# 6	8 965	W 10 K	±10 mm	10.38	19 11 2003
7	# 7	8 971	W 10 K	±10 mm	10.26	19 11 2003
8	# 8	8 968	W 10 K	±10 mm	10.39	19 11 2003
9	# 9	18 235	W 20	±20 mm	20.34	04 11 2003
10	# 10	5 355	W 20	±20 mm	20.35	20 11 2003
11	# 11	5 354	W 20	±20 mm	20.35	20 11 2003
12	# 12	5 364	W 20	±20 mm	20.29	05 11 2003
13	# 13	5 343	W 20	±20 mm	20.61	05 11 2003
14	# 14	5 131	W 20	±20 mm	20.14	05 11 2003
18	force N	709	E 100	1000 kN	408.07	19 11 2003
19	force S	712	E 100	1000 kN	455.72	19 11 2003

* channel nos. 18 and 19 are force transducers

Table A.2: Calibration list of experiments *C2-1* and *C3-1*

channel no.	id.	serial no.	type	capacity	k-factor	date
1	# 1	8 541	W 100	±100 mm	117.7	30 10 2003
2	# 2	1 484	W 100 K	±100 mm	99.88	30 10 2003
3	# 3	62 775	W 100 K	±100 mm	102.0	30 10 2003
4	# 4	1 486	W 100 K	±100 mm	100.3	30 10 2003
5	# 5	13 488	W 5 K	±5 mm	6.056	01 03 2004
6	# 6	2 583	W 5 K	±5 mm	4.7702	01 03 2004
7	# 7	13 486	W 5 K	±5 mm	5.9704	01 03 2004
8	# 8	13 482	W 5 K	±5 mm	5.4068	01 03 2004
9	# 9	2 598	W 5 K	±5 mm	4.6464	01 03 2004
10	# 10	2 597	W 5 K	±5 mm	4.5928	01 03 2004
11	# 11	5 354	W 20	±20 mm	20.35	20 11 2003
12	# 12	10 665	W 5 K	±5 mm	5.0885	01 03 2004
13	# 13	2 585	W 5 K	±5 mm	5.2974	01 03 2004
14	# 14	5 131	W 20	±20 mm	20.14	05 11 2003

Table A.3: Calibration list of experiments *C2-2* and *C3-2*

channel no.	id.	serial no.	type	capacity	k-factor	date
0	# 0	8 541	W 100	±100 mm	115.6	07 07 2004
1	# 1	6 747	W 100	±100 mm	99.43	07 07 2004
2	# 2	1 486	W 100 K	±100 mm	100.4	07 07 2004
3	# 3	9 843	W 100 K	±100 mm	101.8	07 07 2004
4	# 4	15 929	W 10	±10 mm	10.25	07 07 2004
5	# 5	13 487	W 5 K	±5 mm	5.1339	07 07 2004
6	# 6	2 611	W 5 K	±5 mm	5.0478	07 07 2004
7	# 7	2 607	W 5 K	±5 mm	5.2168	07 07 2004
8	# 8	2 586	W 5 K	±5 mm	5.0446	07 07 2004
9	# 9	2 584	W 5 K	±5 mm	4.0809	07 07 2004
10	force N	712	E 100	1000 kN	957.8	08 07 2004
10	force N	712	E 100	1000 kN	903.9	23 07 2004
11	force S	709	E 100	1000 kN	861.6	08 07 2004
11	force S	709	E 100	1000 kN	920.9	23 07 2004
12	# 12	8 970	W 10 K	±10 mm	10.42	08 07 2004

A.1 Diagrams of exp. *C1-1*

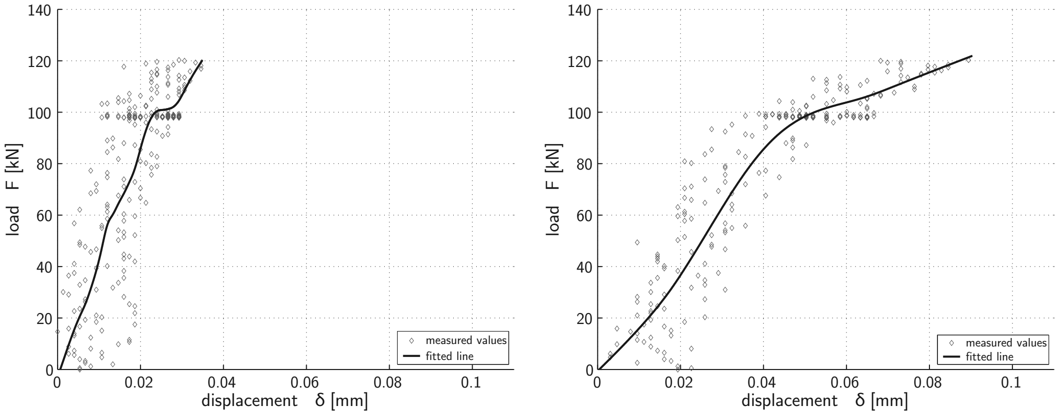

(a) Transducer # 11 (b) Transducer # 12

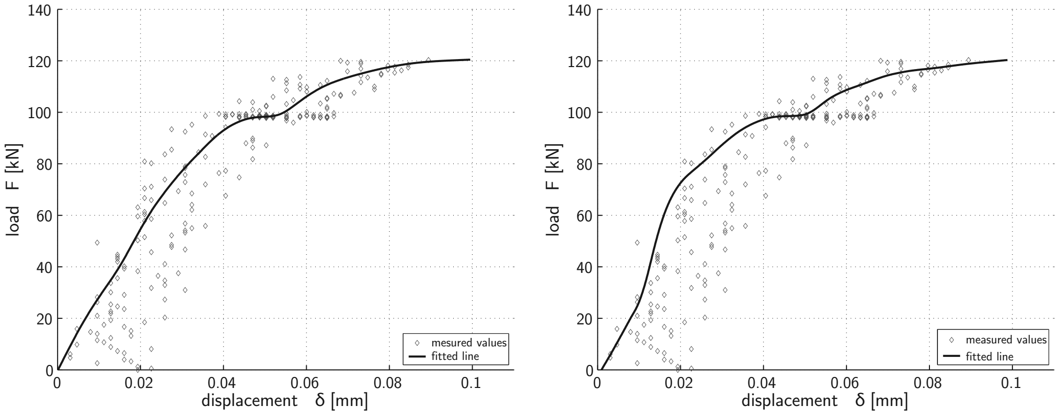

(c) Transducer # 13 (d) Transducer # 14

Figure A.3: Load-displacement curves on outer side of adhesive connection *(C1-1)*

A.2 Diagrams of exp. *C1-2*

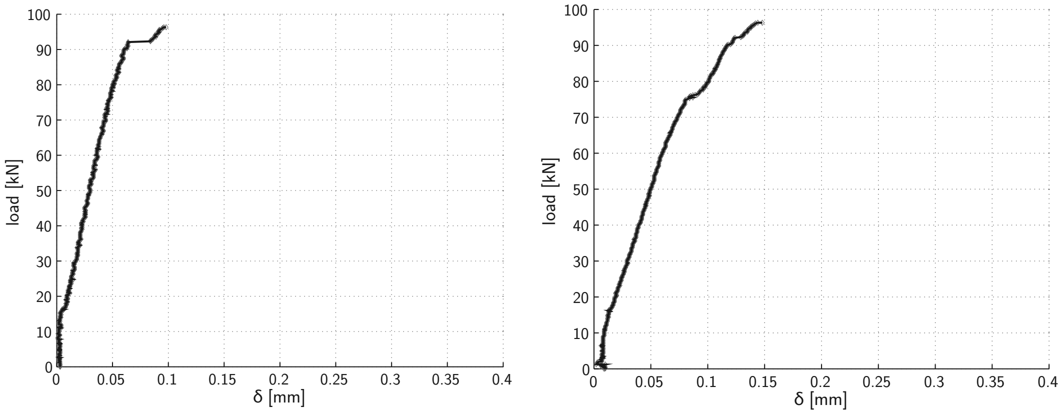

(a) Transducer # 5 (b) Transducer # 6

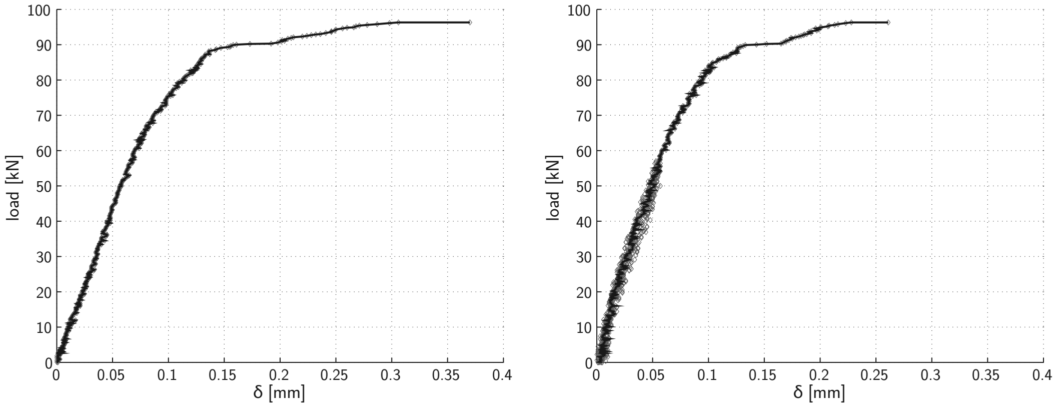

(c) Transducer # 7 (d) Transducer # 8

Figure A.4: Load-displacement curves on inner side of adhesive connection *(C1-2)*

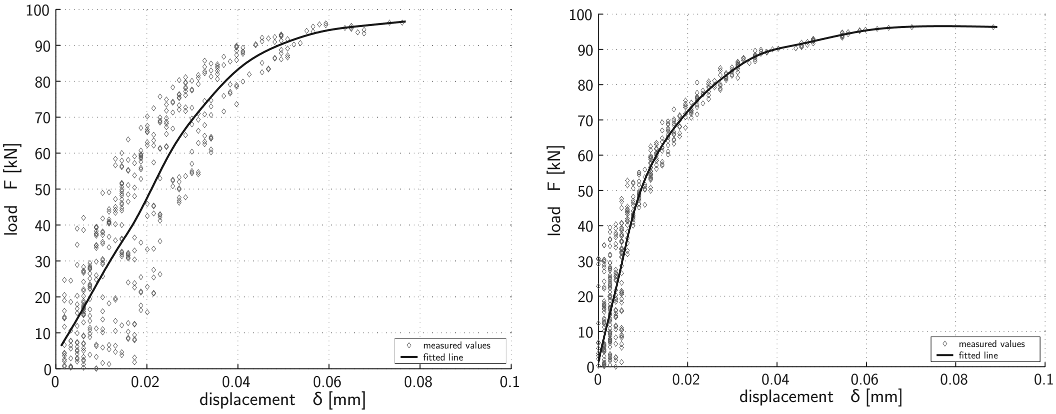

(a) Transducer # 12

(b) Transducer # 13

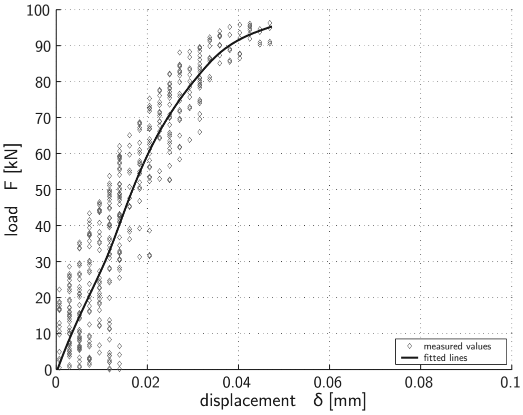

(c) Transducer # 14

Figure A.5: Load-displacement curves on outer side of adhesive connection *(C1-2)*

A.3 Diagrams and photos of exp. *C2-1*

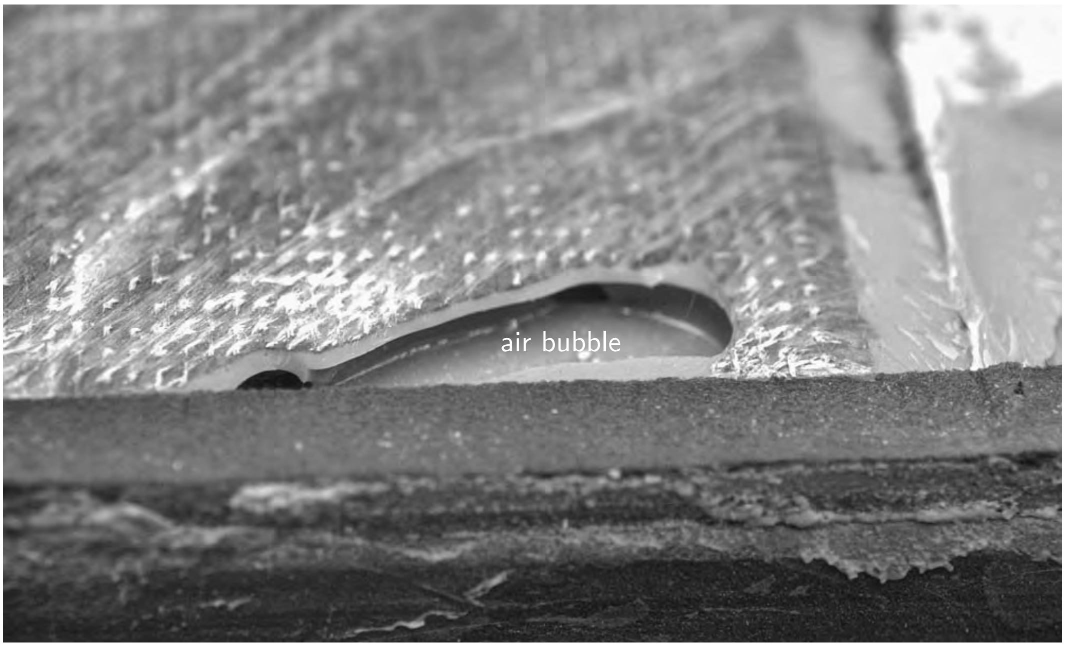

Figure A.6: Air bubble near edge of failed adhesive connection on steel girder (*C2-1*)

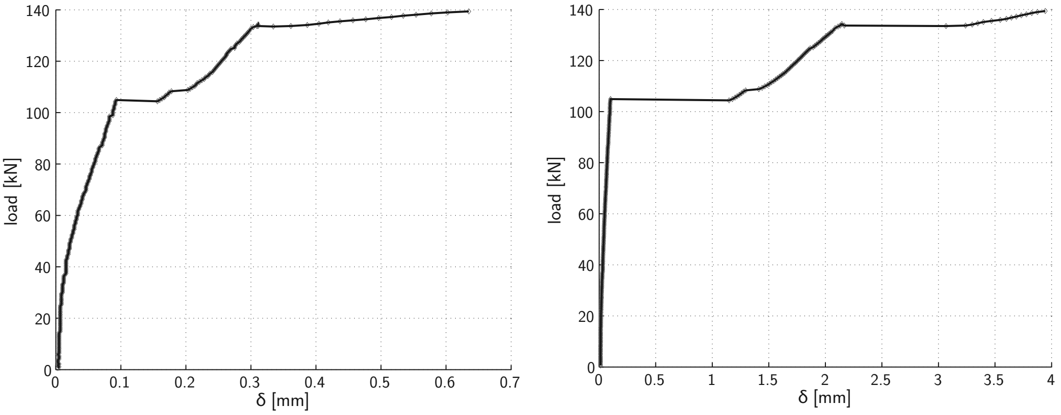

(a) Transducer # 6 (b) Transducer # 7

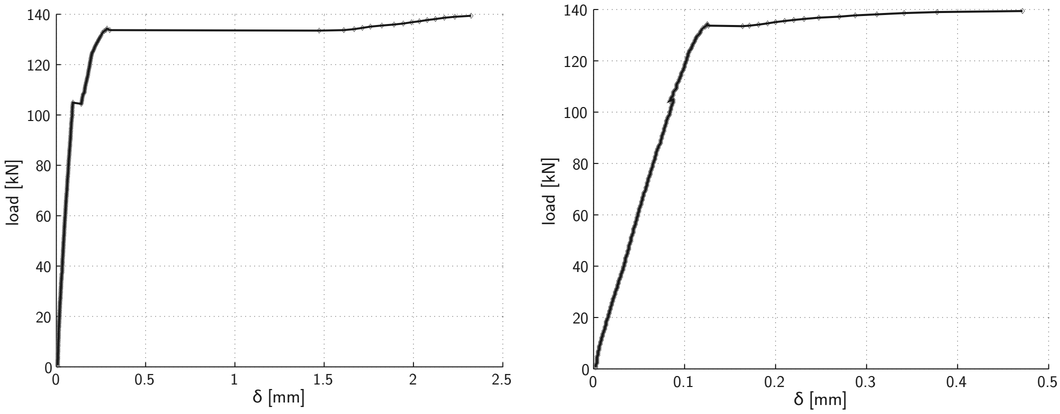

(c) Transducer # 8 (d) Transducer # 9

Figure A.7: Load-displacement curves on inner side of adhesive connection *(C2-1)*

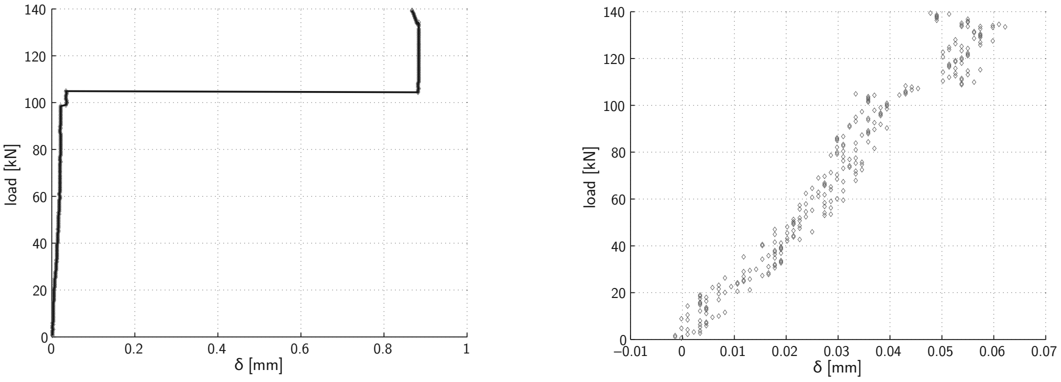

(a) Transducer # 10 (b) Transducer # 11

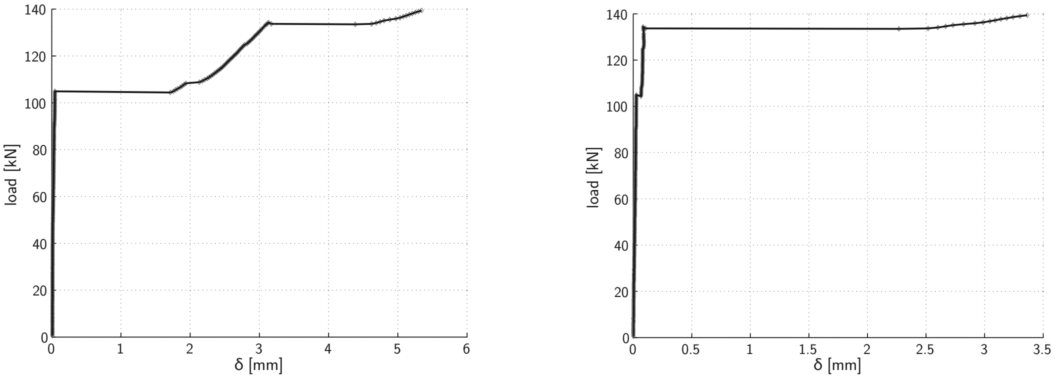

(c) Transducer # 12 (d) Transducer # 13

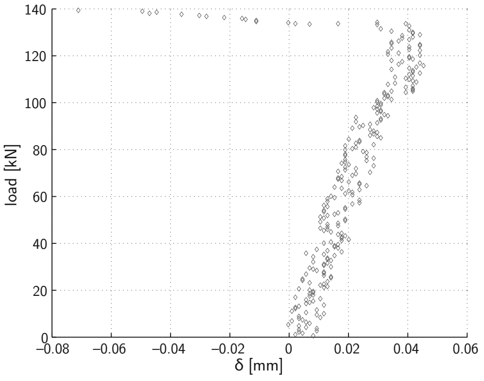

(e) Transducer # 14

Figure A.8: Load-displacement curves on outer side of adhesive connection *(C2-1)*

A.4 Diagrams and photos of exp. *C2-2*

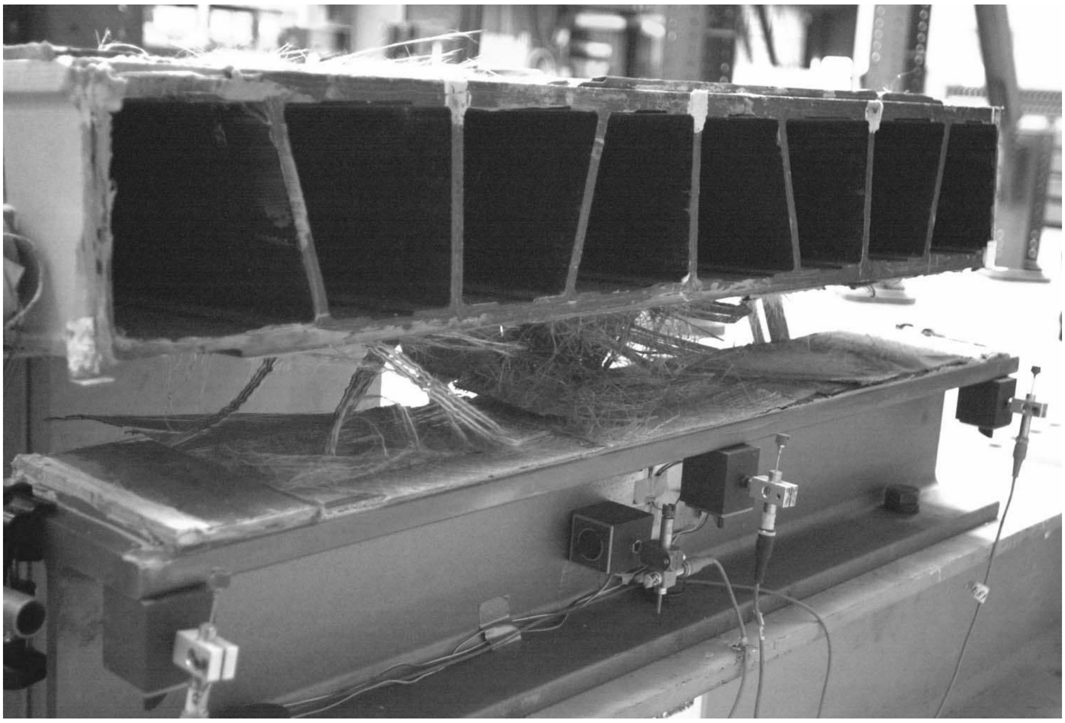

Figure A.9: Failed adhesively-bonded connection (*C2-2*)

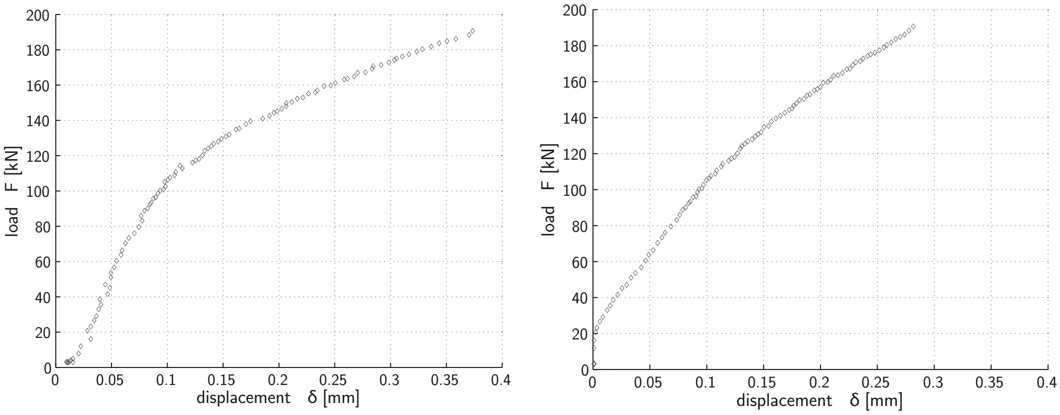

(a) Transducer # 5 (b) Transducer # 7

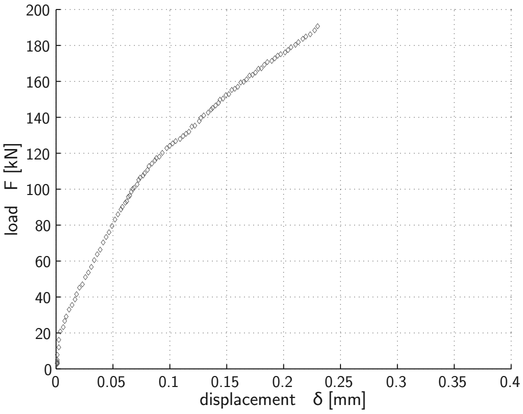

(c) Transducer # 9

Figure A.10: Load-displacement curves on inner side of adhesive connection *(C2-2)*

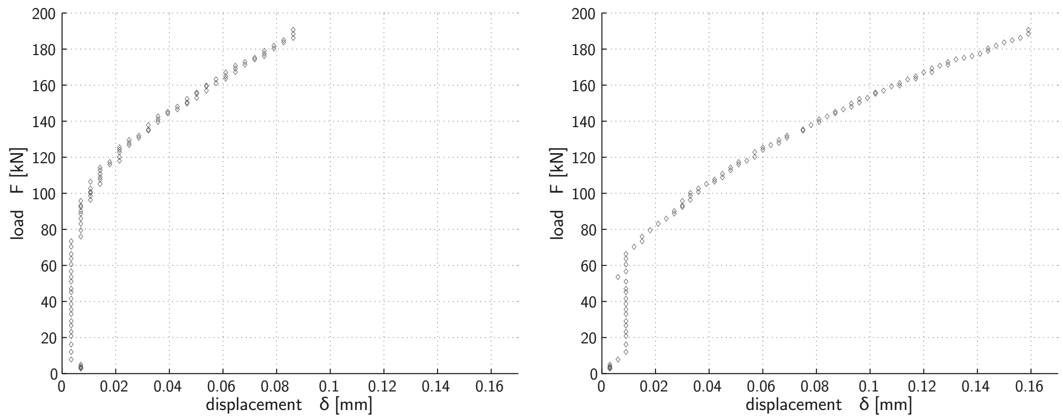

(a) Transducer # 12 (b) Transducer # 14

Figure A.11: Load-displacement curves on outer side of adhesive connection *(C2-2)*

A.5 Diagrams and photos of exp. *C3-1*

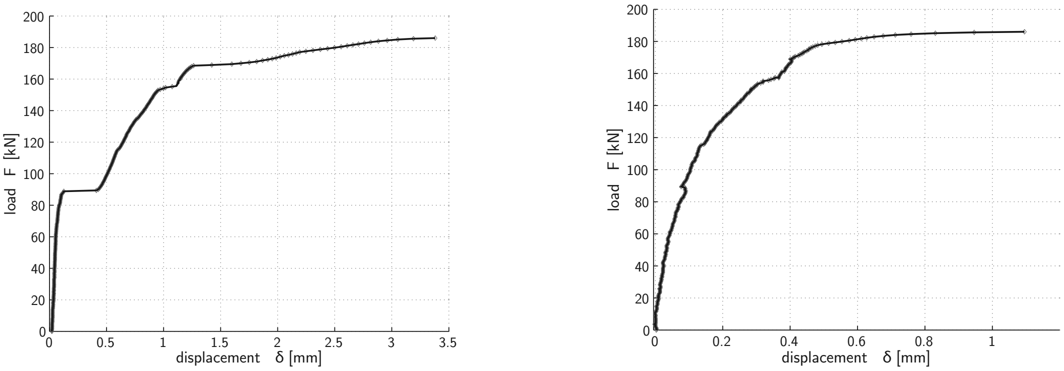

(a) Transducer # 5 (b) Transducer # 6

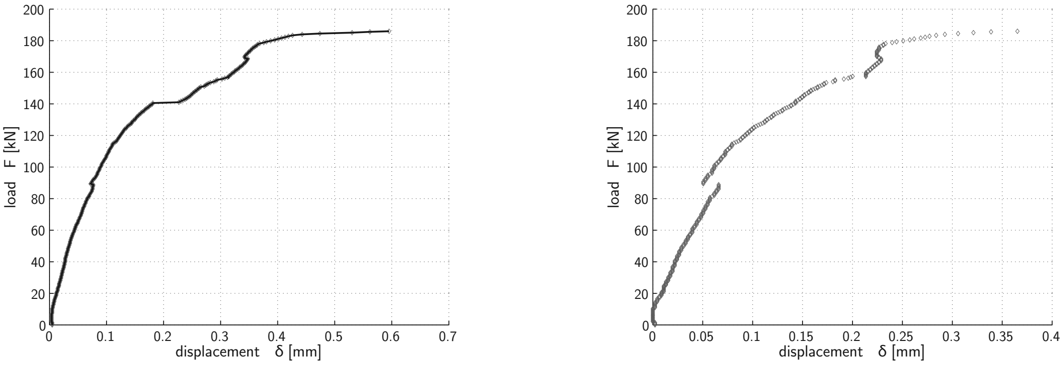

(c) Transducer # 7 (d) Transducer # 8

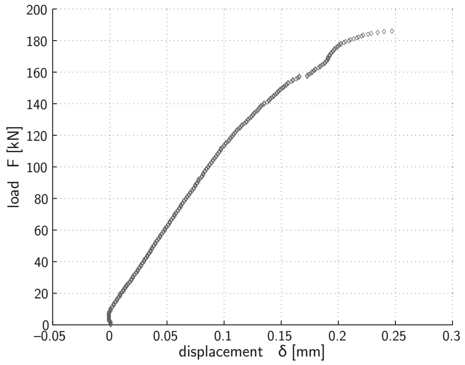

(e) Transducer # 9

Figure A.12: Load-displacement curves on inner side of adhesive connection *(C3-1)*

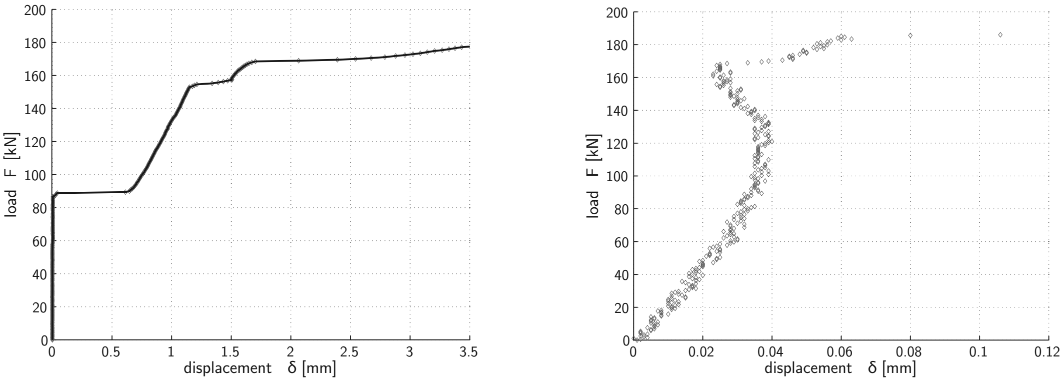

(a) Transducer # 10 (b) Transducer # 11

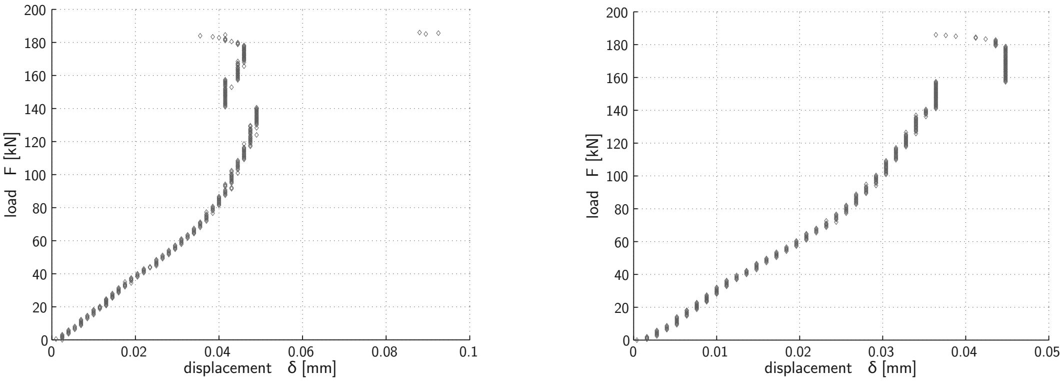

(c) Transducer # 12 (d) Transducer # 13

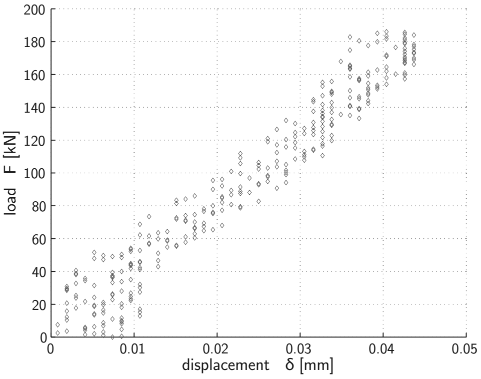

(e) Transducer # 14

Figure A.13: Load-displacement curves on outer side of adhesive connection *(C3-1)*

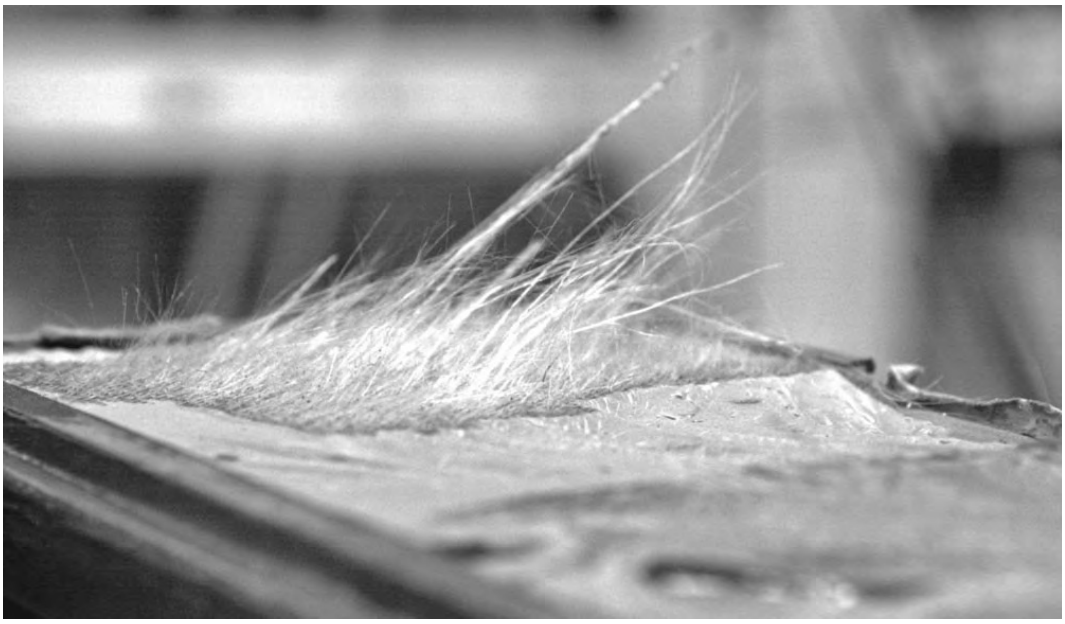

Figure A.14: Fiber-tear failure on surface and adhesive failure (*C3-1*)

A.6 Diagrams and photos of exp. *C3-2*

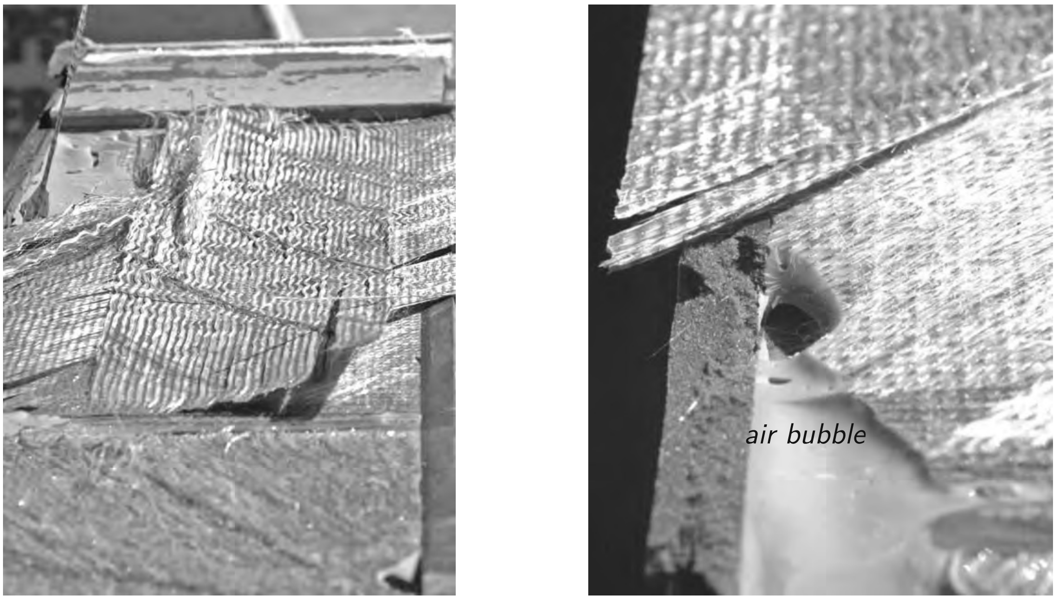

(a) Fiber mats pulled out of bridge deck surface

(b) Air bubble near to the edge

Figure A.15: Surface of failed adhesive layer *(C3-2)*

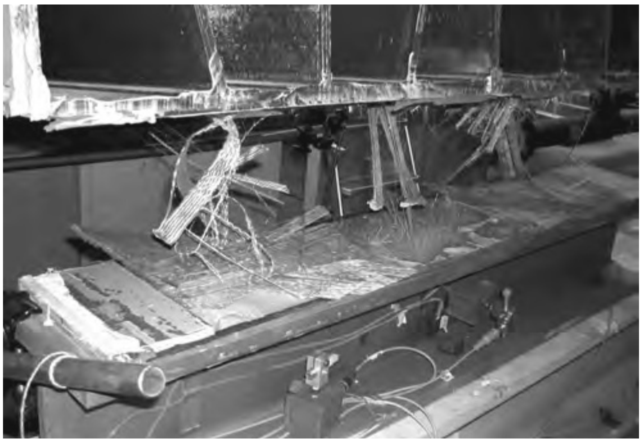

Figure A.16: Failed adhesively-bonded connection (*C3-2*)

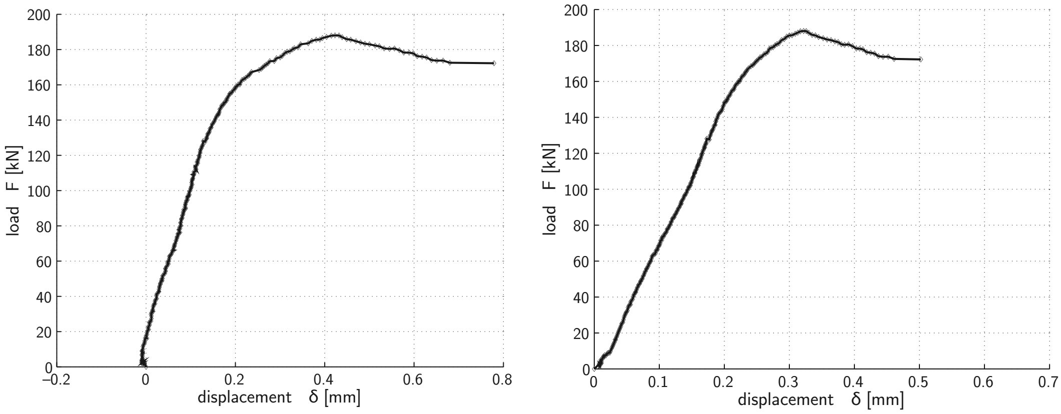

(a) Transducer # 5

(b) Transducer # 7

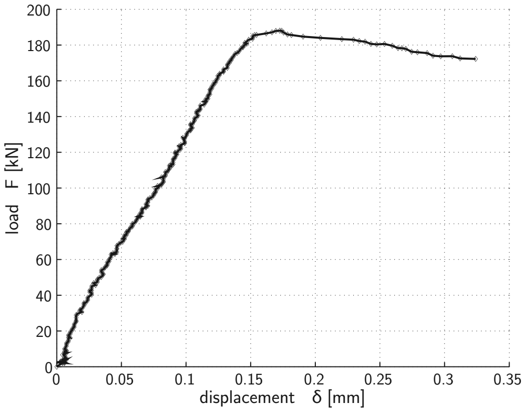

(c) Transducer # 9

Figure A.17: Load-displacement curves on inner side of adhesive connection *(C3-2)*

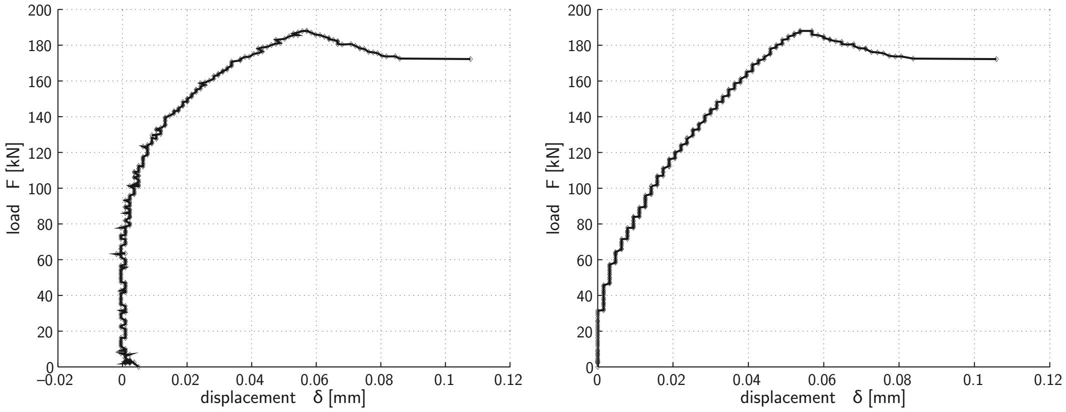

(a) Transducer # 10 (b) Transducer # 12

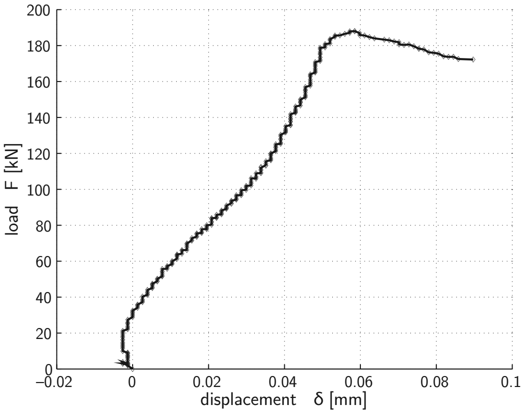

(c) Transducer # 14

Figure A.18: Load-displacement curves on outer side of adhesive connection *(C3-2)*

A.7 Comparison of experimental results and calculations

Table A.4: Comparison of measured and calculated deflections at loading point for a loading of 80 kN

	transducer # 1	transducer # 2	average value
C1-1	32.53 mm	30.20 mm	31.37 mm
C1-2	32.09 mm	31.69 mm	31.89 mm
C2-1	28.76 mm	26.40 mm	27.58 mm
C2-2	29.64 mm	31.08 mm	30.72 mm
C3-1	30.66 mm	26.09 mm	28.38 mm
C3-2	31.72 mm	31.97 mm	31.85 mm
mean value			30.30 mm
std. dev.			1.86 mm
FEA			32.33 mm

Table A.5: Comparison of measured and calculated deflections at transducers # 3 and # 4 for a loading of 80 kN

	transducer # 3	transducer # 4	average value
C1-1	-1.86 mm	-2.83 mm	-2.35 mm
C1-2	-1.70 mm	-2.59 mm	-2.15 mm
C2-1	-1.71 mm	-1.82 mm	-1.77 mm
C2-2	—	—	—
C3-1	-1.65 mm	-1.73 mm	-1.69 mm
C3-2	-1.05 mm	-1.63 mm	-1.34 mm
mean value			-1.86 mm
std. dev.			0.40 mm
FEA			-2.02 mm

Table A.6: Comparison of measured and calculated deflections at transducer # 5 to # 9 for a loading of 80 kN

(a) # 5 and # 9

	transducer # 5	transducer # 9
C1-2	—	—
C1-2	0.050 mm	—
C2-1	—	0.065 mm
C2-2	0.075 mm	0.049 mm
C3-1	0.084 mm	0.066 mm
C3-2	0.078 mm	0.059 mm
mean value	0.072 mm	0.060 mm
std. dev.	0.015 mm	0.008 mm
FEA	0.053 mm	

(b) # 6 and # 8

	transducer # 6	transducer # 8
C1-1	—	—
C1-2	0.101 mm	0.094 mm
C2-1	0.059 mm	0.068 mm
C2-2	—	—
C3-1	0.073 mm	0.057 mm
C3-2	—	—
mean value	0.078 mm	0.073 mm
std. dev.	0.021 mm	0.019 mm
FEA	0.062 mm	

(c) # 7

	transducer # 7
C1-1	—
C1-2	0.115 mm
C2-1	0.071 mm
C2-2	0.069 mm
C3-1	0.066 mm
C3-2	0.116 mm
mean value	0.087 mm
std. dev.	0.026 mm
FEA	0.066 mm

Table A.7: Comparison of measured and calculated deflections at transducers # 10 to # 14 for a loading of 80 kN

(a) # 10 and # 14

	transducer # 10	transducer # 14
C1-1	—	0.026 mm
C1-2	—	0.029 mm
C2-1	0.012 mm	0.019 mm
C2-2	—	0.018 mm
C3-1	0.002 mm	0.023 mm
C3-2	0.002 mm	0.020 mm
mean value	0.009 mm	0.023 mm
std. dev.	0.011 mm	0.004 mm
FEA	0.019 mm	

(b) # 11 and # 13

	transducer # 11	transducer # 13
C1-1	0.020 mm	0.034 mm
C1-2	—	0.026 mm
C2-1	0.025 mm	0.022 mm
C2-2	—	—
C3-1	0.032 mm	0.026 mm
C3-2	—	—
mean value	0.031 mm	0.027 mm
std. dev.	0.001 mm	0.005 mm
FEA	0.023 mm	

(c) # 12

	transducer # 12
C1-1	0.036 mm
C1-2	0.038 mm
C2-1	0.033 mm
C2-2	0.007 mm
C3-1	0.039 mm
C3-2	0.010 mm
mean value	0.032 mm
std. dev.	0.013 mm
FEA	0.024 mm

B Steel girder geometries with respective torsional stiffnesses k_ϑ

Table B.1: Torsional stiffnesses for a girder ($\ell = 10\,\mathrm{m}$) and various dimensions

h [mm]	b_f [mm]	t_f [mm]	t_w [mm]	A_{st} [cm^2]	k_ϑ [kNm]
550	370	40	6	324	66.39
600	340	36	6	276	58.92
650	300	33	6	233	52.02
700	280	30	6	206	65.22
750	250	28	7	189	56.61
800	250	25	7	178	63.78
850	230	24	8	175	56.76
900	210	24	8	169	52.50

Table B.2: Torsional stiffnesses for a girder ($\ell = 15\,\mathrm{m}$) and various dimensions

h [mm]	b_f [mm]	t_f [mm]	t_w [mm]	A_{st} [cm^2]	k_ϑ [kNm]
850	400	40	8	382	124.03
900	370	38	8	347	112.21
950	350	35	9	324	97.27
1000	310	35	9	301	85.56
1050	270	34	10	282	115.35
1100	240	34	10	266	103.22
1150	220	32	11	260	98.78
1200	200	32	11	253	90.09

Table B.3: Torsional stiffnesses for a girder ($\ell = 20\,\text{m}$) and various dimensions

h [mm]	b_f [mm]	t_f [mm]	t_w [mm]	A_{st} [cm^2]	k_ϑ [kNm]
1150	450	40	10	467	183.42
1200	400	40	11	443	196.56
1250	400	40	11	443	194.17
1300	350	37	12	406	177.54
1350	350	32	12	378	146.53
1400	350	30	13	384	142.77
1450	300	29	13	354	120.97
1500	270	29	14	358	117.20

Table B.4: Torsional stiffnesses for a girder ($\ell = 25\,\text{m}$) and various dimensions

h [mm]	b_f [mm]	t_f [mm]	t_w [mm]	A_{st} [cm^2]	k_ϑ [kNm]
1400	420	50	13	589	311.66
1500	390	45	13	534	250.99
1600	350	42	14	506	222.73
1700	300	40	15	483	163.64
1800	290	32	16	463	144.01
1900	250	29	17	458	117.04
2000	200	27	18	458	94.79
2100	160	23	19	464	78.05

Table B.5: Torsional stiffnesses for a girder ($\ell = 30\,\text{m}$) and various dimensions

h [mm]	b_f [mm]	t_f [mm]	t_w [mm]	A_{st} [cm^2]	k_ϑ [kNm]
1700	440	50	15	680	349.46
1800	390	48	16	647	311.68
1900	350	45	17	622	268.64
2000	320	40	18	602	191.76
2100	300	34	19	590	173.08
2200	270	30	20	590	144.64
2300	240	25	21	592	120.00
2400	230	23	22	596	121.89

C Stress analysis parameter study diagrams

C.1 Dependence of factor n_x on ratio $\frac{t_{sw}}{t_p}$

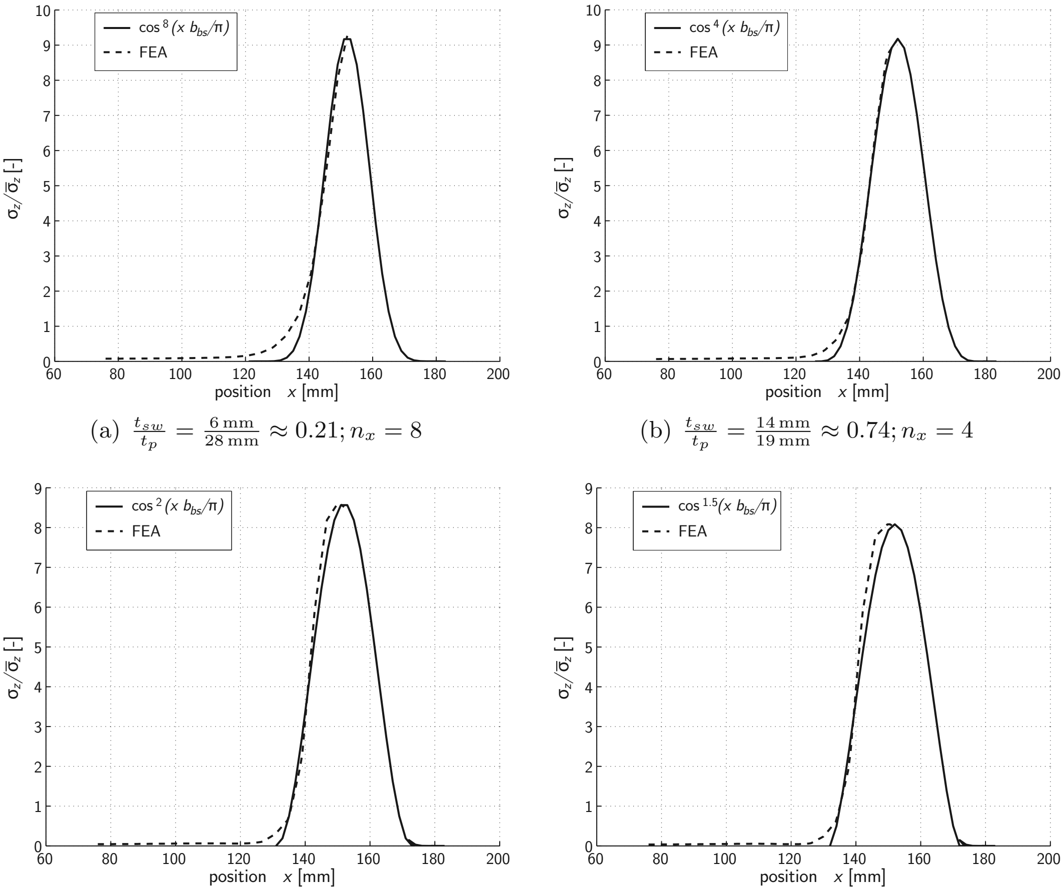

(a) $\frac{t_{sw}}{t_p} = \frac{6\,\mathrm{mm}}{28\,\mathrm{mm}} \approx 0.21; n_x = 8$

(b) $\frac{t_{sw}}{t_p} = \frac{14\,\mathrm{mm}}{19\,\mathrm{mm}} \approx 0.74; n_x = 4$

(c) $\frac{t_{sw}}{t_p} = \frac{18\,\mathrm{mm}}{12\,\mathrm{mm}} = 1.5; n_x = 2$

(d) $\frac{t_{sw}}{t_p} = \frac{20\,\mathrm{mm}}{10\,\mathrm{mm}} = 2; n_x = 1.5$

Figure C.1: Comparison of FE results (*VS*-geometry) and analytical stress distribution in FRP-adhesive interface

C.2 Comparison of analytical and numerical results

The key for the denomination of the geometry is the following: $VS^{t_w/r}_{b_f/t_f}$.

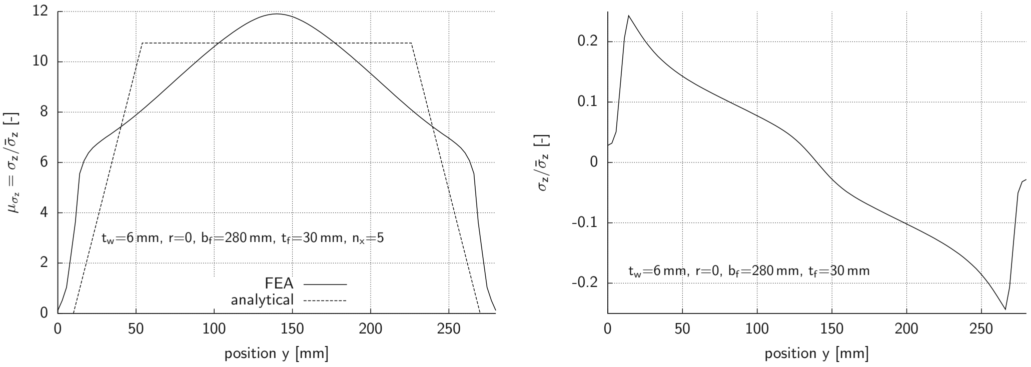

(a) (b)

Figure C.2: Stress distribution shapes in adhesive layer of geometry $VS^{06/0}_{280/30}$

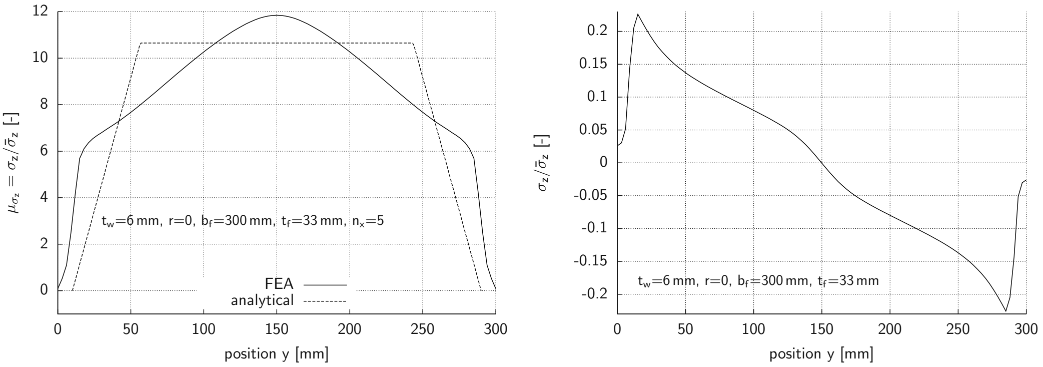

(a) (b)

Figure C.3: Stress distribution shapes in adhesive layer of geometry $VS^{06/0}_{300/33}$

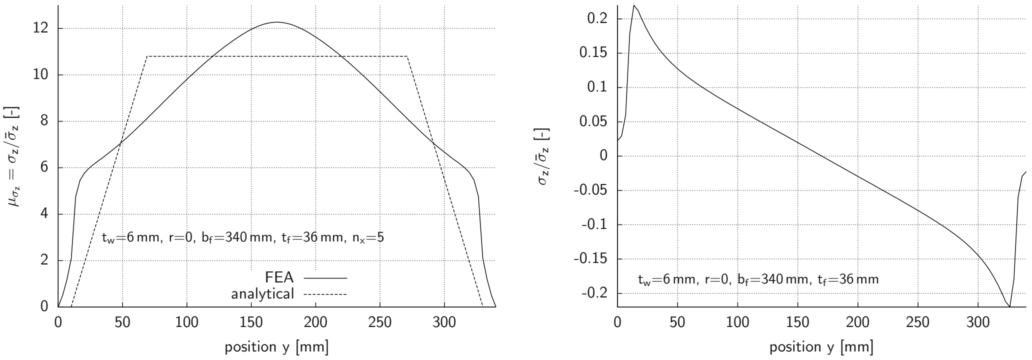

(a) (b)

Figure C.4: Stress distribution shapes in adhesive layer of geometry $VS^{06/0}_{340/36}$

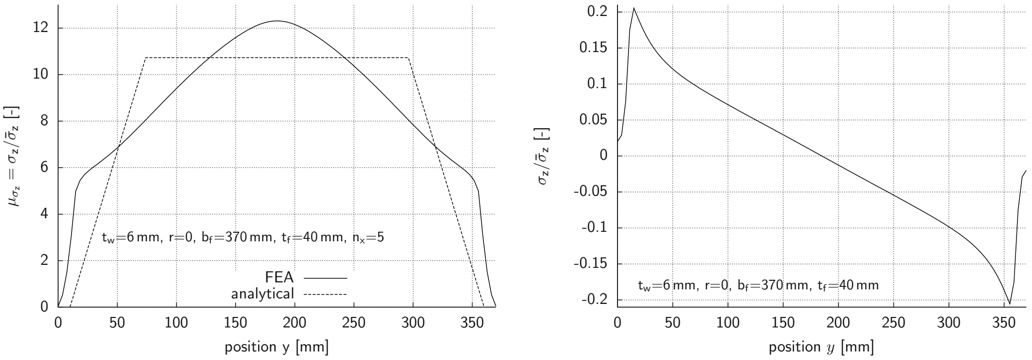

(a) (b)

Figure C.5: Stress distribution shapes in adhesive layer of geometry $VS^{06/0}_{370/40}$

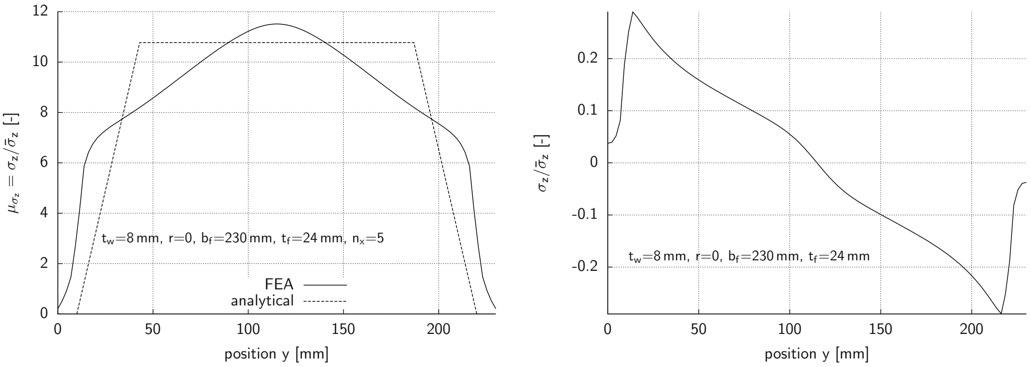

(a) (b)

Figure C.6: Stress distribution shapes in adhesive layer of geometry $VS^{08/0}_{230/24}$

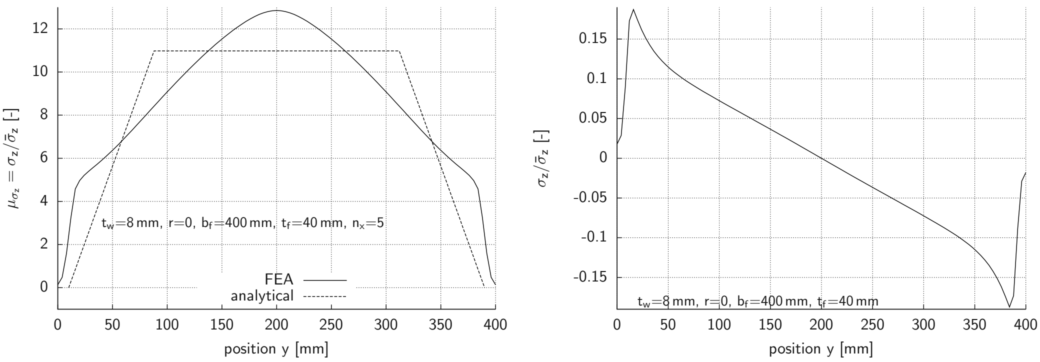

(a) (b)

Figure C.7: Stress distribution shapes in adhesive layer of geometry $VS^{08/0}_{400/40}$

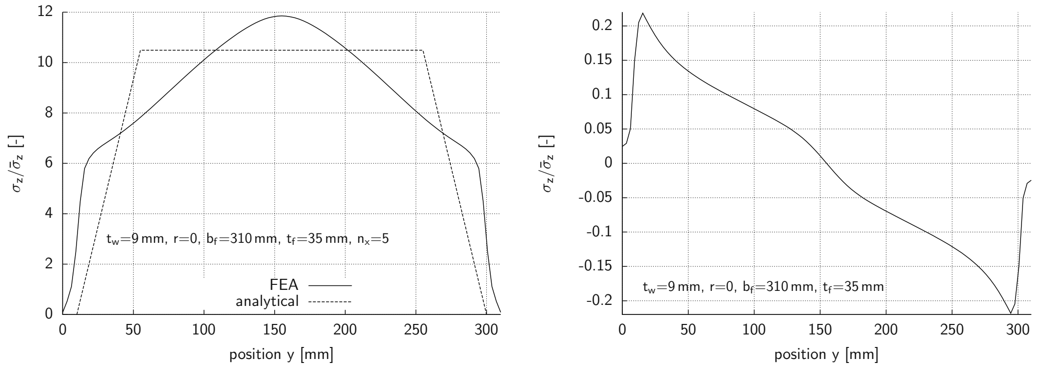

(a) (b)

Figure C.8: Stress distribution shapes in adhesive layer of geometry $VS^{09/0}_{310/35}$

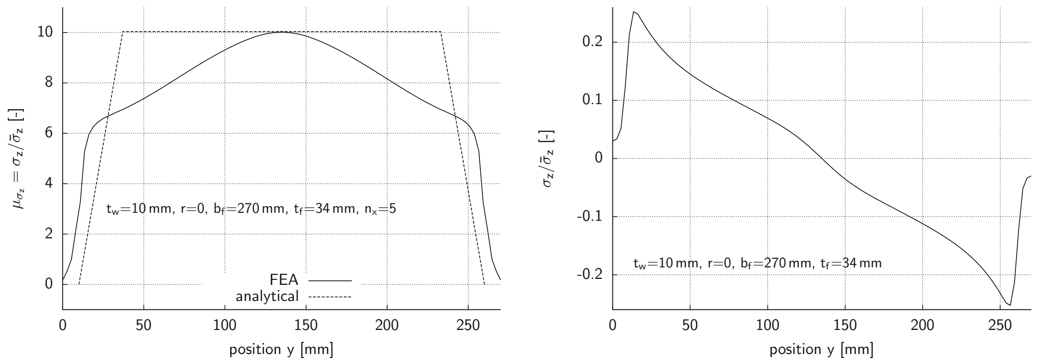

(a) (b)

Figure C.9: Stress distribution shapes in adhesive layer of geometry $VS^{10/0}_{270/34}$

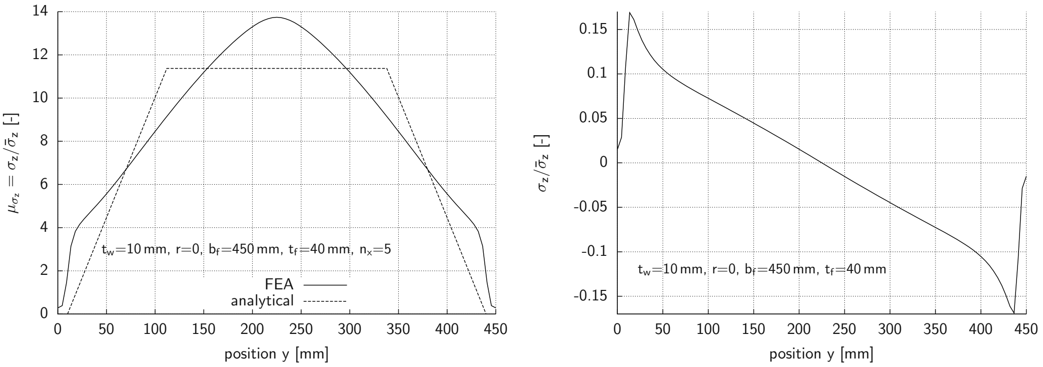

(a) (b)

Figure C.10: Stress distribution shapes in adhesive layer of geometry $VS^{10/0}_{450/40}$

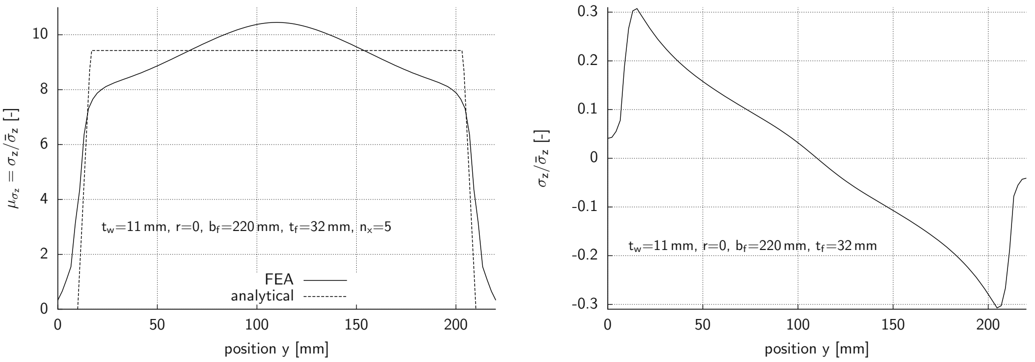

(a) (b)

Figure C.11: Stress distribution shapes in adhesive layer of geometry $VS^{11/0}_{220/32}$

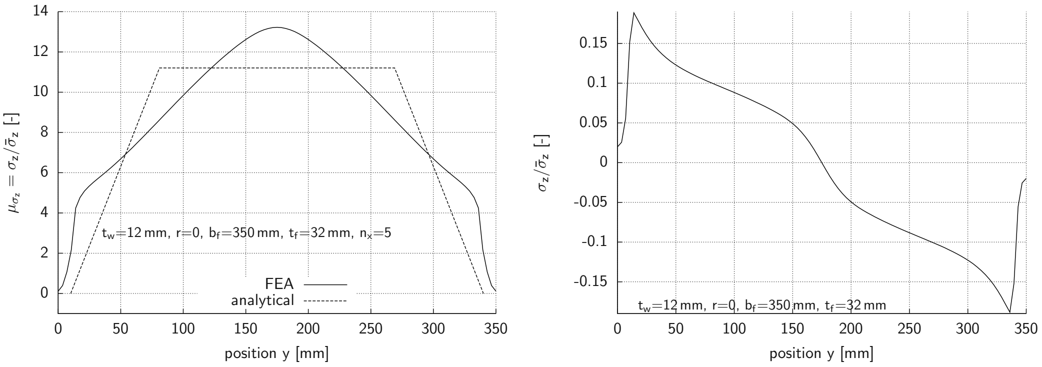

(a) (b)

Figure C.12: Stress distribution shapes in adhesive layer of geometry $VS^{12/0}_{350/32}$

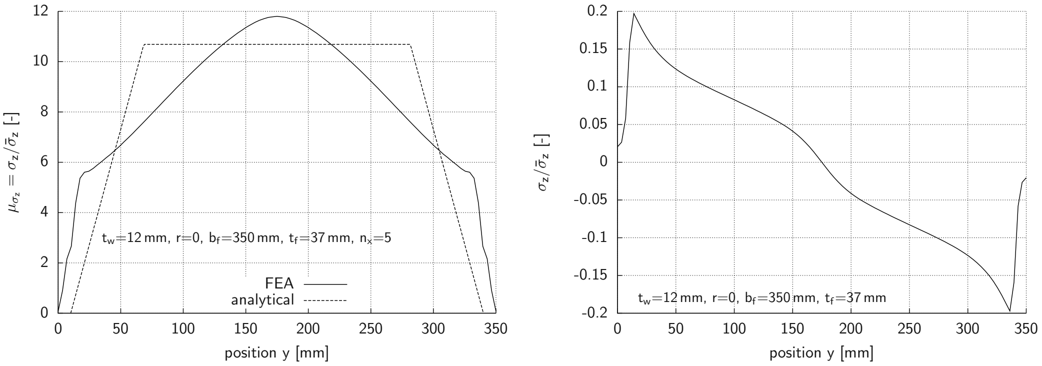

(a) (b)

Figure C.13: Stress distribution shapes in adhesive layer of geometry $VS^{12/0}_{350/37}$

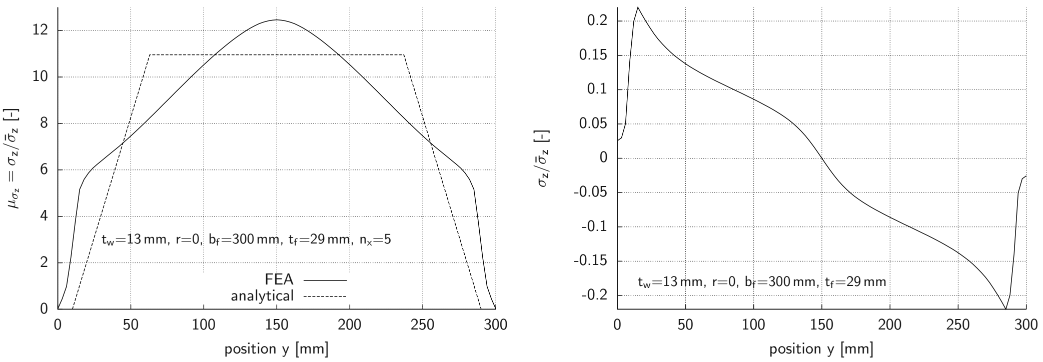

(a) (b)

Figure C.14: Stress distribution shapes in adhesive layer of geometry $VS^{13/0}_{300/29}$

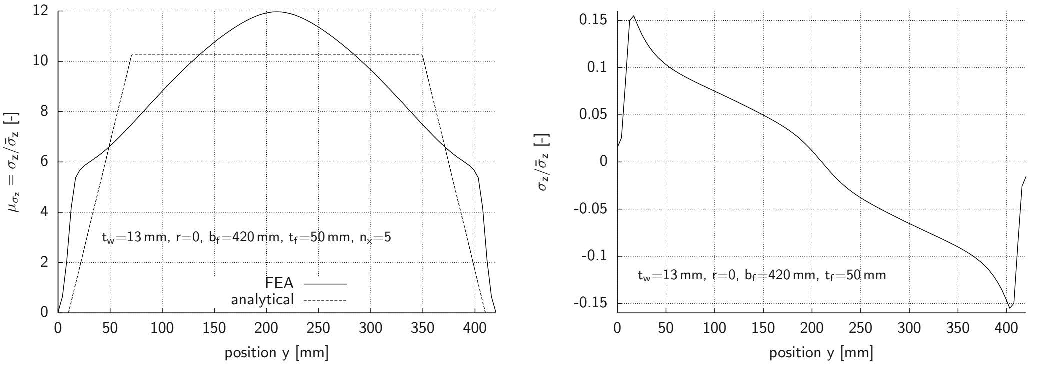

(a) (b)

Figure C.15: Stress distribution shapes in adhesive layer of geometry $VS^{13/0}_{420/50}$

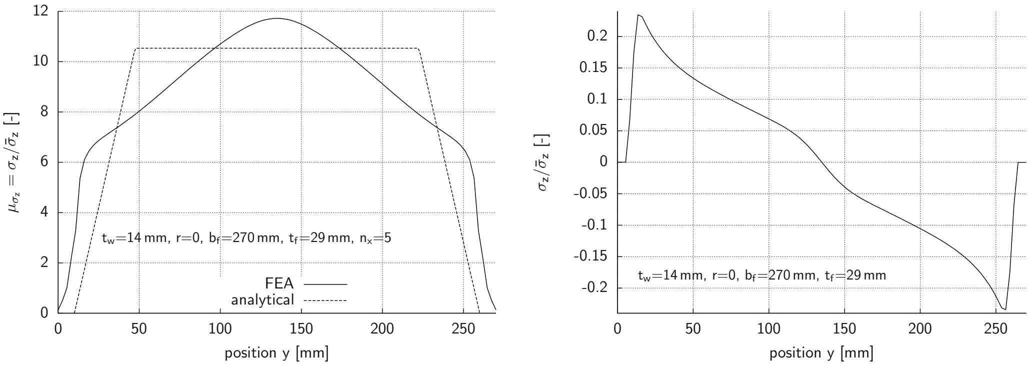

(a) (b)

Figure C.16: Stress distribution shapes in adhesive layer of geometry $VS^{14/0}_{270/29}$

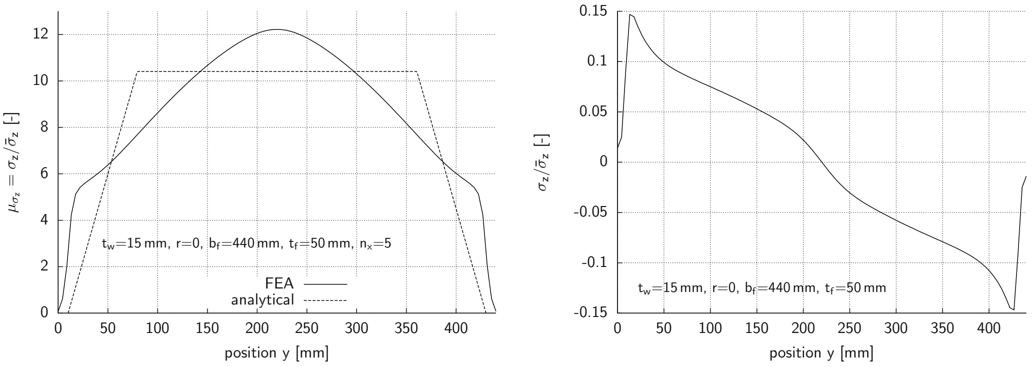

(a) (b)

Figure C.17: Stress distribution shapes in adhesive layer of geometry $VS^{15/0}_{440/50}$

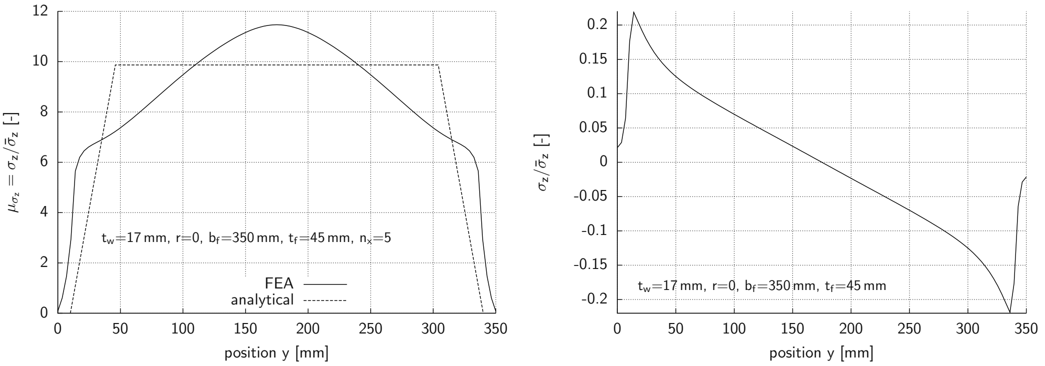

(a) (b)

Figure C.18: Stress distribution shapes in adhesive layer of geometry $VS^{17/0}_{350/45}$

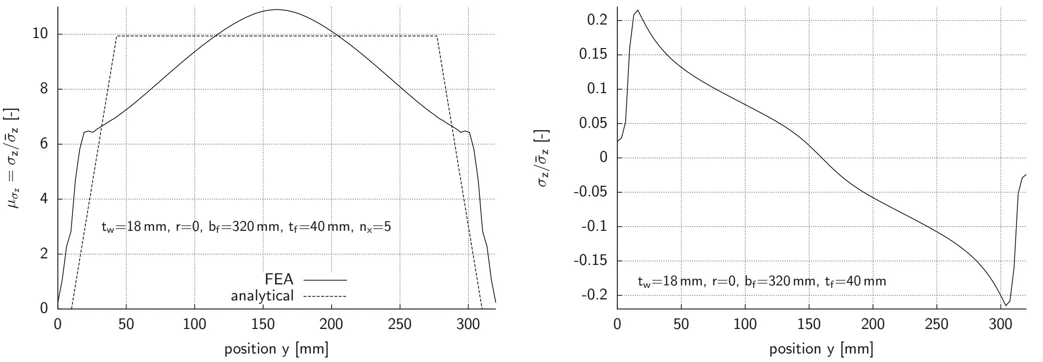

(a) (b)

Figure C.19: Stress distribution shapes in adhesive layer of geometry $VS^{18/0}_{320/40}$

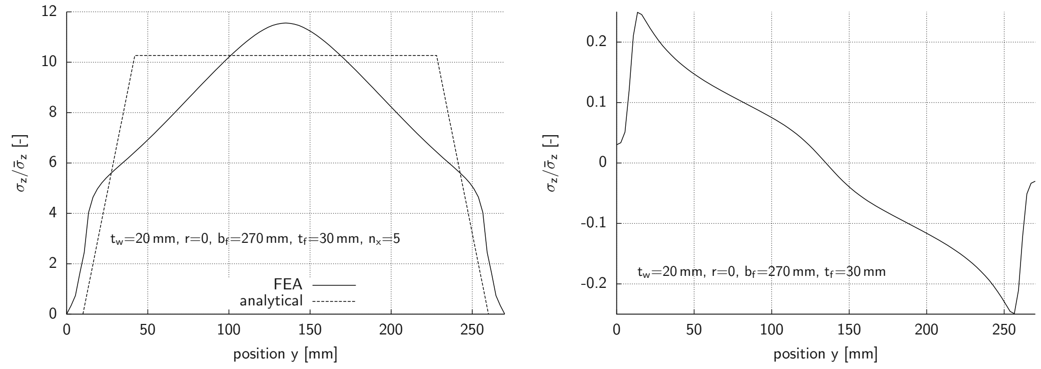

(a) (b)

Figure C.20: Stress distribution shapes in adhesive layer of geometry $VS^{20/0}_{270/30}$

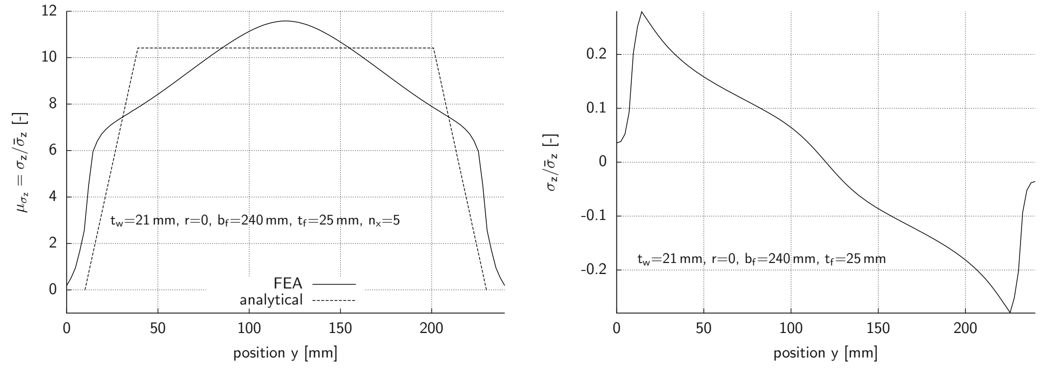

(a) (b)

Figure C.21: Stress distribution shapes in adhesive layer of geometry $VS^{21/0}_{240/25}$

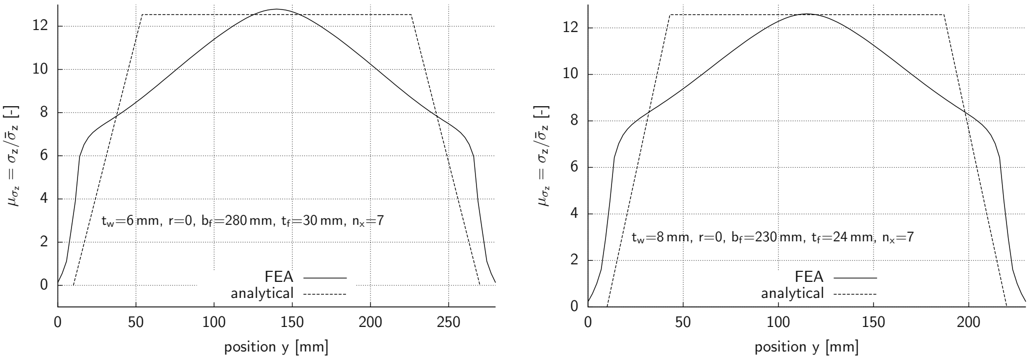

(a) $VS^{06/0}_{280/30}$ (b) $VS^{08/0}_{230/24}$

Figure C.22: Stress distribution shapes in adhesive layer

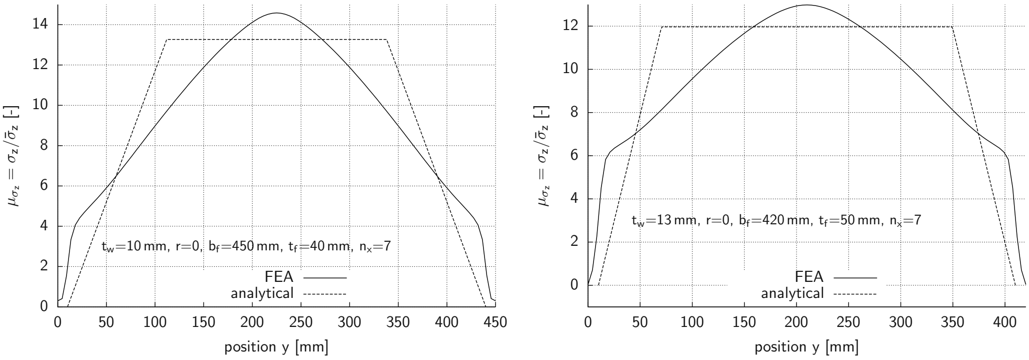

(a) $VS^{10/0}_{450/40}$ (b) $VS^{13/0}_{420/50}$

Figure C.23: Stress distribution shapes in adhesive layer

C.3 Superposed stress distributions

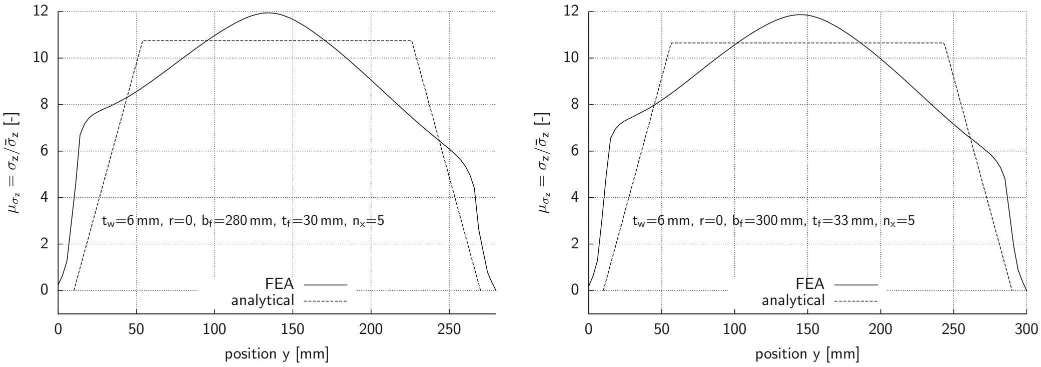

(a) Geometry $VS^{06/0}_{280/30}$ (b) Geometry $VS^{06/0}_{300/33}$

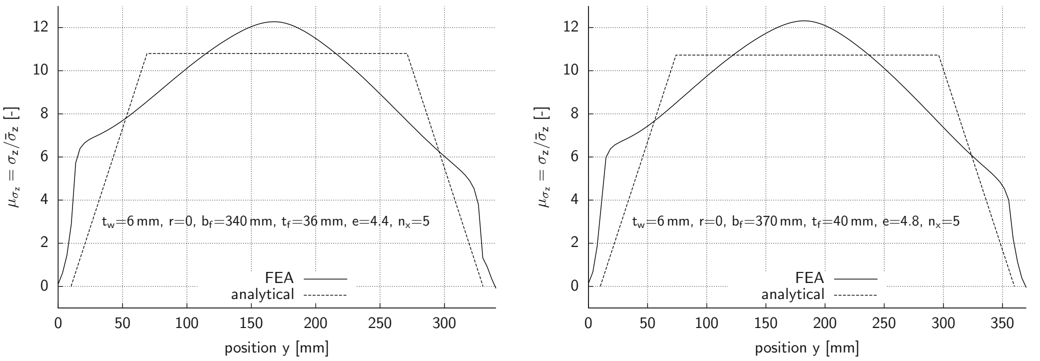

(c) Geometry $VS^{06/0}_{340/36}$ (d) Geometry $VS^{06/0}_{370/40}$

Figure C.24: Superposition of distributions due to uplift force and moment

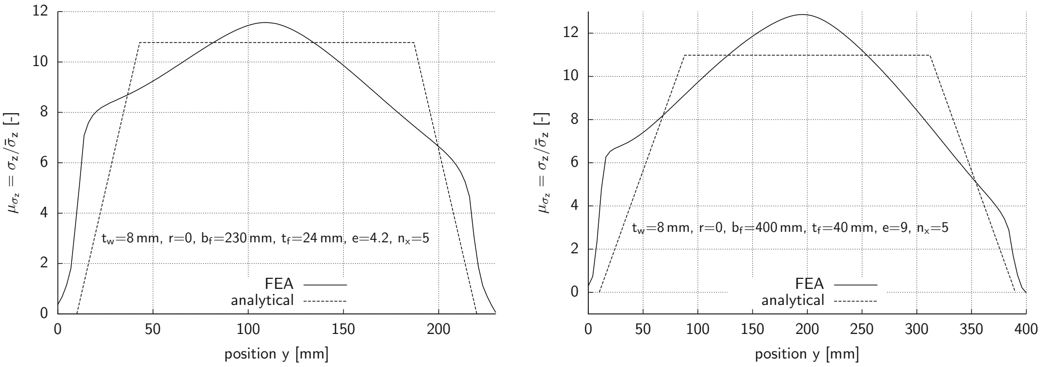

(a) Geometry $VS^{08/0}_{230/24}$ (b) Geometry $VS^{08/0}_{400/40}$

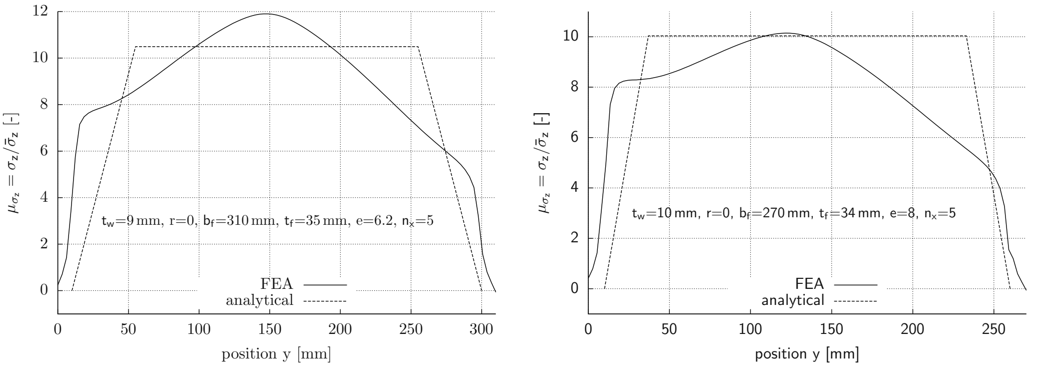

(c) Geometry $VS^{09/0}_{310/35}$ (d) Geometry $VS^{10/0}_{270/34}$

Figure C.25: Superposition of distributions due to uplift force and moment

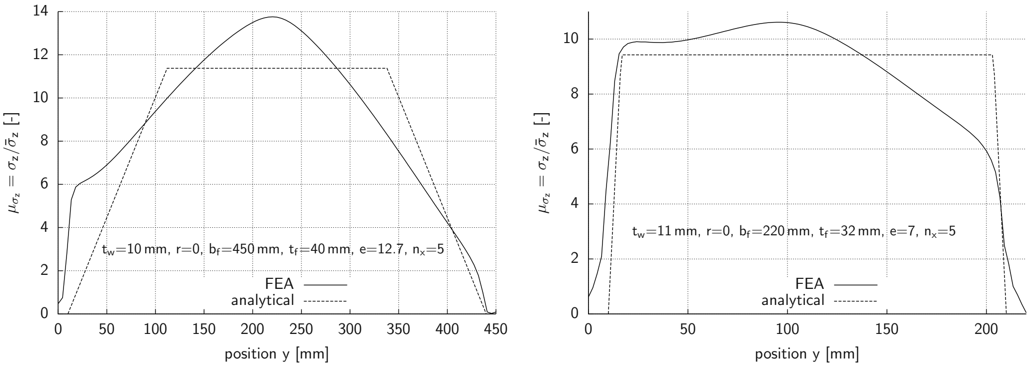

(a) Geometry $VS^{10/0}_{450/40}$ (b) Geometry $VS^{11/0}_{220/32}$

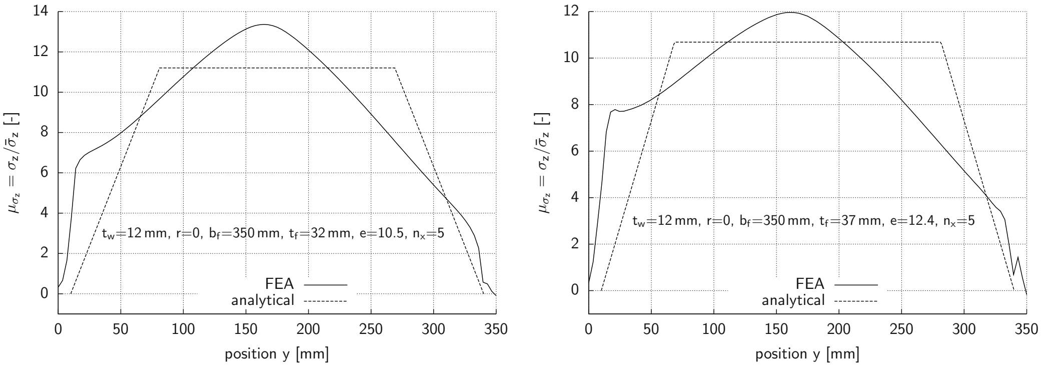

(c) Geometry $VS^{12/0}_{350/32}$ (d) Geometry $VS^{12/0}_{350/37}$

Figure C.26: Superposition of distributions due to uplift force and moment

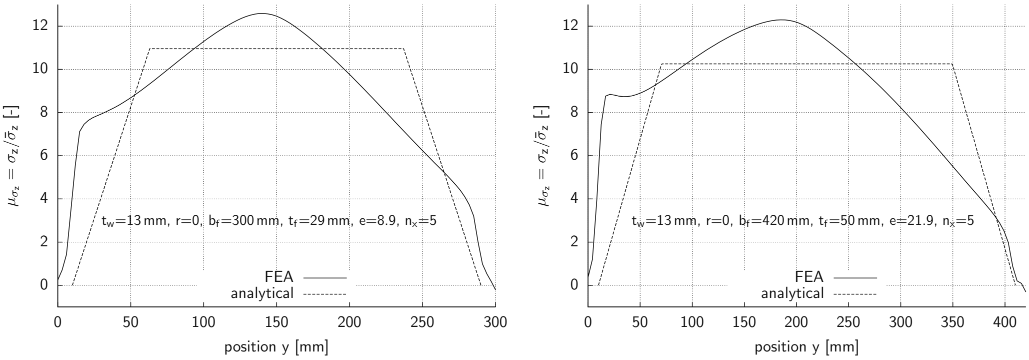

(a) Geometry $VS^{13/0}_{300/29}$ (b) Geometry $VS^{13/0}_{420/50}$

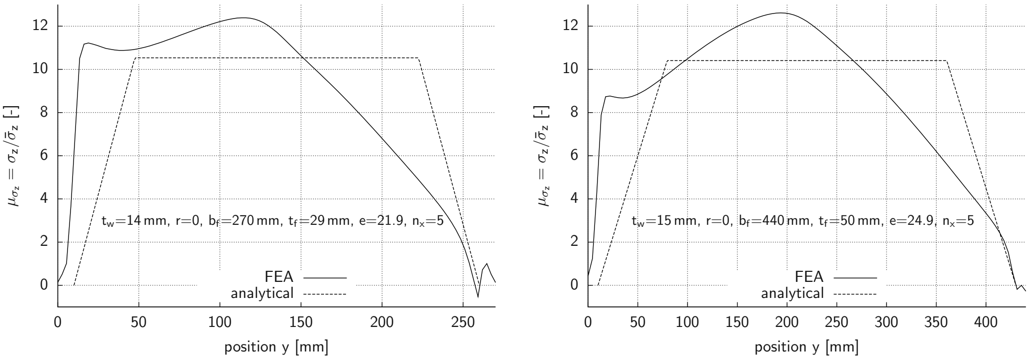

(c) Geometry $VS^{14/0}_{270/29}$ (d) Geometry $VS^{15/0}_{440/50}$

Figure C.27: Superposition of distributions due to uplift force and moment

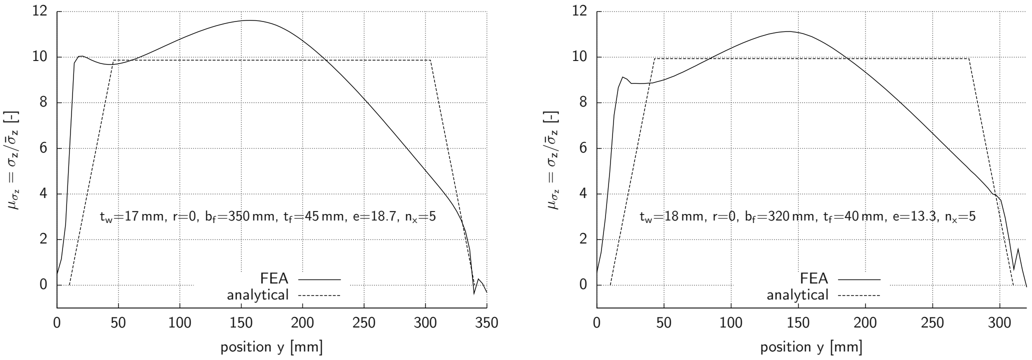

(a) Geometry $VS^{17/0}_{350/45}$ (b) Geometry $VS^{18/0}_{320/40}$

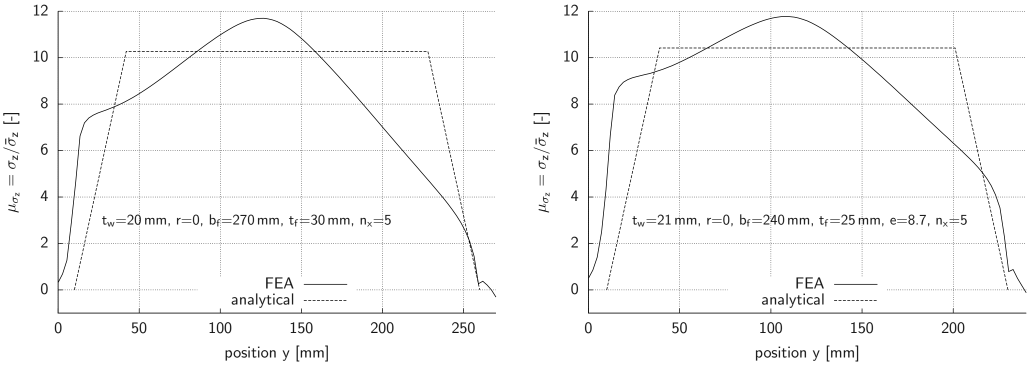

(c) Geometry $VS^{20/0}_{270/30}$ (d) Geometry $VS^{21/0}_{240/25}$

Figure C.28: Superposition of distributions due to uplift force and moment

Bibliography

[AK02] Alampalli, Sreenivas ; Kunin, Jonathan: Rehabilitation and field testing of an FRP bridge deck on a truss bridge. In: *Composite Structures* 57 (2002), p. 373–375

[Ame] American Composites Manufacturers Association. *www.mdacomposites.org*

[ast00] *Annual book of ASTM standards – 2000*. Volume 15.06. American Society for Testing and Materials, 2000

[AZ01] Acosta, Felipe J. ; Zureick, Abdul-Hamid: Determinación de las propiedades macánicas de losas para puentes de polímeros reforzados con fibras. In: *Revista Internacional de Desastres Naturales, Accidentes e Infraestructura Civil* 1 (2001), p. 3–20. – http://civil.uprm.edu/revistadesastres/Vol1Num1/Vol1Num1.htm

[Ban06] Bank, L.C.: *Composites for Construction: Structural Design with FRP Materials*. New York : John Wiley & Sons, 2006. – ISBN 0–471–68126–1

[BBB$^+$02] Bakis, C. E. ; Bank, L. C. ; Brown, V. L. ; Cosenza, E. ; Davalos, J. F. ; Lesko, J. J. ; Machida, A. ; Rizkalla, S. H. ; Triantafillou, T. C.: Fiber-Reinforced Polymer Composites for Construction—State-of-the-Art Review. In: *Journal of Composites for Construction (ASCE)* (2002), May, p. 73–87

[BKSK01] Burgueño, R. ; Karbhari, V. M. ; Seible, F. ; Kolozs, R. T.: Experimental dynamic characterization of an FRP composite bridge superstructure assembly. In: *Composite Structures* 54 (2001), p. 427–444

[Bod04] Bode, Frederik: *Tragverhalten von GFK-Brückenplatten unter Zugbelastung*. Darmstadt, T.U. Darmstadt, Diplomarbeit, February 2004

[BW94] Bruneau, M. ; Walker, D.: Cyclic Testing of Pultruded Fiber-Reinforced Plastic Beam-Column Rigid Connection. In: *Journal of Structural Engineering* 120 (1994), no. 9, p. 2637–2652

[BZL+00] Burgueño, R. ; Zhao, L. ; La Rovere, H. ; Seible, F. ; Karbhari, V. M.: Characterization of hybrid FRP beam-slab bridge systems. In: [HR00], p. 793–800. – ISBN 0–7709–0447–5

[Cla96] Clarke, John L. (editor): *Structural Design of Polymer Composite*. 1. E & FN Spon, 1996. – EUROCOMP Design and Handbook. – ISBN 0–419–19450–9

[DIN90] DIN (Deutsches Institut für Normung e. V.): *DIN 18 800 Teil 1 — Stahlbauten – Bemessung und Konstruktion*. November 1990

[DQX+01] Davalos, Julio F. ; Qiao, Pizhong ; Xu, X. F. ; Robinson, Justin ; Barth, Karl E.: Modeling and characterization of fiber-reinforced plastic honeycomb sandwich panels for highway bridge applications. In: *Composite Structures* 52 (2001), p. 441–452

[EB96] El-Badry, M.M. (editor): *Advanced Composite Materials in Bridges and Structures*. 1. Montréal, Québec : The Canadian Society for Civil Engineering, August 1996 (2nd International Conference). – ISBN 0–921303–64–5

[Eis04] Eisenbach, Philipp: The influence of torsional stiffnesses of different steel girder geometries on global bearing behaviour of bridges built with GFRP bridge decks / TU Darmstadt/EPF Lausanne. Lausanne, 2004. – technical report

[Eur02] European Commitee for Standarization: *EN 1990 – Eurocode: Basis of structural design, European Standard*. 2002

[Fie01] Fiedler, E.: Die Entwicklung des Stahlbrückenbaus in der DDR bis zum Zeitpunkt der Wende — Ein Rückblick (Teil II). In: *Der Stahlbau* 70 (2001), no. 5, p. 317–328

[FJF01] Figueiras, J. ; Juvandes, L. ; Faria, R.: *Composites in Constructions – Proceedings of the international conference CCC2001 in Porto, Portugal*. Lisse, NL : A. A. Balkema Publishers, 2001. – ISBN 90 2651 858 7

[Fri83] Friemann, Harald: *Schub und Torsion in geraden Stäben*. 1st edition. Darmstadt : Werner-Verlag GmbH, 1983. – ISBN 3–8041–1546–2

[GRG04] Gama, Bazle A. ; Rahman, Mostafezur ; Gillespie Jr., John W.: Mechanical characterization of *Duraspan 766 & 500* bridge decks / Center for Composite Materials, University of Delaware. Newark, DE 19 716, USA, 2004. – technical report

[Gür04] GÜRTLER, Herbert: *Composite Action of FRP Bridge Decks Adhesively bonded to Steel Main Girders.* Lausanne, École Polytechnique Fédérale de Lausanne, Diss., 2004. – Thèse No 3135

[HA03] HE, Yihong ; AREF, Amjad J.: An optimization design procedure for fiber reinforced polymer web-core sandwich bridge deck systems. In: *Composite Structures* 60 (2003), p. 183—195

[Hän76] HÄNSCH, H.: Anwendung der Klebetechnik zur Schnellmontage einer Trägerrost-Verbundbrücke. In: *Die Straße* (1976), January, no. 1, p. 27–30

[Hen01] HENRY, Scott D. (editor): *ASM Handbook – Composites.* Volume 21. 2nd printing. Material Park, Ohio 44073-0002 : ASM International®, 2001

[HK68] HÄNSCH, H. ; KRÄMER, W.: Versuche mit geklebten Verbundkonstruktionen. In: *Die Straße* (1968), March, no. 3, p. 137–141

[Hol94] HOLLAWAY, L. (editor): *Handbook of polymer composites for engineers.* 1. Cambridge, England : British Plastics Federation, Woodhead publishing limited, 1994

[HR00] HUMAR, Jagmohan L. (editor) ; RAZAQPUR, A. G. (editor): *Advanced Composite Materials in Bridges and Structures.* Ottawa, Ontario, Canada : The Canadian Society for Civil Engineering, August 2000 (3rd International Conference). – ISBN 0–7709–0447–5

[HS98a] HART-SMITH, L. J.: Predictions of a generalized maximum-shear-stress failure criterion for certain fibrous composite laminates. In: *Composites Science and Technology* 58 (1998), p. 1179–1208

[HS98b] HART-SMITH, L. J.: Predictions of the original and truncated maximum-strain failure modells for certain fibrous composite laminates. In: *Composites Science and Technology* 58 (1998), p. 1151–1178

[HS02] HART-SMITH, L. J.: Expanding the capabilities of the ten-percent rule for predicting the strength of fibre-polymer composites. In: *Composites Science and Technology* 62 (2002), p. 1515–1544

[Kar96] KARBHARI, V.M.: *Fiber reinforced composites decks for infrastructure renewal.* `In:` [EB96]. – ISBN 0–921303–64–5

[KCDD01] KELLER, Thomas ; DE CASTRO, Julia ; DOOLEY, Sean ; DUBOIS, V.: Anwendung von Faserverbundstoffen im Brückenbau – Sachstand mit

Anwendungs- und Forschungsempfehlungen / Eidgenössisches Departement für Umwelt, Verkehr, Energie und Kommunikation / Bundesamt für Strassen. Lausanne, 2001. – technical report

[KCS04] Keller, Thomas ; de Castro, Julia ; Schollmayer, Martin: Adhesively Bonded and Translucent Glass Fiber Reinforced Polymer Sandwich Girders. In: *Journal of Composites for Construction* 8 (2004), September/October, no. 5, p. 461–470. – http://dx.doi.org/10.1061/(ASCE)1090-0268(2004)8:5(461)

[KG05a] Keller, Thomas ; Gürtler, Herbert: Composite action and adhesive bond between FRP bridge decks and main girders. In: *Journal of Composites for Construction (ASCE)* 9 (2005), July/August, no. Issue 4, p. 360–368. – http://dx.doi.org/10.1061/(ASCE)1090-0268(2005)9:4(360)

[KG05b] Keller, Thomas ; Gürtler, Herbert: Quasi-static and fatigue performance of a cellular FRP bridge deck adhesively bonded to steel girders. In: *Composite Structures* 70 (2005), October, no. Issue 4, p. 484–496. – http://dx.doi.org/10.1016/j.compstruct.2004.09.028

[Kla02] Klapp, Oliver: *Mechanisches Verhalten elastomerer Klebeverbindungen.* Kassel, Universität Kassel, Diss., June 2002

[Klu03] Klug, Uwe: *Bemessung und Test einer DuraSpan 766 Brückendeckplatte*, École Polytechnique Fédérale de Lausanne, submitted at the Technical University of Darmstadt, Diplomarbeit, January 2003

[Krä69] Krämer, W.: Straßenbrücke mit Stahlbetonfertigteilen im Klebeverbund. In: *Die Straße* (1969), March, no. 3, p. 121–125

[KS04] Keller, Thomas ; Schollmayer, Martin: Plate bending behavior of a pultruded GFRP bridge deck system. In: *Composite Structures* (2004), June, no. 64, p. 285–295. – http://dx.doi.org/10.1016/j.compstruct.2003.08.011

[KS06] Keller, Thomas ; Schollmayer, Martin: In-plane tensile performance of a cellular FRP bridge deck acting as top chord of continuous bridge girders. In: *Composite Structures* 72 (2006), January, p. 130–140. – http://dx.doi.org/doi:10.1016/j.compstruct.2004.11.003

[KS09] Keller, Thomas ; Schollmayer, Martin: Through-thickness performance of adhesive joints between FRP bridge decks and steel girders. In: *Composite Structures* 87 (2009), February, no. 3, p. 232–241

[KSB$^+$00] Karbhari, V. ; Seible, F. ; Burgueño, R. ; Davol, A. ; Wernli, M. ; Zhao, L.: Structural characterization of fiber-reinforced composite short- and medium-span bridge systems. In: *Applied Composite Materials* 7 (2000), p. 151–182

[KSC] Kansas Structural Composites, Inc. *Kansas Structural Composites homepage — http://www.ksci.com/*

[LCC$^+$02] Luke, Sam ; Canning, Lee ; Collins, Simon ; Knudsen, Eric ; Brown, Peter ; Taljsten, Bjorn ; Olofsson, Ingvar: The development of an advanced composite bridge decking system – Project *ASSET*. In: *Structural Engineering International* 12 (2002), May, no. 2, p. 76–79

[LHTH95] Lee, J. ; Holloway, L. ; Thorne, A. ; Head, P.: The structural characteristics of a polymer composite cellular box ceam in bending. In: *Construction and Building Materials* 9 (1995), no. 6, p. 333–340

[mmc05] *DuraSpan – fiber-reinforced polymer bridge deck systems.* May 2005

[OH96] Kap. 8 A Stahlbau nach DIN 18 800 In: Oberegge, Otto ; Hockelmann, Hans-Peter: *Stahlbau nach DIN 18 800.* `In:` [Sch96]

[Opp05] Oppel, Sebastian: *Design of a temporary road bridge with an FRP deck adhesively bonded to steel main girders.* Lausanne, École Polytechnique Fédérale de Lausanne, submitted at the Technical University of Darmstadt, Diplomarbeit, January 2005

[PA91] Plecnik, J. ; Azar, W.: Structural Components, Highway Bridge Deck Applications. In: *International Enzyclopedia of Composites 6*, 1991, p. 430–445

[Pet98] Petersen, Christian: *Stahlbau.* Braunschweig : Friedr. Vieweg & Sohn Verlagsgesellschaft mbH, 1998. – ISBN 3–528–08837–0

[Puc96] Puck, A.: *Festigkeitsanalyse von Faser-Matrix-Laminaten: Modelle für die Praxis.* München : Carl Hanser Verlag, 1996. – ISBN 3–446–18194–6

[RBD04] Righman, Jennifer ; Barth, Karl ; Davalos, Julio: Development of an efficient connector system for fiber reinforced polymer bridge decks to steel girders. In: *Journal of Composites for Construction* 8 (2004), August, no. 4, p. 279–288

[RCL72] Roik, Karlheinz ; Carl, Jürgen ; Lindner, Joachim: *Biegetorsionsprobleme gerader dünnwandiger Stäbe.* 1st edition. Berlin : Verlag von Wilhelm Ernst & Sohn, 1972. – ISBN 34–33–00510–9

[Sch43] Schleicher, Ferdinand (editor): *Taschenbuch für Bauingenieure.* Berlin : Springer-Verlag, 1943

[Sch89] Schardt, Richard: *Verallgemeinerte Technische Biegetheorie.* 1st edition. Darmstadt : Springer-Verlag, 1989. – ISBN 3–540–51339–6

[Sch96] Schneider, Klaus-Jürgen (editor): *Bautabellen für Ingenieure.* 12th edition. Düsseldorf : Werner-Verlag, 1996

[Sei01] Seible, Frieder: Designing with FRP Composites in the Civil Structural Environment. In: [Ten01a], p. 73–84

[SG02] Solomon, G. ; Godwin, G.: Expanded use of composite deck projects in USA. In: *Structural Engineering International* 2 (2002), p. 102–104

[SK99] Strehler, B. ; Künzle, Otto: Static and Dynamic Testing of Fiber-Reinforced Bridge Girders. In: *Structural Engineering International* (1999), no. 4, p. 300–301

[SKZH01] Seible, F. ; Karbhari, V. ; Zhao, L. ; Hose, Y.: *Development and implementation of modular bridge systems.* `In:` [FJF01]. – ISBN 90 2651 858 7

[Sta05] Stahlbau Zentrum Schweiz (editor): *C5/05 steelwork – Konstruktionstafeln.* Revision 2005. Zürich : Verlag Stahlbau Zentrum Schweiz, 2005

[Str99] Stroetmann, Richard: *Zur Stabilität räumlicher Tragsysteme mit* `I`*-Profilen nach der Methode der finiten Elemente.* Darmstadt, T.U. Darmstadt, Institut für Stahlbau und Werkstoffmechanik, Diss., 1999

[TD64] Trittler, G. ; Dörnen, K.: Die vorgespannte Klebeverbindung (VK-Verbindung), eine Weiterentwicklung der Verbindungstechnik im Stahlbau. In: *Der Stahlbau* 33 (1964), September, no. 9, p. 257–268

[Ten01a] Teng, J. G. (editor): *FRP Composites in Civil Engineering – Proceedings of the International Conference on FRP Composites in Civil Engineering.* Volume 1. Hong Kong : Elsevier Science Ltd., 12th to 15th December 2001

[Ten01b] Teng, J. G. (editor): *FRP Composites in Civil Engineering – Proceedings of the International Conference on FRP Composites in Civil Engineering.* Volume 2. Hong Kong : Elsevier Science Ltd., 12th to 15th December 2001

[THPR04] Turner, Michael K. ; Harries, Kent A. ; Petrou, Michael F. ; Rizos, Dimitris: In situ structural evaluation of a GFRP bridge deck system. In: *Composite Structures* (2004), August, no. 65, p. 157–165

[TL00] Temeles, A. ; Lesko, J.: Composite plate & tube bridge deck design: Evaluation in the Troutville, Virginia West Station Test Bed. In: [HR00], p. 801–808. – ISBN 0–7709–0447–5

[TW71] Tsai, S. W. ; Wu, E. M.: A general theory of strength for anisotropic materials. In: *Journal of Composite Materials* 5 (1971), p. 58–81

[Val04] Vallée, Till: *Adhesively Bonded Lap Joints of Pultruded GFRP Shapes*. Lausanne, École Polytechnique Fédérale de Lausanne, Thèse pour l'obtention du grade de docteur ès sciences, April 2004. – Thèse No 2964

[ZÅBB01] Zetterberg, Tobias ; Åström, B. T. ; Bäcklund, Jan ; Burman, Magnus: On design of joints between composite profiles for bridge deck applications. In: *Composite Structures* 51 (2001), p. 83–91

[ZCLC01] Zhou, Aixi ; Coleman, Jason T. ; Lesko, John J. ; Cousins, Thomas E.: Structural analysis of FRP bridge deck systems from adhesively bonded pultrusions. In: [Ten01b],

[ZK04] Zhou, Aixi ; Keller, Thomas: Connections of Fiber Reinforced Polymer Bridge Decks. In: *Metropolitan Habitats and Infrastructure – IABSE Symposium 2004, Shanghai* (2004), September 22–24

[ZKHS04] Zhao, Lei ; Karbhari, V. M. ; Hegemier, G. A. ; Seible, F.: Connection of concrete barrier rails to FRP bridge decks. In: *Composites Part B: Engineering* 35 (2004), p. 269–278

List of Figures

1.1 Pultruded FRP bridge deck on steel girders 4
1.2 Adhesively-bonded connection between steel girder and bridge deck . 5
1.3 Uplift force and bending moment in adhesive layer 5
1.4 Failure in surface mat layers of pultruded FRP material 7
1.5 Methodology and organization 10

2.1 Different FRP bridge deck systems 15
2.2 Cross section of the *Kings Stormwater* bridge 16
2.3 Cross section of *West Mill* bridge 16
2.4 Cross section of girder with shear stud connections 18
2.5 Deck-to-girder connection using dowels 18
2.6 Hook bolt connection 19
2.7 Bolted connection 19
2.8 Cross section of girder and clamped connection 20
2.9 Hybrid bridge girder in four-point bending test 21

3.1 FE model of reference bridge 27
3.2 Through-thickness tensile stress distribution in adhesive layer 27
3.3 Structural system of test set-up 28
3.4 Set-up for *C2fat*, *C2-1* and *C3-1* 29
3.5 Roller support at $\ell/2$ 29
3.6 *HEM* geometry 30
3.7 FE model of test set-up 31
3.8 Top view of steel girder surface 31
3.9 Normalized stress distribution in adhesive layer (FE model) 32
3.10 Normalized stress distribution in adhesive layer (FE model) 32
3.11 Cross section of a *DuraSpan*$^{\text{TM}}$ *766* element 33
3.12 Sample after pyrolysis 34
3.13 Microscopical cut 35
3.14 Elevation of specimen in set-up 38
3.15 Detail of Figure 3.14 38
3.16 Measurement instruments 39
3.17 Displacement transducers (inner side) 39
3.18 Measurement instruments 40

3.19 Displacement transducers (outer side) 40
3.20 Average deflection at loading points 43
3.21 Surface of failed adhesive connection on steel girder *(C1-1)* 44
3.22 Displacement distribution 45
3.24 Surface of failed adhesive connection on steel girder (*C1-2*) 46
3.25 Load-displacement curves of transducers *(C2-1)* 47
3.26 Displacement distribution in bonded connection 47
3.27 Surface of failed connection, specimen *C2-1* 48
3.28 Specimen *C2-2*: transducer # 5 49

3.29 Displacement distribution 49
3.30 Failed adhesively-bonded connection (*C2-2*) 50
3.31 Load-displacement curves of transducers *(C3-1)* 51
3.32 Displacement distribution 51
3.33 Failed bonded connection (*C3-1*) 52
3.34 Load-displacement curves of transducers *(C3-2)* 53
3.35 Displacement distribution 53
3.36 Failed bonded connection (*C3-2*) 54
3.37 Fatigue test *C2-fat* 55
3.38 Comparison of calculated and measured displacements 56
3.39 Comparison of calculated and measured displacements 57

4.1 Shear-Tensile Interaction Device 60
4.2 Diagram of Shear-Tensile Interaction Device 60
4.3 Material strength diagram based on experimentally obtained values . 62

4.4 Failure modes of STI coupons (tensile-dominated) 64
4.5 Failure modes of STI coupons (shear-dominated) 65

5.1 Influence of steel girder's torsional stiffness on bending moment . . . 72
5.2 Components of φ 74
5.3 Steel girder loaded with a pair of forces 76
5.4 Key points of cross section in FE model 77
5.5 Meshed girder 77
5.6 Deflections of upper flange 80
5.7 Influence of variation of web thicknesses on torsional stiffness of girder 81

5.8 Influence of stiffener height at supports 82

5.9 Influence of number of stiffeners on k_ϑ 83

5.10 Model used for analytical and FE calculations 83
5.11 Analytic and FE results for torsional stiffnesses 85
5.12 Cross section of a bridge system with bonded connections 86
5.13 Load setting for the maximum $\Delta M/F_{\mathrm{up}}$ ratio with tension 88
5.14 Load setting for maximum tensile stress in the adhesive 88

6.1 Static system 93
6.2 Symmetric 3D-model 94
6.3 FE models with different web inclinations 95
6.4 Distribution of σ_z stresses in x-direction in adhesive layer 96
6.5 κ_{σ_z} depending on different web inclinations 96

6.6 Modeled section 97
6.7 Model with vertical webs: *VS*-geometry 98
6.8 Model with inclined webs: *IS*-geometry 98
6.9 Model with inclined webs: *DS*-geometry 99
6.10 Stress distribution in FRP-adhesive interface (*VS*-geometry) 101
6.11 Stress distribution of vertical through-thickness stresses 101
6.12 Normalized stress distribution in FRP-adhesive interface (*DS*-geometry) 102
6.13 Stress distribution in longitudinal direction 102
6.14 Effective width b_{bs} 105
6.15 Comparison of FE results and analytical stress distribution 106
6.16 Comparison of FE results and analytical stress distribution 106
6.17 Comparison of FE results and analytical stress distribution 107
6.18 Comparison of FE results and analytical stress distribution 107
6.19 Determination of n_x 108
6.20 Simplified stress distribution in y-direction 110
6.21 Analytically determined stress distribution in surface material . . . 111
6.22 Stress distribution shapes 113
6.23 Loading of FE model 115
6.24 Stress distribution shapes in adhesive layer 115
6.25 Superposition of distributions due to uplift force and moment 117

7.1 Strain and stress distribution in steel girder and FRP bridge deck . 122

7.2 Strain distribution in steel girder and FRP bridge decks 123
7.3 Original and adapted cross sections 124
7.4 Normalized through-thickness tensile stresses 126

7.5 Material resistance and shear-tensile stress combinations 128

A.1 Set-up for *C1-1*, *C1-2*, *C2-2* and *C3-2* 139
A.2 Roughened surface before bonding 140
A.3 Load-displacement curves on outer side of adhesive connection *(C1-1)* 142
A.4 Load-displacement curves on inner side of adhesive connection *(C1-2)* 143
A.5 Load-displacement curves on outer side of adhesive connection *(C1-2)* 144
A.6 Air bubble (*C2-1*) 145
A.7 Load-displacement curves on inner side of adhesive connection *(C2-1)* 146
A.8 Load-displacement curves on outer side of adhesive connection *(C2-1)* 147
A.9 Failed adhesively-bonded connection (*C2-2*) 148
A.10 Load-displacement curves on inner side of adhesive connection *(C2-2)* 149
A.11 Load-displacement curves on outer side of adhesive connection *(C2-2)* 150
A.12 Load-displacement curves on inner side of adhesive connection *(C3-1)* 151
A.13 Load-displacement curves on outer side of adhesive connection *(C3-1)* 152
A.14 Fiber-tear failure on surface and adhesive failure 153
A.15 Surface of failed adhesive layer *(C3-2)* 154
A.16 Failed adhesively-bonded connection (*C3-2*) 154
A.17 Load-displacement curves on inner side of adhesive connection *(C3-2)* 155
A.18 Load-displacement curves on outer side of adhesive connection *(C3-2)* 156

C.1 Comparison of FE results and analytical stress distribution 163
C.2 Stress distribution shapes in adhesive layer of geometry $VS^{06/0}_{280/30}$ . . 164
C.3 Stress distribution shapes in adhesive layer of geometry $VS^{06/0}_{300/33}$ . . 164
C.4 Stress distribution shapes in adhesive layer of geometry $VS^{06/0}_{340/36}$ . . 165
C.5 Stress distribution shapes in adhesive layer of geometry $VS^{06/0}_{370/40}$ . . 165
C.6 Stress distribution shapes in adhesive layer of geometry $VS^{08/0}_{230/24}$ . . 166
C.7 Stress distribution shapes in adhesive layer of geometry $VS^{08/0}_{400/40}$ . . 166
C.8 Stress distribution shapes in adhesive layer of geometry $VS^{09/0}_{310/35}$ . . 167
C.9 Stress distribution shapes in adhesive layer of geometry $VS^{10/0}_{270/34}$ . . 167
C.10 Stress distribution shapes in adhesive layer of geometry $VS^{10/0}_{450/40}$ . . 168
C.11 Stress distribution shapes in adhesive layer of geometry $VS^{11/0}_{220/32}$ . . 168
C.12 Stress distribution shapes in adhesive layer of geometry $VS^{12/0}_{350/32}$ . . 169
C.13 Stress distribution shapes in adhesive layer of geometry $VS^{12/0}_{350/37}$ . . 169
C.14 Stress distribution shapes in adhesive layer of geometry $VS^{13/0}_{300/29}$ . . 170
C.15 Stress distribution shapes in adhesive layer of geometry $VS^{13/0}_{420/50}$ . . 170
C.16 Stress distribution shapes in adhesive layer of geometry $VS^{14/0}_{270/29}$ . . 171

C.17 Stress distribution shapes in adhesive layer of geometry $VS^{15/0}_{440/50}$ . . 171
C.18 Stress distribution shapes in adhesive layer of geometry $VS^{17/0}_{350/45}$ . . 172
C.19 Stress distribution shapes in adhesive layer of geometry $VS^{18/0}_{320/40}$ . . 172
C.20 Stress distribution shapes in adhesive layer of geometry $VS^{20/0}_{270/30}$ . . 173
C.21 Stress distribution shapes in adhesive layer of geometry $VS^{21/0}_{240/25}$ . . 173
C.22 Stress distribution shapes in adhesive layer 174
C.23 Stress distribution shapes in adhesive layer 174
C.24 Superposition of distributions due to uplift force and moment 175
C.25 Superposition of distributions due to uplift force and moment 176
C.26 Superposition of distributions due to uplift force and moment 177
C.27 Superposition of distributions due to uplift force and moment 178
C.28 Superposition of distributions due to uplift force and moment 179

List of Tables

3.1 *HEM 200* steel girder geometry 30
3.2 Material properties of fibers and resin 34
3.3 Mechanical properties of *DuraSpan 766* deck 35
3.4 Specimens and test dates 36
3.5 Material properties of *Sikadur 330* adhesive 37
3.6 Experimental results 42

4.1 Experimental values 63

5.1 Dimensions of modeled girder 78
5.2 Dimensions of modeled girder 84

5.3 Maximum $\Delta M/F_{\mathrm{up}}$-ratio with tension in the adhesive 87
5.4 Maximum tension in adhesive layer 89

6.1 Bridge deck geometry of beam model 95
6.2 Specific values used for calculation of *VS*-, *IS*- and *DS*-geometries . 100
6.3 Geometric values for determination of μ_{σ_z} 117
6.4 Comparison of experimental and computed results 119
6.5 Experimental results 119

7.1 Geometric data concerning steel girder 124

A.1 Calibration list of experiments *C1-1* and *C1-2* 140
A.2 Calibration list of experiments *C2-1* and *C3-1* 141
A.3 Calibration list of experiments *C2-2* and *C3-2* 141
A.4 Comparison of measured and calculated deflections at loading point 157
A.5 Comparison of measured and calculated deflections (# 3 and # 4) . . 157
A.6 Comparison of measured and calculated deflections (# 5 to # 9) . . . 158
A.7 Comparison of measured and calculated deflections (# 10 to # 14) . 159

B.1 Torsional stiffnesses for a girder ($\ell = 10\,\mathrm{m}$) and various dimensions . 161
B.2 Torsional stiffnesses for a girder ($\ell = 15\,\mathrm{m}$) and various dimensions . 161

B.3 Torsional stiffnesses for a girder ($\ell = 20\,\mathrm{m}$) and various dimensions . 162
B.4 Torsional stiffnesses for a girder ($\ell = 25\,\mathrm{m}$) and various dimensions . 162
B.5 Torsional stiffnesses for a girder ($\ell = 30\,\mathrm{m}$) and various dimensions . 162

Nomenclatures

Abbreviations

CLT – classical lamination theory
cp. – compare
CSM – continuous strand mats
FEA – finite element analysis
FEM – finite element method
FRP – fiber-reinforced polymers
GFRP – glass-fiber reinforced polymers
max – maximum
MDU – modular deck unit
SF – stitched fabrics
SLS – serviceability limit state
STD – shear tensile device
UD – unidirectional
ULS – ultimate limit state

Latin letters

A – area
b – width
c – core
d – static height of bridge deck
b_f – steel flange width
E – Young's modulus
e – excentricity
F – load
F_u – failure load
f – flange
$\mathfrak{F}$ – stress failure criterion
G – shear modulus
h – steel girder height

H_{ds} – bridge deck height
I – moment of inertia
I_T – 2^{nd} degree torsional moment of inertia
I_ω – 2^{nd} degree warping moment of inertia
ℓ – length
l_m – distance between two bridge deck webs
M – matrix
P – load
R – resistance
r – curvature in angle between web and flange of a I-cross-section
S – solicitation
S_z – first moment of area
s – standard deviation
t – thickness
t_{adh} – adhesive thickness
t_f – steel flange thickness
t_w – steel web thickness
V_F – fiber volume fractions, $V_F = \frac{w}{\rho \cdot t}$
V_M – matrix volume fractions
w – weight
x, y, z – global cartesian coordinate directions

Subscript characters

adh – adhesive; e. g. t_{adh} for adhesive thickness
ds – bridge deck
f – steel flange
f, b – bottom steel flange
f, t – top steel flange
p – panel
s – stiffener
sw – bridge deck web
u – ultimate
w – web

Greek letters

α_{sw} – inclination of the bridge deck webs
β – angle
γ – partial safety factor

Δ – difference
ε – strain
ζ – local cartesian coordinate direction
ϑ – torsion
κ_{σ_z} – web inclination factor
μ – factor of maximum over mean through-thickness stress
ξ – local cartesian coordinate direction
ρ – density $\left[\frac{\text{weight}}{\text{volume}}\right]$
σ – axial stress
$\sigma_{z,u}^{+}$ – through-thickness tensile strength
$\bar{\sigma}$, σ_m – mean axial stresses
τ – shear stress
$\tau_{xz,u}$ – shear x-z in-plane strength
φ – rotation

Index

– Symbols –

γ_M (partial safety factor) 66
σ_z-stresses
    analytical determination 104–114

– A –

abstract iii
    (in german) v
adhesive connection
    description 3
    resistance 127
appendix 139–180

– B –

bridge decks 13
    connection methods 17
        bolts 18
        bonding 20
        clamps 19
        shear studs 17
    DuraSpan 766 bridge deck 33
    pultruded bridge decks 14
    sandwich bridge decks 17
bridge system 4

– C –

concept for a design method 121
conclusions 131

– D –

design method 121
DuraSpan 766 bridge deck 33

– E –

experiments
    coupons 59
    full-scale adhesive connection 25
        materials 33
        specimens 36
    shear-tensile strength 59

– F –

full-scale adhesive connection experiments 25

– I –

introduction 3

– L –

literature review 13

– N –

nomenclatures 197

– P –

partial safety factor γ_M 66
preface i

– S –

Shear-Tensile Interaction Device 59
shear-tensile strength 59
state of the art 13
STI-Device 59

– Z –

Zusammenfassung v

Curriculum vitæ

Martin Schollmayer

Date of birth	October 23rd, 1974 in Würzburg, Germany
Nationality	German

Professional experience

since 02/2005	Walt+Galmarini AG, Zurich Main projects: Letzigrund Stadium in Zurich, 350-m-span cable-stayed Grimselsee bridge in the Bernese Alps, 103-m-span pedestrian suspension bridge, 136-m-tall Prime Tower in Zurich
03/2002–01/2005	École Polytechnique Fédérale de Lausanne (EPFL), research assistant/ PhD student at the Composite Construction Laboratory (CCLab)
08/2001–10/2001	Philipp Holzmann AG, International Division, Frankfurt, part-time post
10/2000–11/2000	Associated Consulting Engineers S.A.L., Beirut (Lebanon), internship
10/1999–08/2001	Technische Universität Darmstadt, student research assistant at the Institute of Structural Analysis
03/1997	Arcadis, Trischler and Partners, office for geotechnical engineering, Darmstadt, internship

Education

10/2001–01/2002	École Polytechnique Fédérale de Lausanne (EPFL), diploma thesis
09/1998–07/1999	Politecnico di Torino, exchange year
10/1995–01/2002	Technische Universität Darmstadt, civil engineering studies leading to engineer's degree
08/1985–06/1994	Theresianum Gymnasium Mainz

Selected publications

Through-thickness performance of adhesive joints between FRP bridge decks and steel girders Thomas Keller and Martin Schollmayer, Composite Structures, article in press, `http://dx.doi.org/10.1016/j.compstruct.2008.01.007`

Das Letzigrundstadion in Zürich Carlo Galmarini, Martin Schollmayer and Martin Mensinger, Stahlbau, Volume 77, Issue 6, June 2008, pp. 391–398, `http://dx.doi.org/doi:10.1002/stab.200810052`

Stadion Letzigrund – tanzende *Verbundstützen* Martin Schollmayer, Stahl-Beton-Verbund im Hochbau – Dauerhafte und innovative Tragwerke, Dokumentation SIA D 0219, Schweizerischer Ingenieur- und Architektenverein, 2007, pp. 81–84

In-plane tensile performance of a cellular FRP bridge deck acting as top chord of continuous bridge girders Thomas Keller and Martin Schollmayer, Composite Structures, Volume 72, Issue 1, January 2006, pp. 130–140, `http://dx.doi.org/doi:10.1016/j.compstruct.2004.11.003`

Adhesively bonded and translucent glass fiber reinforced plastic sandwich girders Thomas Keller, Julia de Castro and Martin Schollmayer, Journal of Composites for Construction, Volume 8, Issue 5, September/October 2004, pp. 461–470, `http://dx.doi.org/10.1061/(ASCE)1090-0268(2004)8:5(461)` — awarded as the Best Applied Research Paper published in the Journal of Composites for Construction in 2004

Plate bending behavior of a pultruded GFRP bridge deck system Thomas Keller and Martin Schollmayer, Composite Structures, Volume 64, Issues 3–4, June 2004, pp. 285–295, `http://dx.doi.org/10.1016/j.compstruct.2003.08.011`